Study of He-II Spallation UCN Source

Ryohei Matsumiya

Department of Physics
Graduate School of Science
Osaka University, Osaka, JAPAN

1-1 Machikaneyama-cho, Toyonaka, Osaka 560-0043, Japan
Ryohei.Matsumiya@rcnp.osaka-u.ac.jp

Submitted: June 2013

Abstract

Ultracold neutron (UCN) is an extremely cold neutron and can be confined in a vessel. So, UCN is useful for fundamental physics researches related to neutrons. Among them, we pay attention to the neutron electric dipole moment (EDM).

The neutron EDM arise from the CP violation which also gives rise to the baryon asymmetry in the universe, and is expected to be one of the most powerful test for new theories beyond the standard model of particle physics such as supersymmetric theory (SUSY) proposed to solve these problems such as baryon asymmetry in the universe. The measurement of the neutron EDM has been continued since 1950 ' s, but the finite value has not been discovered yet.

Recent neutron EDM measurements use UCN confined in a vessel and determine the resonance frequency as a result of the spin manipulation based on the nuclear magnetic resonance. So, the UCN density at a certain critical energy inside the vessel determines the precision of EDM. Conventional UCN sources extract UCN from a small fraction of low energy neutron flux after moderated in a cold source such as liquid heavy hydrogen located in a reactor. Since the UCN density obtained by this technique is saturated, a new kind of UCN production method is necessary to obtain higher UCN density at a certain critical energy.

Superthermal method is proposed as such a new method of UCN production. In this method, UCN is produced by phonon scattering of cold neutrons in superfluid helium (He-II). High UCN production rate is expected by use of the phase space of phonons to moderate neutrons.

We have been developing a high intensity UCN source which couples the superthermal method and a spallation neutron source at RCNP. Neutrons are produced by spallation reaction induced by a proton beam accelerated by the ring cyclotron, and moderated by the room-temperature and the solid heavy water moderators, then converted to UCN in He-II by phonon scattering. We developed a cryostat to cool down the heavy water and He-II, and succeeded to produce UCN in He-II. Then, we improved the cooling power of the cryostat by reducing heat load, removed ^{3}He impurity in He-II, and developed proper treatment of the UCN guide. As a result, high UCN density of 26 UCN cm^{-3} at critical energy 90 neV was achieved at the exit of the UCN source with 400 W proton beam. This is the world competitive UCN density. The UCN production rate in He-II was estimated to be 4 UCN cm^{-3} s^{-1}.

We observed the energy spectrum of UCN extracted from the UCN source. No measurement of energy spectrum of UCN produced in a superthermal UCN source had been reported so far. We confined UCN in a cylindrical vessel with a top plate which absorbs UCN. UCN critical energy in the vessel can be adjusted by setting the height of the top plate. We obtained

the energy spectrum in the vessel from the height dependence of UCN counts. The obtained energy spectrum is well reproduced by the simulation with Geant4 based UCN transport code, assuming the energy spectrum of UCN to be proportional to square root of UCN energy at the UCN source based on the uniform distribution in the phase space.

In the present study, the world competitive UCN density and the proper analysis method for UCN transport simulation was established. This study leads to the more intense UCN source and the precise measurement of neutron EDM in the future.

Acknowledgement

I would like to express my gratitude to my thesis advisor, Prof. Kensaku Matsuta. I also thank members of the KEK-RCNP UCN group, Prof. Yasuhiro Masuda, Prof. Kichiji Hatanaka, Dr. Shinsuke Kawasaki, Prof. Sun-Chan Jeong, Dr. Yutaka Watanabe and Dr. Mototsugu Mihara.

Special thanks to Prof. Toshio Kitagaki for your advises about the UCN counter.

I am grateful to Prof. Toshikazu Adachi for many advises on the Monte Carlo simulation with Geant4-UCN code.

Many thanks to ICEPP group of the University of Tokyo, Prof. Toru Yamashita, Dr. Tamaki Yoshioka, Hitoshi Hano, Yasuko Hisamatsu, Dr. Hideyuki Oide, Dr. Hidetoshi Otono and Toru Suehiro, for collaborating to my UCN storage experiment and the UCN polarization experiment.

I am grateful to the members of North Carolina State University, Prof. Robert Golub, Dr. Ekaterina Korobkina, Dr. Adam Holley and Dr. Grant Palmquist, for collaborating to my UCN storage experiment.

I would like to thank the members from TRIUMF, the University of Winnipeg and the University of Northern British Columbia, Prof. Jeff Martin, Dr. Charles Davis, Dr. Larry Lee, Dr. Lothar Buchmann, David Harrison, Troy Dawson, Dr. Des Ramsay, Prof. William van Oers, Prof. Elie Korkmaz, Dr. Andy Miller, Dr. Chris Bidinosti and Dr. Akira Konaka. I hope the 2nd generation He-II spallation UCN source will work and the KEK-RCNP-TRIUMF collaboration for the neutron EDM measurement will succeed.

Special thanks to the present and past members of Nuclear and Solid State Physics group (Van der Graaff group) of Osaka University, especially, Dr. Daiki Nishimura, Mr. Michio Sakamoto, Mr. Taro Sakurai and Mr. Yusuke Morita, for participating our experiment or making the appatuses.

Lastly, many thanks to my family and my friends, especially my parents, for their understanding and support.

Contents

Chapter 1

Introduction

1.1 Ultracold Neutron

Ultracold neutrons (UCN) are extremely slow neutrons with energies below ~ 300 neV which can be confined in a material vessel. These energies correspond to velocities below ~ 8 m/s. Since UCN can be confined by material bottles or magnetic potential or gravity, UCN is very useful to study fundamental physics with neutrons.

It was E. Fermi who found for the first time that slow neutrons could be totally reflected by materials, when their kinetic energies E and glancing angle θ satisfy the following condition,

$$E \sin^2 \theta \leq V_F, \text{ or } \sin\theta \leq \sin\theta_c = \left(\frac{V_F}{E}\right)^{1/2} \tag{1.1}$$

where critical angle θ_c and effective potential V_F depends on materials.

The effective potential V_F in this formula is called "Fermi pseudo potential". Fermi and Zinn [1], and Fermi and Marshall [2] first performed the experimental demonstration of this effect, and found the typical value of V_F in the order of 10^2 neV or less.

Neutrons with energies smaller than V_F are totally reflected [1] on the material surfaces, regardless of their glancing angle. Thus UCN are these slow neutrons satisfying $E \leq V_F$ and they can be stored in a material vessel. The highest Fermi pseudo potential 335 neV is given by ^{58}Ni.

1.2 Neutron Electric Dipole Moment

One of the exciting physics which can be carried out by use of UCN is the measurement of neutron electric dipole moment (neutron EDM, nEDM), which gives us an important clue for the baryogenesis in the universe.

The measurements of SDSS (Sloan Digital Sky Survey) [3] and WMAP (Wilkinson Microwave Anisotropy Probe) [4] concluded that the ratio of the baryon number density n_B

[1] $V_F = 2\pi\hbar^2 N b_c/m_n$ where m_n, N and b_c are the neutron mass, the number density of the material and the bound coherent scattering length of the scatterer nucleus.

to the CMB (Cosmic Microwave Background) photon number density n_γ in the universe is $n_B/n_\gamma = (6.3 \pm 0.3) \times 10^{-10}$. On the other hand, the standard model of particle physics (the SM) predicts much smaller ratio of $\sim 10^{-26}$, showing clear contradiction. To solve this contradiction, some theoretical extensions were applied to the SM. The supersymmetric theory (SUSY) is one of those extensions.

The neutron EDM is one of the good tests of these new physics beyond SM, breaking time reversal symmetry (T-symmetry), hence CP symmetry. The SUSY predicts the nEDM in the range of $10^{-26\sim28}$ e cm which is about 10^3 times larger than the nEDM predicted by the SM.

The latest nEDM measurement carried out at the Institute Laue Langevin (ILL) in Grenoble, France [5], and set the upper limit of nEDM d_n to be

$$|d_n| \leq 2.9 \times 10^{-26} \ [e \text{ cm}]. \tag{1.2}$$

For the precision measurement of EDM, number of UCN counts N is crucial, since the statistical error σ_d of the neutron EDM is given by $\hbar/(2\alpha E \tau_c \sqrt{N})$, and decreases inversely proportional to square root of N, where α, E and τ_c are the neutron polarization, the electric field and the measurement time of the ramsey resonance technique [6]. Actually, the history of the upper limit to the nEDM is as shown in Fig. 1.1. Although the measurement of nEDM comes to the order of 10^{-26} e cm, and starts to set restriction to the SUSY, the improvement of the upper limit is disturbed by the statistical error limited by the UCN density. For the fixed volume of EDM cell, UCN density ρ_{ucn} should be important. We cannot simply increase the cell size to increase N for fixed ρ_{ucn}, because of another concern about systematic error. The systematic error arises mainly from the geometric phase effect (GPE) which comes from magnetic field inhomogeneity. The systematic error $d_{af\mathrm{Hg}n}$ due to GPE of atomic magnetometer (Hg in this case) in the EDM cell is given by

$$d_{af\mathrm{Hg}n} = \frac{\hbar}{8} |\gamma_n \gamma_{\mathrm{Hg}}| \frac{\partial B_{0z}}{\partial z} \frac{R^2}{c^2} \tag{1.3}$$

where γ_n and γ_{Hg} are the gyromagnetic ratio of neutron and atomic magnetometer, c is the speed of light. So, the error is proportional to both the magnetic field gradient $\partial B_{0z}/\partial z$ along the z (vertical) axis and square of the radius R [7]. To reduce the systematic error, it is necessary to reduce the radius reducing volume of the cell, instead of increasing volume. To have higher N in a small cell, improvement of the UCN density in the EDM cell is crucial.

1.3 UCN Source at ILL

Before discussing the newly developed superthermal method for efficient UCN production, conventional production technique and the history of UCN density are shown in this section.

ILL in Grenoble, France, has been the most active UCN facility for fundamental neutron research for recent 30 years. Fig. 1.2 shows the schematic view of the UCN facility at the ILL. A liquid heavy hydrogen (D_2) cold source at a temperature of 25 K is located in thermal neutron flux of 4.5×10^{14} n cm^{-2} s^{-1} from the 58 MW reactor core. After moderated by the liquid D_2

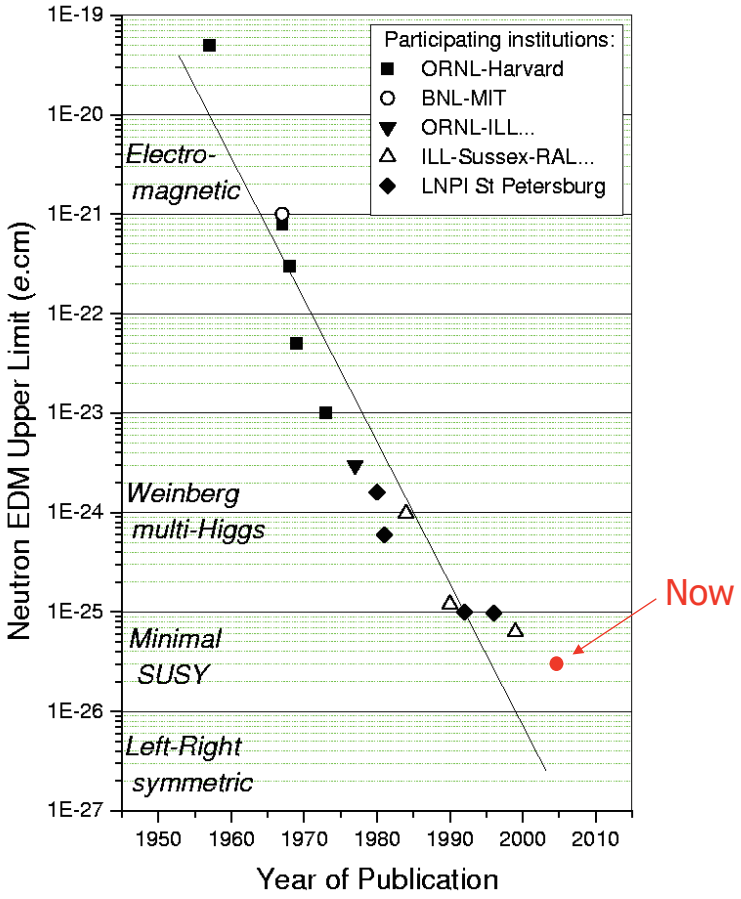

Figure 1.1: The history of the upper limit to the nEDM since 1950's. (Plot by P. Harris, University of Sussex.)

cold moderators, cold neutrons are extracted from the cold source and transported through the vertical and curved nickel guides. The cold neutrons in the guides are further decelerated by the gravity. Cold neutrons are then brought into UCN range by reflections from a set of rotating curved turbine blades called "the neutron turbine" or "the doppler shifter".

The neutron turbine blades are moving in the same direction as the incident cold neutrons with basically a half of the velocity [8]. The incident velocity is approximately 50 m/s, so the velocity of blades is set to be 25 m/s. Considering a neutron with a velocity $\mathbf{v}$ striking a wall moving in the same direction with a velocity $\mathbf{v}/2$, after the collision the neutron is moving at a velocity $2(\mathbf{v}/2) - \mathbf{v} = \mathbf{0}$ in the laboratory system.

The obtained UCN density was 19 UCN cm^{-3} with the critical energy $E_c = 200$ neV at the exit of the vertical guide system without the neutron turbine, and was 36 UCN cm^{-3} at the exit of the neutron turbine [9].

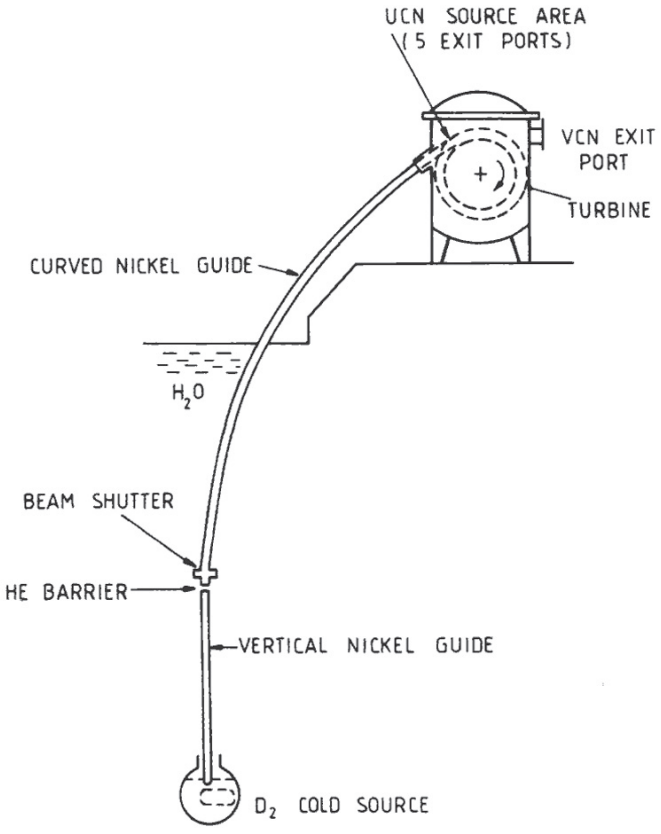

Figure 1.2: Schematic view of the UCN/VCN source at ILL. A straight and a curved nickel guide tube conduct slow neutrons ($E < 0.2$ meV) from the cold source to the neutron turbine. The straight vertical nickel guide is 5 m long. The curved nickel guide has a length of 13 m. (From ref. [8].)

As is in the case of EDM measurement, the best material Ni cannot be always used. In many cases, EDM cell is made of SiO_2 which has relatively low Fermi potential 90 neV. Since

the phase space volume is proportional to $\sqrt{E}$, hence the UCN density is proportional to $E^{3/2}$. So, the UCN density ρ_{ucn} at the ILL corresponds to be 6 UCN cm^{-3} without the turbine and 11 UCN cm^{-3} with the turbine for $E_c = 90$ neV at the beam power 58 MW.

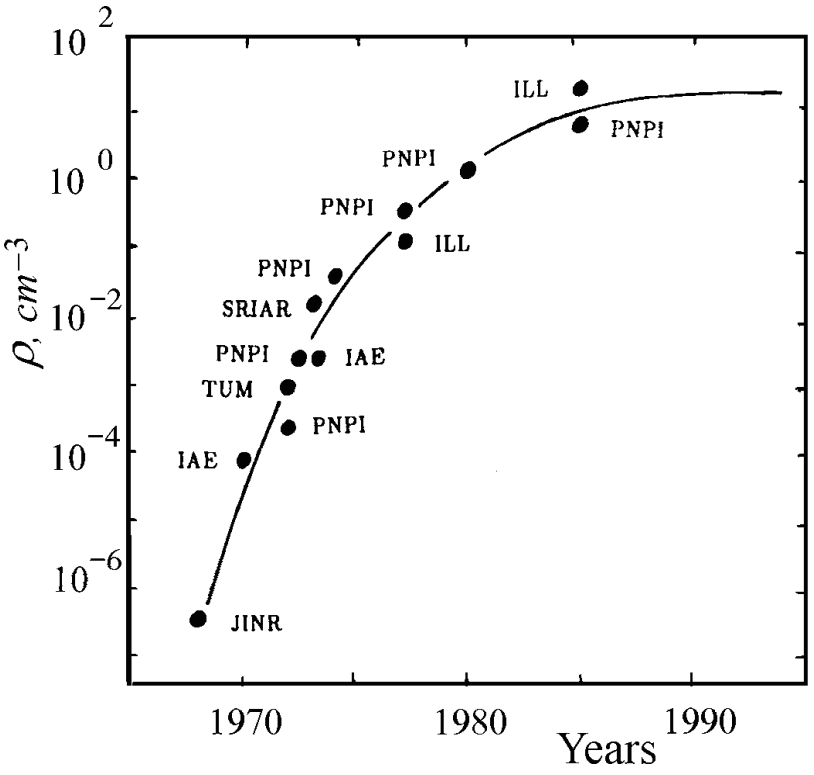

Figure 1.3: Evolution of UCN sources (Plot by A. P. Serebrov.)

Ya. B. Zeldovich pointed out the existence of UCN in a neutron source. F. L. Shapiro et al. first succeeded to extract UCN from a reactor in 1968 [10]. A. Steyerl also succeeded [11]. Since then, UCN density has been improved. Fig. 1.3 shows the history of the evolution of UCN sources since Shapiro. As shown in this figure, the maximum UCN density was saturated in the 1980's, and the ILL has been the highest intensity UCN source for recent 30 years.

The saturation of UCN density is due to the Liouville's theorem. Systems which uses the gravity potential to alter the neutron energy, e.g. transport through a vertical guide cannot produce a higher UCN density than that of the initial source. This is because the neutrons move through such systems in such a way as to keep the phase space density ρ_{ph} constant. This is a statement of the Liouville's theorem. The volume of phase space occupied by a group of particles is constant if the particles move under the action of forces which are derivable from a potential. This theorem holds in the case of reflections from a matter with a Fermi potential of V_F.

The Maxwell-Boltzmann distribution gives us the phase space density ρ_{ph} as follows.

$$\rho_{ph} = \frac{\Phi_0}{2\pi\alpha^4} \exp(-v^2/\alpha^2),\ \alpha = \left(\frac{2k_B T_n}{m}\right)^{1/2} \tag{1.4}$$

where Φ_0 is the total thermal neutron flux, and T_n is the neutron temperature. ρ_{ph} is constant for low momentum region, $v/\alpha \ll 1$. And ρ_{ph} is small outside this region. Therefore, to increase a UCN density, we have to increase the thermal neutron flux or to cool the temperature of the thermalized neutrons.

As is already explained, for the fundamental neutron experiments, a much more UCN density is necessary. Recently, a new method called "superthermal" technique is paid attention. In the following sections, this new UCN production method is introduced and the necessary development of a new generation UCN source with the superthermal method will be discussed.

1.4 Superthermal UCN Production

Superthermal UCN production was proposed by R. Golub and J. M. Pendlebury in 1977 [12]. They pointed out that UCN produced via an inelastic down-scattering process in superfluid ^{4}He (He-II) could achieve much higher UCN densities than in conventional moderators.

Here, we consider the underlying principle of a superthermal UCN source which has only two energy levels; a ground state and an excited state with an excitation energy of Δ. An incident neutron with an energy near Δ can excite the energy level of the moderator and lose almost all its energy to become an UCN. This is the "down-scattering process". However, this UCN can gain some energy (Δ or more) by interaction with the excited states of the moderator and cease to be an UCN. This is the "up-scattering process". It is necessary to minimize the up-scattering probability to maintain a high UCN density. The principle of detailed balance between the down-scattering process and the up-scattering process is given by

$$\sigma_{up} = \frac{E_{ucn} + \Delta}{E_{ucn}}\ e^{-\Delta/k_B T} \sigma_{down} \tag{1.5}$$

where σ_{up} and σ_{down} are the up- and down-scattering cross sections, and T is the temperature of the moderator. Typically, the down-scattering cross section σ_{down} is practically independent of T, so the up-scattering cross section can be small at low temperatures satisfying $k_B T \ll \Delta$. Therefore, the UCN density in such a superthermal UCN source can reach the value proportional to $E_{ucn}/(E_{ucn}+\Delta)\ e^{\Delta/k_B T}$ increasing exponentially as the temperature decreases, while the UCN density in a conventional UCN source is proportional to $1/T^2$.

An ideal material for producing UCN via the superthermal process has to be also suitable for storing the produced UCN. In this case, He-II could be the best material for converter, since ^{4}He nucleus has no neutron absorption cross section σ_{abs}.

The superthermal UCN production in He-II uses the dispersion curve of He-II as is shown in Fig. 1.4 (Cowley and Woods [13]). At intersection of the dispersion curve of He-II and free neutron dispersion curve ($E = \hbar^2 k^2/2m_n$), all the momentum and the energy of the incident

neutron can be transferred to the phonon in He-II and the neutron becomes an UCN. The intersection is at $k_i = 0.706$ Å^{-1}, or $\lambda = 2\pi/k_i = 8.9$ Å. The excitation energy at the intersection is 1.03 meV or the temperature is 11.8 K.

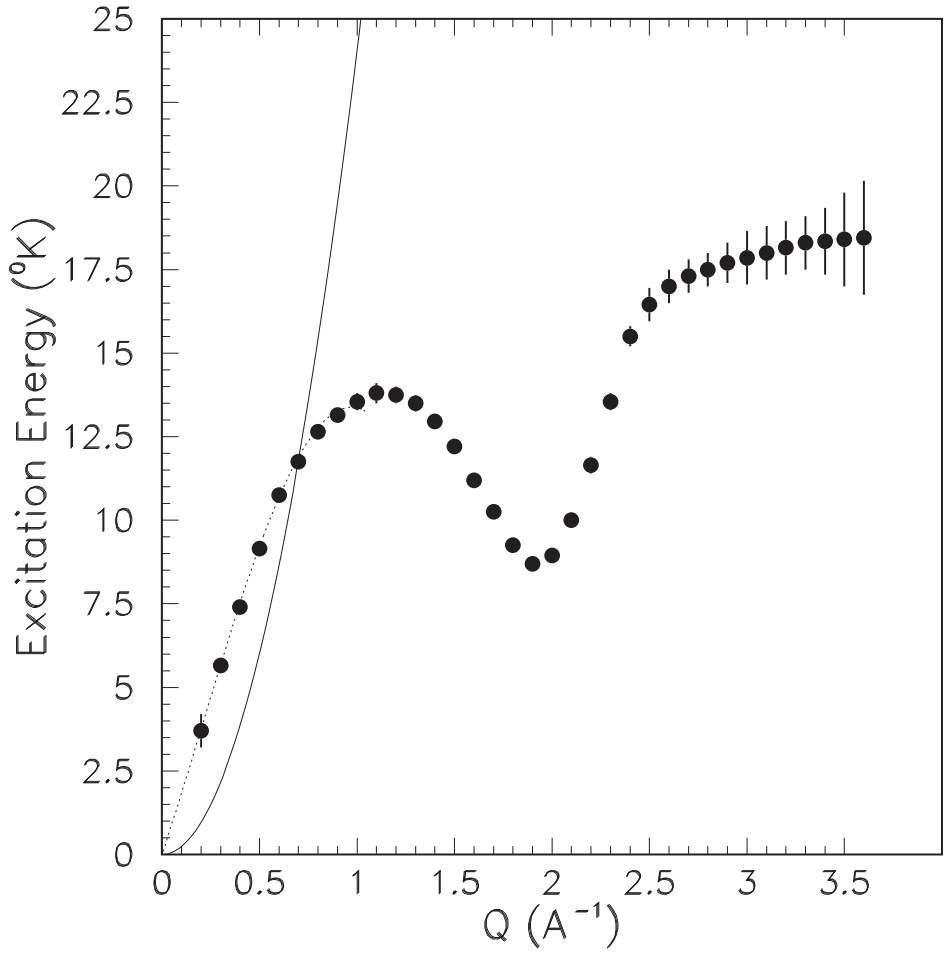

Figure 1.4: The dispersion curve for He-II for the single phonon excitations at $T = 1.1$ K. The data was measured by R. A. Cowley and A. D. B. Woods [13]. The dotted curve is a parameterization by Maris [14]. The solid curve is the dispersion curve for neutrons ($E = \hbar^2 Q^2/2m_n$). (From ref. [15].)

1.5 Our He-II Spallation UCN Source and World Status of UCN Sources

We have developed a new He-II superthermal UCN source. By the compact combination of He-II superthermal UCN converter and a spallation neutron source, much larger UCN density than the traditional UCN sources can be achieved. Our He-II spallation UCN source consists of the He-II converter inserted into a cold neutron moderators of 10 K and room temperature heavy water (D_2O) just above a spallation target.

In addition to He-II, solid deuterium (sD_2) is an another candidate for superthermal UCN converter which is expected to have large UCN production rate [16], [17]. The advantages of sD_2 are high UCN production cross section and relatively high operating temperature ($\sim$ 5 K).

However, the UCN storage lifetime in sD_2 is very short ($\sim$ 24 msec) due to absorption, up-scattering by phonons, ortho-para transition and so on [20]. This leads to short mean free path and high extraction loss. In addition, the Fermi potential of sD_2 is about 100 neV, which is much higher than that of He-II ($\sim$ 20 neV). When UCN come out from the material, UCN are accelerated by the Fermi potential and exceed UCN energy range. Thus, He-II has more advantages. ^{4}He nucleus has no absorption cross section, hence the long storage lifetime can be obtained in He-II and long mean free path assures no extraction loss, compared with sD_2. Since the achievable UCN density is the multiplication of production rate and the storage lifetime, long storage lifetime for He-II can overcome the small production cross section over the sD_2. There are good reasons why we adopted He-II as our UCN converter.

Here, we compare our UCN source with some facilities developing new superthermal UCN sources in the world. There are 3 types of the superthermal UCN sources.

The first type is the close coupling of the He-II converter with the cold neutron source like our UCN source. Close coupling helps us to gain high UCN density without losing by extraction efficiency. PNPI has a similar plan to couple the cold neutrons from the WWR-M reactor (Gatchina) and He-II, and expect to obtain 12,000 UCN cm^{-3} at E_c = 250 neV in He-II (plan). They changed their plan from sD_2 to He-II following our success in the present configuration.

The second one uses a He-II converter, but it is installed in a cold neutron beam line, where the cold neutron flux can not be so high. ILL, SNS at Oak Ridge National Laboratory (ORNL) adopted He-II for their UCN sources. The ILL groups coupled a cold neutron beam and He-II. They obtained a UCN production rate of 1 UCN cm^{-3} s^{-1} at E_c = 250 neV [18]. O. Zimmer's group at ILL obtained a UCN density of 55 UCN cm^{-3} at E_c = 250 neV in He-II which corresponds to 12 UCN cm^{-3} at E_c = 90 neV with their 58 MW reactor [19]. The SNS group has a plan to construct a He-II superthermal UCN source on the proton beam line (FNPB at SNS) with a power of 1.4 MW. The UCN density in He-II is expected to be 430 UCN cm^{-3} at E_c = 134 neV [15] which corresponds to 237 UCN cm^{-3} at E_c = 90 neV (plan).

The third one uses sD_2 converter installed in a cold moderators. Los Alamos, PSI and Munich adopted sD_2 for their UCN sources. Los Alamos developed a sD_2 UCN source with a

1 MW proton beam. They obtained a UCN density of 145 UCN cm^{-3} at $E_c = 335$ neV near the source, which corresponds to 20 UCN cm^{-3} at $E_c = 90$ neV ([20], [21], [22]). PSI also coupled a sD_2 UCN source and a spallation neutron source using a 1.2 MW proton beam and showed the UCN density of 23 UCN cm^{-3} at $E_c = 235$ neV which corresponds to 6 UCN cm^{-3} at $E_c = 90$ neV [23]. Munich have a plan to construct a sD_2 UCN source at FRM-II reactor and expect to obtain 10^3 polarized UCN cm^{-3} in an experiment chamber (plan).

1.6 Thesis Objects

In the present study, we developed the He-II spallation UCN source, coupling the He-II superthermal UCN source and a spallation neutron production. We have studied the UCN source to improve its performance to get world competitive UCN density, and observed UCN energy spectrum of superthermal UCN source for the first time .

The advantage of the superthermal UCN production is prominent at lower temperatures. The He-II temperature is mainly determined by heat loads including radiation by γ-ray (γ-heating). To reduce the heat loads, we suppressed the film flow of He-II which enhances the heat load. The cooling power of the He-II cryostat became large enough, and we have achieved the He-II temperature of 0.8 K by the heat exchange between He-II and the ^{3}He cryostat.

The γ-heating is also studied and compared with the simulation results using PHITS code. It is crucial to remove the γ-heating when we increase the proton beam power for the future extension.

UCN density depends directly on the UCN losses inside the UCN source. UCN loss in the He-II UCN source is caused by up-scattering by phonons in He-II which is suppressed at lower temperatures, inelastic scattering by ^{4}He gas, absorption by ^{3}He impurity in He-II and wall loss. We reduced these UCN losses to obtain a high UCN density of 26 UCN cm^{-3} which is world competitive performance.

Energy spectrum of UCN is also very important because UCN densities depend directly on the spectrum and the critical energy. For the future neutron EDM experiment, systematic error e.g. GPE depends strongly on the UCN spectrum in the EDM cell.

This thesis consists of the following objects.

In Chapter 2, principles of superthermal UCN production in He-II, cause of UCN loss in He-II and energy distribution of produced UCN are shown.

In Chapter 3 and 4, the structure of our He-II spallation UCN source and its operation are explained.

In Chapter 5, improvement of UCN source and the results from the UCN production experiments are shown.

In Chapter 6, observation of the UCN energy spectrum with a UCN storage bottle is explained.

In Chapter 7, our simulation results using Geant4 code are explained to reproduce our results with some of the theoretical assumption.

Chapter 2

The Basic Principles of UCN

2.1 UCN Production via Phonon Scattering

The superthermal UCN production in He-II uses the energy-versus-momentum relation, i.e. the dispersion curve of He-II. Placzek and Van Hove first pointed out that the dispersion curve of a solid could be measured with cold neutrons inelastically scattered by the solid [24]. Cohen and Feynman suggested that the dispersion curve of liquid helium could be measured by this technique [25]. Now we consider the case in which a incident neutron with a momentum of $\hbar\mathbf{k_i}$ inelastically scattered in He-II to a momentum of $\hbar\mathbf{k_f}$ while the He-II is excited into an excited state with an energy of E. The conservation law of energy and momentum requires

$$\mathbf{Q} = \mathbf{k_i} - \mathbf{k_f} \tag{2.1}$$

and

$$\hbar^2 k_i^2/2m = \hbar^2 k_f^2/2m + E(Q) \tag{2.2}$$

where $\hbar\mathbf{Q}$ is the momentum transfer and $E(Q)$ is the dispersion relation of He-II. For single phonon excitation, the Landau-Feynman dispersion curve has been well determined from neutron scattering experiments. Cowley and Woods measured the dispersion curve [13]. The result is already shown in Fig. 1.4. For the low momentum region ($Q < 1$ Å^{-1}), the dispersion curve is approximately linear and is well parameterized as follows [14].

$$\omega = sQ(1 + \gamma Q^2 \frac{1 - Q^2/Q_A^2}{1 + Q^2/Q_B^2}) \tag{2.3}$$

where $s = 2.383 \times 10^2$ m/s, $\gamma = 1.112$ Å^2, $Q_A = 0.5418$ Å^{-1}, and $Q_B = 0.3322$ Å^{-1}. This approximated curve is also shown as the dotted curve in Fig. 1.4.

At a certain momentum, all the momentum and the energy of the incident neutron can be transferred to the phonon in He-II and the neutron becomes an UCN. This condition is met where the free neutron dispersion curve ($E = \hbar^2 k^2/2m_n$) intersects the dispersion curve of He-II. Using the above parameterization for the single phonon excitation, this process occures at $k_i = 0.706$ Å^{-1}, or $\lambda = 2\pi/k_i = 8.9$ Å, as shown in Fig. 1.4.

The superthermal UCN production in He-II can be calculated as follows [26]. The double differential cross section for neutron scattering by phonons in He-II is given by the Fourier transform $S(q,\omega)$ of the van Hove correlation function [27],

$$\frac{\mathrm{d}^2\sigma}{\mathrm{d}\Omega\mathrm{d}\omega} = b_{coh}^2 \frac{k_f}{k_i} S(q,\omega). \tag{2.4}$$

where b_{coh} is the bound coherent scattering length of ^{4}He and $\hbar q$ is the momentum transfer. $S(q,\omega)$ of He-II has been measured in great detail [28] [29] [30] [31] [32] [33]. We transform the solid angle as follows.

$$d\Omega = 2\pi \sin\theta d\theta = 2\pi \frac{qdq}{k_1 k_2} \ . \tag{2.5}$$

Then

$$\begin{aligned} \frac{\mathrm{d}\sigma}{\mathrm{d}\omega} &= \int \frac{\mathrm{d}^2\sigma}{\mathrm{d}\Omega\mathrm{d}\omega} d\Omega & (2.6)\\ &= \int 2\pi b_{coh}^2 \frac{k_f}{k_i} S(q,\omega) \frac{qdq}{k_1 k_2} & (2.7)\\ &= \int 2\pi b_{coh}^2 S(q,\omega) \frac{qdq}{k_1^2} \ . & (2.8) \end{aligned}$$

Here, we take the following limits on q into account.

$$\begin{aligned} k_1 - \quad k_2 \quad &< q < k_1 + k_2 & (2.9)\\ k_2 = \quad k_u \quad &\ll k_1, \ q \sim k_1 & (2.10) \end{aligned}$$

where $\hbar k_u$ is the UCN momentum. We have $\int dq = 2k_u$. Then,

$$\frac{\mathrm{d}\sigma}{\mathrm{d}\omega} = 4\pi b_{coh}^2 \frac{k_u}{k_1} S(q = k_1, \omega = \frac{\hbar k_1^2}{2m_n}) \ , \tag{2.11}$$

where we assumed $S(q,\omega)$ is constant over the narrow range dq, and

$$\omega = \frac{\hbar(k_1^2 - k_2^2)}{2m_n} \sim \frac{\hbar k_1^2}{2m_n} \ . \tag{2.12}$$

The UCN production rate per volume with energies between E_u and $(E_u + dE_u)$ is given by

$$P(E_u)dE_u = \left[\int dE_1 \frac{d\Phi(E_1)}{dE} N_{He} \frac{d\sigma}{d\omega}(E_1 \to E_u) \right] dE_u \tag{2.13}$$

where N_{He} is the number density of He-II, $E_1 = \hbar^2 k_1^2/2m_n$, and $E_u = \hbar^2 k_u^2/2m_n$. $d\Phi(E_1)/dE$ is the energy spectrum of the incident neutron flux. Then, the total UCN production rate per volume P is given by

$$\begin{aligned} P &= \int_0^{E_c} P(E_u) dE_u & (2.14)\\ &= N_{He} 4\pi b_{coh}^2 \alpha^2 \left[\int dk_1 \frac{d\Phi(k_1)}{dE_1} S(k_1, \omega = \frac{\hbar k_1^2}{2m_n}) \right] \int_0^{k_c} k_u^2 dk_u & (2.15)\\ &= N_{He} \sigma_{He} \alpha^2 \frac{k_c^3}{3} \left[\int dk_1 \frac{d\Phi(k_1)}{dE_1} S(k_1, \omega = \frac{\hbar k_1^2}{2m_n}) \right] \ \text{UCN cm}^{-3}\ \text{s}^{-1} & (2.16) \end{aligned}$$

where E_c is the UCN critical energy and $E_c = \hbar^2 k_c^2/2m_n$. $\sigma_{He} = 4\pi b_{coh}^2$, which is the scattering cross section of ^{4}He. $\alpha = \hbar^2/m_n$. Note that the unit of $S(k_1, \omega)$ is meV^{-1}.

2.1.1 Single Phonon Process

The UCN production rate per volume by single phonon process, P_I, can be calculated by integrating Eqn.(2.16) over the single phonon peak. The dynamic structure function $S(q, \omega)$ is decomposed into the single phonon part and the multi phonon part.

$$S(q, \omega) = S_I(q, \omega) + S_{II}(q, \omega) \tag{2.17}$$

The single phonon part, $S_I(q, \omega)$, has a large peak at the intersection of the neutron dispersion curve and the He-II dispersion curve. So, we replace the single phonon part by the following expression.

$$\begin{aligned} S_I(q, \hbar\omega) &= S^* \ \delta(q - k^*) && (2.18) \\ S^* &= \hbar \int_{peak} S_I(q = k^*, \hbar\omega) d\omega && (2.19) \end{aligned}$$

where $k^* = 0.706$ Å^{-1} as discussed above. Then, P_I is given by

$$\begin{aligned} P_I &= N_{He}\sigma_{He}\alpha^2 \frac{k_c^3}{3} \left[\int dk_1 \frac{d\Phi(k_1)}{dE_1} S^* \delta(k_1 - k^*) \right] && (2.20) \\ &= N_{He}\sigma_{He}\alpha\beta \frac{k_c^3}{3k^*} S^* \frac{d\Phi(k^*)}{dE} \ [\text{UCN cm}^{-3}\ \text{s}^{-1}] && (2.21) \end{aligned}$$

where β is given by

$$\beta = \frac{v_n^*}{v_n^* - c_g^*} \ . \tag{2.22}$$

Here, v_n^* is the neutron velocity at the intersection of the two dispersion curves. So, $v_n^* = \hbar k^*/m_n$. c_g^* is the phonon group velocity at the intersection. β represents the increase of the value of integral due to the fact that the path of the integration becomes longer since the two dispersion curves intersect with some angle.

The physics parameters in (2.21) are given as follows.

$$\begin{aligned} N_{He} &= 2.1901 \times 10^{22} \ [\text{cm}^{-3}] \ (T_{He-II} = 1.2 \text{ K}) && (2.23) \\ \sigma_{He} &= 1.34(2) \ [\text{b}] && (2.24) \\ k_c &= 0.01016 \ [\text{Å}^{-1}] \ \left(E_c = \frac{\hbar^2 k_c^2}{2m_n} = 214 \text{ neV} \right) && (2.25) \\ \alpha &= \hbar^2/m_n = 4.14425 \ [\text{meV Å}^{-2}] && (2.26) \\ \beta &= 1.42(1) \text{ (from ref. [33])} && (2.27) \\ S^* &= 0.118(8) \text{ (from ref. [33])} && (2.28) \end{aligned}$$

Then, the UCN production rate per volume by single phonon process is given by

$$P_I = (1.010 \pm 0.070) \times 10^{-8} \cdot \frac{d\Phi(k^*)}{dE} \ . \tag{2.29}$$

The energy spectrum of the incident neutron flux, $d\Phi(k^*)/dE$, will be calculated by a Monte Carlo simulation code PHITS [34] in the later section.

2.1.2 Multi Phonon Process

UCN is also produced via the scattering by multi phonons. Unlike the single phonon excitation which has a peak like a form of a delta function at the intersection of the two dispersion curves, the multi phonon process is given by a wide broadening of the multi phonon part of $S(q, \omega)$ in an energy-versus-momentum space.

Fig. 2.1 shows the contour plot of $S(q, \omega)$ in He-II at a temperature of 0.5 K and a pressure of 20 bars. The deepest black line is the dispersion curve of phonons and rotons in supefluid helium. The UCN production by the single phonon scattering occurs at the intersection of this deepest black line and the dispersion curve of a neutron. The gray-colored region above the dispersion curve is the area of the multi phonon excitations. The UCN production in this region is caused by the multi phonon scattering.

The UCN production rate per volume by the multi phonon scattering, P_{II}, is given by

$$\begin{aligned} P_{II} &= P - P_I & (2.30)\\ &= N_{He}\sigma_{He}\alpha^2\frac{k_c^3}{3}\left[\int dk_1 \frac{d\Phi(k_1)}{dE_1} S(k_1, \omega = \frac{\hbar k_1^2}{2m_n})\right] - P_I & (2.31)\\ &= (1.763 \pm 0.026) \times 10^{-7} \cdot \left[\int dk_1 \frac{d\Phi(k_1)}{dE_1} S(k_1, \frac{\hbar k_1^2}{2m_n})\right] - P_I & (2.32) \end{aligned}$$

where P_I is given by (2.21). To calculate the integral of the first term in the right side of (2.32), the value of $S(q, \omega)$ along the dispersion curve of a neutron, $S(k_1, \omega = \hbar k_1^2/2m_n)$, is necessary. It is shown in Fig. 2.2.

We calculated the energy spectrum of the incident neutron flux in our UCN cryostat by the Monte Carlo simulation code, PHITS. Then we obtained the UCN production rate per volume P by both the single and the multi phonon process. The results will be shown in the later section.

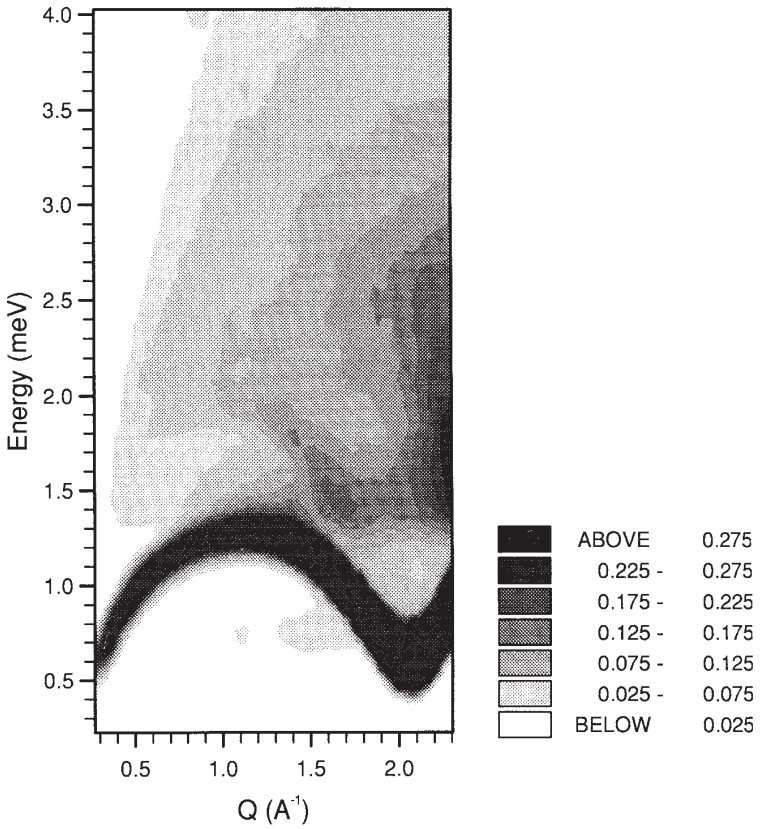

Figure 2.1: Contour plot of the dynamic structure function $S(q, \omega)$ of He-II at a temperature of 0.5 K and a pressure of 20 bars. The unit of $S(q, \omega)$ is meV^{-1}. The single phonon-roton excitations have been removed to reveal the multi phonon structure. (From ref. [31] [32].)

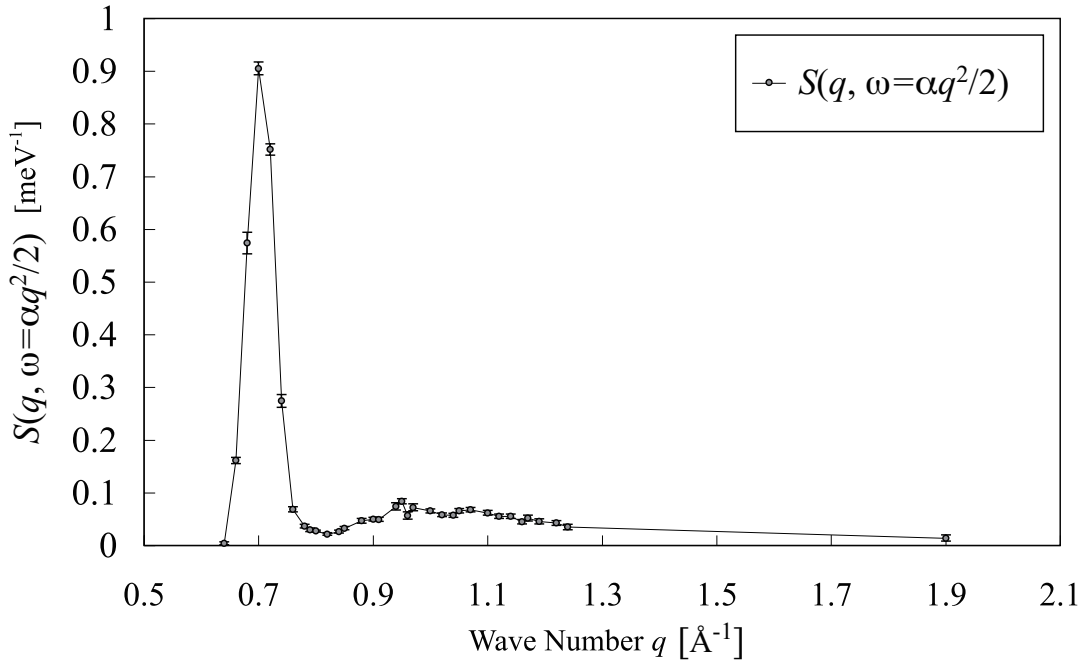

Figure 2.2: $S(q, \omega)$ of He-II at 0.5 K and SVP (saturated vapor pressure) on the neutron dispersion curve, i.e. $E = \hbar\omega = \hbar^2 q^2 / 2m_n$. A peak around $q = 0.7$ Å^{-1} is the single phonon peak. (The data from ref. [33].)

2.2 Loss of UCN

In this section, we discuss the amount of the produced UCN in the He-II source and the improvement of the production and extraction rate.

In the superfluid helium, using the UCN production rate P and a specific time constant τ which is called "UCN storage time", the UCN density in the He-II source ρ is written as follows.

$$\rho = P \times \tau \tag{2.33}$$

The time constant τ is called "UCN storage time". Number of UCN in the He-II source decreases as time goes by with a certain loss probability per time. The loss probability is inversion of the UCN storage time τ. Therefore, UCN storage time τ means the averaged UCN life time in the He-II UCN source or other vessels for UCN.

The UCN production rate P in the He-II is proportional to the phonon down-scattering cross section, cold neutron flux in the He-II bottle, and the density of He-II. This P is almost independent on the temperature of the He-II and the environment inside the He-II bottle.

To improve the UCN density, we have to pay attention to the UCN storage time τ. In the He-II UCN source, UCN are lost due to the following sources.

1. up-scattering by phonons in He-II
2. inelastic scattering by Helium gas molecules
3. absorption by Helium-3
4. wall loss
5. leakage through holes and gaps
6. neutron β-decay

Each loss probability $1/\tau_i$ contributes to the total loss probability $1/\tau$. The relation is simply written as follows.

$$\frac{1}{\tau} = \sum \frac{1}{\tau_i} \tag{2.34}$$

τ_i is the life time determined by each lossy source.

2.2.1 Up-scattering by Phonons in He-II

Cold neutrons are down-scattered to be UCN by phonons in the He-II. On the other hand, some of such UCN are scattered by phonons again, and gain some energy to be a higher energy neutrons. This process is up-scattering by phonons and causes loss of UCN in He-II.

The loss probability per time by the phonon up-scattering in He-II was discussed by R. Golub [35]. According to R. Golub, the loss by phonon is decomposed to three parts. They are one phonon process, two phonon process with one phonon exchange, and roton scattering with one phonon exchange. The loss probability by one phonon process is

$$\frac{1}{\tau_{1p}} = N\sigma(\hbar k^*/m)(E^*/m_{He}s^2)e^{-E^*/T} \tag{2.35}$$

where $\sigma = 4\pi a^2$ is the coherent scattering cross section for Helium and $E^* = \hbar s k^*$. s is the sound velocity in Helium ($\sim$222.3m/s). The loss probability by two phonon process with one phonon exchange is

$$\frac{1}{\tau_{2p}} = (4\pi)^{-1}(k_t a)^2(T/mc^2)^2(T/m_{He}c^2)^2(T/\hbar)I \tag{2.36}$$

where $k_t = T/\hbar s$, and I is a dimensionless integral (see (14) of ref. [35]). The roton scattering with one phonon exchange is

$$\frac{1}{\tau_r} = 18\ T^{3/2}e^{-\Delta/T} \tag{2.37}$$

where Δ is the minimum value of the He-II dispersion curve $E(k)$ around the energy region of roton ($k \sim 2$ Å^{-1}). Here, $\Delta = 8.6$ K.

UCN loss in He-II was experimentally confirmed by R. Golub et al [36]. E. Gutsmiedl et al. [37] and H. Yoshiki et al. [38] also confirmed later. According to ref. [36] and [37], the cross section shows a T^7 dependence in the 2-phonon regime (0.5 - 0.9 Kelvin). H. Yoshiki [38] shows the total loss probability $1/\tau_{ph}$ can be expressed as

$$\frac{1}{\tau_{ph}} = Ae^{-12/T} + BT^7 + CT^{3/2}e^{-8.6/T} \tag{2.38}$$

with some sets of parameters A, B, C. The best parameters are $A = 0, B = 0.008, C = 0$.

In our experimental region ($T = 0.8 \sim 0.9$ K), the two phonon process is dominant. Therefore, $1/\tau_{ph}$ can be assumed to be proportional to T^7. The loss rate $1/\tau_{ph}$ or life time τ_{ph} at each temperature is shown in Fig. 2.3 and Table 2.1.

2.2.2 Inelastic Scattering by Helium Gas Molecules

In the present setup, the UCN guide between the He-II bottle and the experimental port is filled with Helium-4 gas of the saturated vapor pressure. UCN in the UCN guide are inelastically scattered by these helium atoms to gain energy. These energy gained UCN penetrate vessel walls and will be lost. The loss by this scattering process is written as follows.

$$\frac{1}{\tau_{He}} = n\sigma_s v \tag{2.39}$$

where n is the number density of Helium-4 gas, σ_s is the coherent scattering cross section for Helium and v is the velocity of a Helium gas molecule (UCN is much slower than the Helium, so the UCN velocity can be ignored).

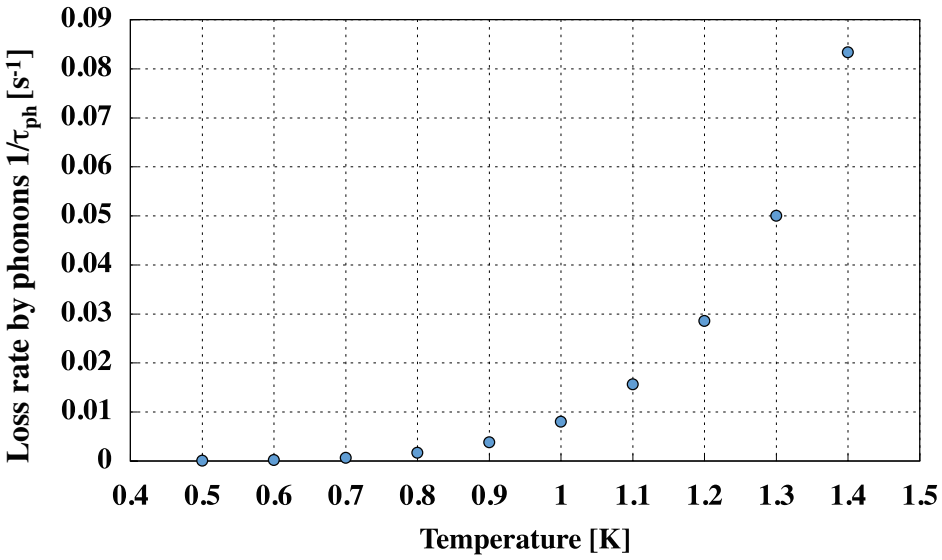

Figure 2.3: Loss rate of UCN due to phonon up-scattering in He-II. $1/\tau_{ph} = 0.008\ T^7$.

For example, in the case that the He-II temperature is 0.8 K, assuming the pressure in the UCN guide is same as the vapor pressure of the He-II and the UCN are the thermal equilibrium at $T = 0.8$ K and can be regarded as ideal gas, $n = 1.33 \times 10^{17}$ cm^{-3} and $v = 70.6$ m/s. The coherent scattering cross section for free Helium is $\sigma_s = 0.8547$ b. So the life time is $\tau_{He} = 1246$ sec at $T = 0.8$ K. The loss rate $1/\tau_{He}$ at each temperature is shown in Fig. 2.4 and Table 2.2.

2.2.3 Absorption by Helium-3

^{3}He has very large neutron absorption cross section. For a thermal neutron whose velocity is 2200 m/s, the absorption cross section σ_a is known to be 5333 b. The neutron absorption cross section is proportional to the inverse of velocity for slow neutrons. Namely, $\sigma_a \propto 1/v$. The loss of UCN by the absorption process is

$$\frac{1}{\tau_{abs}} = n_{3He}\sigma_a v. \tag{2.40}$$

Since σ_a is proportional to $1/v$, $1/\tau_{abs}$ is independent of UCN velocity.

In our system, the number density of ^{3}He is unknown. The natural abundance of ^{3}He and ^{4}He is ^{3}He/^{4}He $= 1.37 \times 10^{-6}$. If this value is valid for the He-II, the number density of ^{3}He in the 0.8 K He-II is $n_{3He} = 3.0 \times 10^{16}$ cm^{-3}. Therefore,

T [K]	$1/\tau_{ph}$ [s^{-1}]	τ_{ph} [s]
0.5	6.25×10^{-5}	16000
0.6	2.24×10^{-4}	4465
0.7	6.59×10^{-4}	1518
0.8	1.68×10^{-3}	596
0.9	3.83×10^{-3}	261
1.0	0.008	125
1.1	1.56×10^{-2}	64
1.2	2.87×10^{-2}	35
1.3	5.02×10^{-2}	20
1.4	8.43×10^{-2}	12

Table 2.1: Loss rate and life time of UCN due to phonon up-scattering in He-II. $1/\tau_{ph} = 0.008\ T^7$.

T [K]	P [mTorr]	n [cm^{-3}]	v [m/s]	$1/\tau_{He}$ [s^{-1}]	τ_{He} [s]
0.8	11	1.33×10^{17}	70.6	8.03×10^{-4}	1246
0.9	40	4.29×10^{17}	74.9	2.75×10^{-3}	364
1.0	117	1.13×10^{18}	78.9	7.63×10^{-3}	131
1.1	290	2.55×10^{18}	82.8	1.80×10^{-2}	55
1.2	610	4.91×10^{18}	86.5	3.63×10^{-2}	28
1.3	1180	8.77×10^{18}	90.0	6.75×10^{-2}	15
1.4	2100	1.45×10^{19}	93.4	1.16×10^{-1}	9

Table 2.2: Loss rate and life time of UCN due to inelastic scattering with Helium gas

$$\frac{1}{\tau_{abs}} = n_{3He}\sigma_a v \tag{2.41}$$

$$= 3.0 \times 10^{16}\ (\mathrm{cm}^{-3}) \times 5333\ (\mathrm{b}) \times 2200\ (\mathrm{m/s}) \tag{2.42}$$

$$= 35.2\ \mathrm{s}^{-1} \tag{2.43}$$

$$\tau_{abs} = 28\ (\mathrm{ms}) \tag{2.44}$$

is obtained. Our UCN production experiment shows the UCN storage time τ is longer than 30 s in our system, which is much longer than the above prediction, so this value is too short.

As a reason, it is considered that Helium gas used in Japan is imported from the USA. This commercial Helium gas is produced at Helium gas fields. In such gas fields, Helium gas is produced via α-decay of Uranium, Thorium, and so on. Such Helium gas has less ^{3}He impurities than the natural abundance. The ^{3}He abundance from such gas fields is said to be about 10^{-7}. In addition, the Helium gas is condensed to be liquid state to transport from USA to Japan. During the condensation, ^{3}He may be removed.

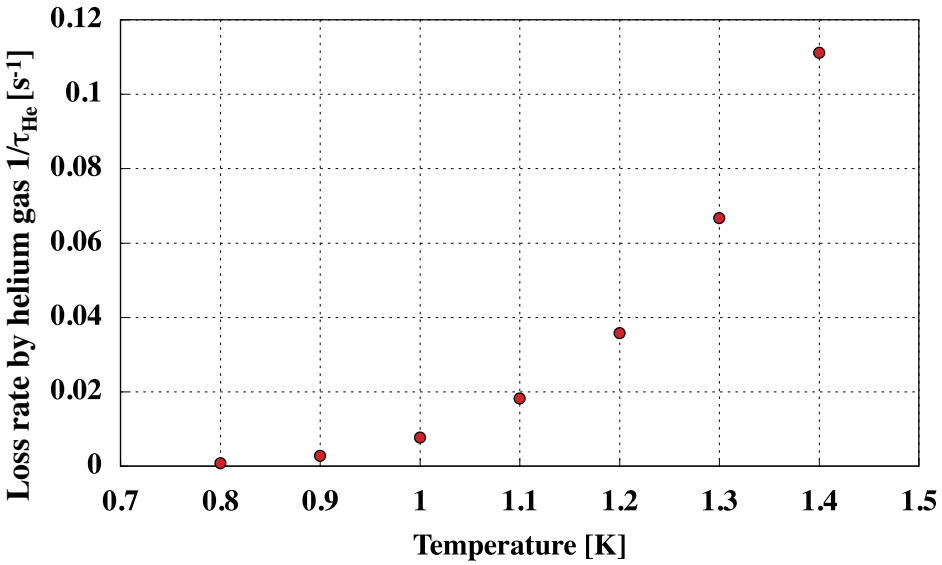

Figure 2.4: Loss rate of UCN due to inelastic scattering with Helium gas.

After 2007, we have used the isopure (= isotopically pure) Helium made by the method called "superleak" [39]. The isopure Helium has much less ^{3}He impurities than the natural abundance. The ^{3}He abundance of the isopure Helium is said to be smaller than 10^{-10}. So the life time τ_{abs} of the isopure Helium is expected to be about 300 sec or longer.

2.2.4 Wall Loss

UCN in a vessel are reflected by the vessel's inner surface. However, some of them are inelastically scattered or absorbed by a nucleus in the surface and lost when they are reflected. So the number of UCN in a vessel gradually decreases with a life time τ_{wall}. This process is called "wall loss". We assume the vessel surface to be represented by a complex step change in Fermi potential

$$U = V - iW = \frac{2\pi\hbar^2}{m_n} N(b_r - ib_i) \tag{2.45}$$

where

$$b_i = \left(\frac{\sigma_l k}{4\pi}\right). \tag{2.46}$$

σ_l is the sum of inelastic cross section σ_i and absorption cross section σ_a. k is wave number of an incident UCN. Using this potential, the wall loss probability per bounce $\mu(E,\theta)$ is written as follows.

$$\mu(E,\theta) = 2\eta \left(\frac{E\cos^2\theta}{V - E\cos^2\theta}\right)^{1/2} \tag{2.47}$$

where E is the total energy of reflecting UCN and θ is the angle of incidence with respect to the surface normal. η is a parameter of wall loss. It is written as

$$\eta = \frac{W}{V} = \frac{\sigma_l k}{4\pi b_r}. \tag{2.48}$$

σ_l is proportional to $1/v$, so the parameter η is independent of UCN velocity.

Considering UCN in a closed vessel, they can be assumed to be isotropic gas after a sufficient number of wall collisions. In this case, we can average μ over the angle of incidence for a given energy. The averaged loss probability per bounce for UCN of energy E is given by

$$\overline{\mu}(E) = 2\eta \left[\frac{V}{E} \sin^{-1} \left(\frac{E}{V} \right)^{1/2} - \left(\frac{V}{E} - 1 \right)^{1/2} \right]. \tag{2.49}$$

In the case of a vessel whose surfaces are not perfectly flat, there will be some fraction of the wall collisions that result in diffuse reflection which is described by the cosine law, $P(\theta)d\Omega = \cos\theta d\Omega$ where $P(\theta)d\Omega$ is the reflection probability that a particle leaves the surface at an angle θ into the solid angle $d\Omega$. Such reflection on surfaces is simply represented by a mixture of diffuse reflection of the probability f and specular reflection of the rest $1 - f$. In the case of a good polished surface, f is not so large ($1 \sim 10\%$).

If UCN with the energy E and the velocity v are confined in a bottle with the volume V and the surface area S, the wall loss probability per unit time is written as follows.

$$\frac{1}{\tau_{wall}} = \frac{\overline{\mu}(E) v S}{4V} = \overline{\mu}(E) \frac{v}{l} \tag{2.50}$$

when the motion of UCN can be assumed to be isotropic after a sufficient number of wall collisions. $l = 4V/S$ is the mean free path of isotropic UCN in the bottle.

Typical value of $\overline{\mu}$ is $10^{-2} \sim 10^{-3}$ and typical value of τ_{wall} is $10 \sim 10^2$ s. The typical value of η is almost in the same order as $\overline{\mu}$ because $\overline{\mu}(E)/\eta$ ranges 0 to π. These experimental values are pretty large compared to the theoretically predicted μ or η, sometimes a hundred times larger. The cause of this excess losses is mainly explained by the hydrogen hypothesis. Hydrogen impurities on material surfaces are considered to cause losses of UCN because hydrogen has large neutron scattering cross section ($\sigma_{scatt} = 82$b).

According to the experiment on neutron mirrors by W. A. Lanford and R. Golub [40], hydrogen impurities distribute on material surfaces to the depth of $5 \sim 10$ nm with the density of $(2 \sim 10) \times 10^{22}$ H/cm^3. These values are common among some kinds of materials. Measurement using Elastic recoil data analysis (ERDA) by Y. Kawabata et al. [41] also shows hydrogen with the density of $(2 \sim 5) \times 10^{15}$ H/cm^2 exists on material surfaces. Assuming the depth is $5 \sim 10$ nm, the density is about 5×10^{21} H/cm^3 at the maximum.

The increase of wall loss parameter η_{surfH} is $\sim 10^{-4}$ by extremely rough estimation. However, it is difficult to know the binding energy and the density of state of hydrogen impurities on surfaces accurately, and the exact value of η_{surfH} is unknown. In addition, it is known that the wall loss anomaly can not be fully explained only by the hydrogen hypothesis. The discrepancy between the theory and the experiment still remains not fully explained.

2.2.5 Leakage through Holes and Gaps

If a vessel or a guide containing UCN have some holes or gaps, UCN go out through them and are lost. This case corresponds to the wall loss with $\mu = 1$. Namely,

$$\frac{1}{\tau_{hole,gap}} = \frac{vS}{4V} \tag{2.51}$$

where S is the area of the hole or gap.

2.2.6 Neutron β Decay

Neutron decays to proton, electron, and anti-neutrino by the weak interation. The life time of neutron is $\tau_\beta = 885.7 \pm 0.8$ s. So, the loss rate through the β decay is simply expressed by $1/\tau_\beta = 1/885.7 = 1.129 \times 10^{-3}$ s^{-1}.

2.3 UCN Energy Spectrum

S. K Lamoreaux and R. Golub calculated the angular distribution of UCN produced in He-II [42]. The UCN production rate in He-II P follows

$$\frac{d^2P}{d\cos\theta dk_u} = 2\pi N b_c^2 S(q^*)\frac{d\Phi(q^*)}{dk_i}(1.438)\left(\frac{k_u}{q^*}\right)^2\left(1 + (1.56)\left(\frac{k_u}{q^*}\right)\cos\theta\right) \tag{2.52}$$

where N is the ^{4}He density, b_c is the coherent scattering length of ^{4}He, k_i is the incident neutron wave number, k_u is the produced UCN wave number, q^* is the neutron momentum at the intersection of the dispersion curves, $S(q^*)$ is the single phonon peak of the Van Hove scattering function, and θ is the scattering angle.

The angular distribution is proportional to $(1 + (1.56)(k_u/q^*)\cos\theta) = 1 + 0.022\cos\theta$ for UCN with an energy of 214 neV. Therefore, the angular distribution of the produced UCN can be ignored. The differential UCN production rate dP is $dP \propto k_u^2 dk_u \propto \sqrt{E_{ucn}}dE_{ucn}$ where E_{ucn} is the produced UCN energy. It is predicted that the UCN energy spectrum is proportional to $\sqrt{E_{ucn}}$.

Chapter 3

KEK-RCNP UCN Source

In this chapter, the proton beam line at the ring cyclotron facility of Research Center for Nuclear Physics (RCNP) in Osaka University and the structure of KEK-RCNP He-II spallation UCN source are shown. The spallation neutron production and the neutron moderation in the heavy water moderators by PHITS2 Monte Carlo simulation are also shown. The UCN production rate in He-II was obtained, based on the PHITS2 simulation.

3.1 Proton Beam Line

The KEK-RCNP He-II spallation UCN souce is installed on the proton beam line called "ES (East South) course" at the ring cyclotron facility of RCNP. The schematic view of the AVF cyclotron, the ring cyclotron, and other facilities on the beam line are shown in Fig. 3.1. The He-II spallation UCN source is installed at the end of the ES course.

The proton beam from the ion source is accelerated to be about 65 MeV by the AVF cyclotron. Then, the proton beam is transported to the Ring cyclotron facility, and further accelerated to be 392 MeV by the ring cyclotron. The maximum value of the proton beam current is 1 μA. The accelerated proton beam is transported to the ES course, and bombarded to a lead target for spallation neutron production.

3.2 He-II Cryostat

The schematic structure of the He-II spallation UCN source is shown in Fig. 3.2. In the UCN source, UCN are produced as follows.

1. The proton beam with an energy of 392 MeV and a current of 1 μA, is bombarded to the lead target just below the UCN source. Fast neutrons with energies of a few MeV are produced by the spallation reaction in the lead target. About 7 neutrons per incident proton are obtained.

2. The obtained fast neutrons are moderated to be thermal neutrons in a room temperature (RT) heavy water (D_2O) moderator.

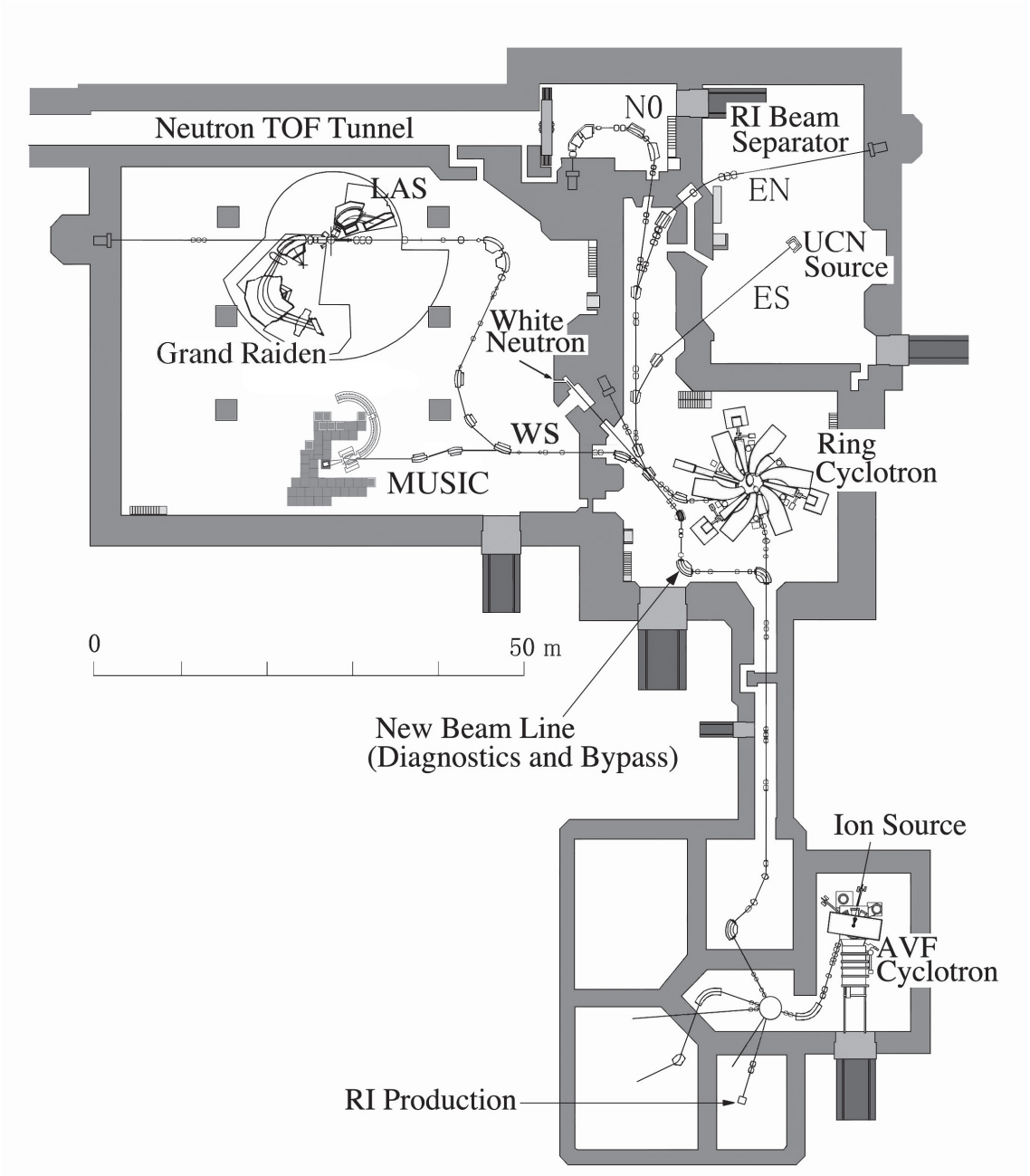

Figure 3.1: The schematic view of RCNP cyclotron facility. The He-II spallation UCN source is installed at the end of the ES course. The proton beam from the ion source is accelerated by the AVF cyclotron and the ring cyclotron to be 392 MeV. The maximum proton beam current is 1μA and the power is 392 Mev $\times$ 1μA = 400 W. The proton beam is transported and bombarded to a lead target installed just below the UCN source for spallation neutron production.

3. Then, the thermal neutrons are moderated to be cold neutrons in the 10 K solid D_2O moderator.

4. The cold neutrons are down-scattered to be UCN by phonons in the He-II bottle. The temperature of He-II is 0.8 K.

5. The produced UCN in the He-II bottle is transported to the exit of the UCN source through the UCN guide. The exit of the UCN source is called "experimental port". A VAT gate valve is attached to the experimental port. We call this gate valve "UCN valve". It is used to separate the upstream region of the UCN source from the atmosphere when an apparatus is attached to the experimental port.

6. The gravity accelerator tube and the ^{3}He UCN detector are attached at the experimental port in Fig. 3.2. UCN go through the gravity acceleration tube and are observed by the UCN detector.

The graphite neutron reflectors are installed around the lead target to reflect neutrons and increase the neutron flux into the RT D_2O moderator.

The 10 K D_2O moderator is cooled by the Gifford McMahon (GM) refrigerator (type SRD-220, Sumitomo Juuki). The second stage of SRD-220 is connected to the top plate of the 10 K solid D_2O bottle. The 1st stage of SRD-220 is connected to the thermal shield covering the 10 K solid D_2O bottle and the He-II cooling system. The temperature of the 1st stage and the thermal shield is $40 \sim 50$ K.

The He-II cooling system is a main part of the UCN source. In the upper region of the UCN source, the apparatuses for He-II condensation are installed. The operation of the He-II cooling system is explained in the next chapter.

The He-II spallation UCN source installed at the ES couse and the peripheral apparatuses for operation of He-II condensation are shown in Fig. 3.3.

Lead Spallation Target

The lead (Pb) target is installed at the end of the ES course, just below the UCN source. The size of the lead target block is $100 \times 100 \times 200$ mm length. The proton beam with an energy of 392 MeV and a current of 1 μA from the ring cyclotron at RCNP is bombarded to the lead target. The profile of the proton beam is a circle with a diameter of about 5 mm. Since the range of a 392 MeV proton in Pb is about 15 cm, the size of the lead target is large enough for the proton beam to stop inside the target. Fast neutrons are produced by the spallation reaction of the incident proton beam and the lead target. About 7 fast neutrons per incident proton at 392 MeV are produced by the reaction [43] [44].

Fig. 3.4 shows the view around the lead target just below the UCN source. The lead target with a size of $100 \times 100 \times 200$ mm^3 is installed at the end of the beam guide. The lead target is surrounded by the graphite neutron reflectors.

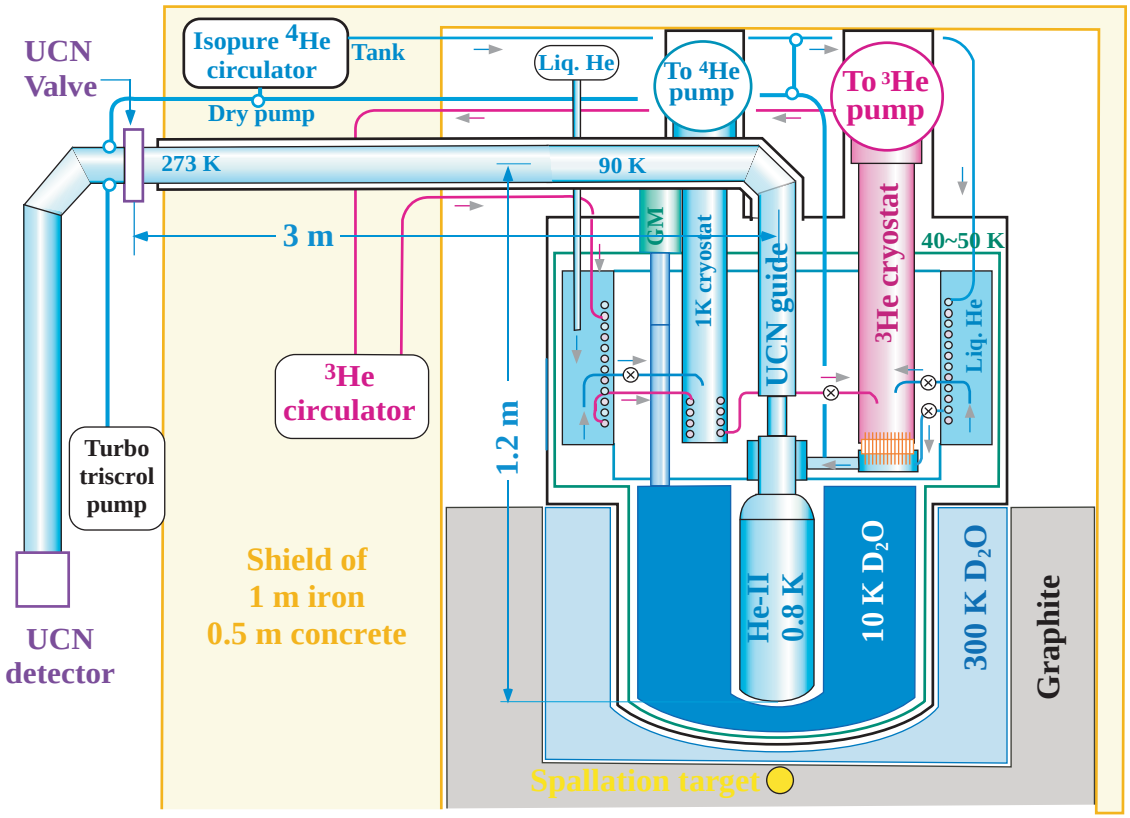

Figure 3.2: The schematic structure of the KEK-RCNP He-II spallation UCN source. The proton beam with an energy of 392 MeV and a current of 1 μA, is bombarded to the lead target. Fast neutrons are produced by the spallation reaction. They are moderated to be cold neutrons by the RT and the 10 K D_2O moderators. The cold neutrons are down-scattered to be UCN by phonons in He-II. The obtained UCN are transported to the experimental port through the UCN guide.

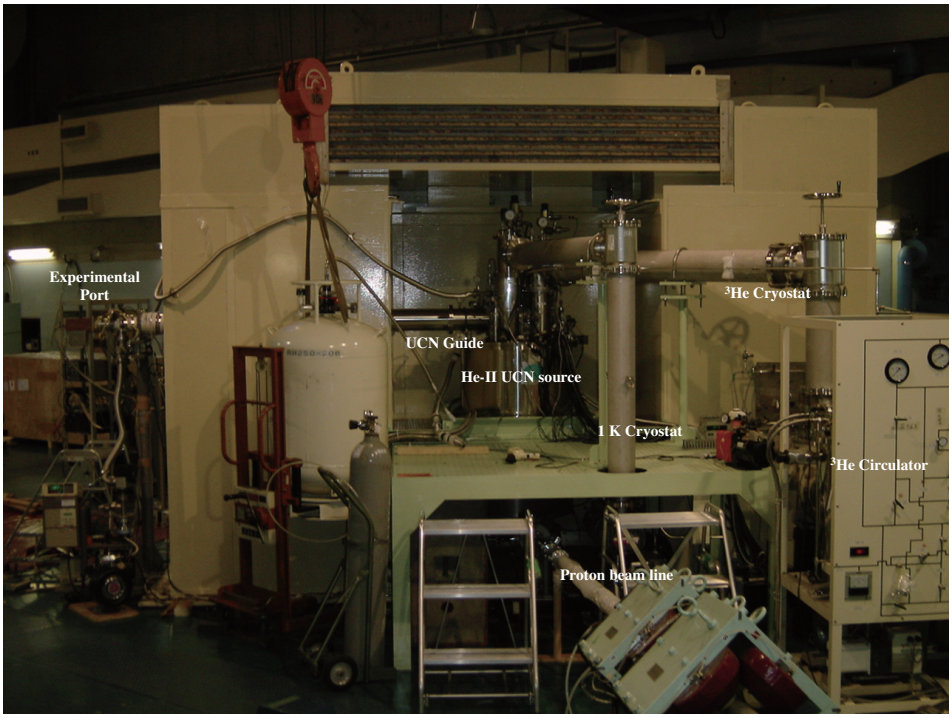

Figure 3.3: The view of the He-II superthermal UCN source and peripheral apparatuses at the ES couse. This photograph was shot in 2004.

D_2O Thermal and Cold Moderators

Fast neutrons produced via the spallation reaction are moderated to be thermal neutrons by the RT D_2O moderator at first. Then, the obtained thermal neutrons are moderated to be cold neutrons by the 10 K solid D_2O moderator. The schematic structure of the moderators is shown in Fig. 3.5.

The RT D_2O bottle is made of aluminum. The inner diameter is 630 mm, the outer diameter is 850 mm, and the height is 630 mm. The thickness of the inner wall is 5mm and that of the outer wall is 20 mm. The thickness of the bottom is 30 mm except for the position just above the lead target where the thickness is 4 mm to reduce neutron absorption.

The 10 K solid D_2O bottle is also made of aluminum. It has the 167 mm inner diameter, the 586 mm outer diameter and the 563 mm height. The thickness of the inner wall is 3 mm and the outer wall is 5 mm. The thickness of the top plate is 20 mm.

The cold finger is attached between the 2nd stage of SRD-220 GM refrigerator and the top plate of the 10 K solid D_2O bottle.

He-II Bottle

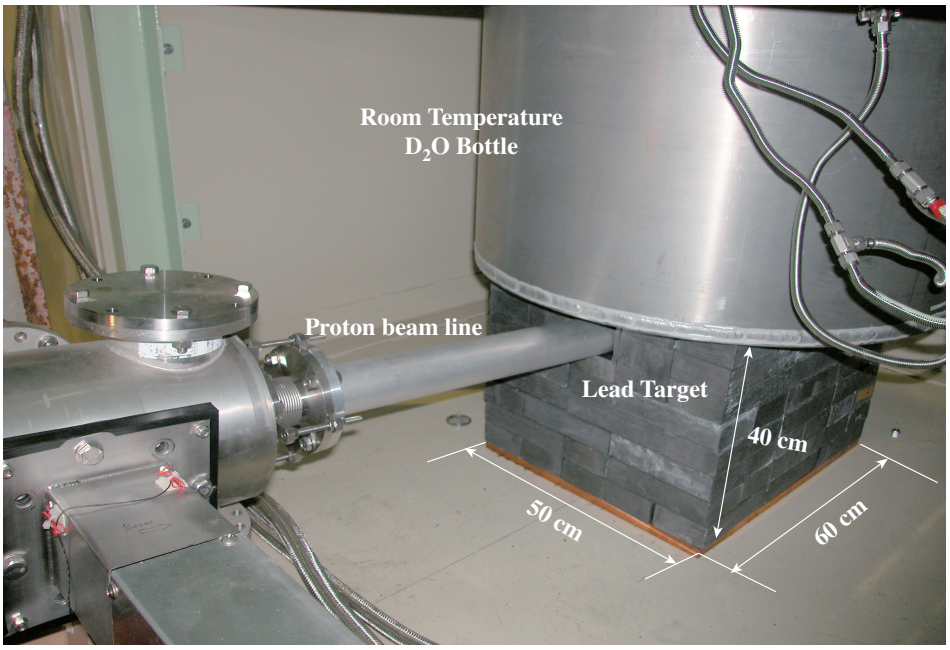

Figure 3.4: The view around the lead spallation target just below the UCN source. The lead target with a size of $100 \times 100 \times 200$ mm^3 is installed at the end of the beam guide. The lead target is now surrounded by the graphite reflectors. The graphite reflectors are not shown in this figure.

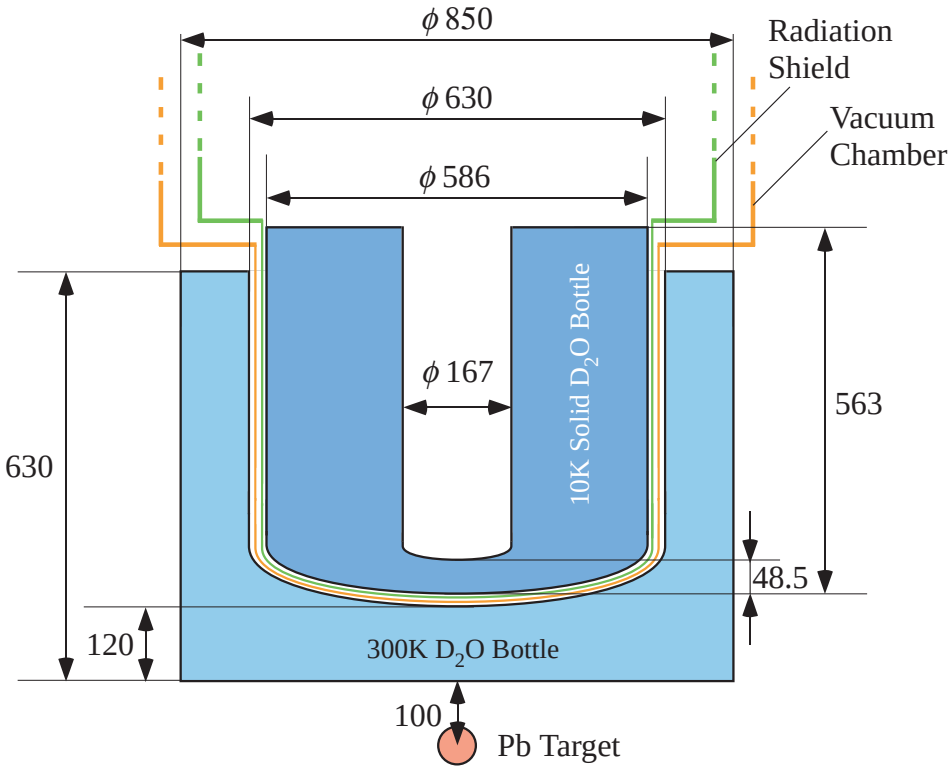

Figure 3.5: The schematic view of the RT (300 K) and 10 K solid D_2O moderators.

UCN are produced in the He-II bottle. The view of the He-II bottle is shown in Fig. 3.6. The He-II bottle has a 153 mm inner diameter and a 408 mm height. It is made of aluminum with a thickness of 2 mm. The inner surface of the He-II bottle is coated with the electroless nickel plating (Ni-P coating). The chemical components of the Ni-P coating are 85 % of nickel (Ni) and 15 % of phosphorus (P). The thickness of the Ni-P coating film is about $10 \sim 15$ μm and the density is 7.8 g/cm^3. The Fermi potential of the Ni-P coating is 214 neV. Therefore, UCN with energies below 214 neV are confined in the He-II bottle. In other words, the UCN critical energy, E_c, is 214 neV in this bottle.

During the experiments, the He-II bottle is filled with He-II at a temperature of 0.8 K. The volume of He-II is 8.5 liters. The He-II bottle is surrounded by the nichrome wire heaters. This heaters are used for the baking of the He-II bottle before UCN production experiments.

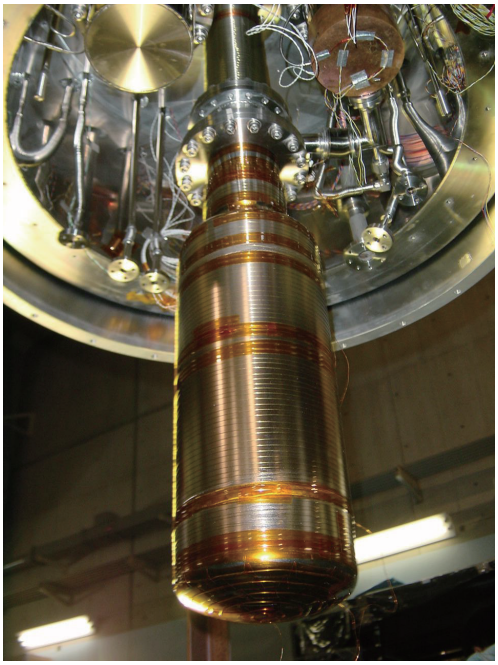

Figure 3.6: The view of the He-II bottle. The size of the He-II bottle is 153 mm inner diameter and 408 mm height. During the experiments, this bottle is filled with He-II at a temperature of 0.8 K with a volume of 8.5 liters. The He-II bottle is surrounded by the nichrome heater wires used for the baking.

UCN Guide and UCN Valve

UCN produced in the He-II bottle are extracted via diffusion through a long UCN guide. As shown In Fig. 3.2, the He-II bottle is located at the centre of the 10 K solid D_2O moderator. The top flange of the He-II bottle is connected to the UCN vertical guide. UCN diffuse from the He-II bottle to the upper direction through the UCN vertical guide. Then, UCN go into the UCN horizontal guide through the 90 degree elbow guide. Those UCN go through the

UCN horizontal guide, then arrive at the experimental port. At the experimental port, a VAT gate valve ("UCN Valve") is attached to the flange to separate the UCN source from the atmosphere. The scheme of the UCN guide is shown in Fig. 3.7.

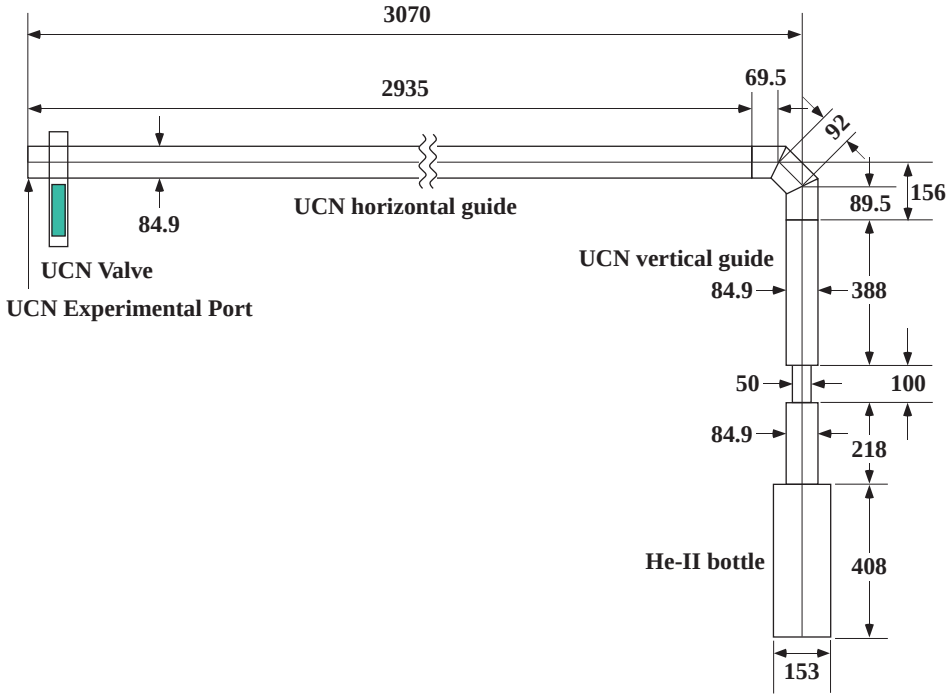

Figure 3.7: The geometry of the UCN guide and the He-II bottle. UCN produced in the He-II bottle diffuse from the He-II bottle to the experimental port through the UCN vertical and horizontal guides. UCN with energies below 130 neV are trapped by the gravity and cannot be extracted from the UCN source.

The distance between from the bottom of the He-II bottle and the center axis of the UCN horizontal guide is 127 cm. This height is corresponding to the gravity potential of 130 neV. Therefore, UCN with energies below 130 neV are trapped by the gravity and confined in the UCN vertical guide or the He-II bottle. We cannot extract them. This vertical extraction reduces the UCN density at the experimental port. The UCN critical energy at the experimental port is $E_c = 214 - 130 = 84$ neV.

The UCN vertical guide, the UCN horizontal guide and the UCN valve are made of stainless steel (SUS316L). The chemical components of SUS316L are 68 % of iron (Fe), 18 % of nichkel (Ni), 12 % of chromium (Cr) and 2 % of molybdenim (Mo). The Fermi potential of SUS316L is 188 neV. The inner surface of the UCN vertical and horizontal guides were polished by the Electro-Chemical Buffing (ECB). The ECB is a combination of electropolishing and mechanical buffing by abrasive, and enable us to obtain more flat surfaces than the standard electropolishing.

Gravity Accelerator Tube

The ^{3}He gas proportional detector (type Dunia-10, [45] [46]) is used to detect the UCN extracted from the source. At the entrance window of the Dunia-10 UCN detector, there is an aluminum foil with a thickness of 100 μm. The Fermi potential of aluminum is 54 neV. Therefore, we must accelerate the UCN to be with an energy above 54 neV to detect them.

When we use the Dunia-10 UCN detector, a vertical UCN guide with a length of about 1 m is attached to the experimental port before the UCN detector. Fig. 3.8 shows the view of the gravity accelerator tube attached to the experimental port. The distance between the UCN horizontal guide and the end of the gravity accelerator tube where the UCN detector is attached is about 1 m. The height of 1 m corresponds to the gravity potential of 102.5 neV. UCN are accelerated by the gravity and gain an energy of about 100 neV. This energy is enough large for UCN to go into the UCN detector through the aluminum foil.

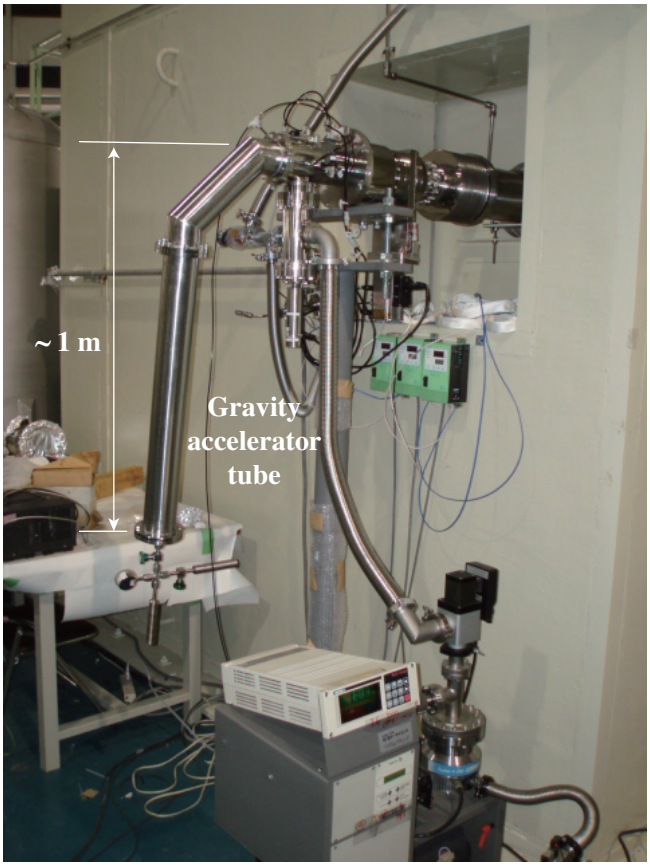

Figure 3.8: The view of the gravity accelerator tube attached to the experimental port. The distance between the UCN horizontal guide and the end of the gravity accelerator tube is about 1 m.

3.3 Spallation Neutron Production and Moderation

3.3.1 Spallation Neutron Production by PHITS

The spallation reaction with a proton beam of 392 MeV and the lead target is used to produce fast neutrons. We estimated the spallation neutron production in our experiment by PHITS [34]. The lead target with a size of $100 \times 100 \times 200$ mm^3 and the incident proton beam with an energy of 392 MeV were reconstructed by PHITS. The obtained neutron yield per incident proton was 7.7 n/p. The surface area of the lead target is 1,000 cm^2, so the neutron flux on the target surface per incident proton is 7.7×10^{-3} n cm^{-2} p^{-1}. Since a 1 μA proton beam corresponds to 6.24×10^{12} p/s, the neutron flux on the target surface per 1 μA proton beam, Φ_0, is given by

$$\Phi_0 = 4.8 \times 10^{10} \text{ [n cm}^{-2} \text{ s}^{-1}] \ . \tag{3.1}$$

The appearance of collisions between the incident proton and the lead target is shown in Fig. 3.9. Fig. 3.10 shows the emission of neutrons by the spallation reaction simulated by PHITS.

PHITS can also calculate the energy spectrum of neutrons obtained by spallation reaction. Fig. 3.11 shows the energy spectrum of the neutron flux crossing the surface of the lead target. The peak of the neutron flux is around 1 MeV. Most of the neutrons are in the region below 10 MeV, although the incident proton energy was 392 MeV.

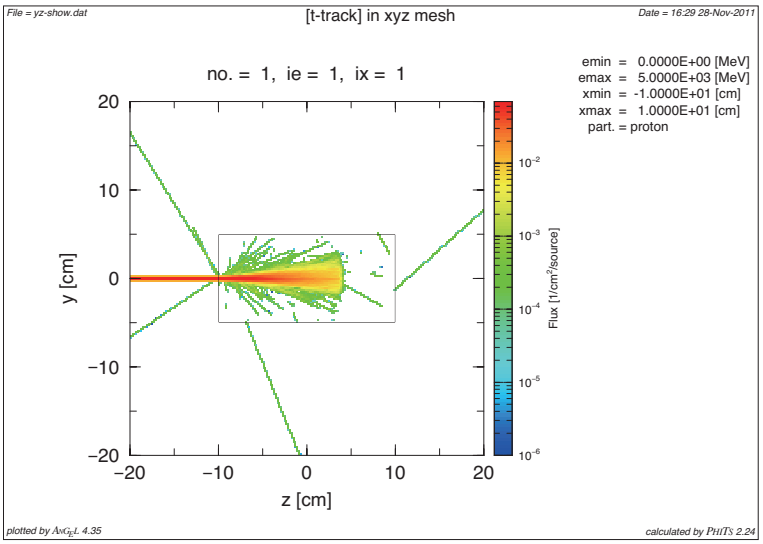

Figure 3.9: The incident proton in the lead target. Output by PHITS. The energy of the incident proton is 392 MeV. The target size is $100 \times 100 \times 200$ mm^3. The number of the proton is 1,000.

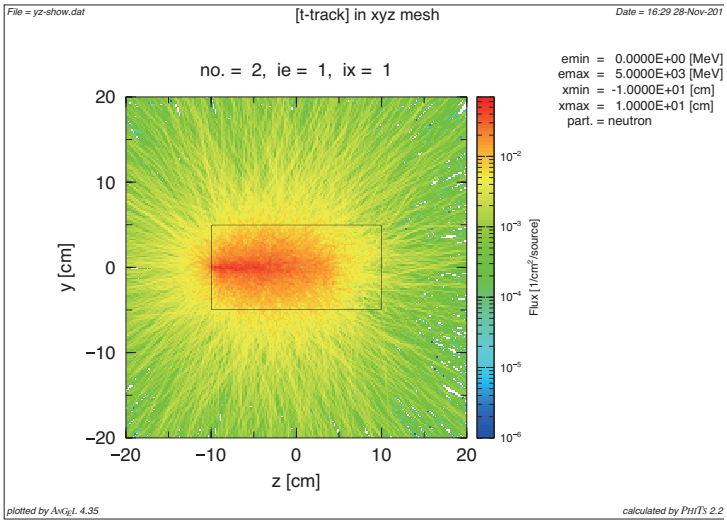

Figure 3.10: The emission of neutrons from the lead target by the spallation reaction. Output by PHITS.

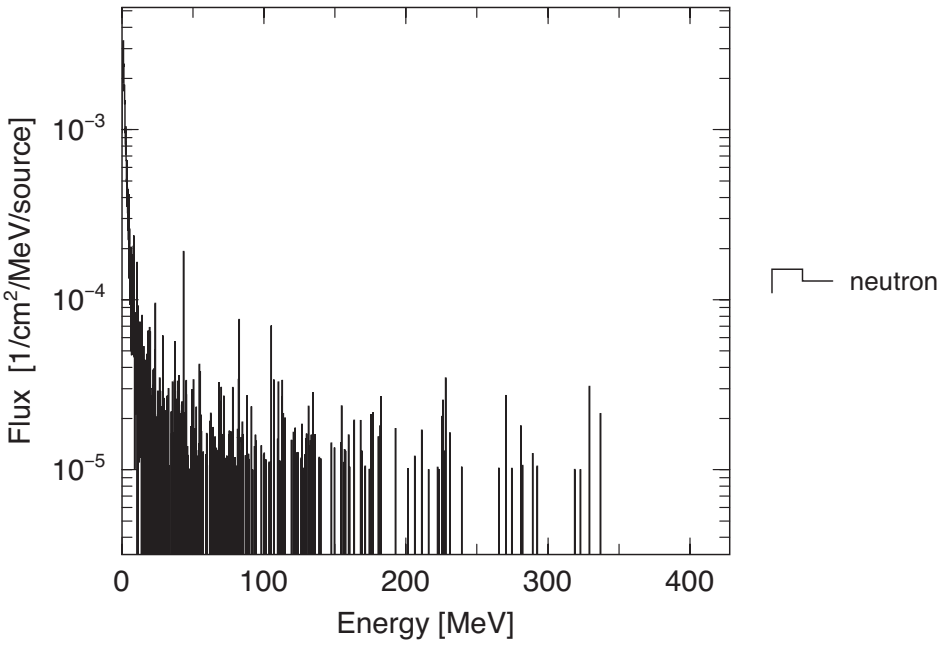

Figure 3.11: The energy spectrum of the neutron flux crossing the surface of the lead target. Output by PHITS. The peak of the neutron flux is around 1 MeV. Most of the neutrons are in the region below 10 MeV.

3.3.2 Neutron Moderation in D_2O

We also simulated the moderation of the fast neutrons obtained by the spallation reaction with PHITS. The geometry of the He-II spallation UCN source was reconstructed as shown in Fig. 3.12. The lead target, the graphite reflectors around the target, the RT D_2O moderator, the 10 K solid D_2O moderator, the He-II bottle and the lower part of the UCN vertical guide were reconstructed in the geometry.

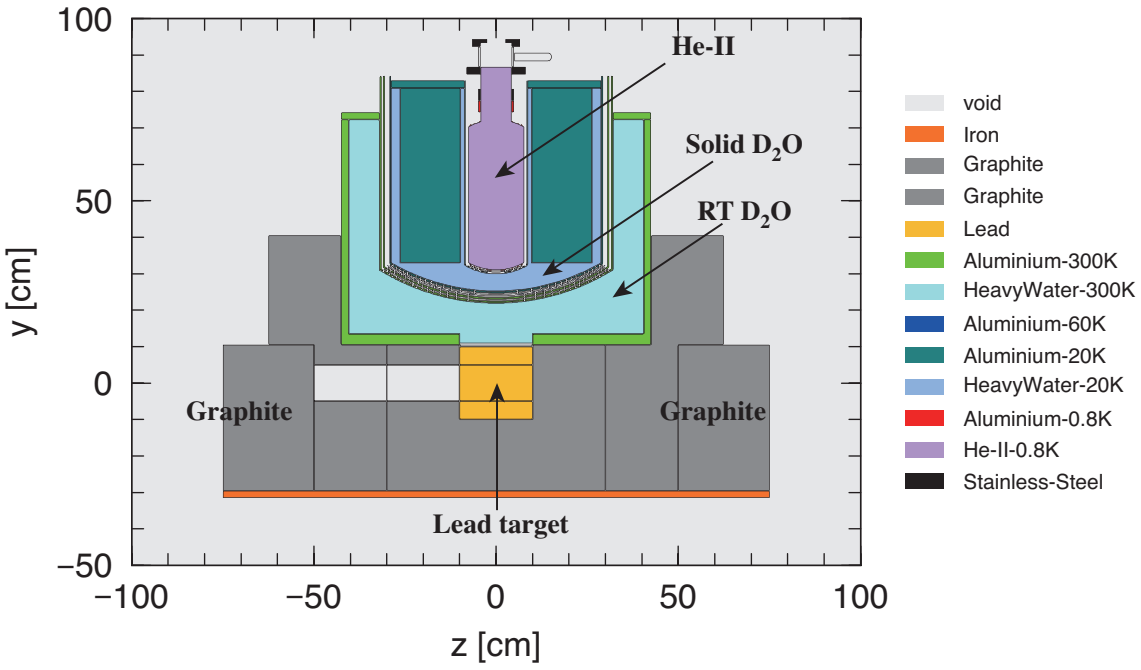

Figure 3.12: The geometry of the He-II superthermal UCN source at RCNP reconstructed by PHITS. The temperature of the solid D_2O moderator is 20 K in this output.

We simulated the cold neutron flux in the He-II bottle, changing the temperature of the solid D_2O moderator. The simulation was carried out in the case at a temperature of 20 K, 50 K and 80 K. Although the temperature of the solid D_2O is 10 K during the experiments, heavy water atoms are tightly bounded mutually due to van deer Waals' force at a low temperature. Such bounded atoms work as a wall with a large mass against an incident neutron. Therefore, the neutrons in the 10 K solid D_2O moderator are not scattered efficiently and the neutron temperature cannot become same as the moderator. According to ref. [47], a neutron temperature moderated in a light water (H_2O) moderator could not become below 50 K, even if the moderator's temperature was below 50 K. So, it is expected that the cold neutron flux obtained from our cold moderator has a temperature above 50 K.

On the other hand, PHITS does not include the data of the form factors of light and heavy waters at low temperatures (the form factors at the RT are included). The heavy water atoms are treated as a group of free particles. We assumed that, in PHITS calculation, the temperature of the cold neutrons from the solid D_2O moderatator has same or near temperature

as the solid D_2O. The actual temperature of the cold neutrons in the experiments is 50 K or higher. And if we change the solid D_2O temperature T, the cold neutron flux obtained by PHITS will coincide with the actual cold neutron flux at a certain temperature T.

Fig. 3.13 shows the energy spectra of the cold neutron flux in the He-II bottle obtained by PHITS. The temperature of the solid D_2O moderator is 20 K, 50 K and 80 K, respectively.

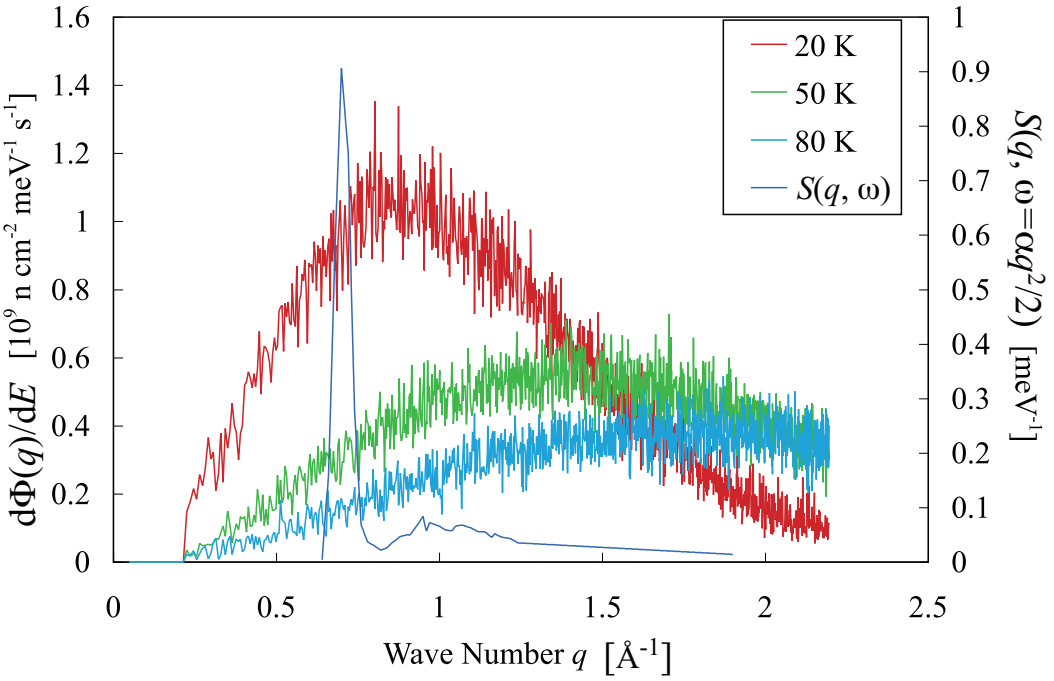

Figure 3.13: The energy spectra of the cold neutron flux in the He-II bottle obtained by PHITS. The temperature of the solid D_2O moderator is 20 K, 50 K and 80 K, respectively. $S(q, \omega)$ on the neutron dispersion curve is also shown.

The total cold neutron flux in the He-II bottle is given by

$$\Phi = \int dE \frac{d\Phi(q)}{dE} = \begin{cases} 5.038 \pm 0.020 & (T = 20 \text{ K}) \\ 4.371 \pm 0.018 & (T = 50 \text{ K}) \\ 3.123 \pm 0.015 & (T = 80 \text{ K}) \end{cases} [10^9 \text{ n cm}^{-2} \text{ s}^{-1}] \, . \tag{3.2}$$

The cold neutron flux at $q = k^* = 0.706$ Å (or $\lambda^* = 8.9$ Å) where the dispersion curves of He-II and a neutron intersect is given by

$$\frac{d\Phi(k^*)}{dE} = \begin{cases} 9.44 \pm 0.81 & (T = 20 \text{ K}) \\ 2.92 \pm 0.45 & (T = 50 \text{ K}) \\ 1.54 \pm 0.34 & (T = 80 \text{ K}) \end{cases} [10^8 \text{ n cm}^{-2} \text{ meV}^{-1} \text{ s}^{-1}] \, . \tag{3.3}$$

3.4 UCN Production Rate in He-II Bottle

The UCN production rate per volume P is given by

$$P = N_{He}\sigma_{He}\alpha^2\frac{k_c^3}{3}\left[\int dk_1 \frac{d\Phi(k_1)}{dE_1} S(k_1, \hbar\omega = \frac{\hbar^2 k_1^2}{2m_n})\right] \tag{3.4}$$

$$= (1.763 \pm 0.026) \times 10^{-7} \cdot \left[\int dk_1 \frac{d\Phi(k_1)}{dE_1} S(k_1, \hbar\omega = \frac{\hbar^2 k_1^2}{2m_n})\right] \text{ UCN cm}^{-3}\text{ s}^{-1} \tag{3.5}$$

from Eqn.(2.16). The UCN production rate by single phonon process P_I is given by

$$P_I = (1.010 \pm 0.070) \times 10^{-8} \times \frac{d\Phi(k^*)}{dE} \ . \tag{3.6}$$

from Eqn.(2.29). The UCN production rate by multi phonon process is $P_{II} = P - P_I$.

To estimate P, we calculated the integral of Eqn.(3.5), using the cold neutron flux spectrum $d\Phi(q)/dE$ obtained by PHITS. The integral range is $0.64 \leq q \leq 1.9$ Å^{-1}. $S(q, \hbar\omega = \alpha q^2/2)$ is enough small outside this range. Since there is no measured data of $S(q, \hbar\omega)$ in the range of $1.2 < q < 1.9$ Å^{-1}, we approximated this range by linear fitting. The number of the data points of $d\Phi/dE$ by PHITS is much more than that of $S(q, \hbar\omega)$. So, we linearly interpolated the adjacent two points of $S(q, \hbar\omega)$. The results of the integration were given by

$$\int_{0.64}^{1.9} \frac{d\Phi(q)}{dE} S(q, \hbar\omega = \frac{\alpha q^2}{2}) dq = \begin{cases} (8.437 \pm 0.095) \times 10^7 & (T = 20 \text{ K}) \\ (3.706 \pm 0.054) \times 10^7 & (T = 50 \text{ K}) \\ (2.079 \pm 0.039) \times 10^7 & (T = 80 \text{ K}) \end{cases} \tag{3.7}$$

where each integral was carried out by trapezoidal integration. Then, the UCN production rates per volume P were obtained to be

$$P = \begin{cases} 14.87 \pm 0.28 & (T = 20 \text{ K}) \\ 6.53 \pm 0.14 & (T = 50 \text{ K}) \\ 3.67 \pm 0.09 & (T = 80 \text{ K}) \end{cases} \text{ [UCN cm}^{-3}\text{ s}^{-1}\text{]} \ . \tag{3.8}$$

The UCN production rates by single phonon process P_I were given by

$$P_I = \begin{cases} 9.5 \pm 1.1 & (T = 20 \text{ K}) \\ 2.9 \pm 0.5 & (T = 50 \text{ K}) \\ 1.6 \pm 0.4 & (T = 80 \text{ K}) \end{cases} \text{ [UCN cm}^{-3}\text{ s}^{-1}\text{]} \ . \tag{3.9}$$

Therefore, $P_{II} = P - P_I$ were obtained to be

$$P_{II} = \begin{cases} 5.4 \pm 1.1 & (T = 20 \text{ K}) \\ 3.6 \pm 0.5 & (T = 50 \text{ K}) \\ 2.1 \pm 0.4 & (T = 80 \text{ K}) \end{cases} \text{ [UCN cm}^{-3}\text{ s}^{-1}\text{]} \ . \tag{3.10}$$

The UCN production rate of the single and multi phonon processes and their total at each temperature are shown in Table. 3.1.

T [K]	P_I	P_{II}	P
20	9.5 ± 1.1	5.4 ± 1.1	14.87 ± 0.28
50	2.9 ± 0.5	3.6 ± 0.5	6.53 ± 0.14
80	1.6 ± 0.4	2.1 ± 0.4	3.67 ± 0.09

Table 3.1: The UCN production rate per volume of the single and multi phonon processes and their total at each temperature. The unit of P_I, P_{II} and P is UCN cm^{-3} s^{-1}.

Chapter 4

Operation of UCN Source

In this chapter, the way how to start up our UCN source is explained. The baking and the deuteration of the He-II bottle and the UCN guide are discussed at first. Then, the solidification of D_2O in the 10 K solid D_2O moderator bottle is shown. The solid D_2O is cooled to be 10 K by Gifford McMahon refrigerator after the solidification. These works have to be done before the He-II condensation.

We begin the He-II condensation after the temperature of the solid D_2O became 10 K. The 4.2 K liquid helium is transported to the liquid helium bottle at first. Then, the liquid helium is transported to the 1K cryostat and is cooled to be around 1 K by pumping. Then, we start the circulation of ^{3}He gas. The circulating ^{3}He gas is cooled by using this 1K liquid helium, and then, it is cooled to be 0.7 K by pumping in the ^{3}He cryostat. Finally, we transport the isopure helium from the reservoir tank to the heat exchange pot which is attached to the bottom of the ^{3}He cryostat. The isopure helium is cooled to be 0.8 K by the 0.7 K liquid ^{3}He and becomes superfluid helium there. The condensed superfluid helium fills the He-II bottle. The He-II condensation needs about 2 days.

After the experiments, we have to recover the D_2O used for the solidification and the isopure helium gas from the UCN cryostat into their reservoir tanks.

4.1 Baking and Deuteration of He-II Bottle and UCN Guide

The UCN loss probability by reflection on a material wall greatly depends on the surface states. UCN are lost due to inelastic scattering and absorption by nuclei of the wall material. The inelastically scattered UCN get out of the UCN energy range. The absorbed UCN are fused to the nuclei with emitting γ-ray. The UCN loss probability per reflection on a surface, $\mu(E, \theta)$, depends on the inelastic scattering cross section σ_i and the absorption cross section σ_a of the

nuclei. $\mu(E,\theta)$ is written as follows.

$$\mu(E,\theta) = 2\eta\left(\frac{E\cos^2\theta}{V_F - E\cos^2\theta}\right)^{1/2} \quad (4.1)$$

$$\eta = \frac{(\sigma_i + \sigma_a)k}{4\pi b_c} \quad (4.2)$$

where E is the UCN energy, θ is the glancing angle of the incident UCN, V_F is the Fermi potential of the wall material, k is the wave number of the incident UCN, and b_c is the bound coherent scattering length of the material's nucleus.

However, the experimentally measured loss probabilities μ (or η) are about $10 \sim 100$ times larger than the theoretical prediction. Although the reason of this anomaly is not understood well, it is thought that impurities on material surfaces have some kinds of influences on the UCN loss mechanism. For example, H_2, O_2, H_2O, CO, CO_2, and other many kinds of atoms are found on material surfaces. These molecules are chemically bounded and form a thin film on pure material surfaces. The thickness of the thin film is about 100 Å in many cases. Especially, hydrogen atoms have a great influence on UCN. The hydrogen nucleus, proton, has the large neutron scattering cross section ($\sigma_s = 82.02(6)$ b). UCN scattered by hydrogen nucleus bounded on a material surface absorb phonons and gain some kinetic energy, and get out of the UCN energy range.

These impurities can be removed by baking the surface. The impurity molecules gain some energies by heating, and they evaporate from the material surfaces. The pure surface leads to the less UCN loss probability and lengthens the UCN storage time.

Before the experiments, we baked the He-II bottle and the UCN guide by the nichrome wire heaters which surround the He-II bottle and the UCN guide. The arrangement of the nichrome wire heaters is shown in Fig. 4.1. The He-II bottle, the UCN vertical guide and the UCN horizontal guide are surrounded by the nichrome wire heaters. In addition, the UCN guide near the experimental port is surrounded by the ribbon heaters (see Fig. 4.2). By these heaters, the He-II bottle, the UCN guides and the UCN valve are baked up to about 120 degree Celsius. The time until the system reaches the 120 degree Celsius is about 4 hours. The temperature of 120 degree Celsius is remained for about 12 hours. After the baking at a temperature of 120 degree Celsius, we turn down the output power of the heaters little by little. Then, we deuterates the He-II bottle and the UCN guides.

"Deuteration" is the process to replace hydrogen (H) atoms on material surfaces by deuteron (D) atoms. The effect of the deuteration was measured in the case of a copper surface [48]. Their result shows that the UCN loss rate of the deuterated Cu surface is about a half of the untreated surface.

Our deuteration is done as follows.

1. Bake the He-II bottle, the UCN guide and the experimental port up to 120 degree Celsius for about 12 hours.

2. Put the appropriate amount of D_2O vapor into the UCN guide and the He-II bottle.

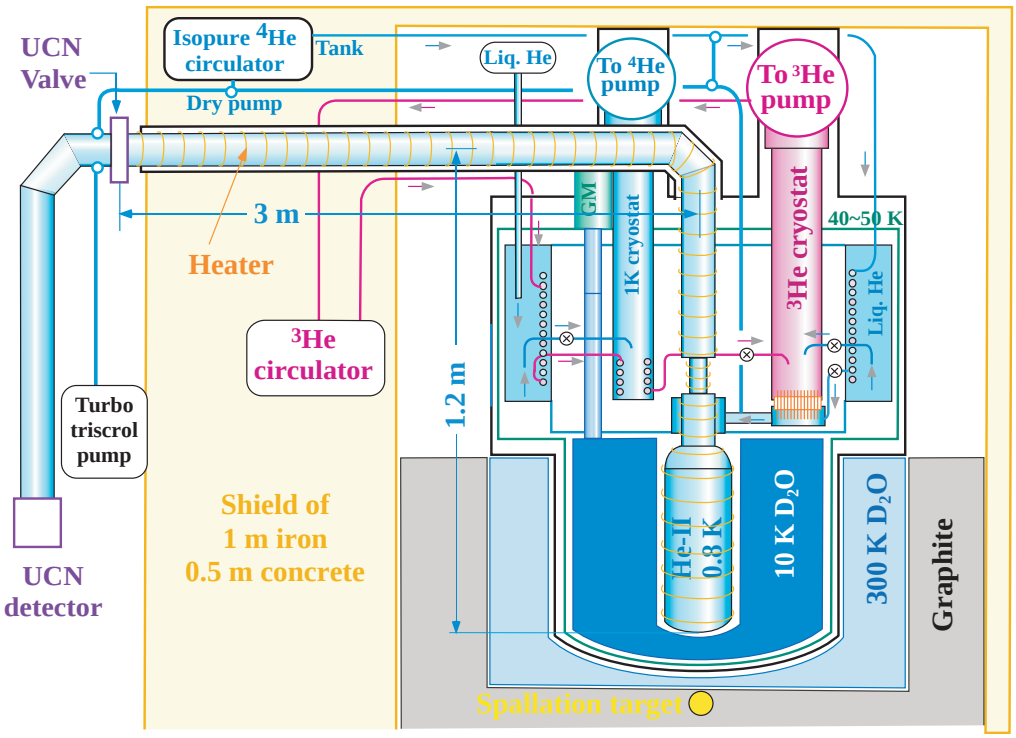

Figure 4.1: The arrangement of the nichrome wire heaters. The heaters surround the He-II bottle and the UCN vertical and horizontal guides.

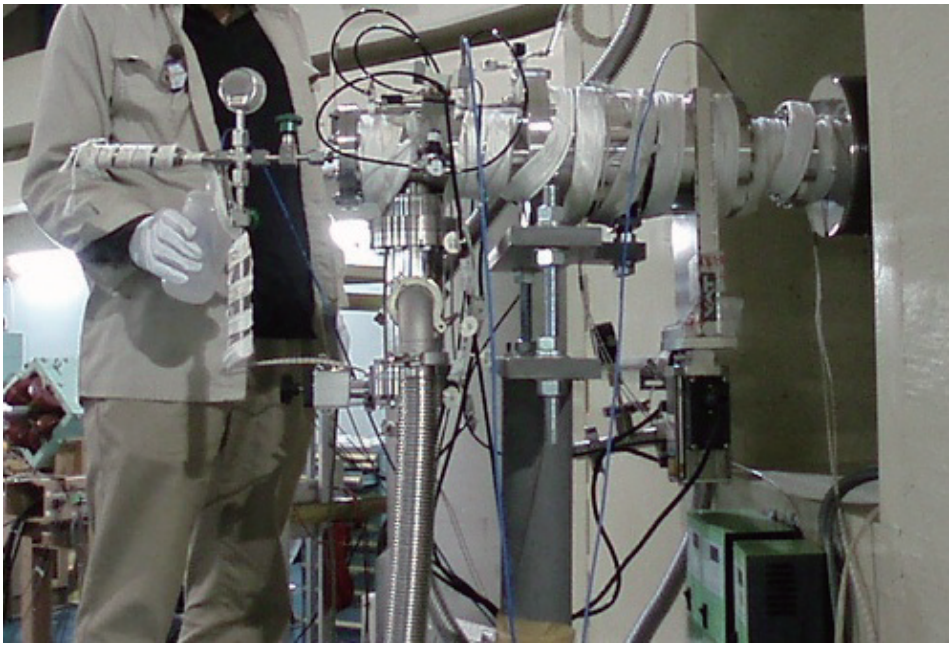

Figure 4.2: The view of the experimental port during the baking. The white belts are the ribbon heaters. The apparatus attached to the experimental port is used for the deuteration.

3. Then, turn down the output power of the nichrome wire heaters little by little.

4. After about 6 hours, turn off the heaters. The temperature of the He-II bottle and the UCN guide at this time is about 340 K. Then, pump the UCN guide and the He-II bottle.

Fig. 4.3 shows the schematic structure of the D_2O vapor pot which is attached to the experimental port in Fig. 4.2. The liquid D_2O in the lower pot are heated up to about 80 degree Celsius during the baking. After the baking, the valve of the lower pot (Valve 1) is opened and the D_2O vapor is confined in the side buffer. The volume of the side buffer is about 50 cm^3 and the pressure of the confined D_2O vapor is about 0.2 atm. The Valve1 is soon closed after filling the side buffer with the vapor. Then, the valve leading to the UCN guide (Valve 2) is opened and the D_2O vapor goes into the UCN source. The D_2O vapor is adsorbed to the surfaces of the UCN guide and the He-II bottle as their temperature goes down.

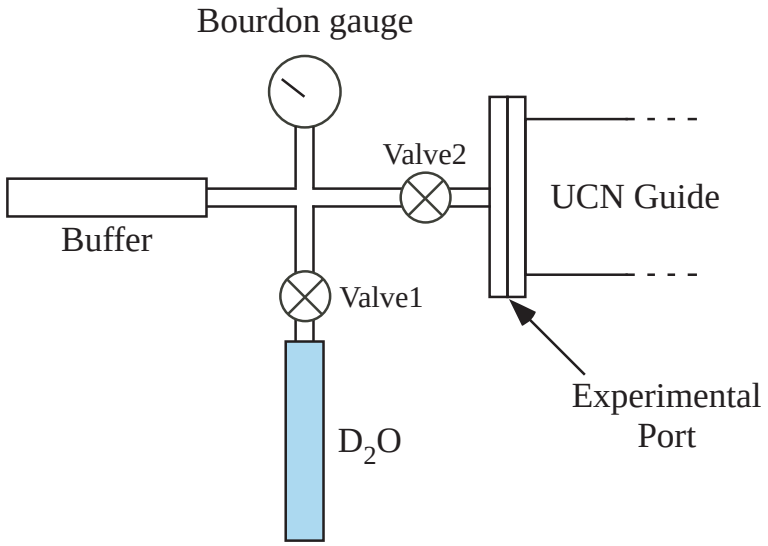

Figure 4.3: The schematic structure of the D_2O vapor pot attached to the experimental port.

The relation between the baking temperature and the amount of the evaporating molecules from surfaces is shown in ref. [49]. It was confirmed that H_2, O_2, H_2O, CO, CO_2 are mainly given off from the stainless steel (SUS304) by baking. If we want to obtain a perfect pure surface, SUS304 must be baked up to about 400 degree Celsius or more. However, in our system, such high temperature is difficult to obtain because the nichrome wire heaters would be damaged by heat. The baking temperature of 120 degree Celsius is determined from the material's limit.

After putting the D_2O vapor into the UCN source, we turn down the output power of the heaters little by little to cool down the UCN guide and the He-II bottle. During this operation, we control the temperatures of the UCN guide and the He-II bottle to be uniform because the adsorption of the D_2O vapor depends on the temperature of the surfaces. The temperature of the surfaces becomes enough low after about 6 hours. Then, the power of the heaters is turned off.

4.2 D_2O Solidification

After the baking and the deuteration of the He-II bottle and the UCN guide, we solidify the D_2O in the 10 K solid D_2O bottle. The liquid D_2O is cooled by the GM refrigerator to be solid state. D_2O with a volume of about 100 liters is solidified. The time for the D_2O solidification is about 9 days. Then, the solidified D_2O is cooled to be 10 K in about 7 days. After the experiments, we turn off the GM refrigerator. The solid D_2O comes back to be the room temperature in one month. Then, the used D_2O is recovered into the reservoir tank.

4.2.1 D_2O Line

Fig. 4.4 shows the scheme of the D_2O lines used to transport the D_2O between the 10 K solid D_2O bottle and the reservoir tank. The D_2O reservoir tank has a inner diameter of 800 mm and a inner height of 1,200 mm. To fill the 10 K solid D_2O bottle with D_2O, a water pump installed on the D_2O is used. This water pump is also used to recover the used D_2O from the UCN cryostat to the D_2O reservoir tank after the experiments.

We have no probe to access the inside of the 10 K solid D_2O bottle during the D_2O solidification. This means that we cannot measure the water level of the D_2O in the 10 K solid D_2O bottle. So, we used the capacitance leveler attached to the D_2O reservoir tank to know the water level in the D_2O reservoir tank and calculated the amount of the solidified D_2O.

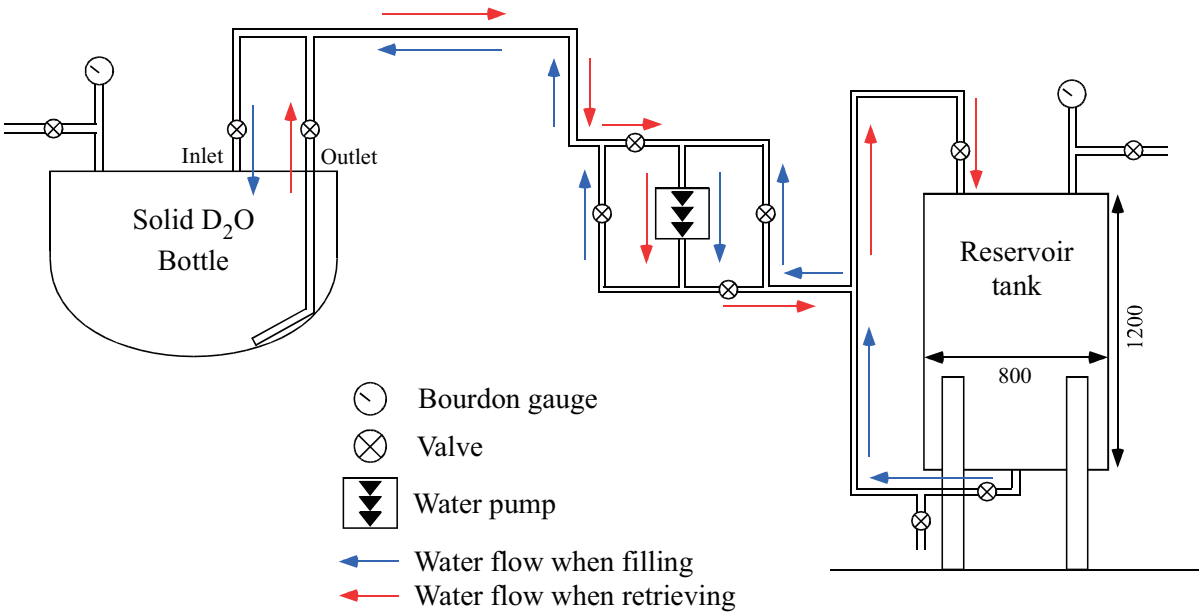

Figure 4.4: The scheme of the D_2O filling/retrieving line.

4.2.2 Cooling Time Estimation

The volume of the D_2O used for the solidification is 103 liters. Since the density of D_2O is 1.1056 g/cm^3 at 293 K, the mass of the solidified D_2O is 114 kg. Here, we estimate the total heat of the D_2O used for the solidification.

The latent heat of D_2O is 1515 cal/mol = 75.6 cal/g = 316.5 J/g. Since we have no data of the specific heat of D_2O, we used the specific heat of H_2O instead. The specific heat of H_2O at each temperature is shown in Fig.4.5.

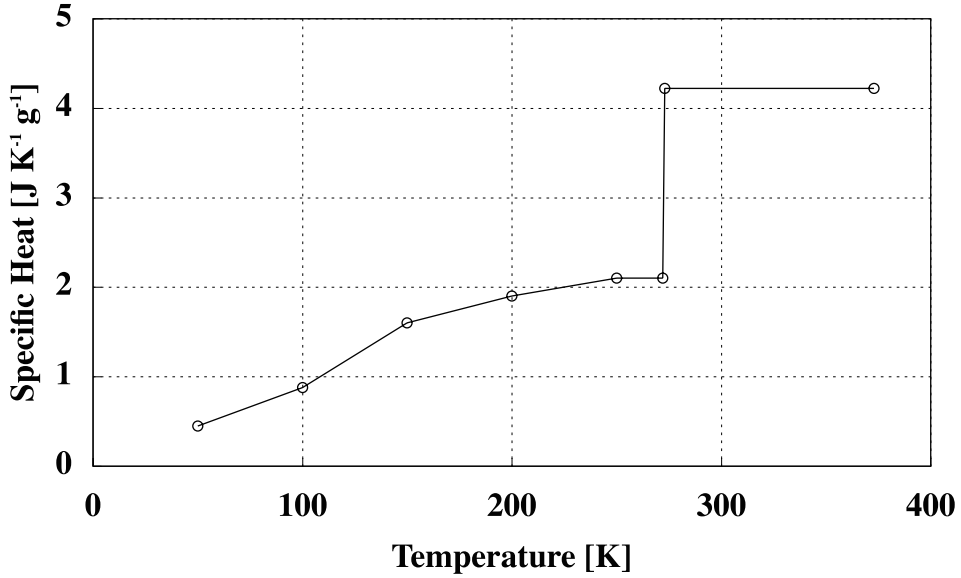

Figure 4.5: The temperature dependence of the specific heat of H_2O.

From the RT (298K) to the melting point of D_2O, 277 K, the heat capacity is given by

$$4.22\ [\mathrm{J\ K^{-1}\ g^{-1}}] \times (298 - 277)\ [\mathrm{K}] \times 114 \times 10^3\ [\mathrm{g}] = 1.01 \times 10^7\ [\mathrm{J}]\ . \tag{4.3}$$

The total latent heat is given by

$$316.5\ [\mathrm{J/g}] \times 114 \times 10^3\ [\mathrm{g}] = 3.61 \times 10^7\ [\mathrm{J}]\ . \tag{4.4}$$

From 277 K to 200 K,

$$2.0\ [\mathrm{J\ K^{-1}\ g^{-1}}] \times (277 - 200)\ [\mathrm{K}] \times 114 \times 10^3\ [\mathrm{g}] = 1.76 \times 10^7\ [\mathrm{J}] \tag{4.5}$$

where the heat capacity of 2.0 J K^{-1} g^{-1} is the average of the heat capacity at 277 K (2.1 J K^{-1} g^{-1}) and at 200 K (1.9 J K^{-1} g^{-1}). Therefore, from the RT to 200 K, the total heat of the solidified D_2O is 6.38×10^7 J. If we were to assume the cooling power of the GM refrigerator to be 80 W, the necessary time for the D_2O solidification is estimated to be

$$\frac{6.38 \times 10^7\ [\mathrm{J}]}{80\ [\mathrm{W}]} = 8.0 \times 10^5\ [\mathrm{s}] = 9.2\ [\mathrm{d}]\ . \tag{4.6}$$

After the D_2O solidification, we have to cool down the temperature of the solid D_2O from 200 K to 10 K. The heat capacity of the D_2O in this range is calculated as follows.

From 200 K to 150K, the heat capacity is

$$1.75\ [\mathrm{J\ K^{-1}\ g^{-1}}] \times (200 - 150)\ [\mathrm{K}] \times 114 \times 10^3\ [\mathrm{g}] = 1.0 \times 10^7\ [\mathrm{J}] \tag{4.7}$$

where the heat capacity of 1.75 J K^{-1} g^{-1} is the average of the heat capacity at 200 K (1.9 J K^{-1} g^{-1}) and at 150 K (1.6 J K^{-1} g^{-1}).

From 150 K to 100K, the heat capacity is given by

$$1.24\ [\mathrm{J\ K^{-1}\ g^{-1}}] \times (150 - 100)\ [\mathrm{K}] \times 114 \times 10^3\ [\mathrm{g}] = 7.1 \times 10^6\ [\mathrm{J}] \tag{4.8}$$

where the heat capacity of 1.24 J K^{-1} g^{-1} is the average of the heat capacity at 150 K (1.6 J K^{-1} g^{-1}) and at 100 K (0.88 J K^{-1} g^{-1}).

From 100 K to 50K, the heat capacity is given as follows.

$$0.67\ [\mathrm{J\ K^{-1}\ g^{-1}}] \times (100 - 50)\ [\mathrm{K}] \times 114 \times 10^3\ [\mathrm{g}] = 3.8 \times 10^6\ [\mathrm{J}] \tag{4.9}$$

where the heat capacity of 0.67 J K^{-1} g^{-1} is the average of the heat capacity at 100 K (0.88 J K^{-1} g^{-1}) and at 50 K (0.45 J K^{-1} g^{-1}).

From 50 K to 10K, the heat capacity is given by

$$0.22\ [\mathrm{J\ K^{-1}\ g^{-1}}] \times (50 - 10)\ [\mathrm{K}] \times 114 \times 10^3\ [\mathrm{g}] = 1.0 \times 10^6\ [\mathrm{J}] \tag{4.10}$$

where the heat capacity of 0.22 J K^{-1} g^{-1} is the average of the heat capacity at 50 K (0.45 J K^{-1} g^{-1}) and at 10 K (0.0036 J K^{-1} g^{-1}, calculated by the Debye model).

Therefore, from 200 K to 10 K, the total heat of the solidified D_2O is 2.2×10^7 J. Assuming the cooling power of the GM refregirator to be 80 W, the necessary time to cool down from 200 K to 10 K is estimated to be

$$\frac{2.2 \times 10^7[\mathrm{J}]}{80[\mathrm{W}]} = 2.7 \times 10^5\ [\mathrm{s}] = 3.2\ [\mathrm{d}]\ . \tag{4.11}$$

Actually, the GM refregirator reduces the cooling power as the temperature decreases. The necessary time from 200 K to 10 K is expected to be longer than this estimation.

4.2.3 D_2O Solidification

Platinum-Cobalt (Pt-Co) resistance thermometers are used to monitor the temperatures of the D_2O, the 10 K solid D_2O bottle and the GM refregirator. Fig. 4.6 shows the positions of the Pt-CO thermometers. The two Pt-Co sensors are installed in the middle of the 10 K solid D_2O bottle, but they were broken.

When water becomes solid state, the volume increases. Therefore, we have to be careful of the 10 K solid D_2O bottle not to be broken by the volume expansion. We injected a small amount of D_2O into the 10 K solid D_2 bottle and repeated it. The volume of D_2O of the first

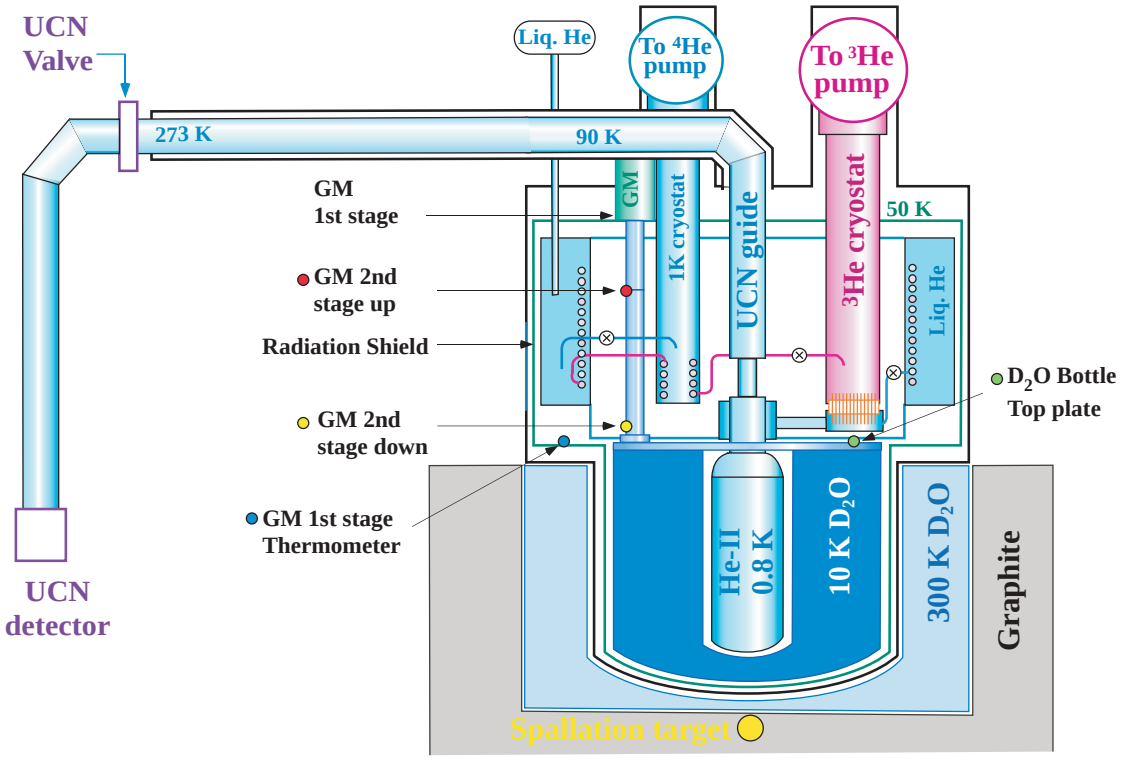

Figure 4.6: The positions of the Pt-Co thermometers.

injection is 15 liters. Then, we repeated to inject the D_2O with a volume of 11 liters 8 times. The injection is 9 times in total and the total volume of the injected D_2O is 103 liters. In the previous section, the necessary time for the D_2O solidification from the RT to 200 K was estimated to be 9.2 days. If this assumption is correct, one injection should be done once per day.

Fig. 4.7 shows the temperature change of the D_2O bottle during the solidification. This is the record between October 20 and November 5 in 2007. We began the first D_2O injection on October 20 and repeated it once per day. The last ninth injection was done on October 28. The D_2O solidification was completed one day later. The total time used for the D_2O solidification was 9.4 days.

After the solidification, the solid D_2O was cooled to be 10 K in 6 days. This time is about 2 times larger than the expectation in the previous section. It is deduced that the GM refregirator reduced the cooling power at low temperature.

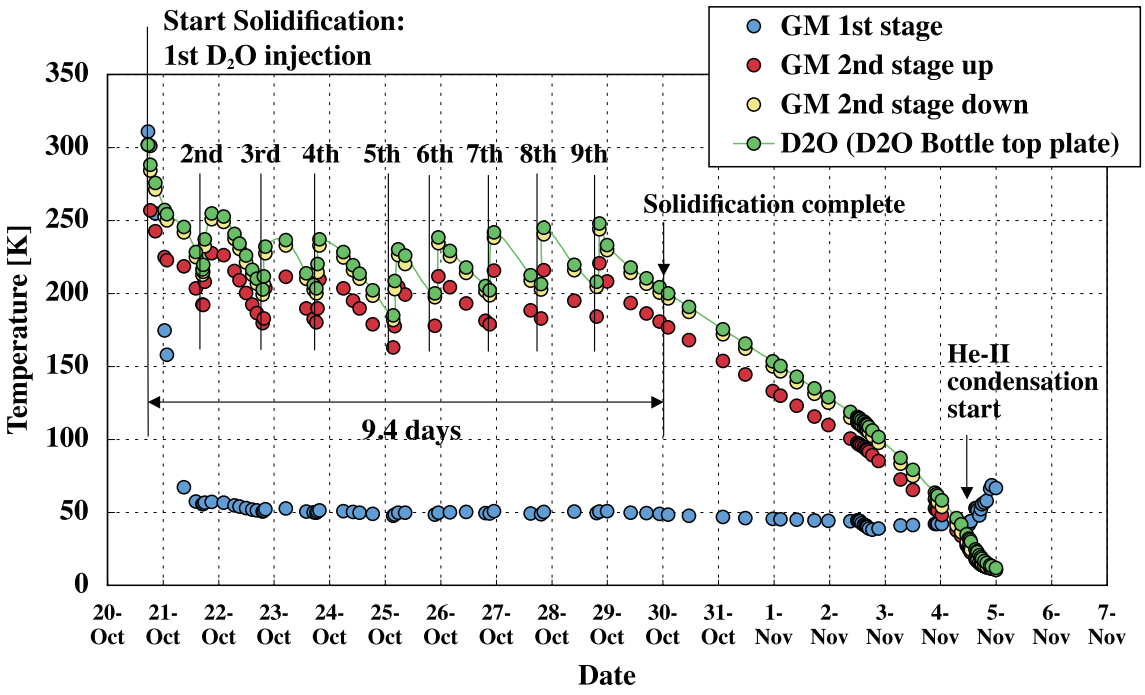

Figure 4.7: The temperature change of the D_2O bottle during the solidification. The rise of the GM 1st stage temperature on November 4 is due to the start of the He-II condensation.

4.2.4 Cooling Power Estimation

The total heat of D_2O with a mass of 114 kg was estimated to be 6.38×10^7 J when it is cooled from the room temperature to 200 K. In our D_2O solidification, the time used for the D_2O solidification was 9.4 days. Therefore, the average cooling power of the GM refregirator P_{GM}

is given by

$$P_{GM} = \frac{6.38 \times 10^7 \text{ [J]}}{9.4 \text{ [d]}} = 79 \text{ [W]} . \tag{4.12}$$

We can also obtain the cooling power of the GM refregirator by using the temperature data shown in Fig. 4.7. In Fig. 4.7, it is shown that the temperature difference between the GM 2nd stage up and the GM 2nd stage down was always about 25 K during the D_2O solidification. Fig. 4.8 shows the positions of the GM 2nd stage thermometers. The thermal flow in the cold finger attached to the GM 2nd stage corresponds to the cooling power P_{GM}.

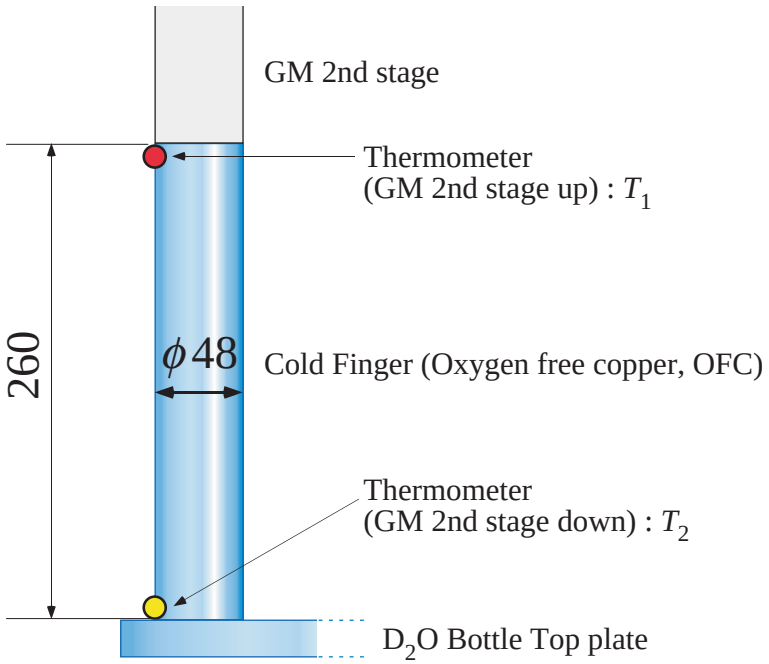

Figure 4.8: The schematic view of the cold finger attached to the GM 2nd stage and the positions of the thermometers.

Using the Hooke's low, the thermal flux between a point with a temperature of T_1 and a point with a temperature of T_2 is given by

$$\frac{dQ}{dt} = \kappa S \frac{\Delta T}{\Delta x}. \tag{4.13}$$

where $\Delta T = T_2 - T_1$, Δx is the distance between the two points, S is the cross sectional area of the heat conductor and κ is the thermal conductivity of the material.

Here, $\Delta T = 25$ K. Δx is the length of the cold finger, 260 mm. S is the cross sectional are of the cold finger, $\pi \times 2.4^2 = 18.1$ cm. κ of the copper is 419 W m^{-1} K^{-1} at 200 K and 450 W

m^{-1} K^{-1} at 150 K. The thermal flux in the cold finger is given by

$$dQ/dt = 4.19\ [\mathrm{W\ cm^{-1}\ K^{-1}}] \times 18.1\ [\mathrm{cm^2}] \times \frac{25\ [\mathrm{K}]}{26\ [\mathrm{cm}]} \tag{4.14}$$

$$= 73\ [\mathrm{W}]. \tag{4.15}$$

where the value of κ at 200 K was used. If we use the value of κ at 150 K,

$$dQ/dt = 4.50\ [\mathrm{W\ cm^{-1}\ K^{-1}}] \times 18.1\ [\mathrm{cm^2}] \times \frac{25\ [\mathrm{K}]}{26\ [\mathrm{cm}]} \tag{4.16}$$

$$= 78\ [\mathrm{W}]. \tag{4.17}$$

is obtained. The thermal flux dQ/dt obtained here are consistent with P_{GM}.

4.3 He-II Condensation

We begin the He-II condensation after the D_2O solidification and precooling to 10 K were finished. This operation is to condense helium gas to be superfluid state.

4.3.1 Liquid Helium Bottle and 1 K Cryostat

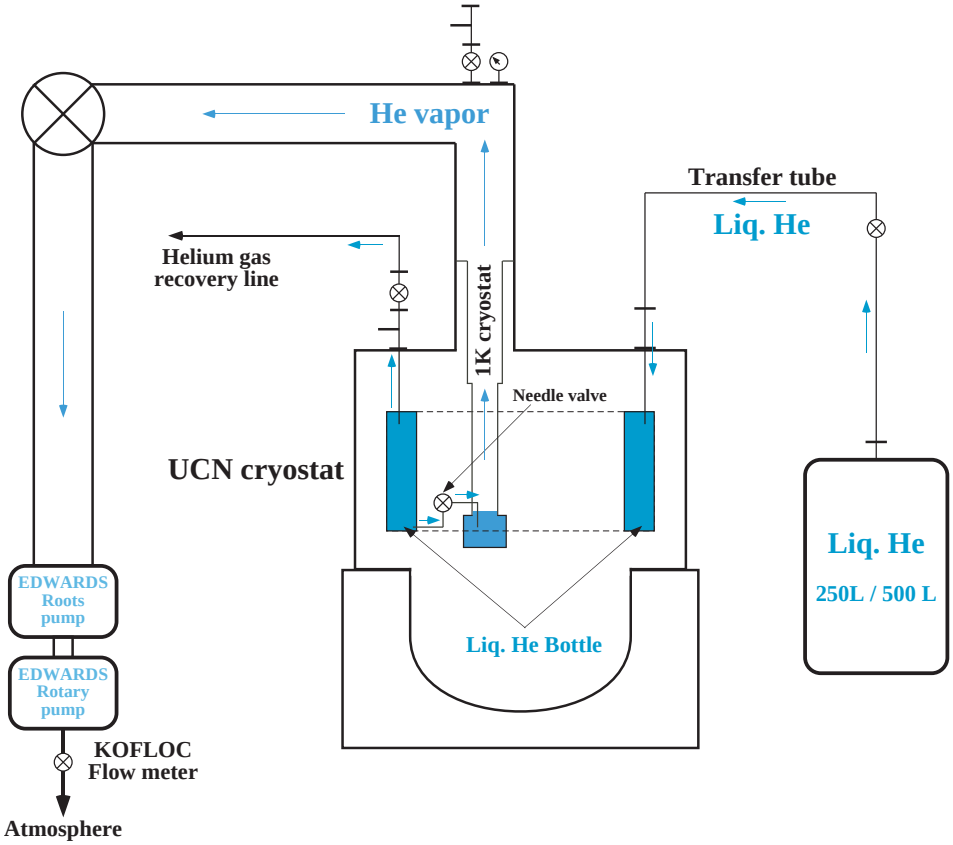

Figure 4.9: The schamtic structure of the liquid helium bottle (Liq. He Bottle in the figure) and the 1 K cryostat.

The schematic structure of the liquid helium bottle and the 1 K cryostat is shown in the Fig. 4.9. We fill the liquid helium bottle in the UCN cryostat with 4.2 K liquid helium at first. The 4.2 K liquid helium is commercially available one. The liquid helium bottle is a cylindrical stainless steel vessel with a 590 mm inner diameter, a 752 mm outer diameter and a 335 mm height. If the precooling was enough, the temperature of the liquid helium bottle is about 55 K before the He-II condensation. The necessary time to fill the bottle with 4.2 K liquid helium for the first time is about $1 \sim 2$ hours. The level of the liquid helium in the bottle is monitored by a liquid helium leveler (AMI, Model 135). The maximum level of the liquid helium is about 26 cm. The full volume of the liquid helium is about 50 liters.

The 4.2 K liquid helium in the bottle is transported to a pot called "1 K cryostat" through a small-bore tube. The flow rate of the transported liquid helium is controlled by a needle valve attached to the small-bore tube. The 1 K cryostat is a cylindrical stanless steel vessel with a diameter of 120 mm and a height of 90 mm. It is always pumped by a pumping system. The pumping system consists of a roots (mechanical booster) pump (EDWARDS, type EH1200IND) and a rotary backing pump (EDWARDS, type E2M80). By this pumping, the temperature of the liquid helium in the 1 K cryostat is cooled to about 1.4 K. The level of the 1.4 K liquid helium is monitored by a liquid helium leveler (AMI, Model 135). The maximum level of the 1.4 K liquid helium is about 15 cm. At this level, the volume of the 1.4 K liquid helium is about 1.3 liter.

The 1.4 K liquid helium is pumped out to the atmosphere through a gas flow meter (KOFLOC, type HFM-201). During the He-II condensation, the flow rate of the pumped helium changes between about 20 to 60 SLM (SLM = standard liter per minute). The time averaged flow rate is 55 SLM. After the He-II condensation was completed, the flow rate becomes stable, and its time average in 6 days beam time was 27 SLM.

We can estimate the cooling power of the 1 K cryostat using the flow rates. The latent heat of liquid helium at 1.4 K is 86 J/mol. The flow rate of the helium gas was 27 SLM, which corresponds to 27 L/m at 1 atm and 0 degree Celsius. This value corresponds to 1.2 mol/min. Therefore, 86 J/mol $\times$ 1.2 mol/min = 104 J/min = 1.7 W was obtained as the cooling power.

The cooling power in an ideal case can be estimated using the spec sheets of the pumps. The nominal pumping speed of EH1200IND is 1435 m^3/h at 60Hz AC and that of E2M80 is 96 m^3/h at 60Hz AC. The cooling power is given by

$$\frac{dQ}{dt} = L \cdot P \cdot \frac{dV}{dt}/(R \cdot T) \tag{4.18}$$

where L is the latent heat at evaporation, P is the pressure of helium, dV/dt is the pumping power, R is the gas constant, and T is the temperature of helium. Here, L = 86 J/mol, and P = 2.1 Torr at 1.4 K. The pumping speed dV/dt is 1435 m^3/h = 399 L/s. Then, dQ/dt = 4.2 W. The actual cooling power becomes smaller than this value because of the guide conductance, the pumping speed at the actual helium pressure and the performance of the backing pump.

In the experiment of February 2011, the consumption rate of the 4.2 K liquid helium during the He-II condensation was 250 L/d. The 4.2 K liquid helium with a volume of 500 L was used for the 2 days He-II condensation. After the He-II condensation was completed, the consumption rate of the 4.2 K liquid helium was 142 L/d. The flow rate of the helium gas pumped out through the 1 K cryostat is 27 SLM. This value corresponds to 56 liters liquid helium per day, assuming the expansion rate of helium to be 700 times when it changes from gas to liquid. Therefore, the spontaneous evaporation of the 4.2 K liquid helium was 86 L/d. These evaporated helium gas is recovered by the helium gas recovery line.

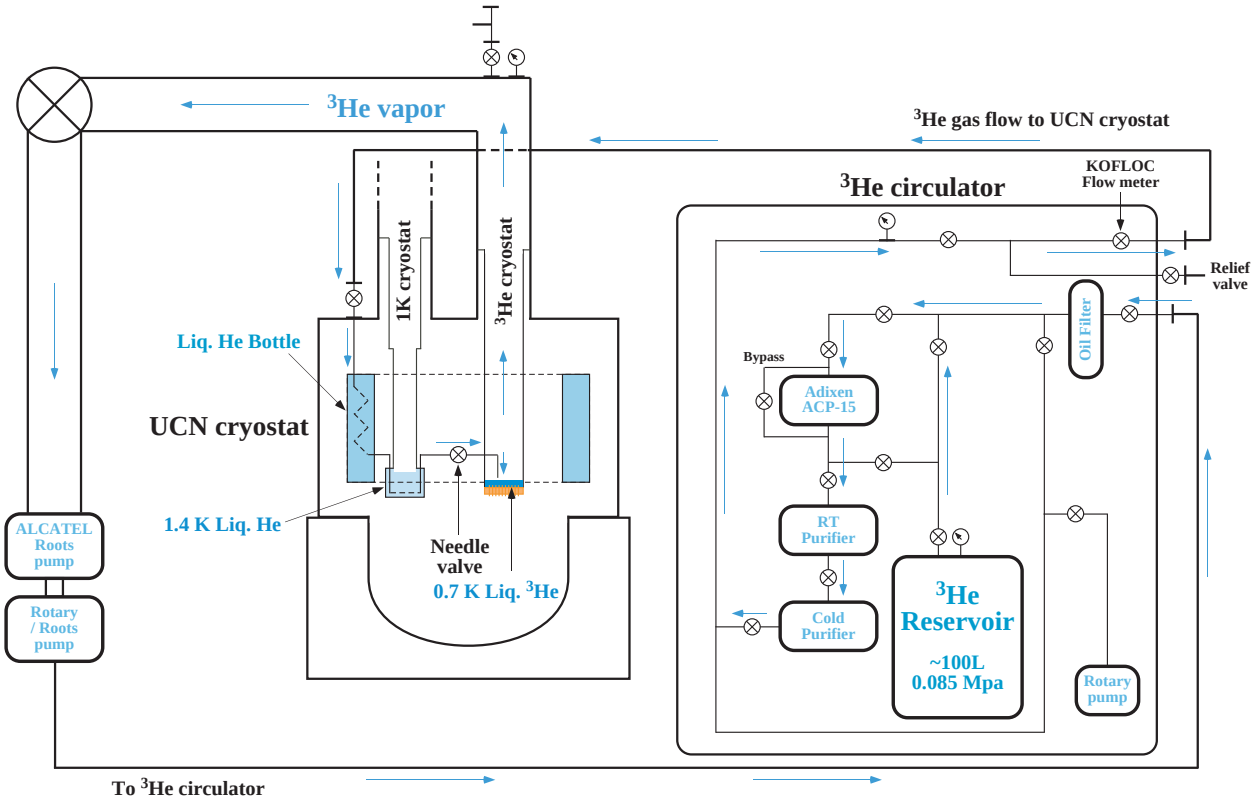

Figure 4.10: The schamtic view of the ^{3}He circulator and the ^{3}He cryostat.

4.3.2 ^{3}He Cryostat and ^{3}He Circulator

Next, we begin the ^{3}He gas circulation and condense the ^{3}He gas in the ^{3}He cryostat. Fig. 4.10 shows the schematic view of the ^{3}He circulation line. The ^{3}He gas is reserved in a reservoir tank. The volume of the reservoir tank is about 100 liters and the pressure of the ^{3}He is 0.085 MPa. The valve of the reservoir tank is opened and the ^{3}He gas begins circulation. The ^{3}He gas goes into the vacuum pump (Adixen, type ACP-15) and is compressed and pumped out to the downstream. There are a room temperature purifier and a cold purifier at the back of the vacuum pump. The RT purifier consists of molecular sieves. The cold purifier is composed by molecular sieves and charcoals at low temperatures. The cold purifiers is cooled by a GM refrigerator. The ^{3}He gas is purified through these purifiers.

The purified ^{3}He goes into the UCN cryostat. In the UCN cryostat, the ^{3}He gas is precooled by the 4.2 K liquid helium at first. Then, the precooled ^{3}He gas is further cooled by the 1 K liquid helium in the 1 K cryostat and is condensed. The condensed ^{3}He is transported to a pot called "^{3}He cryostat". The ^{3}He cryostat is always pumped and the liquid ^{3}He in the ^{3}He cryostat is further cooled to 0.7 K. The level of the 0.7 K liquid ^{3}He is monitored by a liquid helium leveler (AMI, Model 135). However, the level of the 0.7 K liquid ^{3}He is lower than the monitoring range. The ^{3}He cryostat is pumped by a roots pump (ALCATEL, model RSV2000) and a backing pump (ALCATEL model 2063H, later replaced by Adixen ACP-120). The evaporated ^{3}He is pumped out and goes through a oil filter and goes back to the beginning point of the circulation.

The flow rate of the circulating ^{3}He is controlled by a needle valve attached between the 1 K cryostat and the ^{3}He cryostat. The ^{3}He flow rate is monitored by a gas flow meter (KOFLOC, model 3660NV) installed at the exit of the ^{3}He circulator. During the He-II condensation, the flow rate of the ^{3}He gas changes between about 10 to 50 SLM (SLM = standard liter per minute). The time averaged flow rate is 29 SLM. After the He-II condensation was completed, the flow rate becomes stable, and its time average in 6 days beam time was 9.9 SLM.

We can estimate the cooling power of the ^{3}He cryostat using the flow rates. The latent heat of liquid ^{3}He at 0.7 K is 32 J/mol. The flow rate of the ^{3}He gas was 9.9 SLM. This value corresponds to 0.44 mol/min. Therefore, 32 J/mol $\times$ 0.44 mol/min = 14 J/min = 0.24 W was obtained as the cooling power.

The nominal pumping speed of RSV2000 is 2450 m^3/h at 60Hz AC, that of 2063H is 72 m^3/h, and that of ACP-120 is 112 m^3/h. The latent heat is L = 32 J/mol, and the vapor pressure is P = 1.35 Torr, for ^{3}He at 0.7 K. The pumping speed dV/dt is 2450 m^3/h = 681 L/s. Then, the ideal cooling power of the ^{3}He cryostat is obtained to be dQ/dt = 1.7 W.

4.3.3 Isopure Helium and He-II Condensation

After the ^{3}He was condensed and the temperature became 0.7 K, we start the condensation of He-II in the He-II bottle. In our UCN cryostat, we use isotopically pure helium gas (isopure He). The isopure He has ^{3}He impurity much less than the natural abundance. The natural abundance of ^{3}He is 1.37×10^{-6} in the atmosphere. This value is still large because ^{3}He has very large neutron absorption cross section ($\sigma_a = 5333(7)$ b). If this abundance is valid even in condensed helium, the UCN storage time in the UCN source is expected to be very short. On the other hand, the isopure He has a very small amount of ^{3}He impurity. The abundance of ^{3}He in the isopure He is said to be less than 10^{-10}. This value makes it possible for us to obtain the long UCN storage time in the order of 10^2 sec.

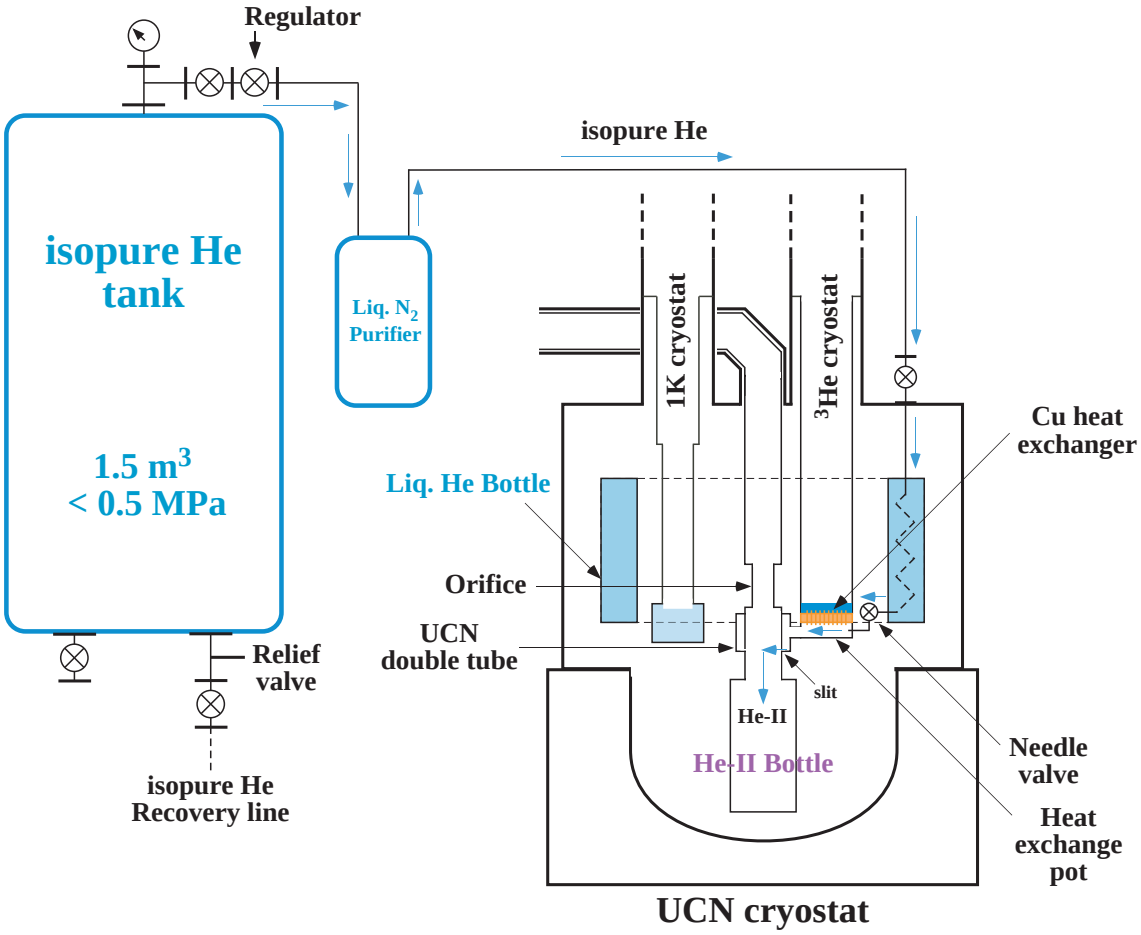

Figure 4.11: The schamtic structure of the isopure helium line.

Fig. 4.11 shows the scheme of the isopure He line. The isopure He is reserved in a tank called "isopure tank". The volume of the isopure tank is 1.5 m^3. The pressure of the isopure He in the isopure tank is +0.38 MPa before the He-II condensation. The valve and the regulator attached at the top of the isopure tank is used to control the flow rate of isopure He going into the UCN cryostat. First, the isopure He is purified by the liquid N_2 purifier. The liquid

purifier is composed of low temperature charcoals cooled by liquid N_2. Then, the isopure He goes into the UCN cryostat. The isopure He is precooled in the 4.2 K liquid helium and goes into the heat exchange pot attached to the bottom of the ^{3}He cryostat. The bottom of the ^{3}He cryostat and the top of the heat exchange pot is connected via the copper (Cu) heat exchanger. The isopure He in the heat exchange pot is cooled by the 0.7 K liquid ^{3}He via the Cu heat exchanger and becomes He-II. The condensed He-II fills the He-II bottle through a 0.05 mm slit at the UCN double tube. The He-II with a volume of 8.5 liters is condensed and the temperature becomes 0.8 K.

The surface level of the He-II is positioned just below the orifice of the UCN guide. The orifice of the UCN guide prevents the He-II film flow from going up along the UCN vertical guide because He-II has very good heat conductivity and the heat is carried by the film flow from the downstream region to the He-II and the ^{3}He cryostat. This heat load raises the He-II temperature and increases the UCN loss rate in He-II.

The pressure of the isopure tank reduces to -0.06 MPa after the He-II condensation. The amount of the isopure He used for the condensation is 0.44 MPa $\times$ 1.5 m^3.

4.3.4 Temperature Monitor

The temperatures at each point are monitored by thermometers installed in the UCN cryostat. Fig. 4.12 shows the positions where the thermometers of the He-II cooling system are installed. In the He-II cooling system, semiconductor resistance thermometers (Lakeshore, Cernox) are installed.

The Cernox thermometers are installed at the 1K cryostat, the ^{3}He cryostat, the heat exchange pot, the bottom of the heat exchange pot, UCN double tube, the external side of the He-II bottle, and the neck part of the UCN guide, respectively. Only the temperature of the 4.2 K liquid helium bottle is measured by the PtCo resistance thermometer installed at the bottom of the bottle.

The He-II temperature can be measured by the thermometer at the UCN double tube because this thermometer is positioned in the He-II. The thermometer of the external side of the He-II bottle has some offset at 0.8 K. So, the temperature of the He-II bottle is not be displayed precisely. This offset is expected to be caused by the loose connection.

Fig. 4.13 shows the one example of the temperature change during the He-II condensation. This data was recorded in November 2007. The temperature of the 1 K cryostat is 80 K just before the He-II condensation and the temperature of the ^{3}He cryostat is 110 K. And also, the temperatures of the He-II system ranges about 100 to 130 K. In this example, the precooling of the UCN cryostat was not enough, so the temperature at each point was relatively high.

The temperature of the 1 K cryostat dropped dramatically after the liquid helium was injected. Following the 1 K cryostat, the temperature of the ^{3}He cryostat dropped dramatically. Then, the condensation of the isopure He started in the late of November 4. The He-II condensation was completed in the late of November 6. The necessary time of the He-II condensation was about 2 $\sim$ 3 days. If the precooling time is enough long, the He-II condensation time is

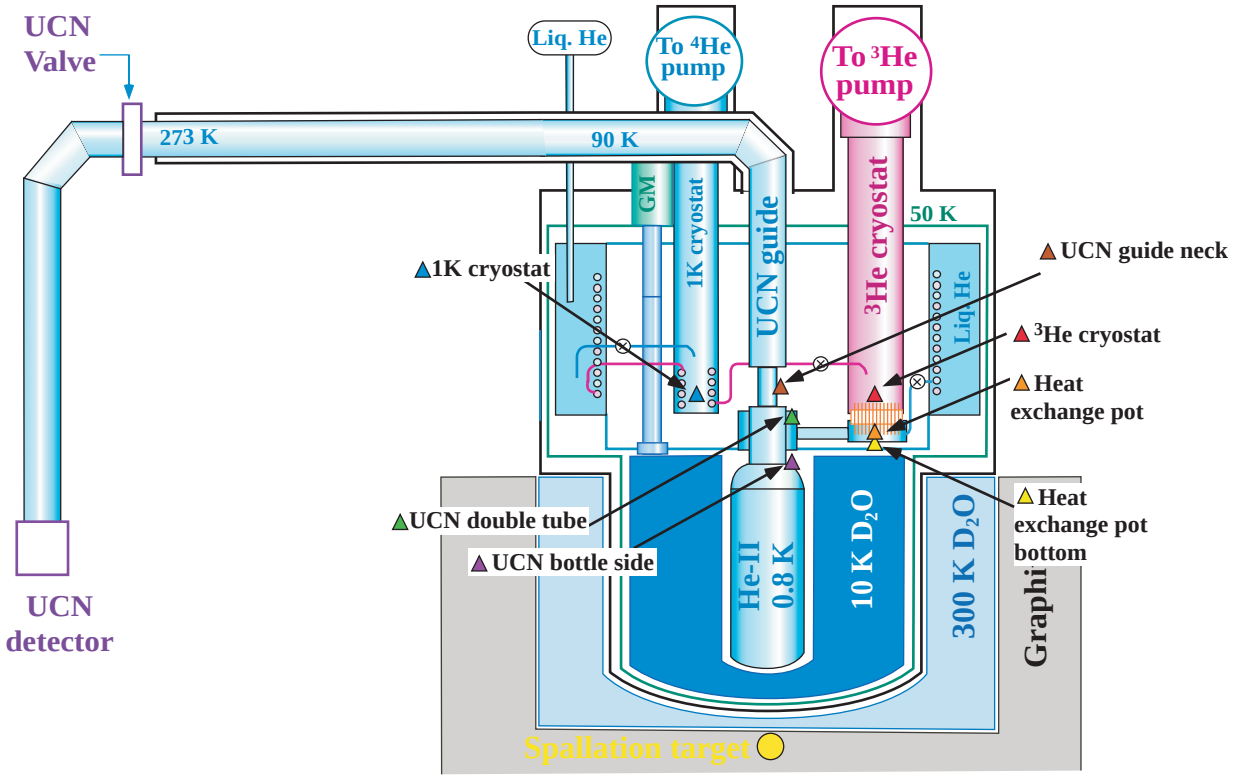

Figure 4.12: The positions of the thermometers in the He-II cooling system.

within 2 days.

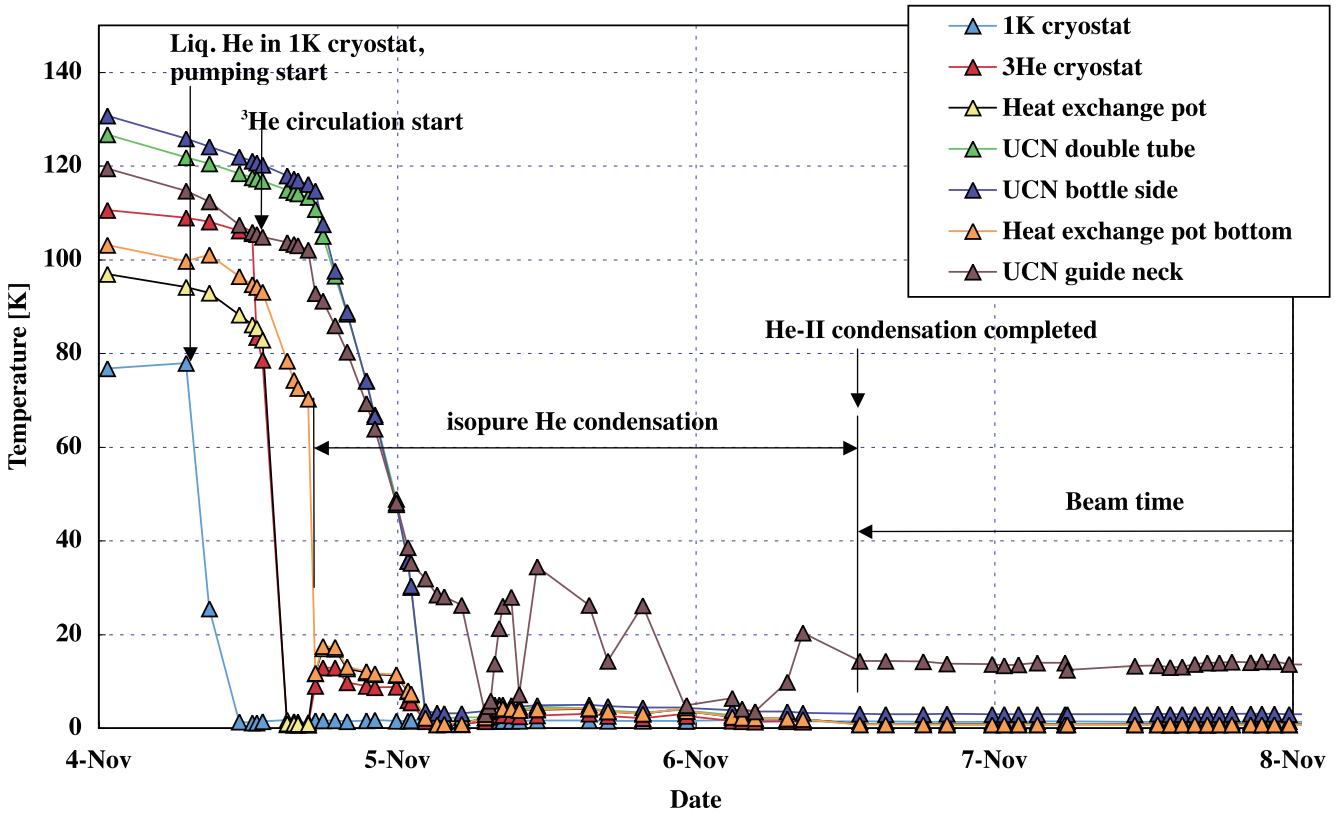

Figure 4.13: Temperature change during the He-II condensation, in November 2007.

4.4 Close Down

After the experiments, the cooling system of the UCN cryostat is stopped and the isopure He is recovered into the isopure tank. The close down process is done as follows.

1. Close the needle valve between the liquid He bottle and the 1 K cryostat. The liquid He in the liquid He bottle evaporates to the atmosphere. The liquid He in the 1 K cryostat is pumped to the atmosphere until the 1 K cryostat becomes empty.

2. Stop the circulation of ^{3}He by closing the valves of the ^{3}He circulator. The ^{3}He is pumped and recovered into the ^{3}He reservoir tank.

3. Recover the isopure He from the He-II bottle into the isopure reservoir tank by pumping.

The schematic structure of the isopure He circulation system is shown in Fig. 4.14. The He-II in the He-II bottle evaporates and is recovered via the UCN guide by the pumping system before the isopure He reservoir tank. The pumping system is composed by an OnTool Booster dry pump, a PFEIFFER piston dry pomp and a KNF diaphragm pump. The OnTool Booster dry pump recoveres the isopure He at middle pressure. The PFEIFFER piston dry pump is used to recover the low pressure helium. The KNF diaphragm pump works as a compressor. It compress the isopure He into the isopure He reservoir tank.

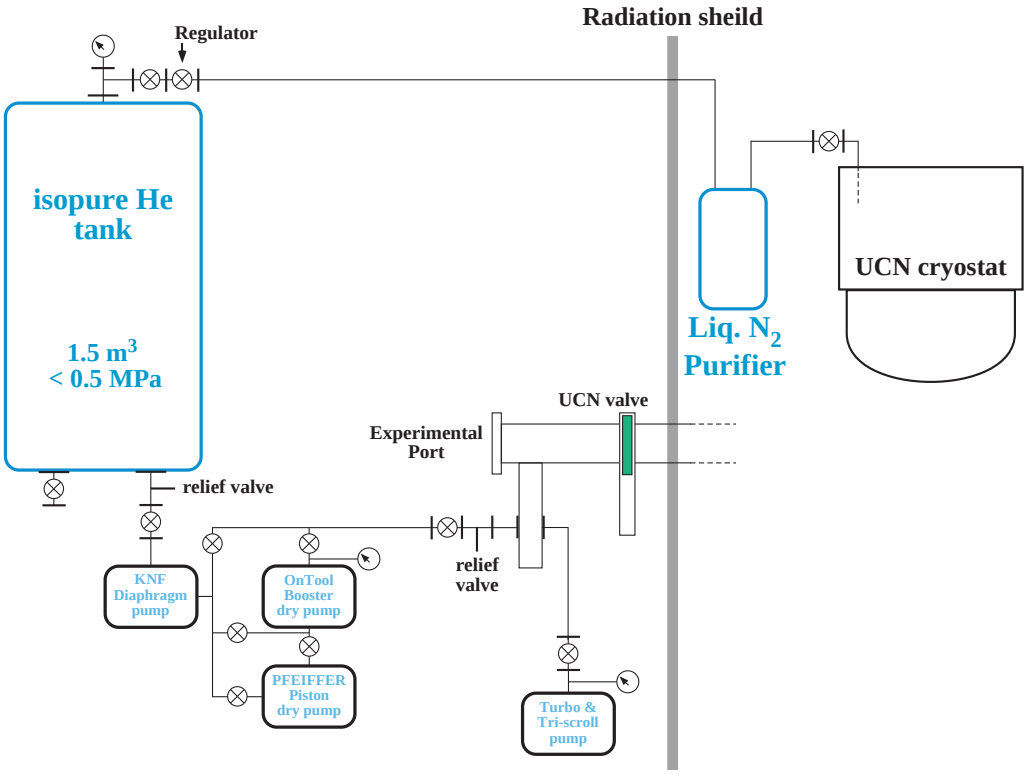

Figure 4.14: The schematic structure of the isopure He circulation system.

When we recovered the isopure He, we monitored the pressure of the isopure He reservoir tank by the Bourdon gauge attached to the top of the reservoir tank. The record of the pressure change is shown in Fig. 4.15. The initial pressure before the gas recovery was - 0.06 MPa. The final pressure after the gas recovery was + 0.38 MPa. The total amount of the recovered isopure He was 0.44 MPa $\times$ 1.5 m^3.

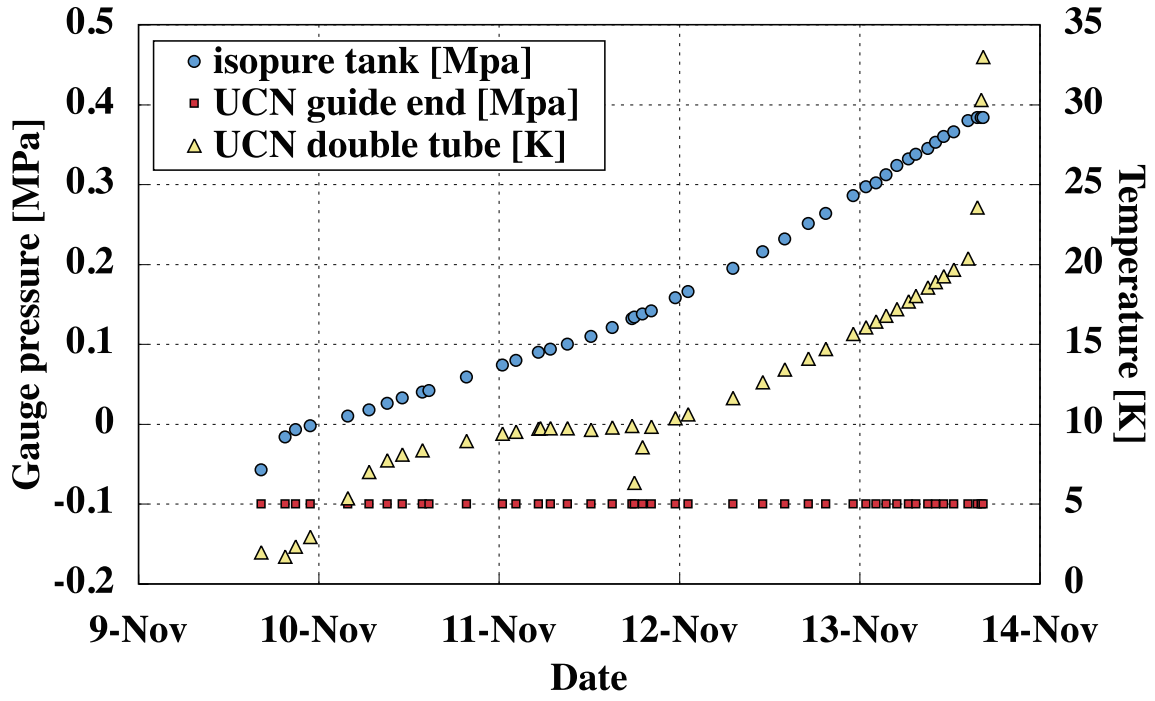

Figure 4.15: The pressure change in the isopure He reservoir tank (blue circles). The initial pressure before the gas recovery was - 0.06 MPa. The final pressure after the gas recovery was + 0.38 MPa. The amount of the condensed isopure He was 0.44 MPa $\times$ 1.5 m^3. The pressure change at the UCN guide end (red squares) shows that the pressure in the UCN guide was remained enough low during the gas recovery. The temperature at the UCN double tube (yellow triangles) is also shown. The dramatic rise of the temperature on November 13 shows the He-II bottle became empty. The drop of the temperature on November 11 was caused by opening the valve on the recovery line fully.

Chapter 5

UCN Source Development

5.1 Sequence of UCN Valve Control

We have two sequences of valve control for the measurement of UCN production. One is "OPEN mode" and the another is "DELAY mode".

In the Open mode, UCN valve is opening during the proton beam irradiation and the produced UCN are counted after the beam was stopped.

In the Delay mode, UCN valve is closing during the beam irradiation. Then, UCN valve is opened with some delay time of Δt after the beam was stopped. The produced UCN are confined in the upstream region before the UCN valve until the UCN valve is opened. After the delay time of Δt, the UCN valve is opened. Then, the produced UCN go into the UCN detector via the gravity accelerator tube and are observed by the detector.

The time diagram of the Delay mode is shown in Fig. 5.1, and the schematic view of UCN flow in the Delay mode is also shown in Fig. 5.2.

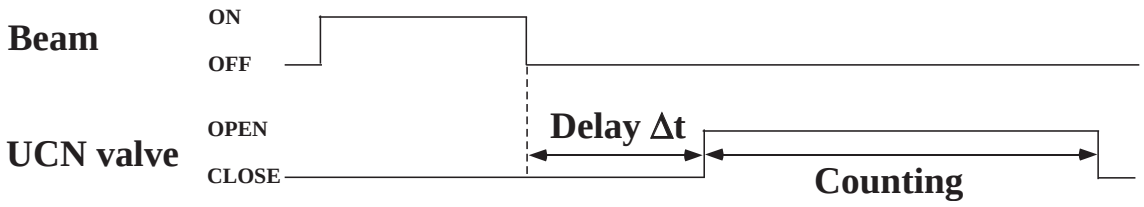

Figure 5.1: Time diagram of Delay mode.

We need to produce UCN and confine them in the UCN source, but the UCN detector itself is one of the sources that cause UCN loss. Therefore, we separate the upstream region of the UCN guide from the UCN detector by closing the UCN valve.

We measured the UCN time spectra in the experiments mainly by the Delay mode because we will connect experimental apparatuses to the experimental port in the following experiments. In such experiments, we close the UCN valve during the beam irradiation. And after

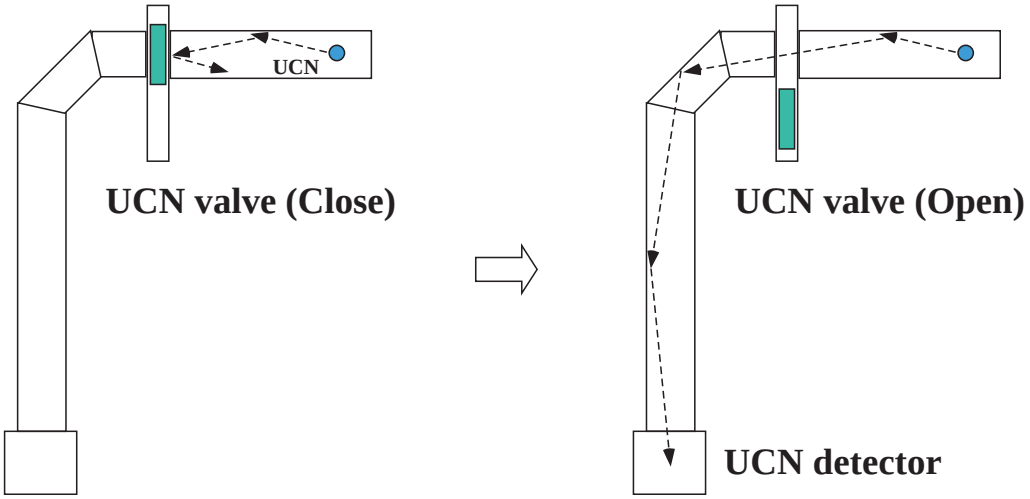

Figure 5.2: Schematic view of UCN flow in Delay mode. The left is before the UCN valve was opened and the right is after the UCN valve was opened.

the beam was stopped, we open the UCN valve and the UCN are transferred to the experimental apparatus.

A typical example of the time spectra by the Delay mode is shown in Fig. 5.3. In Fig. 5.3, the counts before the proton beam was stopped at 100 sec were fast neutrons and background γ-rays. After the beam was stopped, there was no count until the UCN valve was opened. The material of UCN valve is stainless steel and its Fermi potential is 188 neV. Therefore, it is deduced that the maximum energy of neutrons in the UCN horizontal guide was below 188 neV and they were reflected on the surface of the UCN valve. This was a clue that the obtained neutron counts were indeed UCN.

After the UCN valve was opened, the rise of the UCN counts were observed in a few seconds. This was a UCN diffusion in the UCN guide and the gravity accelerator tube. Since the averaged velocity of UCN was about $3 \sim 4$ m/s, some time was necessary for a first UCN to arrive at the UCN detector.

Then, the UCN counts gradually decreased as the time went by. UCN in the UCN source are lost with a certain possibility per unit time by phonon up-scattering, inelastic scattering by ^{4}He, absorption by ^{3}He, wall loss, and the β-decay. The ^{3}He UCN detector itself is the source of UCN loss. The decrease of UCN counts arose from these UCN losses.

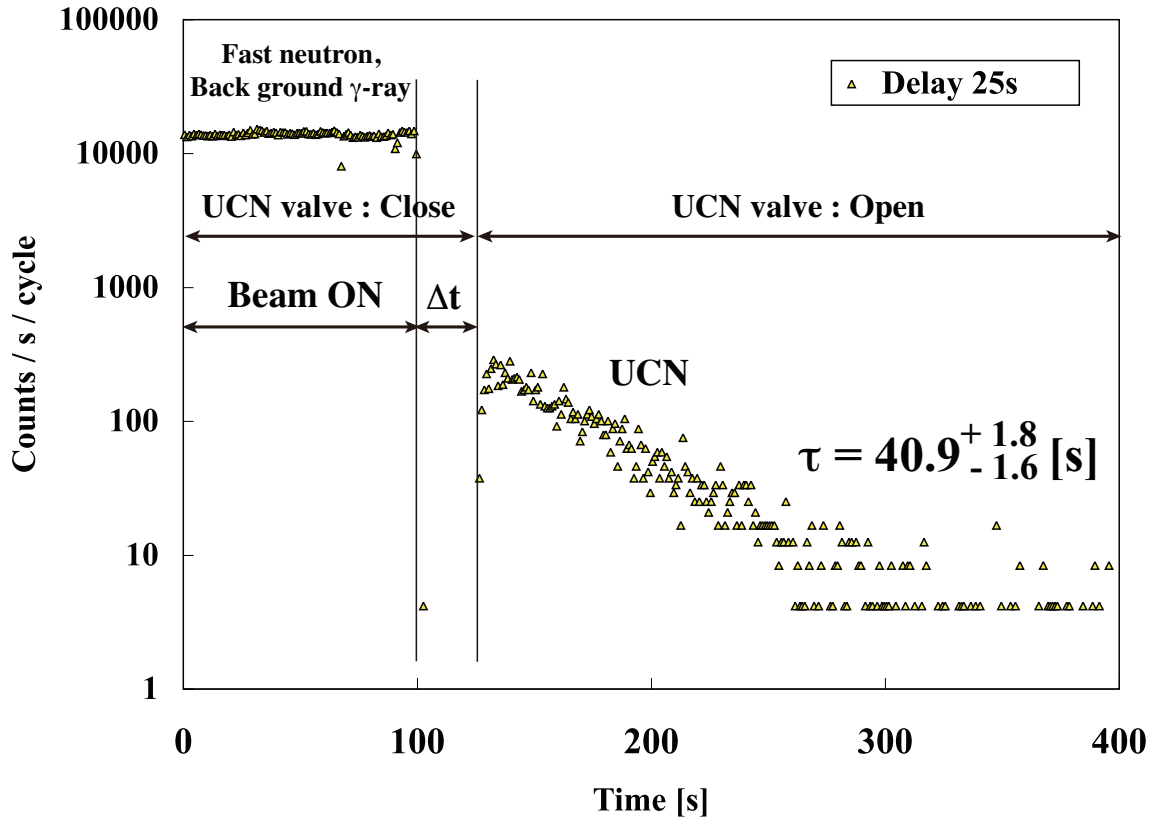

Figure 5.3: One of the time spectra of UCN by the delay mode, obtained in April 2008. The delay time Δt was 25 sec.

5.2 UCN Density at the Experimental Port

We need to estimate the UCN density at the experimental port, using the UCN count rate observed at the UCN detector. If we were to assume some models to treat UCN motion and the velocity distribution of UCN, it can be estimated. We use the following models to estimate the UCN density [50], [51].

1. Knusden's formula for ratified gas flow
2. Diffusion model

A gravity effect was not included in these estimations. An analysis including the gravity effect needs a Monte Carlo simulaion.

5.2.1 Knusden's Formula for Ratified Gas Flow

We begin by mentioning a few relevant results from molecular flow theory which relate to the case of gas flow through long pipes of length Z and circular cross section A. The surface scattering is completely diffuse ($f = 1$) and described by the cosine law, i.e. at each reflection on the guide walls the probability that a particle leaves the surface at an angle θ into the solid angle $\mathrm{d}\Omega$, is given by $P(\theta)\mathrm{d}\Omega = \cos\theta \mathrm{d}\Omega$.

If the entrance to the guide is illuminated by an isotropic angular distribution of velocities, having a density $n(0)$, the flow into the guide is

$$J(0) = \frac{1}{4} n(0) \overline{v} A = U_0 n(0) \tag{5.1}$$

where U_0 is the aperture conductance.

For a long circular tube $Z/R \gg 1$, the transmission probability can be shown to be given by

$$W = \frac{J(Z)}{J(0)} = \frac{8R}{3Z} \tag{5.2}$$

where $J(Z)$ is the flow at the position of Z. This is known as Knusden's long tube formula. The corresponding tube conductance U_1 is given as follows.

$$J(Z) = WJ(0) = \frac{8R}{3Z} J(0) = \frac{8R}{3Z} U_0 n(0) = U_1 n(0) \tag{5.3}$$

$$U_1 = \frac{8R}{3Z} U_0 \tag{5.4}$$

However, for short tubes such as $R/Z > 1$, Knusden's law breaks down. A correction to Knusden's law was suggested by S. Dushman. The corrected tube conductance is given by

$$\frac{1}{U_t} = \frac{1}{U_0} + \frac{1}{U_1} \tag{5.5}$$

and the corresponding transmission probability W is

$$W = \frac{J(Z)}{J(0)} = \frac{U_t n(0)}{U_0 n(0)} = \left(1 + \frac{U_0}{U_1}\right)^{-1} \tag{5.6}$$

$$= \left(1 + \frac{3Z}{8R}\right)^{-1} \tag{5.7}$$

These results are based on an assumption of the completely diffuse wall reflection. If the scattering law is represented by a probability $(1 - f)$ of specular reflection and a probability f of diffuse reflection, the transmission probability is modified to be

$$W = \frac{2 - f}{f}\frac{8R}{3Z} \quad \text{or} \quad W = \left(1 + \frac{3Zf}{8R(2 - f)}\right)^{-1}. \tag{5.8}$$

A typical value of f is in the range from 0.05 to 0.2 for the standard electropolished stainless steel guides. Our UCN guides and UCN storage bottle (discussed in the later section) used the Electro-Chemical Buffing (ECB) to polish their surfaces. The ECB method is a combination of electropolishing and mechanical buffing by abrasive, and enables us to obtain more flat surfaces than the standard electropolishing. According to Geant4 simulation for UCN (discussed in Chapter 7), f of the surfaces obtained by ECB is about 0.06.

5.2.2 UCN Flow after the Experimental Port

We can estimate the UCN density at the experimental port by the Knusden's law. We divide the region between the UCN experimental port and the UCN detector into 4 parts as Fig. 5.4.

The conductance at the UCN experimental port is $U_0 = \overline{v}A/4$. The radius of the UCN guide is $R = 4.25$ cm, and $A = 56.6$ cm^2. $\overline{v}$ is the average velocity of UCN in the experimental port. Assuming the UCN energy spectrum to be proportional to be $\sqrt{E}$ and the critical UCN energy $E_c = 84$ neV, $\overline{v}$ becomes 3.0 m/s.

The conductance in the gravity accelerator tube is $U_1 = (2 - f)/f \cdot 8R/3Z \cdot U_0$. Z is the length of the tube, $Z = 0.8$ m. f is the diffuse reflection probability, and was determined to be $f = (0.057 \pm 0.021)$ by the Geant4 simulation (see Chapter 7). Since f is small, U_1 has little contribution to the total conductance.

An annular disk installed in front of the UCN detector has a hole of $\phi 10$ and a thickness of 1 mm. The conductance U_{hole} is determined by the area of the hole, A_d. $U_{hole} = A_d/A \cdot U_0$, where $A_d = 0.785$ cm^2.

The conductance of the 90 degree elbow guide is $U_{90} = C_{90} \cdot U_0$, where C_{90} is a UCN transmission rate in a 90 degree bending guide. Here, we assume the effect of the length of this 90 degree elbow guide is negligible because f of its surface is small. The UCN transmission rate in a bending guide was discussed by A. Steyerl [52]. According to ref. [52], a transmission rate of a curved neutron guide is

$$C = 1 - 2\frac{R}{r}\frac{v_z^2}{v_l^2} \tag{5.9}$$

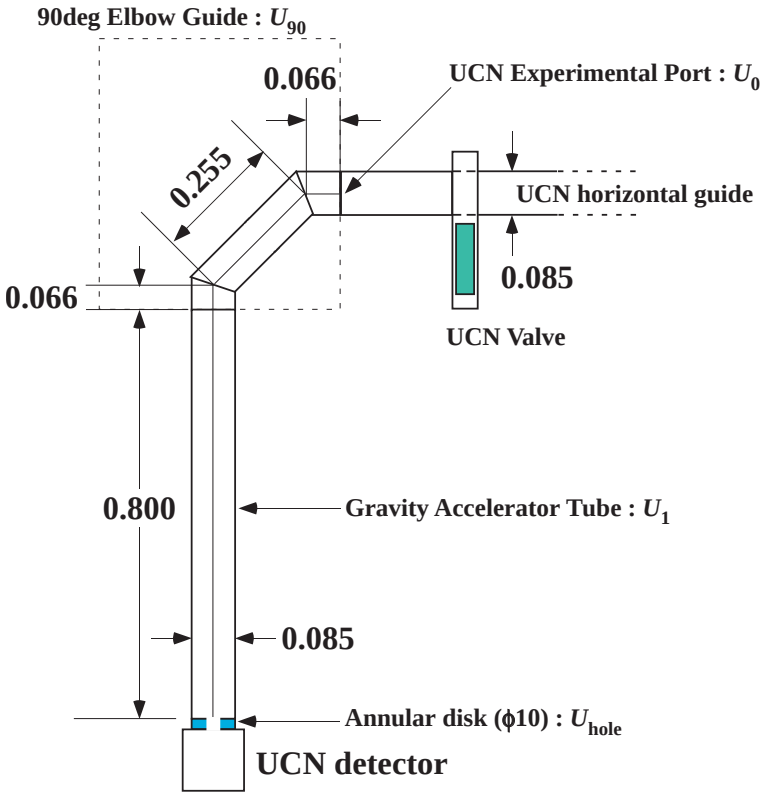

Figure 5.4: The schematic view after the UCN valve and each conductance.

where r is the radius of curvature of the bending guide, v_z is the velocity along the axis, and v_l is the velocity perpendicular to the axis. Our case is $r \sim 25.5/\sqrt{2} = 18$ cm. Assuming the isotropic distribution of UCN velocity, $v_z = v_l$. Then, $C = 1 - 8.5/18 = 0.53$ was obtained. Geant4 simulation for UCN (see Appendix) showed $C_{90} = 0.480 \pm 0.022$ for a 90 degree elbow guide. Here, we use this value.

The total conductance between the UCN experimental port and the UCN detector, U_t, is as follows.

$$\begin{aligned}
\frac{1}{U_t} &= \frac{1}{U_0} + \frac{1}{U_{90}} + \frac{1}{U_1} + \frac{1}{U_{hole}} && (5.10)\\
&= \frac{1}{U_0}\left(1 + \frac{1}{C_{90}} + \frac{f}{2-f}\frac{3Z}{8R} + \frac{A}{A_d}\right) && (5.11)\\
&= \frac{1}{U_0}\left(1 + \frac{1}{0.480 \pm 0.022} + \frac{(0.057 \pm 0.021)}{2 - (0.057 \pm 0.021)} \cdot \frac{3 \cdot 80 \text{ cm}}{8 \cdot 4.25 \text{ cm}} + \frac{56.6 \text{ cm}^2}{0.785 \text{ cm}^2}\right) && (5.12)\\
&= \frac{75.39 \pm 0.12}{U_0} && (5.13)
\end{aligned}$$

Since U_{hole} is much smaller than other conductances, the total conductance U_t is determined mainly by the hole area A_d of the annular disk.

The UCN count rate observed by the UCN detector is $U_t \rho_{ucn} \varepsilon$, where ρ_{ucn} is the UCN density at the experimental port, and ε is the efficiency of the UCN detector. From the above discussion,

$$\text{(UCN count rate)} = U_t \rho_{ucn} \varepsilon = \frac{1}{75.39 \pm 0.12} \cdot \frac{1}{4} \overline{v} A \rho_{ucn} \varepsilon \tag{5.14}$$

The averaged UCN velocity is $\overline{v} = 3.0$ m/s, the cross section of the UCN guide is $A = 56.6$ cm^2, and $\varepsilon = 0.697 \pm 0.023$.

For example, the maximum UCN count rate in delay mode of April 2008 is 599 ± 38 cps (see Table 5.5). Then, we abtained

$$\begin{aligned}
\rho_{ucn} &= (599 \pm 38) \text{ cps} \cdot (75.39 \pm 0.12) \cdot \frac{4}{3.0 \text{ m/s} \cdot 56.6 \text{ cm}^2 \cdot (0.697 \pm 0.023)} && (5.15)\\
&= 15.3 \pm 1.1 \text{ UCN/cm}^3 && (5.16)
\end{aligned}$$

as a UCN density at the experimental port for the critical energy $E_c = 84$ neV.

5.2.3 Diffusion Model

In Knusden's formula for rarified gas, the loss of UCN was not considered. UCN decays with a constant loss rate $1/\tau$, the inverse of UCN storage time. To include the loss of UCN in a transmission of UCN, a model based on diffusion equation is necessary.

A diffusion theory with a constant loss rate $1/\tau$ starts with the following equation.

$$\frac{\partial^2 n}{\partial z^2} = \frac{n}{L^2} + \frac{\partial n}{\partial t} \tag{5.17}$$

where L is the diffusion length, D is the diffusion constant. $L^2 = D\tau$. The diffusion constant is given by

$$D = \frac{1}{3}\overline{v}\overline{l} = \frac{2}{3}\overline{v}R \tag{5.18}$$

where $\overline{l}$ is the mean free path, and it is same as a diameter of the tube, i.e, $\overline{l} = 2R$. Assuming a constant current in a static state,

$$\frac{\partial^2 n}{\partial z^2} = \frac{n}{L^2} \tag{5.19}$$

is obtained. And a net current in a tube is given by

$$J = -D\frac{dn(z)}{dz}A \tag{5.20}$$

where A is the cross section of the tube.

We consider the static UCN flow rate through a guide of length Z and the cross sectional area A. An isotropic distribution of UCN density $n(0)$ at the entrance of the guide, and the isotropic velocity distribution at the exit of the guide are also assumed. The neutron current at a position of Z is $J(Z) = A(1-r)n(Z)\overline{v}/4$. $n(Z)$ is the UCN density at the end of the guide and r is an albedo (neutron reflection rate) of the device attached to the end of the guide. For example, in the case in which the annular disk of ϕ10 mm in front of the UCN detector, $r = (A - A_d)/A = 1 - A_d/A$.

The general solution of (5.19) is given by

$$n(z) = B\sinh(z/L) + C\cosh(z/L). \tag{5.21}$$

And at $z = 0$,

$$n(0) = C \tag{5.22}$$

is obtained. B is determined to satisfy the boundary condition

$$J(Z) = -D\frac{dn(z=Z)}{dz}A = \frac{A(1-r)n(Z)\overline{v}}{4}. \tag{5.23}$$

Then

$$B = -n(0)\frac{\sinh(z/L) + \gamma\cosh(z/L)}{\cosh(z/L) + \gamma\sinh(z/L)} \tag{5.24}$$

with

$$\gamma = \frac{L}{4D}(1-r)\overline{v} \tag{5.25}$$

are obtained. The UCN flow rate into the device attached to the end of the guide is thus given by

$$J(Z) = \frac{n(0)\overline{v}A(1-r)}{4[\cosh(Z/L) + \gamma\sinh(Z/L)]}. \tag{5.26}$$

(5.26) is in the case of perfectly diffuse reflection ($f = 1$). If the scattering law is represented by a probability $(1-f)$ of specular reflection and a probability f of diffuse reflection, the diffusion length L and the diffusion constant D are modified as follows.

$$L \rightarrow L_{specular} = \sqrt{\frac{2-f}{f}}L \tag{5.27}$$

$$D \rightarrow D_{specular} = \frac{2-f}{f}D \tag{5.28}$$

L and D in (5.25) and (5.26) are replaced by $L_{specular}$ and $D_{specular}$.

5.2.4 UCN Density Estimation by Diffusion Model

Here, we estimated the UCN density at the experimental port by the diffusion model equation (5.26). According to Fig. 5.4, the radius od the UCN guide is $R = 4.25$ cm, and the cross sectional area is $A = 56.6$ cm^2. The hole area of the annular disk is $A_d = 0.785$ cm^2. Therefore, an albedo of the UCN detector with the annular disk is $r = 1 - A_d/A = 1 - 0.785/56.6 = 0.986$. The guide length is $Z = 6.6 + 25.5 + 6.6 + 80 = 118.7$ cm. The averaged UCN velocity at the experimental port is $\overline{v} = 3.0$ m/s. The diffusion constant is given by

$$D = \frac{2}{3}\overline{v}R = \frac{2}{3}\cdot 3.0 \text{ m/s}\cdot 4.25 \text{ cm} = 850 \text{ cm}^2/\text{s}, \tag{5.29}$$

$$D_{specular} = \frac{2-f}{f}D = \frac{2-(0.057\pm 0.021)}{(0.057\pm 0.021)}D = (34\pm 18)\cdot D \tag{5.30}$$

$$= 28975 \pm 15096 \text{ cm}^2/\text{s} \tag{5.31}$$

where $f = (0.057 \pm 0.021)$. Then, the diffusion length L and $L_{specular}$ are

$$L = \sqrt{D\tau} = \sqrt{850 \text{ (cm}^2/\text{s)}\cdot \ 38.5^{+0.5}_{-0.4} \text{ (s)}} = 180.9^{+1.2}_{-0.9} \text{ cm}, \tag{5.32}$$

$$L_{specular} = \sqrt{\frac{2-f}{f}}L = \sqrt{34\pm 18}L = 1056^{+255}_{-329} \text{ cm} \tag{5.33}$$

where τ is the UCN storage time after the UCN valve was opened in the delay mode.

Using these parameters, γ was calculated as follows.

$$\begin{aligned}
\gamma &= \frac{L_{specular}}{4D_{specular}}(1-r)\overline{v} && (5.34)\\
&= \frac{1056^{+255}_{-329}\text{ cm}}{4\cdot(28975\pm 15096\text{ cm}^2/\text{s})}(1-0.986)\cdot 3.0\times 10^2\text{ m/s} && (5.35)\\
&= (3.8^{+6.1}_{-2.1})\times 10^{-2} && (5.36)
\end{aligned}$$

And the denominator of (5.26) is

$$\begin{aligned}
& \cosh(Z/L)+\gamma\sinh(Z/L) && (5.37)\\
= \;& \cosh(118.7/1056^{+255}_{-329})+(3.8^{+6.1}_{-2.1})\times 10^{-2}\cdot\sinh(118.7/1056^{+255}_{-329}) && (5.38)\\
= \;& 1.006^{+0.023}_{-0.001} && (5.39)
\end{aligned}$$

Therefore, the UCN flow rate $J(Z)$ is given by

$$\begin{aligned}
J(Z) &= \frac{n(0)\overline{v}A(1-r)}{4[\cosh(Z/L)+\gamma\sinh(Z/L)]} && (5.40)\\
&= \frac{(A_d/A)}{1.006^{+0.023}_{-0.001}}\frac{n(0)\overline{v}A}{4} && (5.41)\\
&= \frac{1}{72.6^{+1.7}_{-0.1}}\cdot\frac{n(0)\overline{v}A_d}{4}. && (5.42)
\end{aligned}$$

The UCN count rate observed by the UCN detector of the efficiency ε is

$$(\text{UCN count rate}) = J(Z)\varepsilon = \frac{1}{72.6^{+1.7}_{-0.1}}\cdot\frac{n(0)\overline{v}A_d\varepsilon}{4}. \quad (5.43)$$

From the Table 5.5, the maximum UCN count rate in delay mode of April 2008 was 599 ± 38 cps. Then, we abtained

$$\begin{aligned}
\rho_{ucn}=n(0) &= (599\pm 38)\text{ cps}\cdot 72.6^{+1.7}_{-0.1}\cdot\frac{4}{3.0\text{ m/s}\cdot 56.6\text{ cm}^2\cdot(0.697\pm 0.023)} && (5.44)\\
&= 14.7^{+1.8}_{-1.4}\text{ UCN cm}^{-3} && (5.45)
\end{aligned}$$

as a UCN density at the experimental port for the critical energy $E_c = 84$ neV. This result is consistent with the previous calculation by Knusden's formula.

In the above discussion, the effect of the 90 degree elbow guide after the UCN experimental port was ignored. A UCN transmission rate in a 90 degree bending guide, C_{90}, was about 0.5. However, in the case in which the annular disk was installed in front of the detector, most of UCN were reflected on the disk and went back to the upstream region of the UCN source. Then, they were reflected again, and went to the UCN detector through the 90 degree elbow guide again. In such case, the UCN flow in the 90 degree elbow guide was going forth and back

between the two guide ends, and the UCN in the guide were under the isotropic distribution. Therefore, the transmission rate C_{90} could be ignored.

The result of these two models imply one thing. The transmission rate in our UCN guide is nearly 1, because its diffuse reflection probability is very small ($f = 0.057$). It is expected that the UCN horizontal guide with a total length of 3 m has almost same UCN density ρ_{ucn} at each guide end.

We used the value of the diffuse reflection probability f determined by the Geant4 simulation. To determine the value of f of a UCN guide experimentally, an application method using the diffusion model was carried out by I. Altarev et al. [53].

5.3 He-II Temperature

The first UCN production in superfluid helium located in a spallation neutron source was carried out by Y. Masuda et al. [54] in 2002. A UCN density of 0.7 UCN/cm^3 was achieved for a proton beam power of 78 W and a He-II temperature of 1.2 K.

In November 2004, a UCN density of 1.4 UCN/cm^3 and a UCN storage time of 14 sec were obtained. The proton beam power was 78 W and the temperature of He-II was 1.2 K. The obtained time spectrum in this experiment is shown in Fig. 5.5.

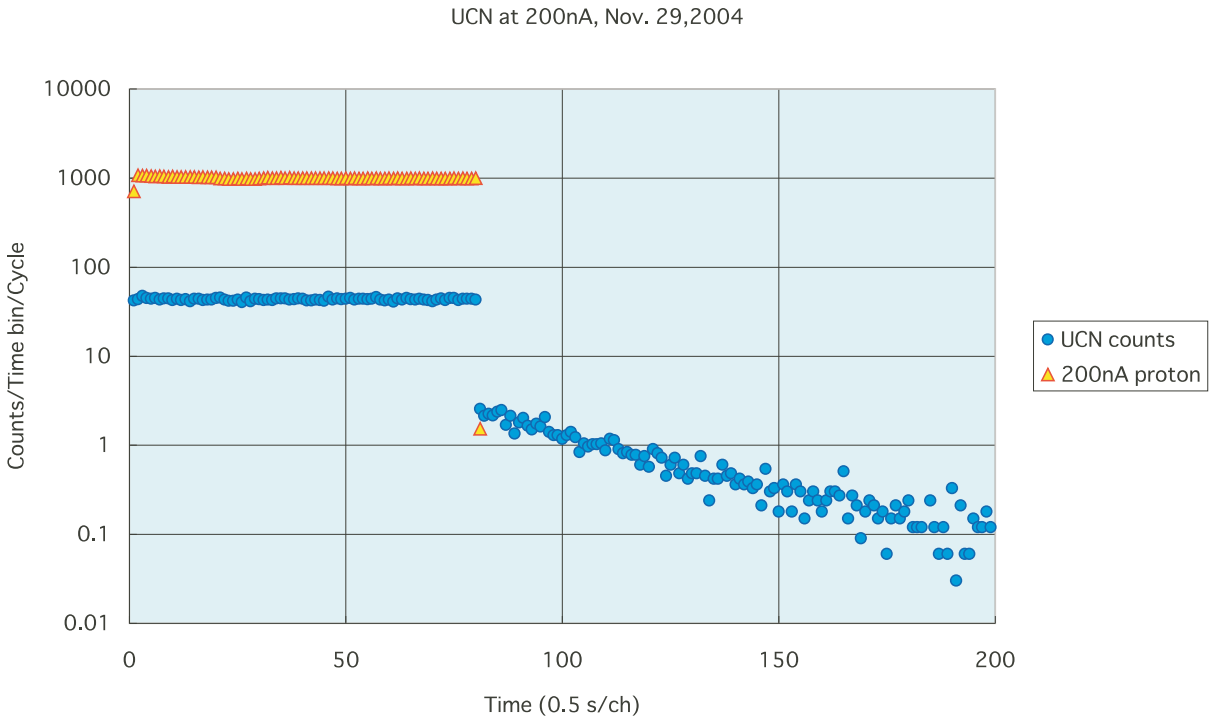

Figure 5.5: The time spectrum obtained in November 2004. The blue circles are UCN counts and the yellow triangles are the proton beam current. The time bin width is 0.5 sec/channel. The beam irradiation time was 40 sec.

After the experiment in November 2004, we have improved the cooling system of the He-II superthemal UCN source. Since a temperature of He-II is critical for phonon up-scattering rate $1/\tau_{ph}$, some important changes to lower the temperature of He-II were applied to the structure of the UCN source. The applied improvements were as follows.

1. Thermal sinks were installed. The 1K cryostat, the ^{3}He cryostat and the UCN vertical guide were connected to the top plate of the solid D_2O bottle by the copper thermal sinks. Heat loads to these parts were transferred to the Gifford-McMahon refrigerator (SRD-220, Sumitomo Juuki company) via the top plate of the solid D_2O bottle.

2. Improvement in the ^{3}He circulation system. The heat exchangers were installed in the 1K cryostat and the ^{3}He cryostat. These heat exchangers are exposed to a vapor of helium evaporating from the bottom of the 1K cryostat and a vapor of ^{3}He evaporating from the bottom of the ^{3}He cryostat, respectively. When the ^{3}He gas passes through the heat exchangers, the ^{3}He gas is pre-cooled. The ^{3}He condensation was achieved by installing these heat exchangers.

By these improvements, a He-II temperature was lowered to be 0.9 K by June 2006.

June 2006

In June 2006, we carried out a UCN production experiment at a He-II temperature of 0.9 K and with a proton beam power of 400 W (392 MeV, 1μA). Fig. 5.6 shows the time spectrum obtained in the delay mode. The delay time Δt were 0, 10, 20, 30, 40, 50, and 60 sec, respectively.

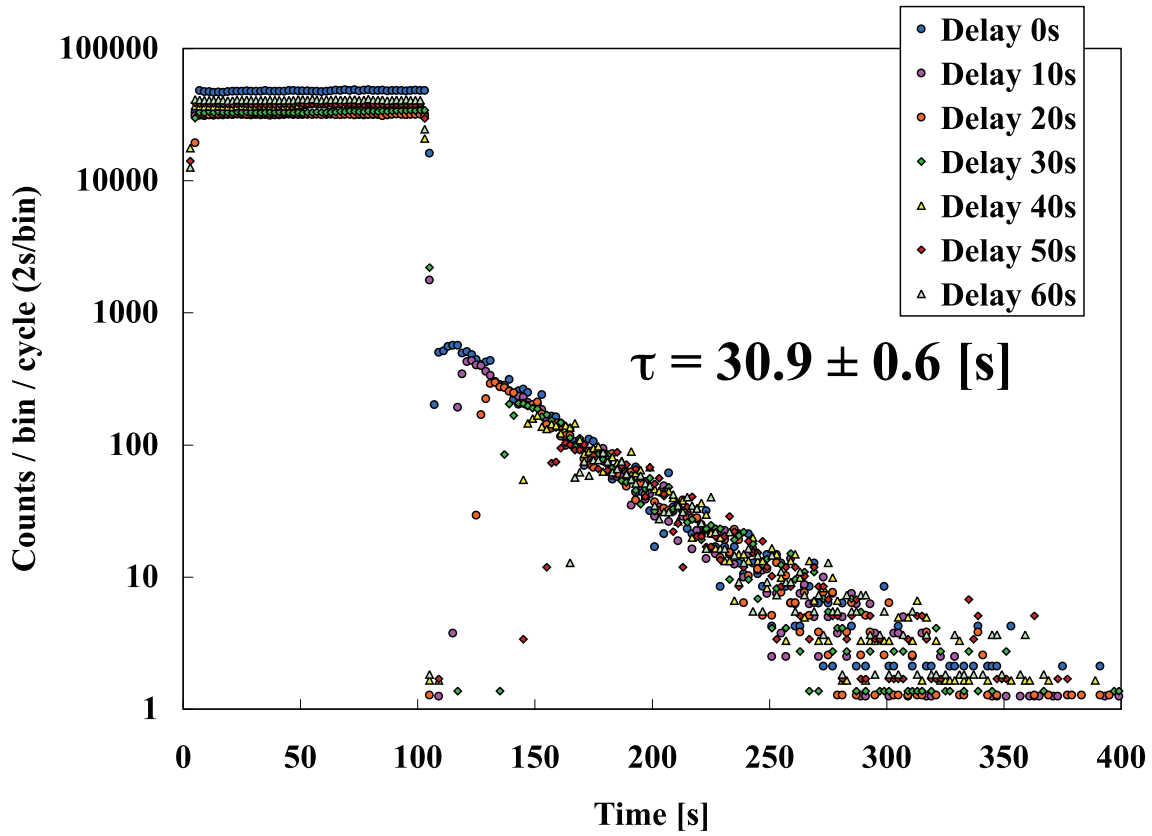

Figure 5.6: Time spectra of delay mode, obtained in June 2006. A 400 W proton beam was irradiated for 100 sec. The time bin width is 2.0 sec/bin. The delay time Δt were 0, 10, 20, 30, 40, 50, and 60 sec, respectively. The annular disk was installed in front of the UCN detector. The decay constant of 0 sec delay mode was 30.9 ± 0.6 sec.

The total UCN counts obtained by the delay mode are shown in Table 5.1. Fig. 5.7 is a plot of the total UCN counts as a function of delay time Δt and the UCN storage time τ_s was obtained to be 33.7 ± 0.6 s.

Delay Δt [s]	total UCN counts	max UCN count rate [cps]	Beam duration [s]
0	11742 ± 256	284 ± 18	100
10	8162 ± 173	217 ± 12	100
20	5956 ± 134	149 ± 10	100
30	4472 ± 110	104 ± 9	100
40	3705 ± 101	84 ± 8	100
50	2492 ± 78	52 ± 7	100
60	1930 ± 68	44 ± 6	100

Table 5.1: The total UCN counts and the maximum UCN count rates obtained by the delay mode in June 2006.

Assuming the diffuse reflection probability f was same as the value in April 2008, the UCN density at the experimental port was calculated by Knusden's formula as follows.

$$284 \pm 18 \text{ cps} = \frac{1}{75.39 \pm 0.12} \cdot \frac{1}{4} \overline{v} A \rho_{ucn} \varepsilon \tag{5.46}$$

Then, we obtained

$$\rho_{ucn} = (284 \pm 18) \text{ cps} \cdot 75.39 \pm 0.12 \cdot 4 \cdot \frac{1}{3.0 \text{ m/s} \cdot 56.6 \text{ cm}^2 \cdot (0.697 \pm 0.023)} \tag{5.47}$$

$$= 7.2 \pm 0.5 \text{ UCN/cm}^3 \ . \tag{5.48}$$

as a UCN density at the experimental port for the critical energy $E_c = 84$ neV.

In this case, the proton beam irradiation time was 100 sec. $(1 - \exp(-t/\tau_s)) = 0.95$ was obtained. For enough long beam irradiation duration, the UCN density is given by

$$\rho_{ucn} = 7.6 \pm 0.5 \text{ UCN/cm}^3 \ . \tag{5.49}$$

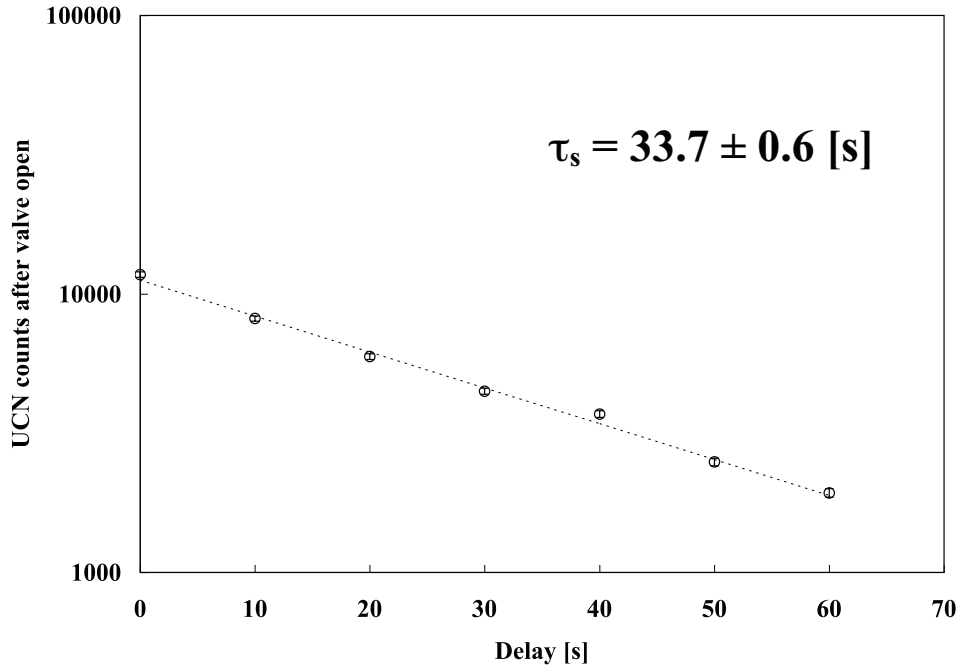

Figure 5.7: The total UCN counts as a function of delay time Δt and a fitting curve. A UCN storage time τ_s was obtained to be 33.7 ± 0.6 s.

November 2006

In November 2006, The following modifications were applied to the structure of the UCN source.

1. The orifice of the UCN vertical guide was installed to cut a film flow from the He-II. The diameter of the orifice is ϕ 50 and the length is 100 mm.

2. A 0.05 mm slit was introduced to obtain better heat conductance between the He-II bottle and ^{3}He pot.

3. An additional copper thermal sink was attached between the ^{3}He pot and the bottom of the liquid He bottle to cut the heat load on the ^{3}He pot.

4. A baffle and fins were inserted into the ^{3}He pot to cut the heat load by radiation.

These modifications are shown in Fig. 5.8. Fig. 5.9 shows the baffle and fins inserted into the ^{3}He pot. The He-II temperature of 0.8 K was obtained by these improvements.

Then, we measured time spectra in delay mode. Fig. 5.10 is the obtained time spectra. The total numbers of UCN are shown as a function of the delay time in Fig. 5.11. Table 5.2 shows the total numbers of UCN and the maximum UCN count rates obtained in the delay mode.

The maximum UCN count rate was 345 ± 33 cps in the delay mode with 0 sec delay. By the Knusden's formula, the UCN density at the experimental port was obtained as follows.

$$\rho_{ucn} = (345 \pm 33)\ \text{cps} \cdot 75.39 \pm 0.12 \cdot 4 \cdot \frac{1}{3.0\ \text{m/s} \cdot 56.6\ \text{cm}^2 \cdot (0.697 \pm 0.023)} \quad (5.50)$$

$$= 8.8 \pm 0.9\ \text{UCN/cm}^3\ . \quad (5.51)$$

In this case, the proton beam irradiation time was 60 sec. So, $(1 - \exp(-t/\tau_s)) = 0.83$. For enough long beam irradiation duration, the UCN density becomes

$$\rho_{ucn} = 10.6 \pm 1.1\ \text{UCN/cm}^3\ . \quad (5.52)$$

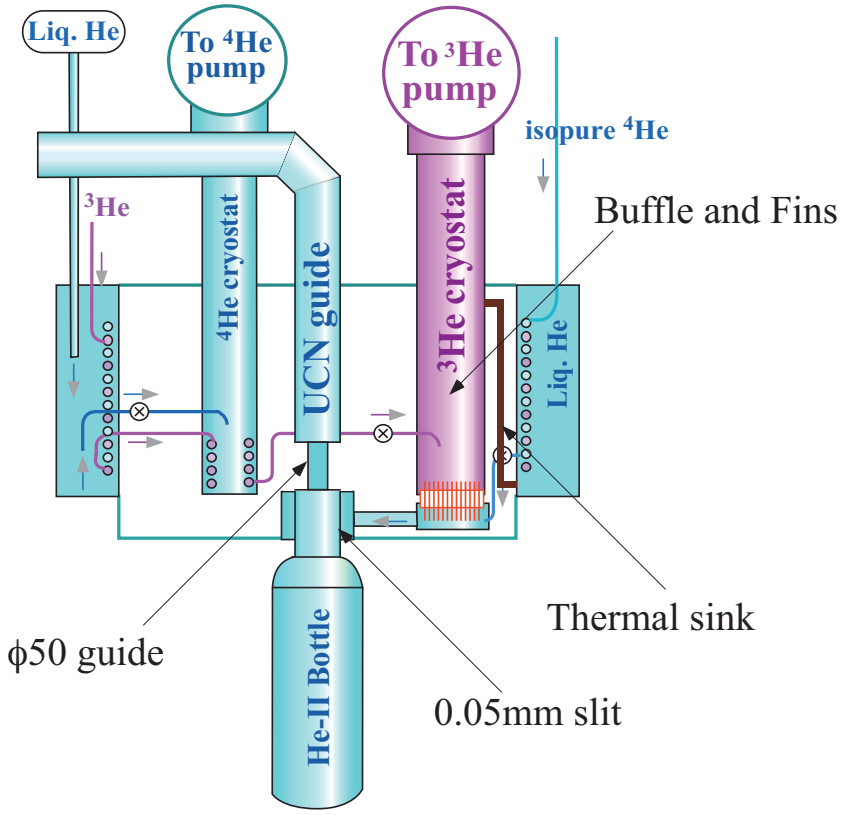

Figure 5.8: Modifications of the UCN source. (1) A ϕ50 UCN vertical guide was installed instead of the previous ϕ84.9 guide in order to cut the film flow of He-II. (2) A 0.05 mm slit was introduced to obtain better heat conductance between the He-II bottle and the ^{3}He pot. (3) A new thermal sink was installed to cut heat load on the ^{3}He pot. (4) A baffle and fins were inserted into the ^{3}He pot to reduce heat load by radiation.

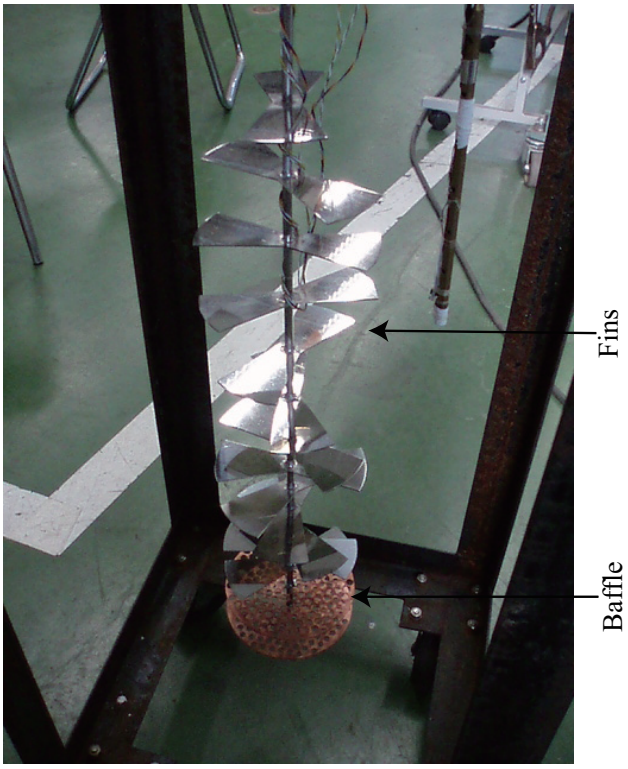

Figure 5.9: Photograph of the baffle and fins inserted into the ^{3}He pot.

Delay Δt [s]	total UCN counts	max UCN count rate [cps]	Beam duration [s]
0	9851 ± 179	345 ± 33	60
10	6988 ± 138	246 ± 27	60
20	4885 ± 107	158 ± 22	60
30	3823 ± 90	131 ± 20	60
40	2769 ± 75	92 ± 17	60
50	2320 ± 69	83 ± 17	60
60	1667 ± 56	81 ± 16	60

Table 5.2: The total UCN counts and the maximum UCN count rates obtained by the delay mode in November 2006.

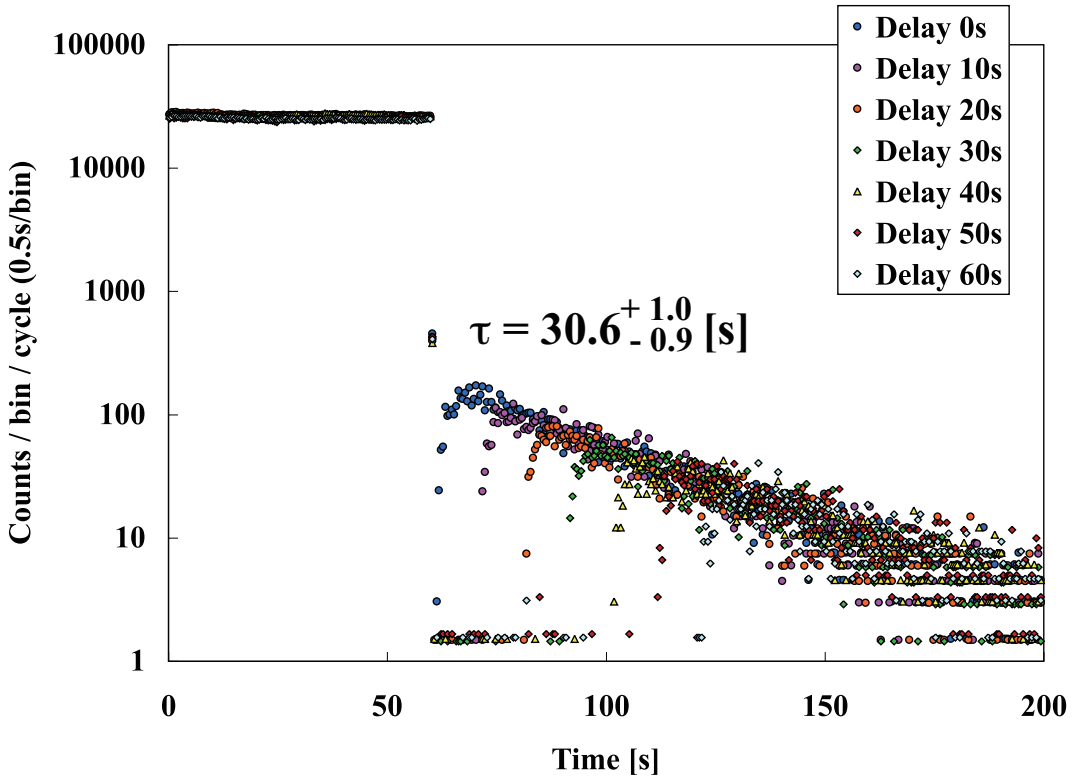

Figure 5.10: Time spectra of the delay mode, obtained in November 2006. A proton beam with a power of 400 W was irradiated for 60 sec. The time bin width is 0.5 sec/bin. The delay time Δt were 0, 10, 20, 30, 40, 50, and 60 sec, respectively. The annular disk was installed in front of the UCN detector. The decay constant of 0 sec delay mode was $30.6^{+1.0}_{-0.9}$ sec.

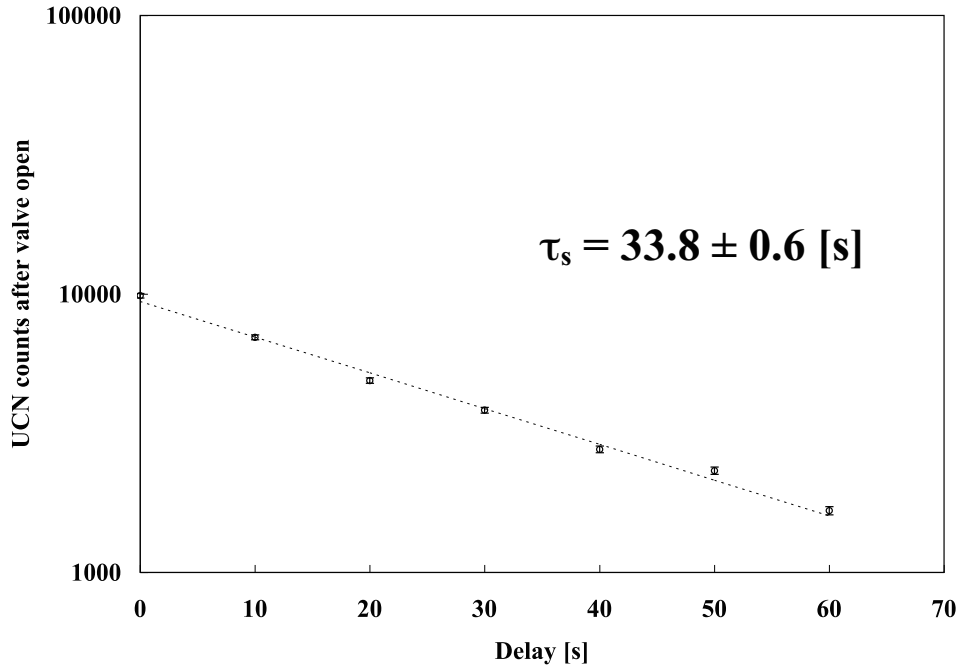

Figure 5.11: The total UCN counts as a function of delay time Δt and a fitting curve. The UCN storage time τ_s was 33.8 ± 0.6 s.

5.4 ^{3}He impurity

In the experiment of year 2006, it was suggested that the main UCN loss was caused by wall loss and absorption by ^{3}He impurities because $\tau_{ph} = 600$ sec at 0.8 K. To resolve these problems, we removed the ^{3}He impurity in the He-II.

Until year 2006, we had used normal helium gases which were commercially available. However, such helium gas was expected to contain ^{3}He impurities. So we introduced isopure (isotopically pure) ^{4}He in which ^{3}He impurities were removed by super leak method [39]. The order of ^{3}He impurities in the isopure ^{4}He is less than 10^{-10}. Therefore, it was expected that the UCN life time by absorption, τ_{abs}, became 300 sec or longer by using the isopure ^{4}He.

July 2007

In July 2007, isopure ^{4}He gas was used for the first time. Fig. 5.12 shows the obtained UCN time spectra by the delay mode. Fig. 5.13 is a plot of the total UCN counts as a function of delay time Δt and the UCN storage time τ_s was obtained to be 39.5 ± 0.5 s. The total UCN counts obtained by the delay mode are shown in Table 5.3.

Delay Δt [s]	total UCN counts	max UCN count rate [cps]	Beam duration [s]
0	17924 ± 361	444 ± 28	100
20	10484 ± 226	244 ± 20	100
50	4853 ± 127	110 ± 14	100
90	1838 ± 62	54 ± 9	100
100	1428 ± 53	32 ± 7	100

Table 5.3: The total UCN counts and maximum UCN count rates obtained by delay mode measurement in July 2007.

The maximum UCN count rate was 444 ± 28 cps by the delay mode with a 0 sec delay. By Knusden's model, the UCN density at the experimental port was given by

$$\rho_{ucn} = (444 \pm 28)\ \text{cps} \cdot 75.39 \pm 0.12 \cdot 4 \cdot \frac{1}{3.0\ \text{m/s} \cdot 56.6\ \text{cm}^2 \cdot (0.697 \pm 0.023)} \quad (5.53)$$

$$= 11.3 \pm 0.8\ \text{UCN/cm}^3 \quad (5.54)$$

for the critical energy $E_c = 84$ neV.

In this case, the proton beam irradiation time was 100 sec. During the beam irradiation, the number of UCN increases as a function of $(1 - \exp(-t/\tau_s))$. If $t = 100$ sec and $\tau_s = 39.5$ sec, $(1 - \exp(-t/\tau_s)) = 0.92$ is obtained. Therefore, for much longer beam irradation time, the UCN density ρ_{ucn} becomes

$$\rho_{ucn} = 12.3 \pm 0.9\ \text{UCN/cm}^3\ . \quad (5.55)$$

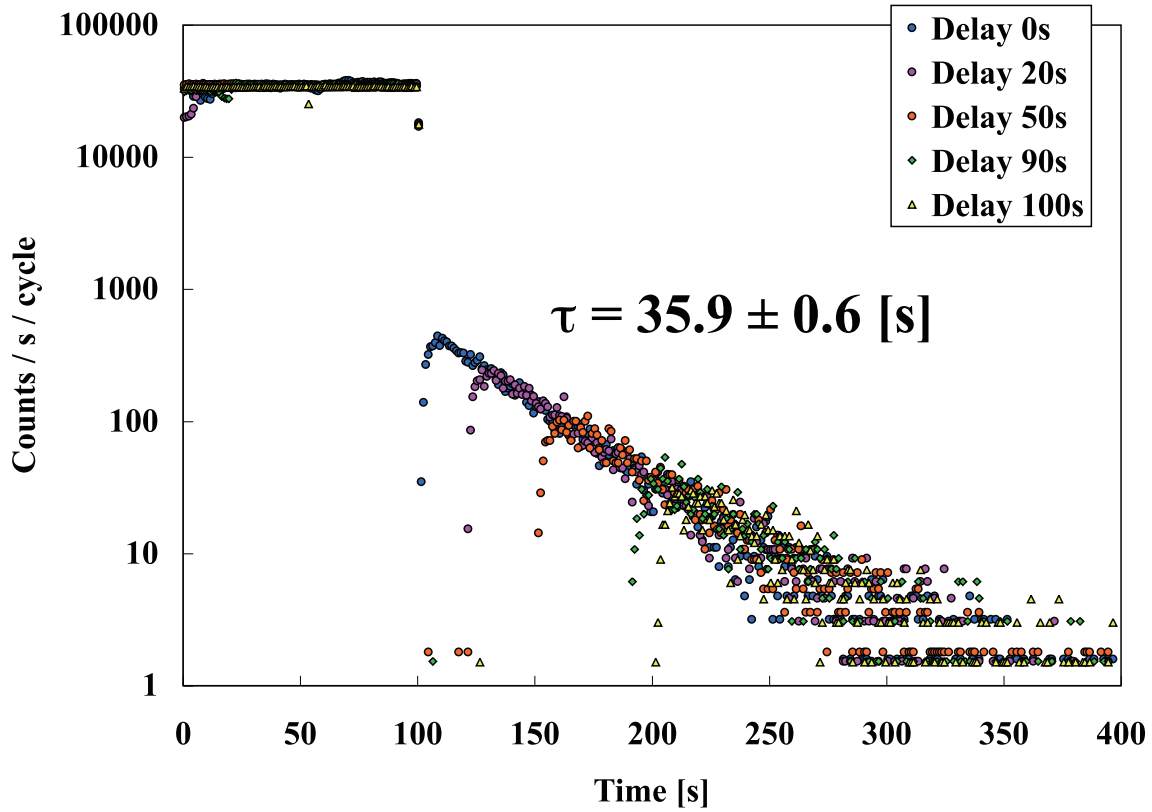

Figure 5.12: Time spectra obtained by the delay mode, obtained in July 2007. A proton beam with a power of 400 W was irradiated for 100 sec. The time bin width is 1.0 sec/bin. The delay time Δt were 0, 20, 50, 90, and 100 sec, respectively. The annular disk was installed in front of the UCN detector. The decay constant of 0 sec delay mode was 35.9 ± 0.6 sec.

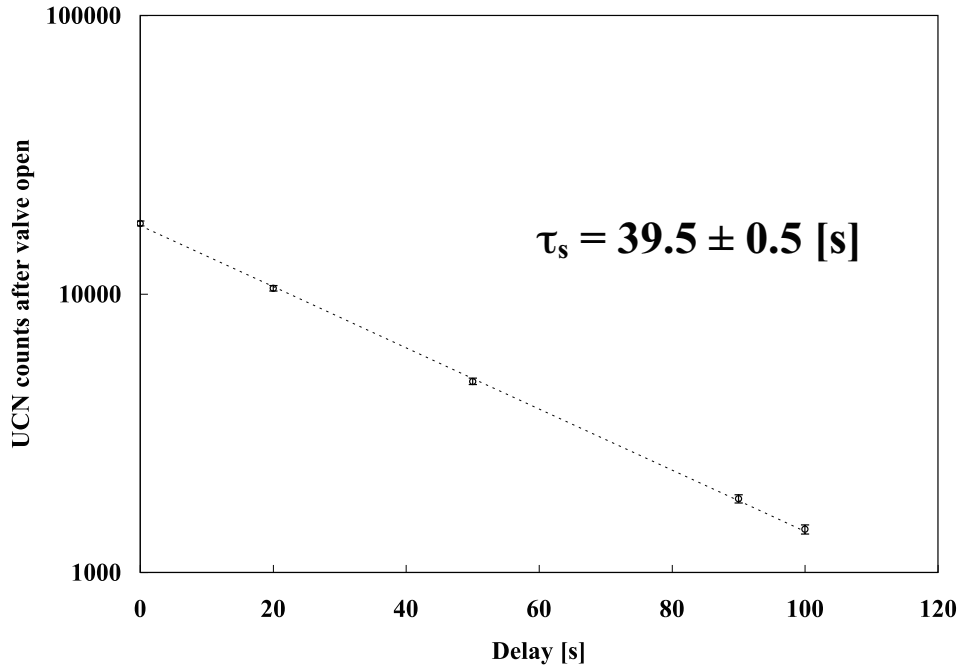

Figure 5.13: The total numbers of UCN as a function of the delay time Δt and a fitting curve. A UCN storage time τ_s was obtained to be 39.5 ± 0.5 s.

5.5 Wall Loss

In the experiment of year 2006 and 2007, UCN loss due to phonon up-scattering and absorption by ^{3}He were removed. The UCN storage time τ_s was lengthened from 14 sec to 39.5 ± 0.5 s. It was suggested that the wall loss still causes the large UCN loss in our UCN source. There are some ways to reduce this wall loss as listed below.

1. Coating the inner surface of the UCN source with a low wall loss material
2. Alkali degreasing
3. Baking at a high temperature

We used these methods in turn. First, we tested the effect of the Fomblin coating with a small teflon vessel in November 2007. After that, we coated the inner surface of the UCN horizontal guide by the Fomblin oil in April 2008. About the characteristics of Fomblin, see the following section.

Then, we cleaned up the UCN horizontal guide, the UCN vertical guide and the He-II bottle by alkali degreasing in April 2010.

Finally, we did the baking of the UCN guide and the He-II bottle at a temperature of 140 degrees Celsius (ordinalily 120 degrees Celsius) in February 2011.

The obtained results are shown in this section.

5.5.1 Fomblin Coating

Fomblin is an oil which is a hydrogen-free fully fluorinated polyether and has excellent reflection characteristics for UCN. Its chemical formula is CF_3-$(C_3F_4O)_M$-$(CF_2O)_N$-O-CF_3. M and N differ by a mean molecular weight of fomblin. We used the oil with the trade name FOMBLIN YH-VAC 18/8 (well known as the name Y-VAC 18/8). This grade possesses a mean molecular weight of 2650. Thus compositions in the range $M = 0, N \sim 39$ to $N = 0, M \sim 15$ appear permissible. However, because of the similar atomic weights and scattering lengths of C, O and F, the Fermi potential is insensitive to permissible choices of M and N. The calculated values are between 106 and 107 neV for most cases. In our discussion, we treat Fomblin's Fermi potential as 106.5 neV. For more detailed discussion, see ref. [55].

November 2007

In November 2007, we measured a UCN storage time of a vessel whose inner surface was covered with Fomblin grease. It is known that Fomblin has very small wall loss probability. We tested the effect of Fomblin grease by a small vessel before coating the inner surface of the UCN source with Fomblin grease.

We used the UCN storage bottle system which was developed to measure the UCN energy spectrum of the UCN source. About the UCN storage bottle system and its experiment, see Section 5. Fig. 5.14 shows the schematic view of the apparatuses used for the Fomblin test.

We connected a vacuum chamber to the experimental port via the filling valve. The vacuum chamber is a cylinder-shaped vessel with a diameter of 210 mm and a height of 500 mm. It is made of SUS316L. We installed a teflon pot inside the vacuum chamber. The teflon pot is a cylinder-shaped vessel with a inner diameter of 175 mm and a inner height of 185 mm. The thickness of the wall is 12.5 mm. The inner surface of the teflon pot was covered with the Fomblin grease. There are two holes with a diameter of 74.8 mm at the bottom of the teflon pot. One is the entrance of UCN, and the another is the exit of the UCN.

The valve system was attached to the bottom of the chamber. The filling valve is used to fill the teflon pot with UCN. And the emptying valve is used to extract UCN from the pot. Each valve has a valving element which is a SUS316L round plate with a diameter of 74.8 mm. The valving element can go up and down by a pneumatic actuator. When it is at the upper position, the valve is closed. UCN cannot go into the teflon pot. When it is at the lower position, the valve is opened. UCN can go into the teflon pot.

The gravity accelerator tube and the ^{3}He UCN detector were attached to the emptying valve. There was no annular disk in front of the UCN detector. When the emptying valve is opened, UCN in the teflon pot goes out from the pot and goes into the ^{3}He UCN detector. Then, they are observed.

Fig. 5.15 shows the time spectra obtained by the Fomblin test experiment. We irradiated a 400 W proton beam for 60 sec. During the beam irradiation, the filling valve was opening, and the teflon pot was filled with UCN. Then, the filling valve was closed. UCN were confined in the teflon pot. After some delay time Δt, the emptying valve was opening. And then, the extracted UCN were observed by the UCN detector.

In Fig. 5.15, there were some UCN counts before the emptying valve was opened. They were UCN leaking through the gap of the valve. There was a gap with a width of $0.04 \sim 0.05$ mm between the valving element and the valve sheet.

Delay Δt [s]	total UCN counts
0	7578 ± 305
60	5686 ± 234
120	4241 ± 194
240	2500 ± 136
300	1935 ± 114

Table 5.4: The total UCN counts in the teflon pot with Fomblin coating.

The total UCN counts as a function of the delay time was shown in Fig. 5.16 and listed on Table 5.4. The UCN storage time of the Fomblin coating was 219 ± 10 sec. Here, we estimated the wall loss probability per bounce of Fomblin. According to (2.50), the wall loss rate per

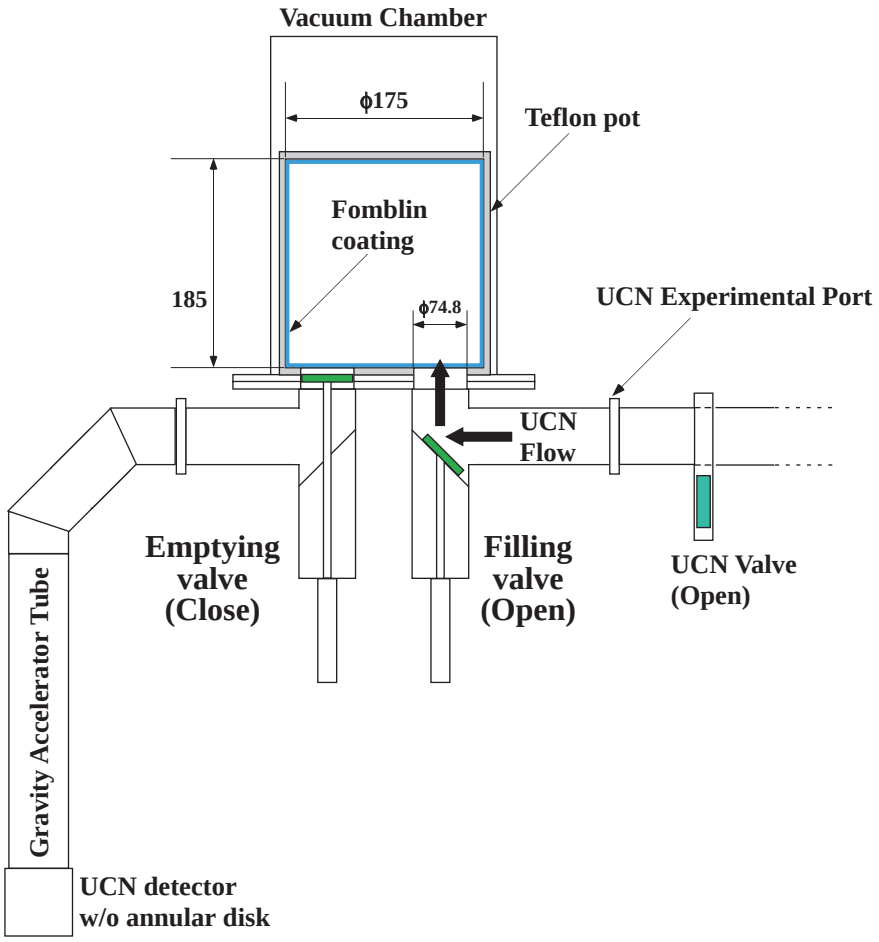

Figure 5.14: Schematic view of the teflon pot with Fomblin coating and peripheral apparatuses.

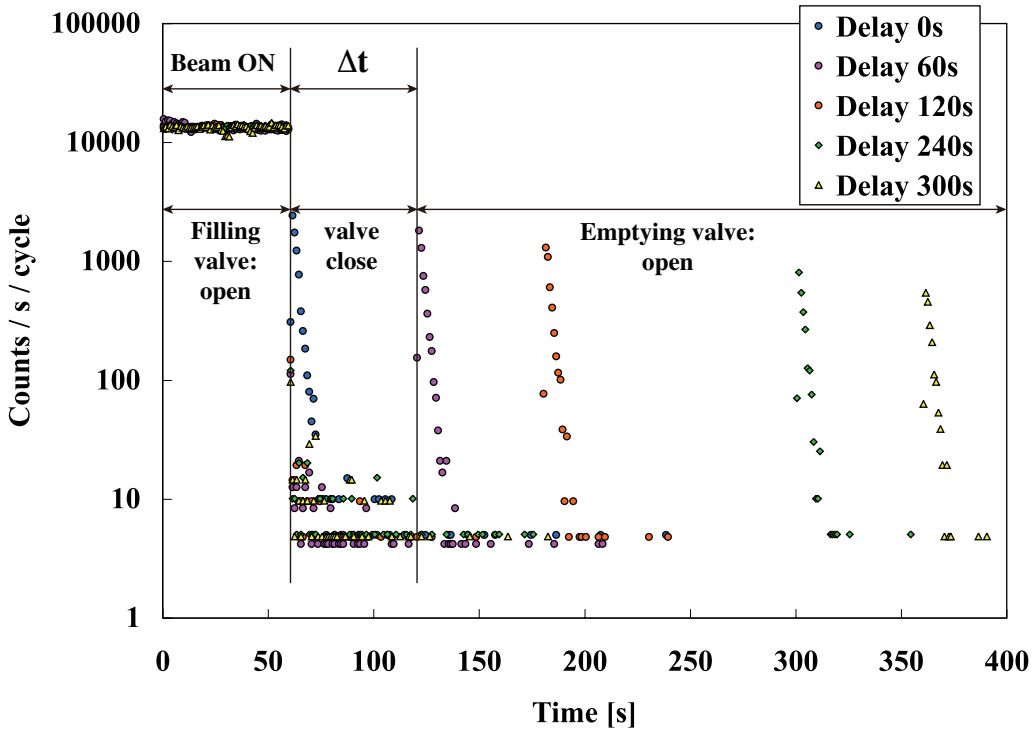

Figure 5.15: Time spectra obtained by using the teflon pot with Fomblin coating. UCN counts observed before the valve was opened were UCN leaking through the gap of the valve.

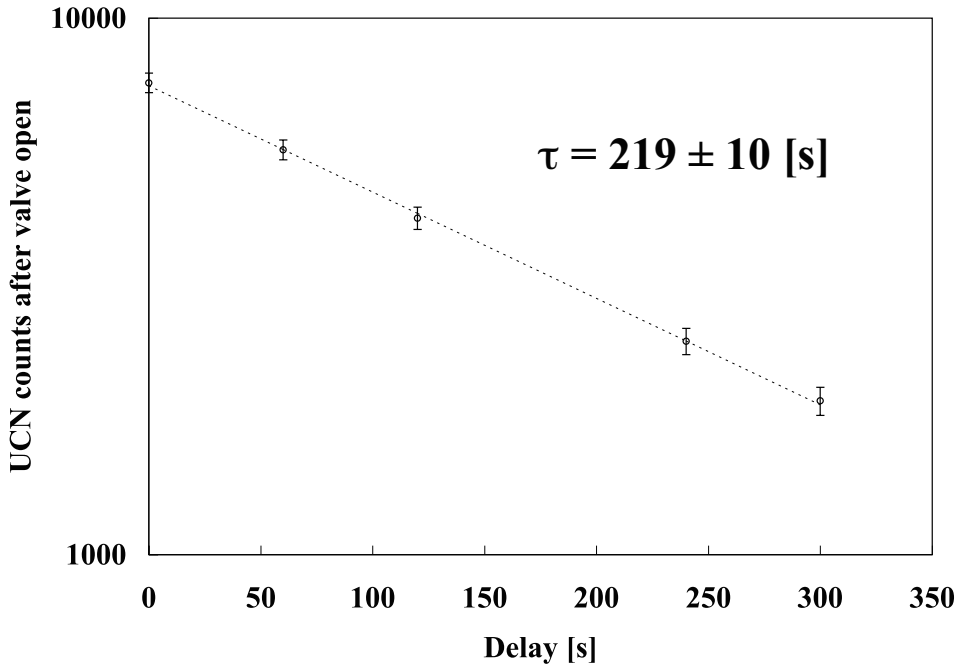

Figure 5.16: Time dependence of the total UCN counts in the teflon pot with Fomblin coating. The UCN storage time was 219 ± 10 sec.

time is given by

$$\frac{1}{\tau_{wall}} = \frac{\overline{\mu v} S}{4V} \ . \tag{5.56}$$

The critical energy at the bottom of the teflon pot is $E_c = 75$ neV. If we assume the UCN energy spectrum is proportional to $\sqrt{E}$, the averaged velocity is $\overline{v} = 2.8$ m/s. The surface area of the teflon pot is $S = 1.7 \times 10^3$ cm^2, and the volume is $V = 5.4 \times 10^3$ cm^3. Therefore, the effective wall loss probability per bounce was given by

$$\begin{aligned}
\frac{1}{\tau_{wall}} &= \frac{1}{\tau} - \frac{1}{\tau_{He}} - \frac{1}{\tau_\beta} && (5.57)\\
&= \frac{1}{219} - \frac{1}{1246} - \frac{1}{885.7} && (5.58)\\
&= 2.63 \times 10^{-3} && (5.59)\\
\overline{\mu} &= \frac{1}{\tau_{wall}} \cdot \frac{4V}{\overline{v} S} && (5.60)\\
&= 2.63 \times 10^{-3} \cdot \frac{4 \cdot 5.4 \times 10^3 \text{ cm}^3}{2.8 \text{ m/s} \cdot 1.7 \times 10^3 \text{ cm}^2} && (5.61)\\
&= 1.2 \times 10^{-4} \ . && (5.62)
\end{aligned}$$

The wall loss parameter, η, is given by

$$\eta \sim \overline{\mu}/2 = 6 \times 10^{-5} \ . \tag{5.63}$$

It was confirmed that Fomblin has very small wall loss probability. Following this result, we decided to coat the UCN horizontal guide with Fomblin grease.

April 2008

In April 2008, we coated the inner surface of the UCN horizontal guide with the fomblin oil, YH-VAC 18/8 (see Fig. 5.17). The thickness of the coating was thin, but the precise value was unknown. Since Fomblin has very low wall loss for UCN, it was expected to lengthen the UCN storage time.

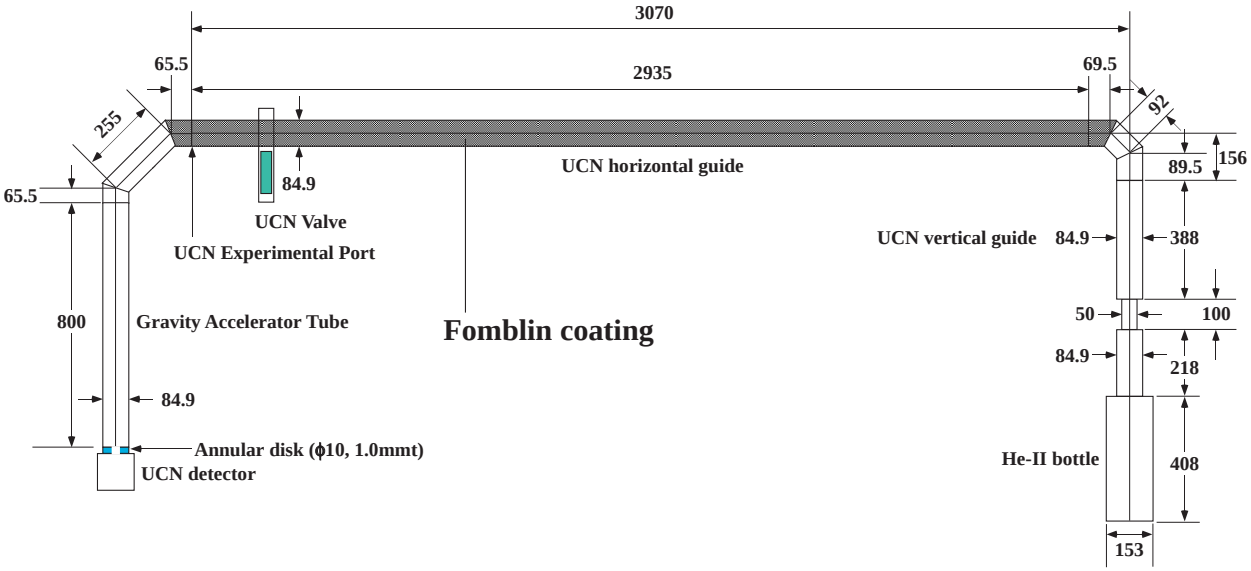

Figure 5.17: Fomblin coating on the UCN horizontal guide. Unit is millimeter.

We measured the UCN time spectra by the delay mode. A 400 W proton beam was irradiated for 100 sec. The delay time Δt were 0, 25, 50, 75, 100, and 125 sec. The obtained UCN time spectra are shown in Fig. 5.18.

The total counts of the obtained UCN in Fig. 5.18 are shown in Table 5.5. Fig. 5.19 is a plot of the total UCN counts as a function of the delay time Δt and a fitting curve by an exponential function $y = \exp(-x/\tau_s)$. The obtained UCN storage time was $\tau_s = 47.8 \pm 1.4$ s. This was longer than the previous experiment result, $\tau_s = 39.5 \pm 0.5$ s, obtained in July 2007. The effect of the Fomblin coating was confirmed.

Then, we irradiated the proton beam for a long time enough to obtain the saturated UCN counts. We irradiated the proton beam for 600 sec and obtained a time spectrum shown in Fig. 5.20. The obtained UCN count rate was 599 ± 38 cps as shown in Table. 5.5. By Knusden's model, the UCN density at the experimental port was given by

$$\rho_{ucn} = (599 \pm 38)\ \text{cps} \cdot (75.39 \pm 0.12) \cdot 4 \cdot \frac{1}{3.0\ \text{m/s} \cdot 56.6\ \text{cm}^2 \cdot (0.697 \pm 0.023)} \quad (5.64)$$

$$= 15.3 \pm 1.1\ \text{UCN/cm}^3 \quad (5.65)$$

for the critical energy $E_c = 84$ neV.

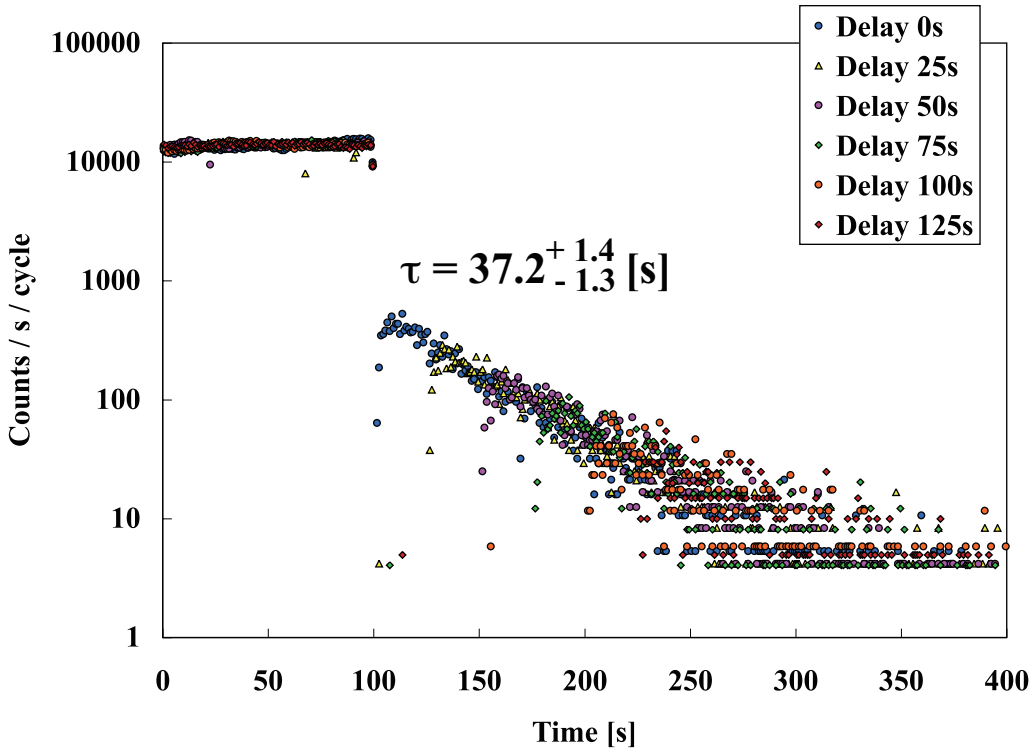

Figure 5.18: Time spectra of UCN by the delay mode, obtained in April 2008. A 400 W proton beam was irradiated for 100 sec. The delay time Δt were 0, 25, 50, 75, 100, and 125 sec. There was an annular disk in front of the UCN detector. The decay constant of 0 sec delay mode was $37.2^{+1.4}_{-1.3}$ sec.

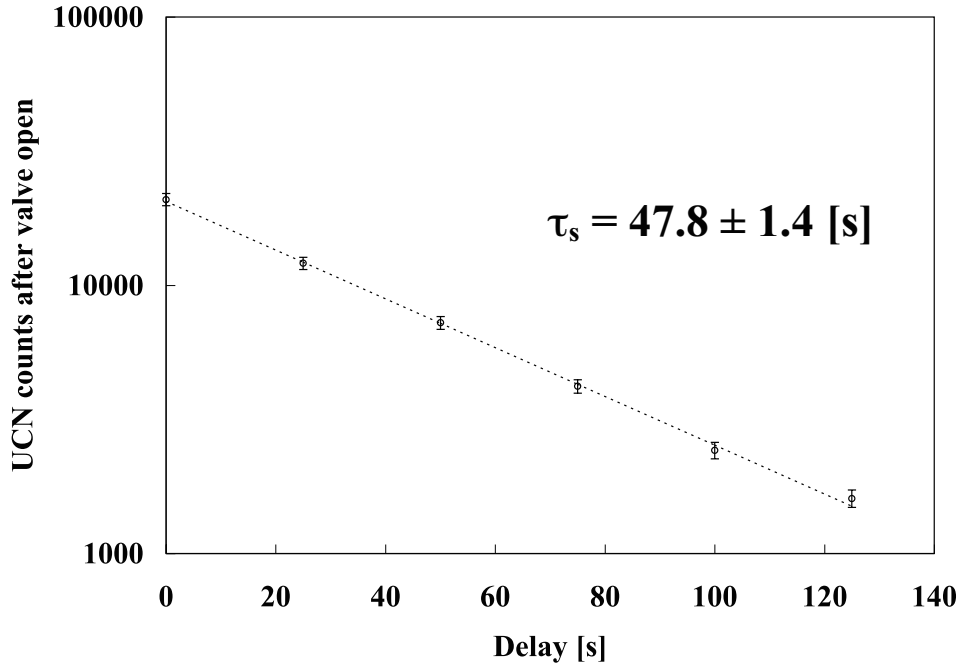

Figure 5.19: The total counts of UCN as a function of the delay time Δt and a fitting curve by an exponential function $y = \exp(-x/\tau_s)$. A UCN storage time of 47.8 ± 1.4 sec was obtained.

Delay Δt [s]	total UCN counts	max UCN count rate [cps]	Beam duration [s]
0	20869 ± 1084	527 ± 59	100
25	12088 ± 636	289 ± 38	100
50	7246 ± 397	163 ± 27	100
75	4120 ± 245	106 ± 21	100
100	2425 ± 169	76 ± 21	100
125	1604 ± 119	55 ± 17	100
0	25406 ± 1243	599 ± 38	600

Table 5.5: The total counts of UCN and maximum UCN count rates obtained in the delay mode measurement of April 2008.

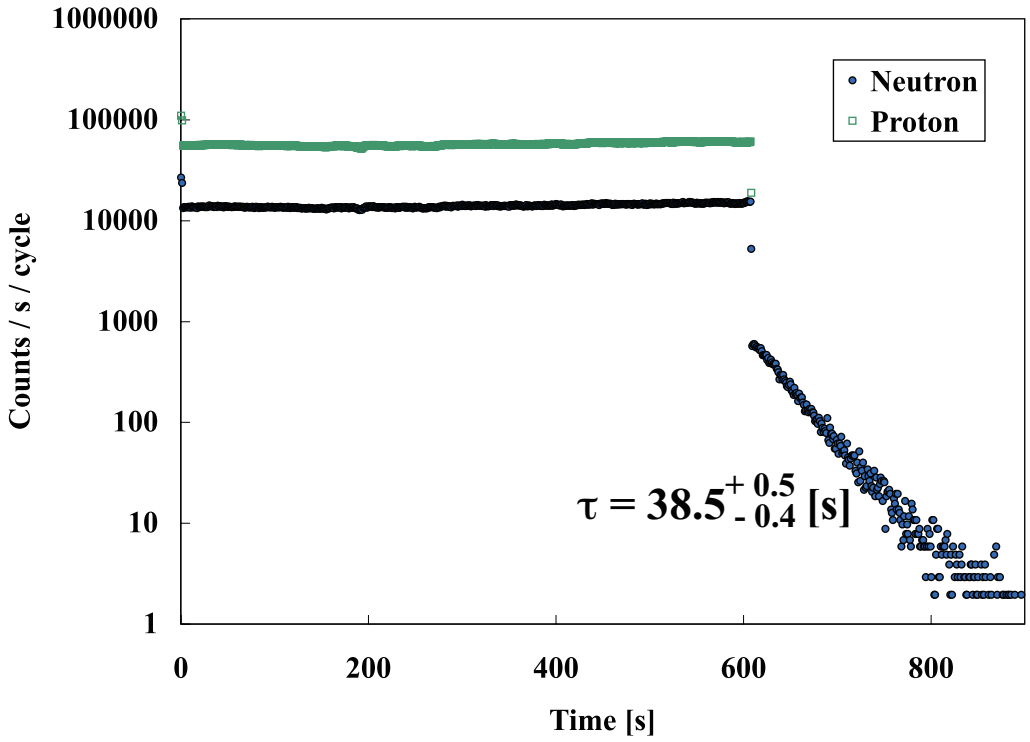

Figure 5.20: A time spectrum of UCN in the delay mode, obtained in April 2008. A 400 W proton beam was irradiated for 600 sec. The delay time Δt was 0 sec. There was an annular disk in front of the UCN detector. The decay constant was $38.5^{+0.5}_{-0.4}$ sec.

5.5.2 Alkali Degreasing

Ethanol or Acetone are usually used to clean up vessel surfaces. However, they are not enough to wash away oil contaminations which cover the surfaces like a thin film. Alkali degreasing is widely used as a washing method after ECB (Electro chemical Buffing). It is more useful to wash away such oil contaminations than alcohols. We used the alkali degreasing to clean up the He-bottle and the UCN guide. Our alkali degreasing was done as follows.

1. Wash surfaces by aqueous sodium hydroxide (NaOH) of 5%
2. Wash surfaces by pure water
3. Wash surfaces by nitric acid (HNO_3) of 5%
4. Wash surfaces by pure water

The original method uses aqueous sodium hydroxide (NaOH) at a temperature of 60 degrees Celsius. However, since we did not have necessary apparatuses, we used NaOH at a room temperature.

April 2010

In April 2010, we cleaned up the UCN horizontal guide, the UCN vertical guide and the He-II bottle to remove the oil contaminations by alkali degreasing. The Fomblin coating on the UCN horizontal guide was also removed by this work. Fig. 5.21 shows the time spectra obtained by the delay mode. A proton beam with a power of 400 W was irradiated for 5 sec. The delay time Δt were 0, 50, 100, and 200 sec. The total UCN counts as a function of the delay time is shown in Fig. 5.22. The UCN storage time in the source τ_s was obtained to be 61.4 ± 0.8 sec.

Then, we measured a time spectrum with a beam irradiation duration of 100 sec to obtain the maximum number of UCN. The obtained spectrum is shown in Fig. 5.23. In this measurement, the total UCN count was $(1.607 \pm 0.024) \times 10^5$, and the maximum UCN count rate was $(1.038 \pm 0.018) \times 10^4$ cps. The total UCN counts and the maximum UCN count rates obtained by the delay mode are shown in Table. 5.6.

As seen in Fig. 5.21 and Fig. 5.23, the time spectra obtained by the delay mode have two exponential components. The fast components consist of fast UCN, and the slow components consist of slow UCN. These results show that the UCN flow in the UCN source was not in the mechanical equilibrium without the annular disk in front of the UCN detector. Therefore, Knusden's formula or the diffusion model can not be used for the analysis.

We can calculate the UCN density at the experimental port by the UCN storage time τ_s. It is expected that a UCN density is proportional to τ_s. In April 2008, the UCN storage time was 47.8 ± 1.4 sec and the UCN density was 15.3 ± 1.1 UCN cm^{-3}. In this experiment, the

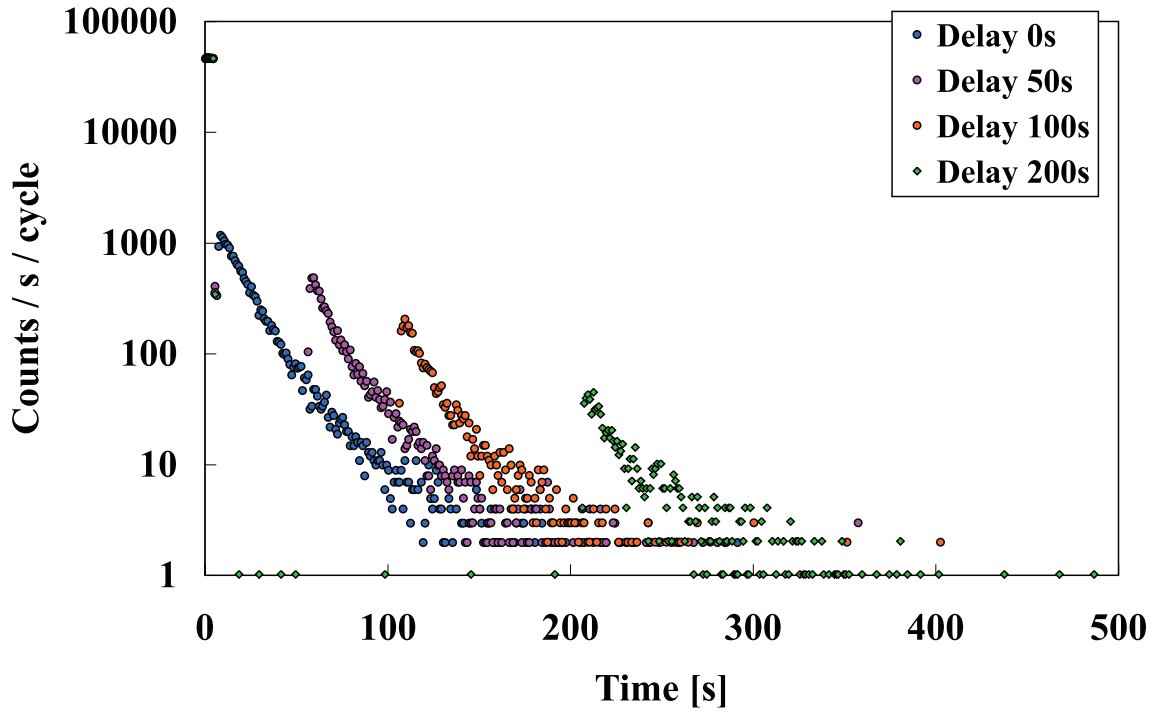

Figure 5.21: Time spectra obtained by the delay mode in April 2010. A proton beam with a power of 400 W was irradiated for 5 sec. The delay time Δt were 0, 50, 100, and 200 sec.

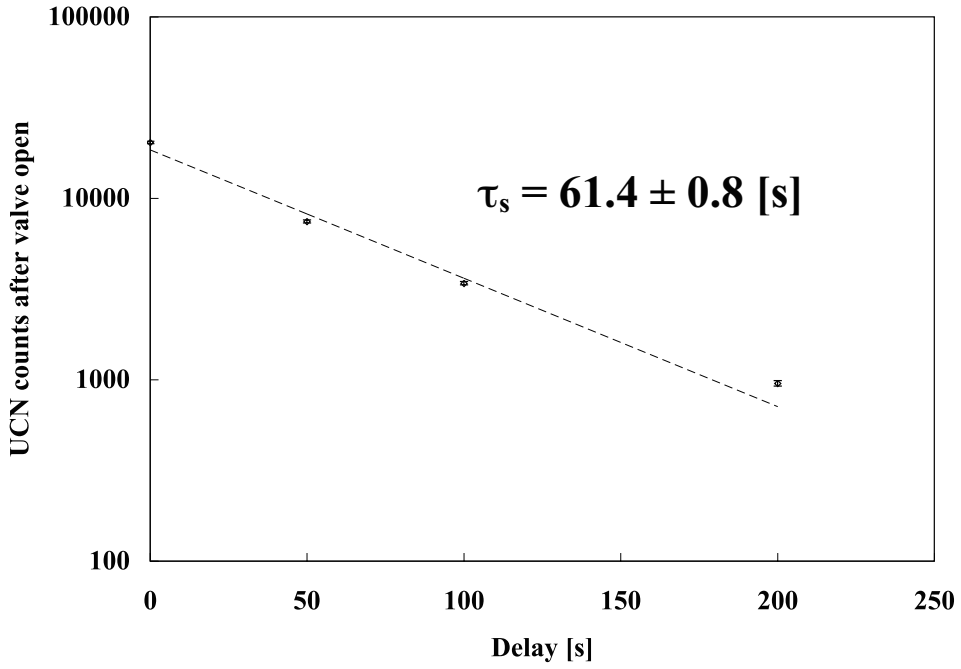

Figure 5.22: The total UCN counts by the delay mode as a function of the delay time. The UCN storage time τ_s was obtained to be 61.4 ± 0.8 sec.

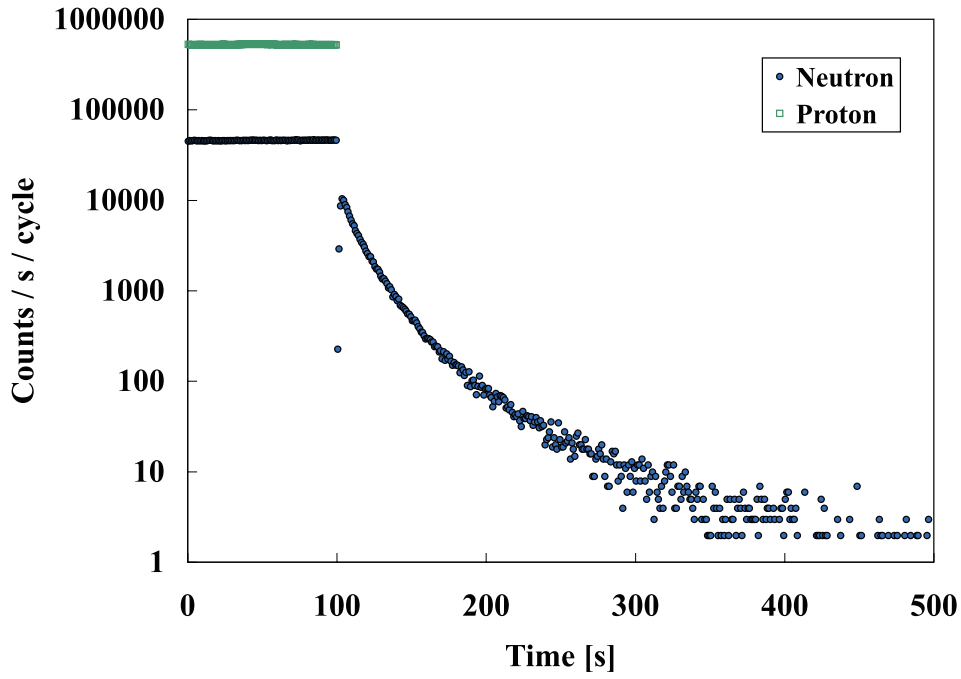

Figure 5.23: Time spectrum obtained by the delay mode with a delay time of 0 sec in April 2010. A proton beam of 400 W power was irradiated for 100 sec. The annular disk in front of the UCN detector was removed.

UCN storage time was 61.4 ± 0.8 sec. Using the UCN storage time in the source, the UCN density at the experimental port was given as follows.

$$\rho_{ucn} = 15.3 \pm 1.1 \text{ UCN cm}^{-3} \times \frac{61.4 \pm 0.8 \text{ s}}{47.8 \pm 1.4 \text{ s}} = 19.5 \pm 1.4 \text{ UCN cm}^{-3} \tag{5.66}$$

for the critical energy $E_c = 84$ neV.

Delay Δt [s]	total UCN counts	max UCN count rate [cps]	Beam [s]
0	20282 ± 326	1172 ± 38	5
50	7460 ± 138	485 ± 23	5
100	3402 ± 76	205 ± 15	5
200	954 ± 34	45 ± 7	5
0	160709 ± 2362	10382 ± 181	100

Table 5.6: The total UCN counts and the maximum UCN count rates obtained by the delay mode measurement in April 2010.

5.5.3 Baking at High Temperature

February 2011

In February 2011, we put up the output power of the heaters surrounding the UCN horizontal guide during the baking. The temperature of the UCN horizontal guide was ordinarily 120 degrees Celsius, but it was 140 degrees Celsius in this time. The UCN storage time τ_s was lengthened to be 81.5 ± 0.6 sec, which was the longest record so far.

Fig. 5.24 shows the time spectra obtained by the delay mode. A proton beam with a power of 400 W was irradiated for 5 sec. The delay time Δt were 0, 20, 50, 100, 150, 200, and 250 sec. The total UCN counts as a function of the delay time is shown in Fig. 5.25. The UCN storage time τ_s was 75.7 ± 1.0 sec.

Then, we measured the time spectra with a beam irradiation duration of 40 sec. The obtained spectra are shown in Fig. 5.26. The total UCN counts as a function of the delay time are shown in Fig. 5.27. The UCN storage time τ_s was 81.5 ± 0.6 sec.

The total UCN counts and the maximum UCN count rates obtained by the delay mode are shown in Table. 5.7.

Using the UCN storage time, the UCN density at the experimental port were given as follows.

$$\rho_{ucn} = 15.3 \pm 1.1 \text{ UCN cm}^{-3} \times \frac{81.5 \pm 0.6 \text{ s}}{47.8 \pm 1.4 \text{ s}} = 26.0 \pm 2.0 \text{ UCN cm}^{-3} \tag{5.67}$$

This is the largest value of the UCN density at the experimental port obtained by using our UCN source.

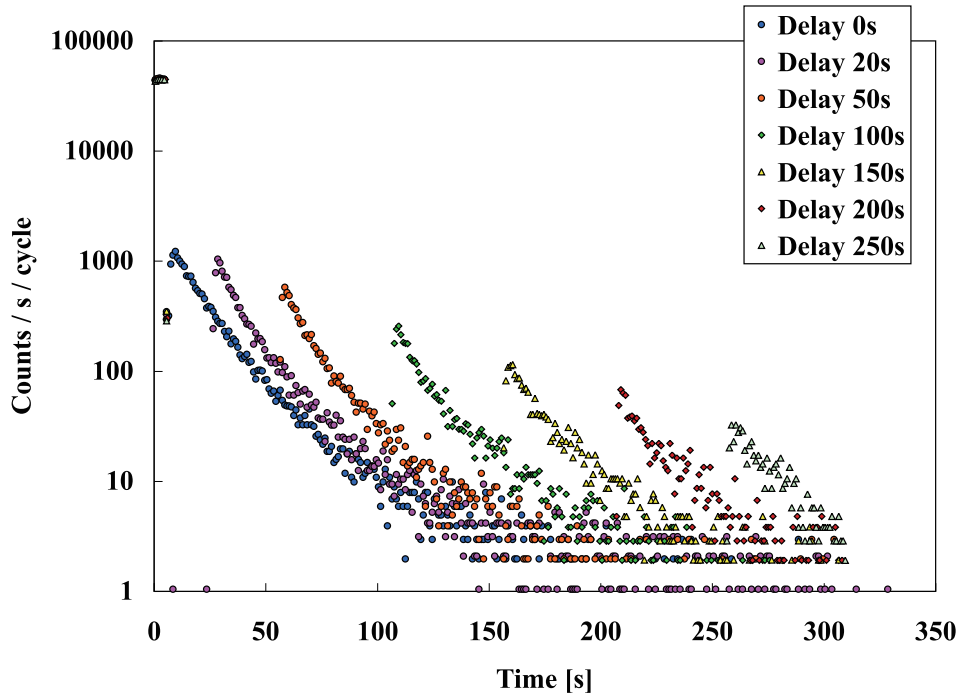

Figure 5.24: Time spectra obtained by the delay mode in April 2010. A proton beam with a power of 400 W was irradiated for 5 sec. The delay time Δt were 0, 20, 50, 100, 150, 200, and 250 sec. The annular disk in front of the UCN detector was removed.

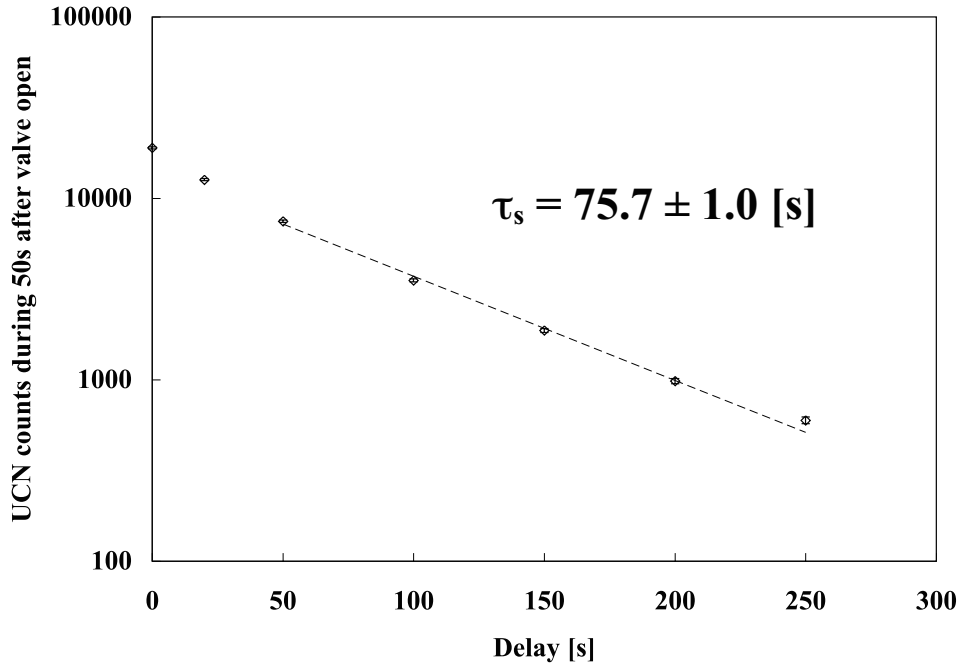

Figure 5.25: The total UCN counts obtained by the delay mode as a function of the delay time. The total UCN counts were the UCN counts that were integrated during 50 sec after the UCN valve was opening. The UCN storage time τ_s was 75.7 ± 1.0 sec.

Delay Δt [s]	total UCN counts	max UCN count rate [cps]	Beam [s]
0	18988 ± 236	1221 ± 37	5
20	12671 ± 172	1044 ± 35	5
50	7472 ± 114	578 ± 25	5
100	3534 ± 68	258 ± 16	5
150	1871 ± 47	115 ± 11	5
200	984 ± 32	68 ± 8	5
250	598 ± 25	33 ± 6	5
0	103019 ± 1091	7437 ± 115	40
20	71912 ± 773	5479 ± 92	40
50	44760 ± 499	3298 ± 66	40
100	21969 ± 266	1457 ± 40	40
150	11718 ± 160	735 ± 28	40
200	6789 ± 106	412 ± 20	40
250	3986 ± 74	237 ± 15	40

Table 5.7: The total UCN counts and the maximum UCN count rates obtained by the delay mode in February 2011. The total UCN counts were the UCN counts which were integrated during 50 sec after the UCN valve was opening.

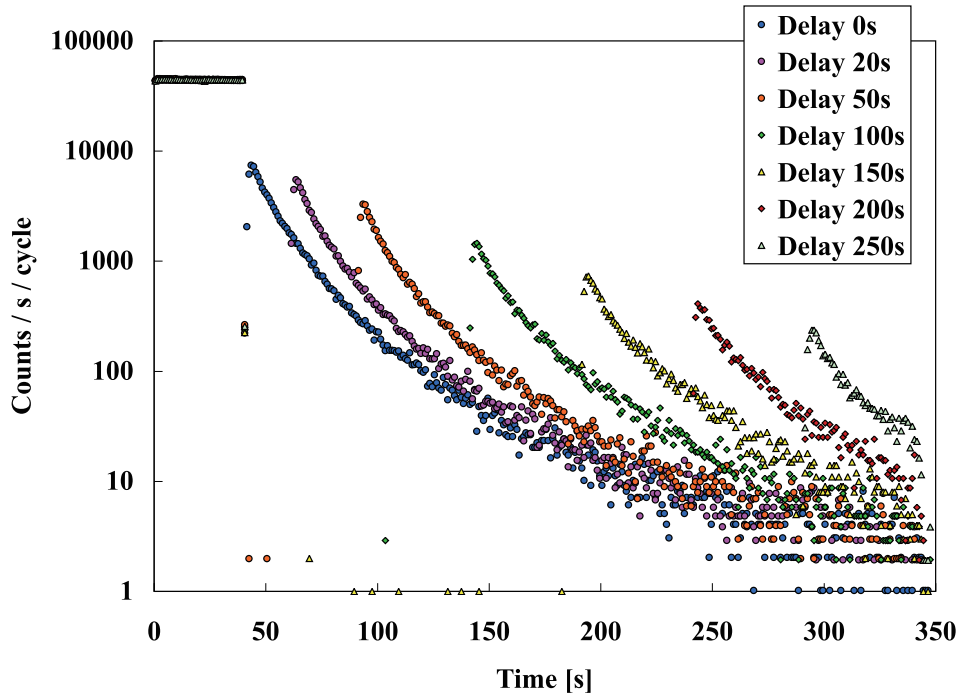

Figure 5.26: Time spectra obtained by the delay mode in April 2010. A proton beam with a power of 400 W was irradiated for 40 sec. The delay time Δt were 0, 20, 50, 100, 150, 200, and 250 sec. The annular disk in front of the UCN detector was removed.

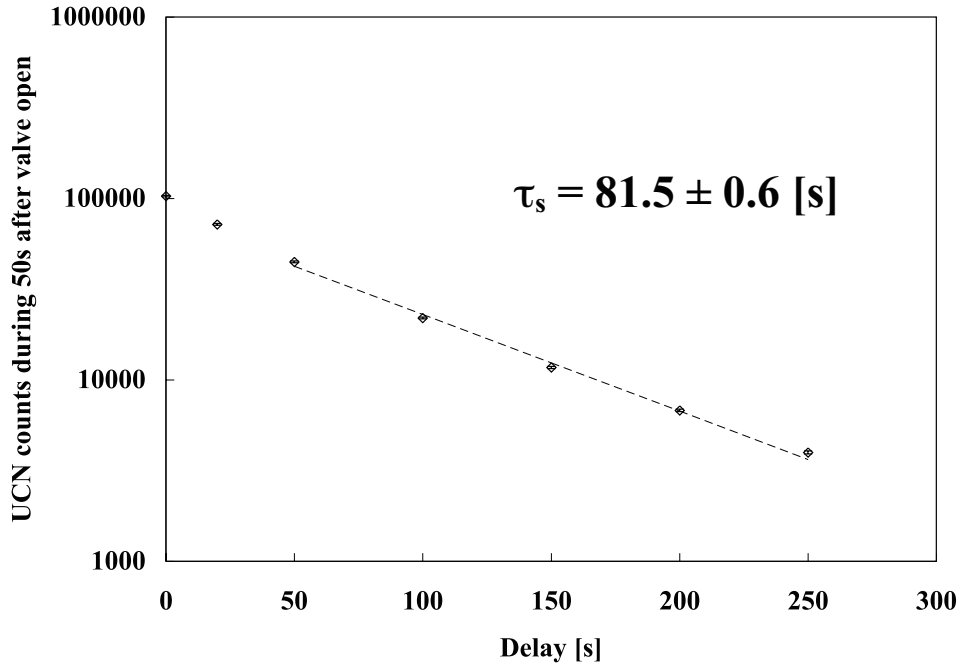

Figure 5.27: The total UCN counts obtained by the delay mode as a function of the delay time. The UCN counts were the UCN counts that were integrated during 50 sec after the UCN valve was opening. The UCN storage time τ_s was 81.5 ± 0.6 sec.

5.6 UCN Production Rate

In Chapter 3, the UCN production rate in He-II was estimated to be

$$P = \begin{cases} 14.87 \pm 0.28 & (T_{D_2O} = 20 \text{ K}) \\ 6.53 \pm 0.14 & (T_{D_2O} = 50 \text{ K}) \\ 3.67 \pm 0.09 & (T_{D_2O} = 80 \text{ K}) \end{cases} \text{ UCN cm}^{-3} \text{ s}^{-1} \tag{5.68}$$

by using the theoretical calculation and PHITS2 monte carlo simulation.

Here, we estimated the UCN production rate in the He-II bottle, using the experimental values. To calculate the UCN production rate in He-II, it is necessarry to calculate the total number of UCN produced in the UCN source. However, UCN are attracted to a lower position by the gravity interaction in the UCN vertical guide and the He-II bottle, and only UCN which can exceed the gravity potential between the He-II bottle and the UCN horizontal guide are contributed to the UCN counts observed by the UCN detector. The height of the UCN horizontal guide is 1.27 m from the bottom of the He-II bottle, and its gravity potential corresponds to 130 neV. UCN with an energy smaller than 130 neV remain confined in the UCN vertical guide and the He-II bottle. These hidden UCN must be included to estimate the UCN production rate.

The theory of phase space density is useful in this case. We obtained the UCN density at the experimental port, $\rho = 15.3 \pm 1.1$ UCN/cm^3 in April 2008, and we know the critical energy of UCN at the same place. So, we can obtain the phase space density of UCN in the UCN source. According to the Liouville's theorem, the phase space density is constant in the system which interacts with the gravity interaction. In this section, we estimated the total UCN number produced in the UCN source and the UCN production rate in He-II by the phase space calculation including the gravity interaction.

5.6.1 Phase Space Density

The total number of UCN in the UCN source, N, is given by

$$N = \int \int \rho_{phase} d^3x d^3p(z) \tag{5.69}$$

where ρ_{phase} is a phase space density of UCN and $\rho_{phase} = \text{const}$, because it is shown that a phase space density in a central force field is constant by Liouville's theorem. The integration element $d^3p(z)$ is dependent on the height z, because of the gravity interaction.

Here, we define the height of the UCN horizontal guide to be $z = h$. And we write the UCN density in the UCN horizontal guide $\rho_{ucn}(h)$. $\rho_{ucn}(h)$ is given by

$$\rho_{ucn}(h) = \frac{N}{\int_{z=h} d^3x} = \frac{N}{V_1} = \rho_{phase} \int d^3p(h) \tag{5.70}$$

where $\rho_{ucn}(h) = 15.3 \pm 1.1$ UCN/cm^3 as discussed before and V_1 is the volume of the UCN horizontal guide.

The energy of UCN in the horizontal guide ranges 0 to $E_c = 84$ neV. Using $p_c = \sqrt{2mE_c}$, the momentum integral of (5.70) is given by

$$\int_0^{p_c} d^3p(h) = \frac{4}{3}\pi p_c^3 \ . \tag{5.71}$$

Therefore, the phase space density of UCN is given by

$$\rho_{phase} = \frac{3}{4\pi p_c^3}\rho_{ucn}(h) \ . \tag{5.72}$$

Here, we consider a vertical guide which the gravity field is applied along its axis. The cross sectional area at a position of z is $A(z)$. The position of the bottom is at $z = 0$, and the top is at $z = h$. The total number of UCN in this guide is given by

$$N = \int_0^h A(z)dz \int d^3p(z)\rho_{phase} \ . \tag{5.73}$$

where $d^3p(z)$ is a momentum space volume at a position of z. The relation between $p(z)$ and $p(0)$ is given by

$$\frac{p(0)^2}{2m_n} = \frac{p(z)^2}{2m_n} + m_n g z \tag{5.74}$$

from the conservation law of energy. Then, $dp(z)$ and $dp(0)$ is related as follows.

$$p(z)dp(z) = p(0)dp(0) \tag{5.75}$$

Therefore,

$$\begin{aligned} d^3p(z) &= 4\pi p(z)^2 dp(z) && (5.76)\\ &= 4\pi p(z)p(0)dp(0) && (5.77)\\ &= \frac{p(z)}{p(0)}dp(0)^3 && (5.78) \end{aligned}$$

was obtained. This is a reduction of a phase space volume by the gravity. (5.73) is

$$N = \rho_{phase}\int_0^h A(z)dz \int d^3p(z) = \rho_{phase}\int_0^h A(z)dz \int \frac{p(z)}{p(0)}dp(0)^3 \ . \tag{5.79}$$

By use of $E_0 = p(0)^2/2m_n = p(z)^2/2m_n + m_n g z$, the momentum integral of (5.79) is

$$\begin{aligned} dE_0 &= \frac{p(0)}{m_n}dp(0), && (5.80)\\ d^3p(0) &= 4\pi p(0)^2 dp(0) && (5.81)\\ &= 4\pi p(0)m_n dE_0 && (5.82)\\ &= 4\pi m_n\sqrt{2m_nE_0}\ dE_0, && (5.83)\\ \int \frac{p(z)}{p(0)}dp(0)^3 &= \int \sqrt{\frac{E_0 - m_n g z}{E_0}}4\pi m_n\sqrt{2m_nE_0}\ dE_0 && (5.84)\\ &= 4\pi m_n\sqrt{2m_n}\int_{m_n g z}^{E_f}\sqrt{E_0 - m_n g z}\ dE_0, && (5.85) \end{aligned}$$

where E_0 ranges $m_n g z$ to E_f, and E_f is the maximum energy of UCN at $z = 0$. In our case, E_f is equal to the Fermi potential of the He-II bottle, 214 neV. The total number of UCN is given by

$$N = \rho_{phase} \int_0^h A(z)dz \int_{m_n g z}^{E_f} 4\pi m_n \sqrt{2m_n} \sqrt{E_0 - m_n g z}\ dE_0\ . \tag{5.86}$$

This equation can be rewritten to be

$$\begin{aligned} N &= \int_0^h A(z)dz \int_{m_n g z}^{E_f} \rho_E(z, E_0) dE_0 & (5.87)\\ \rho_E(z, E_0) &= 2\pi \rho_{phase} (2m_n)^{3/2} \sqrt{E_0 - m_n g z}\ . & (5.88) \end{aligned}$$

$\rho_E(z, E_0)$ is an energy distribution of UCN at a position of z.

The energy integration of $\rho_E(z, E_0)$ gives us a UCN density at a position of z. For example, UCN in the UCN horizontal guide at $z = h$ is given by

$$\begin{aligned} \int_{m_n g h}^{E_f} \rho_E(z = h, E_0) dE_0 &= 2\pi \rho_{phase} (2m_n)^{3/2} \int_{m_n g h}^{E_f} \sqrt{E_0 - m_n g h}\ dE_0 & (5.89)\\ &= \frac{4\pi}{3} \rho_{phase} (2m_n)^{3/2} (E_f - m_n g h)^{3/2} & (5.90) \end{aligned}$$

Here, using $\rho_{phase} = 3\rho_{ucn}(h)/4\pi p_c^3$ and $E_f - m_n g h = E_c = p_c^2/2m_n$,

$$\begin{aligned} \int_{m_n g h}^{E_f} \rho_E(z = h, E_0) dE_0 &= \frac{4\pi}{3} \rho_{phase} (2m_n)^{3/2} (E_f - m_n g h)^{3/2} & (5.91)\\ &= \frac{4\pi}{3} \frac{3}{4\pi p_c^3} \rho_{ucn}(h) (2m_n E_c)^{3/2} & (5.92)\\ &= \rho_{ucn}(h) & (5.93) \end{aligned}$$

was obtained.

On the other hand, the UCN density at a position of $z = 0$, i.e., the bottom of the He-II bottle, is give by

$$\begin{aligned} \rho_{ucn}(0) &= \int_0^{E_f} \rho_E(z = 0, E_0) dE_0 & (5.94)\\ &= \frac{4\pi}{3} \rho_{phase} (2m_n E_f)^{3/2} & (5.95)\\ &= \frac{4\pi}{3} \frac{3}{4\pi p_c^3} \rho_{ucn}(h) p_f^3 & (5.96)\\ &= \rho_{ucn}(h) \frac{p_f^3}{p_c^3} & (5.97) \end{aligned}$$

where $p_f^2 = E_f/2m_n$, and p_f is the critical velocity of UCN at a position of $z = 0$.

5.6.2 UCN Production Rate

Here, we estimated the total number of the produced UCN and the UCN production rate in the He-II bottle. As shown in the previous section, the total number of UCN in the UCN source is given by

$$N = \rho_{phase} \int_0^h A(z)dz \int_{m_n gz}^{E_f} 4\pi m_n \sqrt{2m_n} \sqrt{E_0 - m_n gz}\, dE_0 \tag{5.98}$$

$$= \frac{4\pi}{3} \rho_{phase} (2m_n)^{3/2} \int_0^z dz A(z)(E_f - m_n gz)^{3/2} \ . \tag{5.99}$$

The number of UCN in the UCN horizontal guide, N_1, is given by

$$N_1 = (15.3 \pm 1.1)\ \mathrm{UCN/cm^3} \times (\pi \cdot 4.25^2)\ \mathrm{cm^2} \times 307\ \mathrm{cm} \tag{5.100}$$

$$= (15.3 \pm 1.1)\ \mathrm{UCN/cm^3} \times 17,380\ \mathrm{cm^3} \tag{5.101}$$

$$= (2.66 \pm 0.19) \times 10^5\ \mathrm{UCN} \ . \tag{5.102}$$

The number of UCN in the He-II bottle, N_2, is given by

$$N_2 = \frac{4\pi}{3} \rho_{phase} (2m_n)^{3/2} \int_0^{z_0=40.8cm} dz A(z)(E_f - m_n gz)^{3/2} \tag{5.103}$$

$$= \rho_{ucn}(0) \times \frac{2A}{5m_n g} \left[E_f - \frac{(E_f - m_n g z_0)^{5/2}}{E_f^{3/2}} \right] \tag{5.104}$$

$$= (62.2 \pm 4.5)\ \mathrm{UCN/cm^3} \times 6438\ \mathrm{cm^3} \tag{5.105}$$

$$= (4.00 \pm 0.29) \times 10^5\ \mathrm{UCN} \ . \tag{5.106}$$

The number of UCN in the lower UCN vertical guide, N_3, is given by

$$N_3 = \frac{4\pi}{3} \rho_{phase} (2m_n)^{3/2} \int_{z_0=40.8cm}^{z_1=62.6cm} dz A(z)(E_f - m_n gz)^{3/2} \tag{5.107}$$

$$= \rho_{ucn}(0) \times \frac{2A}{5m_n g} \left[\frac{(E_f - m_n g z_0)^{5/2}}{E_f^{3/2}} - \frac{(E_f - m_n g z_1)^{5/2}}{E_f^{3/2}} \right] \tag{5.108}$$

$$= (62.2 \pm 4.5)\ \mathrm{UCN/cm^3} \times 806\ \mathrm{cm^3} \tag{5.109}$$

$$= (5.0 \pm 0.4) \times 10^4\ \mathrm{UCN} \ . \tag{5.110}$$

The number of UCN in the orifice of the UCN vertical guide, N_4, is given by

$$N_4 = \frac{4\pi}{3}\rho_{phase}(2m_n)^{3/2}\int_{z_1=62.6cm}^{z_2=72.6cm} dzA(z)(E_f - m_n g z)^{3/2} \quad (5.111)$$

$$= \rho_{ucn}(0) \times \frac{2A}{5m_n g}\left[\frac{(E_f - m_n g z_1)^{5/2}}{E_f^{3/2}} - \frac{(E_f - m_n g z_2)^{5/2}}{E_f^{3/2}}\right] \quad (5.112)$$

$$= (62.2 \pm 4.5)\ \mathrm{UCN/cm^3} \times 437\ \mathrm{cm^3} \quad (5.113)$$

$$= (2.72 \pm 0.20) \times 10^4\ \mathrm{UCN}\ . \quad (5.114)$$

The number of UCN in the upper UCN vertical guide, N_5, is given by

$$N_5 = \frac{4\pi}{3}\rho_{phase}(2m_n)^{3/2}\int_{z_2=72.6cm}^{z_3=127.0cm} dzA(z)(E_f - m_n g z)^{3/2} \quad (5.115)$$

$$= \rho_{ucn}(0) \times \frac{2A}{5m_n g}\left[\frac{(E_f - m_n g z_2)^{5/2}}{E_f^{3/2}} - \frac{(E_f - m_n g z_3)^{5/2}}{E_f^{3/2}}\right] \quad (5.116)$$

$$= (62.2 \pm 4.5)\ \mathrm{UCN/cm^3} \times 1170\ \mathrm{cm^3} \quad (5.117)$$

$$= (7.3 \pm 0.5) \times 10^4\ \mathrm{UCN}\ . \quad (5.118)$$

Then, the total number of the produced UCN is given by

$$N = N_1 + N_2 + N_3 + N_4 + N_5 = (8.2 \pm 0.4) \times 10^5\ . \quad (5.119)$$

This value includes only UCN with an energy between 130.2 to 214 neV because we treated UCN with the critical energy E_c of 84 neV at the UCN horizontal guide. Assuming the UCN energy spectrum to be proportional to $\sqrt{E}$, the ratio of UCN densities with an energy between 130.2 neV and 214 neV is given by

$$\int_{130.2}^{214}\sqrt{E}dE / \int_0^{214}\sqrt{E}dE = 1 - \left(\frac{130.2}{214}\right)^{3/2} = 0.5265 \quad (5.120)$$

The total number of UCN with all energies is given by

$$N = (8.2 \pm 0.4) \times 10^5/0.5265 = (1.55 \pm 0.07) \times 10^6\ . \quad (5.121)$$

About 1.5×10^6 UCN were produced in the UCN source. The total number of the produced UCN is given by

$$N = P \times V \times \tau \quad (5.122)$$

where P is the UCN production rate per unit volume, V is the volume where UCN are produced. In this case, it is the volume of the He-II bottle, i.e., $V = 8.4 \times 10^3$ cm^3.

τ is the UCN storage time of the volume where UCN are produced. If we confined the produced UCN in the He-II bottle and the UCN storage time of (47.8 ± 1.4) sec was achieved, the UCN production rate is given by

$$P = \frac{N}{V \cdot \tau} = \frac{(1.55 \pm 0.07) \times 10^6\ \mathrm{UCN}}{8.4 \times 10^3\ \mathrm{cm^3} \cdot (47.8 \pm 1.4)\ \mathrm{sec}} \quad (5.123)$$

$$= 3.84 \pm 0.21\ [\mathrm{UCN\ cm^{-3}\ s^{-1}}]\ . \quad (5.124)$$

The result of $P = (3.84 \pm 0.21)$ UCN cm^{-3} s^{-1} is consistent with theoretical prediction P at a D_2O temperature of 80K. This temperature is much higher than our solid D_2O temperature, $10 \sim 20$ K. The reason is considered to be due to the heavy water atoms tightly bounded each other by Van deer Waal's force at low temperatures. By this effect, heavy water atoms look like a large mass material for neutrons. Neutrons in the solid D_2O moderator are scattered by this large mass material, but does not become at a temperature same as the D_2O moderator. According to K. Inoue [47], a neutron temperature moderated by light water (H_2O) could not become lower than 50 K, even if the temperature of the light water moderator was much lower than 50 K. Therefore, it is expected that neutrons moderated by our solid D_2O moderator has a temperature of 50 K or higher.

On the other hand, in the simulation of PHITS2, light water and heavy water atoms at low temperatures are treated as free ideal particles because their form factors at low temperatures are not included in the code. When the heavy water temperature T_{D_2O} is set to be 50 K, the heavy water atoms are treated as an ideal gas at a temperature of 50 K. Neutrons in the moderator are considered to be moderated to be at the same or a little higher temperature as the D_2O temperature in PHITS2.

Therefore, it is appropriate that the UCN production rate P of (3.84 ± 0.21) UCN cm^{-3} s^{-1} was consistent with the result of 80K D_2O by PHITS2.

Chapter 6

Measurement of Energy Spectrum

6.1 UCN Storage Bottle

In measurements of UCN energy spectrum, the gravity interaction is used to separate the UCN energy. The gravity potential energy of UCN at the height of h is

$$E_{ucn} = m_n g h = 1.0252 \text{ [neV/cm]} \times h\text{[cm]} \ . \tag{6.1}$$

Kinetic energy of a UCN is less than 335 neV which is the Fermi potential of ^{58}Ni. The velocity is slower than 8 m/s. Therefore, The UCN motion is strongly influenced by the gravity interaction. A UCN with an energy of 100 neV can reach only the height of 1m.

To measure the energy spectrum of UCN extracted from the He-II superthermal UCN source, we coupled the gravity potential and a material which has a very large neutron absorption cross section. Fig. 6.1 shows the schematic view of our UCN spectrometer. We call this apparatus "UCN storage bottle". The "cylinder" part is used to confine UCN in itself. The "piston" works as the top plate and we can change its height between 0 to 90 cm. The piston's height h is controlled by the magnetic coupling feedthrough attached to the top flange of the cylinder. For filling and emptying UCN, two valves are attached to the bottom flange of the cylinder. Each valve has a round plate and the plate position can be quickly changed by pneumatic cylinders attached to the bottom of each valve. When the valve is opening, the round plate is at the lower position. And when the valve is closing, the round plate is at the higher position.

In the measurement of the UCN energy spectrum, polyethylene is used as a material of the piston. Polyethylene is a good UCN absorber. If UCN are confined in the cylinder, only UCN with an energy larger than $m_n g h$ are absorbed by the polyethylene piston and they are lost. Then, only UCN with an energy smaller than $m_n g h$ are observed. We can separate the UCN energy in this way.

The chemical formula of polyethylene is $(CH_2)_n$. The coherent scattering length of hydrogen is negative ($b_c = -3.7409(11)$ fm). The Fermi potential of polyethylene is also negative due to this hydrogen, the value is

$$V_F(\text{polyethylene}) = -8.54 \text{ [neV]}. \tag{6.2}$$

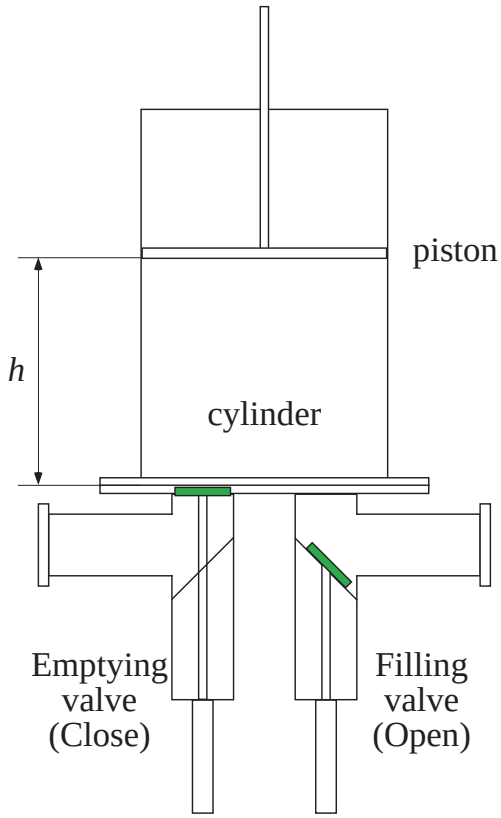

Figure 6.1: Schematic view of our UCN storage bottle.

SInce the Fermi potential is negative, UCN can penetrate the surface of polyethylene. These UCN are soon absorbed and lost in polyethylene. The attenuation length of UCN in polyethylene is about 1 mm, so UCN are absorbed very rapidly.

We attached this UCN storage bottle to the exit of the He-II superthermal UCN source. Fig. 6.2 is the schematic view of the setup of the UCN storage bottle. The filling valve was connected to the experimental port of the UCN source. The gravity accelerator tube and the ^{3}He UCN detector were attached to the emptying valve. There was no annular disk in front of the UCN detector.

The diameter of the cylinder is 20.6 cm and the height is 1 m. The piston's height h can be changed between 0 to 90 cm. Since the UCN critical energy in the UCN horizontal guide is $E_c = 84$ neV, the maximum height 90 cm is enough to cover the UCN energy range.

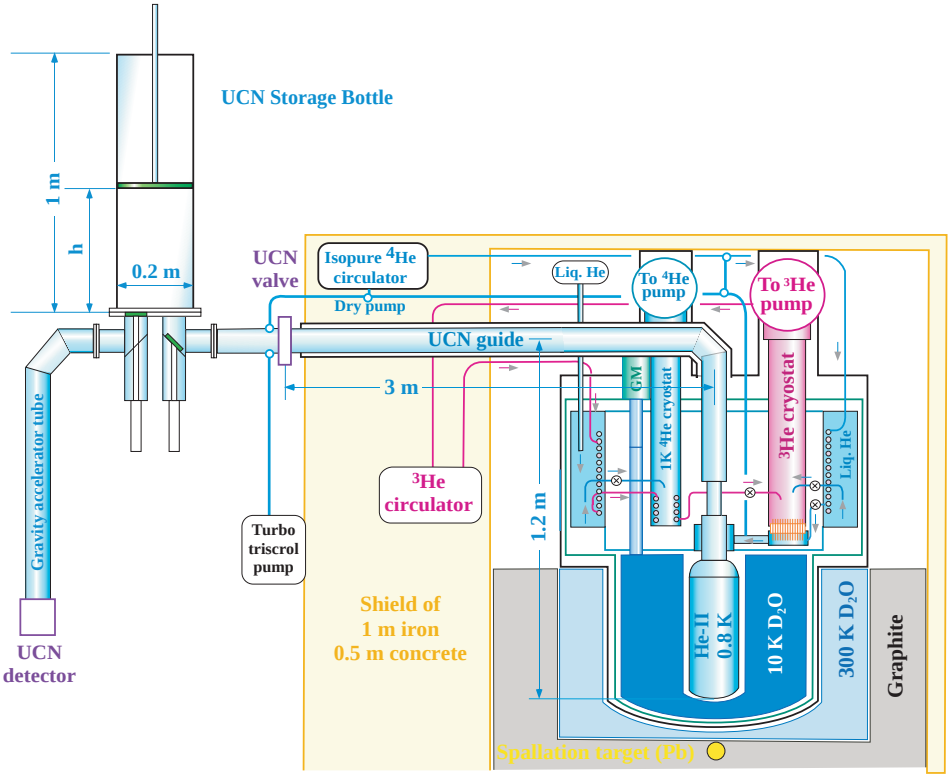

Figure 6.2: Setup of the UCN storage bottle. The UCN storage bottle was attached to the exit of the UCN source via the filling valve.

6.2 Detailed Design

The UCN storage bottle consists of three parts. They are the cylinder, the piston and the filling/emptying valve.

Cylinder Part

The cylinder part is a cylinder-shaped chamber where UCN are confined. The inner diameter of the cylinder is 206 mm and the total length is 1000 mm (Fig. 6.3). The reason why the 1000 mm cylinder is a couple of two 50 cm cylinders is for the accuracy of the center axis of the cylinder. It was difficult to make one 1000 mm length cylinder without bending its center axis.

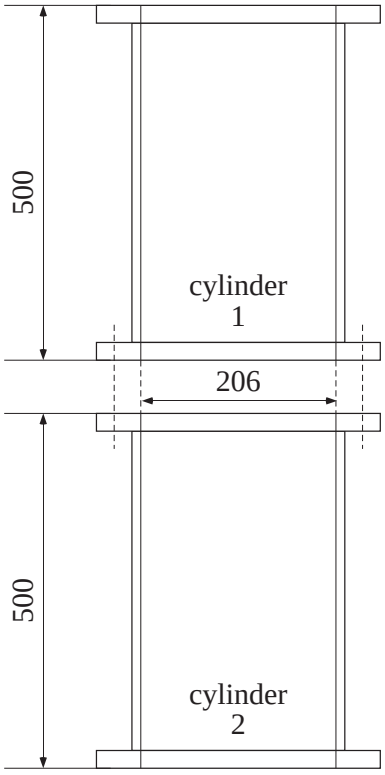

Figure 6.3: Schematic view of the cylinder part.

The inner surface of the cylinder is SUS316L which ECB (Electro-Chemical Buffing) was applied. The ECB enabled us to obtain a surface much flatter and purer than normal electropolishing. The Fermi potential of SUS316L is $V_F(\mathrm{SUS}) = 188$ neV.

Piston Part

The piston part is the top plate of the chamber where UCN are confined. It is made of

SUS316L and ECB was applied on its low side surface. A polyethylene disk with a thickness of 5 mm is attached to the bottom of the SUS disk. The piston part is connected to a feed thorough via an universal joint. We can change the height of the piston between 0 to 90 cm by moving the feed through. Fig. 6.4 shows the schematic view of the piston part.

The diameter of the polyethylene disk and the SUS disk is 206 mm. A gap between the inner surface of the cylinder and the edges of these disks is within 0.1 mm. The gap causes UCN losses by leak. But the gap width of 0.1 mm is enough small, so leak of UCN through this gap can be neglected.

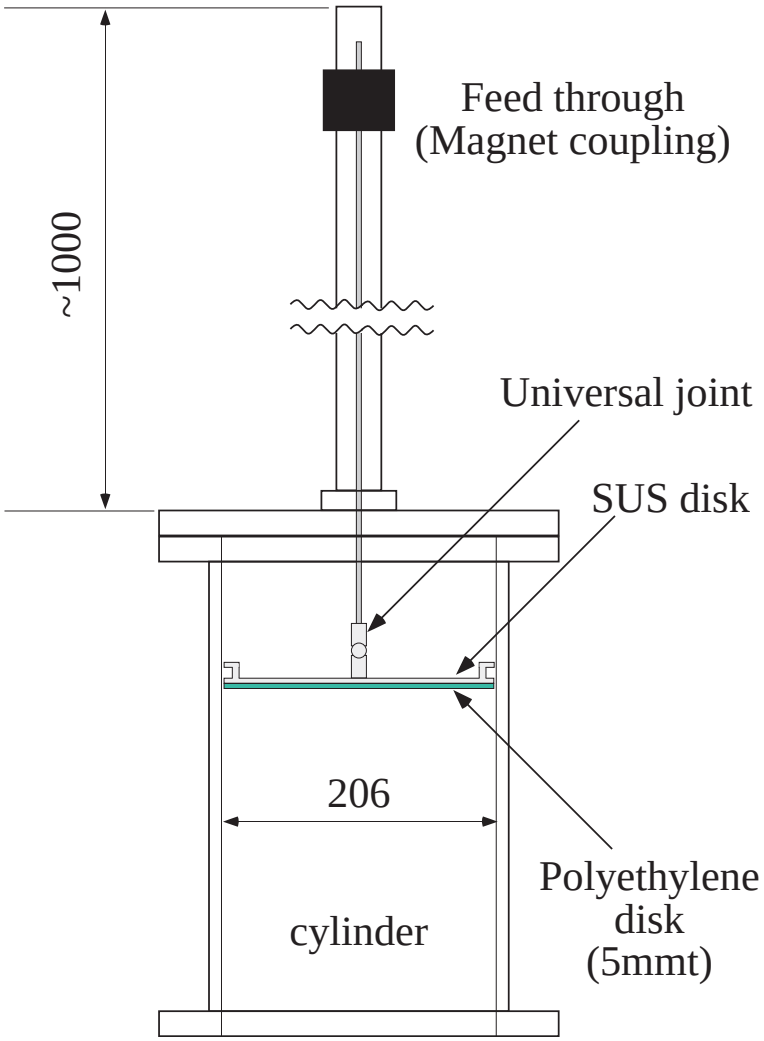

Figure 6.4: Schematic view of the piston part.

Filling / Emptying Valve

The cylinder part is filled with UCN through "the filling valve" attached to the bottom of the cylinder part. And also, UCN are extracted from the cylinder part through "the emptying

valve" attached to the bottom of the cylinder part. The filling and emptying valves are attached as shown in Fig. 6.1. The detail of the valve part is shown in Fig. 6.5.

The filling and emptying valves have the same structures. The valve element which is a disk with a 74.9 mm diameter and a 3 mm thickness is attached to the edge of the rod via a hinge. This rod and the valve element go up and down by the pneumatic actuator attached to the bottom of the valve. When the valve element goes up, it is pressed against the bottom of the cylinder part. This is the closing condition of the valve. The spring attached to the side of the rod pulls the valve element to be at the horizontal position. When the valve element goes down, the valve element stays on the valve seat at a 45 degrees angle. This is the opening condition.

The valve element is made of SUS316L and the ECB (Electro-Chemical Buffing) was applied on the surface. When the emptying valve is at the opening position, UCN from the experimental port are reflected by its surface and go into the cylinder part. When UCN extracted from the cylinder, they are reflected on the surface of the emptying valve at the opening position and go into the UCN detector. When the valve is closing, the valve element surface becomes the bottom surface of the cylinder, and UCN are confined in the cylinder. In any case, UCN touches only the polished surface.

The UCN guides of the valve system are also made of SUS316L. The inner surface of them were electrically polished.

Gap of Valve

When the valve is closing, there is a narrow gap between the valving element and the valve seat at the bottom of the cylinder. The valving element was made of SUS316L, and the valve seat of the bottom of the cylinder was also made of SUS316L. Their metal surfaces directly touch each other when the valve is closing. Therefore, some gap exist between them. We measured the width of the gap by a thickness gauge. The width of the gap was $0.04 \sim 0.05$ mm.

Here, we can estimate the UCN loss rate by leaking through this gap. If we assume the height of the top plate is $h = 90$ cm, the volume of the cylinder is $V = 29,996$ cm^3. The area of the gap ΔS is given by $\Delta S = \pi \times 7.49$ [cm] $\times 0.005$ [cm] $= 0.118$ [cm^2].

The UCN critical energy in the UCN horizontal guide is $E_c = 84$ neV. The height at the bottom of the cylinder is 84.8 mm higher than that of the UCN horizontal guide. This height corresponds to 8.7 neV. Therefore, the critical energy of UCN at the bottom of the cylinder is $E_c = 75$ neV. If we were to assume the UCN energy spectrum in the bottle is proportional to $\sqrt{E}$, the averaged UCN velocity becomes $\overline{v} = 2.8$ m/s. Therefore, the UCN loss rate by this gap is given by

$$\frac{1}{\tau_{gap}} = \frac{\overline{v}\Delta S}{4V} \times 2 = 5.6 \times 10^{-4} \ [\mathrm{s}^{-1}] \tag{6.3}$$

$$\tau_{gap} = 1.8 \times 10^{3} \ [\mathrm{s}] \ . \tag{6.4}$$

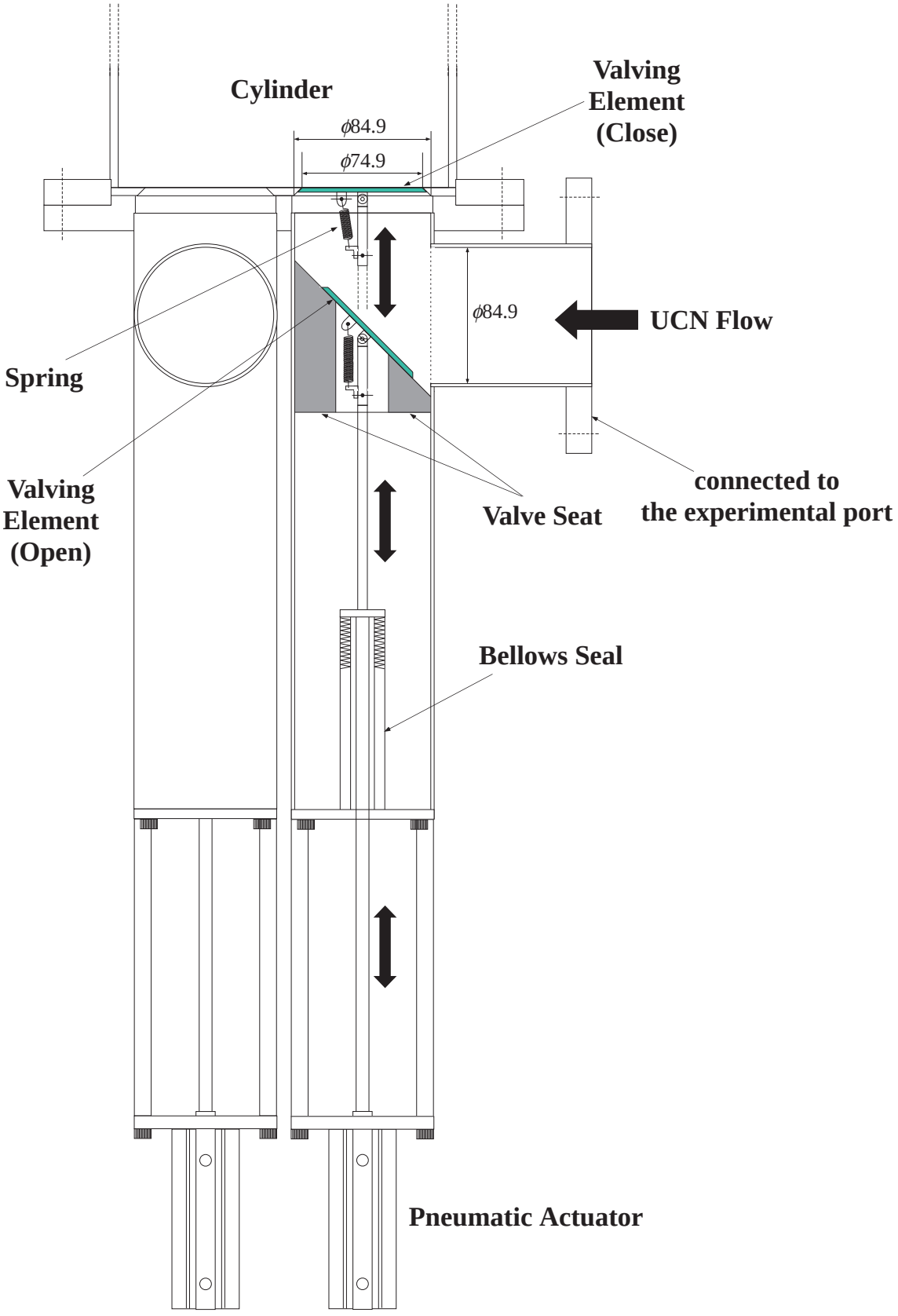

Figure 6.5: Schematic view of the filling / emptying valve part.

This value is much longer than a typical UCN storage time in the UCN storage bottle ($\tau \sim 170$ sec). So, this loss can be ignored.

Setup of UCN Storage Bottle

Before we set up the UCN storage bottle, we did alkali degreasing on the inner surfaces of the UCN storage bottle. As shown in the experiment in April 2010 (Chapter 5), we used NaOH of 5 % and HNO_3 of 5 %. We washed the surfaces by NaOH of 5 % at first. Next, we washed the surfaces by pure water. And then, we washed the surfaces by HNO_3 of 5 %. Finally, we washed the surfaces by pure water again.

After the alkali degreasing, we set up the UCN storage bottle. Before we connected the UCN storage bottle to the experimental port, we did the baking and deuteration of the UCN storage bottle. The cylinder part and the filling / emptying valve part were surrounded with ribbon heaters. We also did the baking of the SUS disk of the piston part. The SUS disk was in the vacuum container, so we installed a nichrome wire heater and a platinum resistance thermometer on the top side of the SUS disk, and controlled them from the atmosphere via a connection port at the top flange of the cylinder part.

During the baking, we kept the temperatures of the cylinder and the valves to be 120 $\sim$ 130 degrees Celsius. And we kept the temperature of the SUS disk to be 100 $\sim$ 110 degrees Celsius. The duration of the baking at the maximum temperatures was about 30 hours.

After the baking, we deuterated the inner surfaces of the UCN storage bottle. The amount of the D_2O vapor used for the deuteration was about 0.3 atm $\times$ 50 cc. Then, we waited for the UCN storage bottle to be room temperature.

Finally, we connected the UCN storage bottle to the experimental port of the UCN source. The photographs of the UCN storage bottle are shown in Fig. 6.6 and Fig. 6.7.

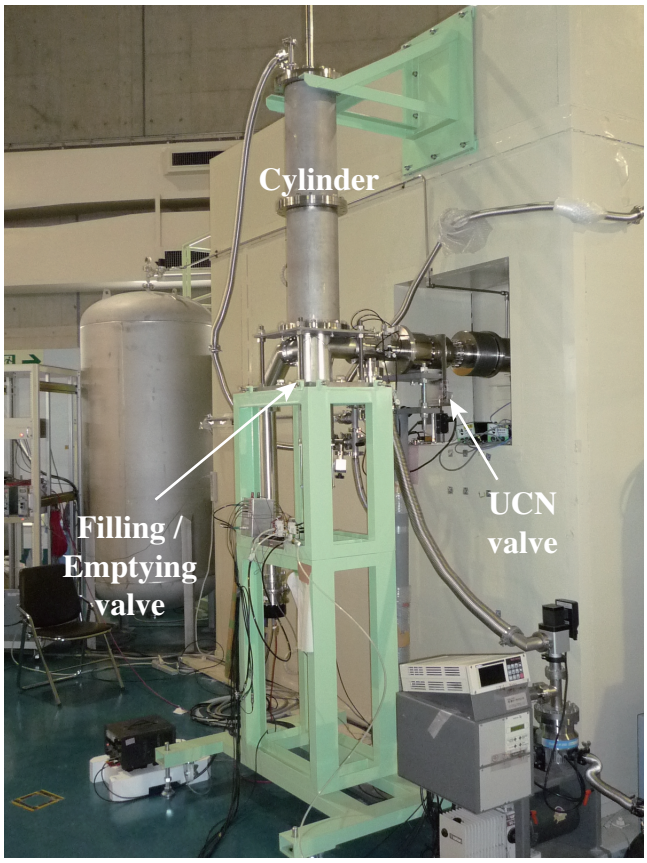

Figure 6.6: Photograph of the UCN storage bottle seen from the right side.

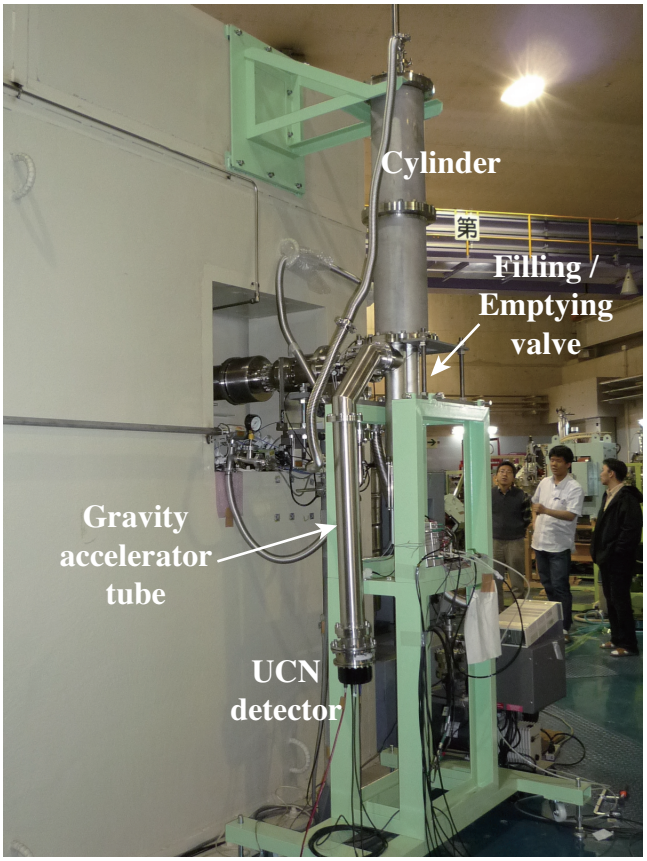

Figure 6.7: Photograph of the UCN storage bottle seen from the left side. The gravity accelerator tube and the ^{3}He UCN detector were attached to the emptying valve.

6.3 UCN Storage Experiment with SUS Disk

Our goal is to measure the energy spectrum of UCN from the He-II superthermal UCN source. Before the measurement of the UCN energy spectrum, we measured the UCN storage time in the UCN storage bottle. In this measurement, we removed the polyethylene disk from the piston. We used the SUS disk as a top plate. The ECB(Electro-Chemical Buffing) was applied on the surface of the SUS disk as well as the inner surface of the cylinder part.

The reason why we removed the polyethylene disk was that we wanted to know the wall loss parameter η of the surface of SUS316L. We measured the UCN storage time in the UCN storage bottle and estimated the wall loss parameter with a rough theoretical model. After the experiment, we simulated the obtained results by Geant4-UCN simulation with the obtained wall loss parameter. See Chapter 7 about the Monte Carlo simulation.

6.3.1 UCN Storage Time in a Cylindrical Bottle

The UCN storage time τ can be disintegrated to four components as follows.

$$\frac{1}{\tau} = \frac{1}{\tau_{wall}} + \frac{1}{\tau_{He}} + \frac{1}{\tau_{\beta}} + \frac{1}{\tau_{gap}} \tag{6.5}$$

where τ_{wall} is a life time by wall loss, τ_{He} is a life time by inelastic scattering by ^{4}He, τ_{β} is the neutron life, and τ_{gap} is a life time by leak through the gap of the valve. τ_{wall} is given by

$$\frac{1}{\tau_{wall}} = \frac{\overline{\mu v} S}{4V} \ . \tag{6.6}$$

In the case of a cylinder-shaped vessel with a diameter of D and a height of h, $S = \pi D h + 2\pi (D/2)^2$ and $V = \pi (D/2)^2 h$. Since $S/V = 2/h + 4/D$ is obtained, τ or τ_{wall} are height dependent. We write them $\tau(h)$ and $\tau_{wall}(h)$, respectively. Then,

$$\frac{1}{\tau(h)} = \frac{1}{\tau_{wall}(h)} + \frac{1}{\tau_{He}} + \frac{1}{\tau_{\beta}} + \frac{1}{\tau_{gap}(h)} \tag{6.7}$$

$$= \frac{\overline{\mu v}}{2} \cdot \frac{1}{h} + \frac{\overline{\mu v}}{D} + \frac{1}{\tau_{He}} + \frac{1}{\tau_{\beta}} + \frac{2\overline{v}\Delta S}{\pi D^2} \cdot \frac{1}{h} \tag{6.8}$$

was obtained. The first term of the right side is a wall loss by the top and bottom surfaces. The second term of the right side is a wall loss by the side surface.

Here, we assume that the wall loss of the top surface is larger than that of the side and bottom surfaces. The baking temperature of the SUS disk was about 10 degrees or more lower than the side and the bottom surfaces. Therefore, it is considered that the top surface have larger wall loss.

We write the averaged wall loss probability per bounce of the top surface $\overline{\mu}_1$, and that of the side and the bottom surfaces $\overline{\mu}_2$. Then, (6.8) was rewritten as follows.

$$\frac{1}{\tau(h)} = \frac{a}{h} + b \tag{6.9}$$

where

$$a = \frac{\overline{\mu}_1 \overline{v}}{4} + \frac{\overline{\mu}_2 \overline{v}}{4} + \frac{2\overline{v}\Delta S}{\pi D^2} \tag{6.10}$$

$$b = \frac{\overline{\mu}_2 \overline{v}}{D} + \frac{1}{\tau_{He}} + \frac{1}{\tau_\beta} \, . \tag{6.11}$$

If we measure the UCN storage time as a function of the height h, we can determine the values of $\overline{\mu}_1$ and $\overline{\mu}_2$.

6.3.2 Sequence of Measurement with SUS Disk

The UCN storage bottle has two valves. One is the filling valve, and the another is the emptying valve. We have to control these valves to confine or extract UCN. Fig. 6.8 shows the time diagram of the valve control. We irradiate a proton beam for 60 sec. During the beam irradiation, the filling valve is opening, and the bottle is filled with UCN from the UCN source. Then, we stop the beam irradiation. At the same time, the filling valve is closed. UCN are holded in the bottle for some delay time Δt. After the delay time Δt passed, the emptying valve is opened. UCN go out from the bottle and go into the UCN detector through the gravity accelerator tube. And then, they are observed by the derector. The UCN valve at the experimental port is opening in this measurement. Fig. 6.9 shows the schematic view of the UCN flow.

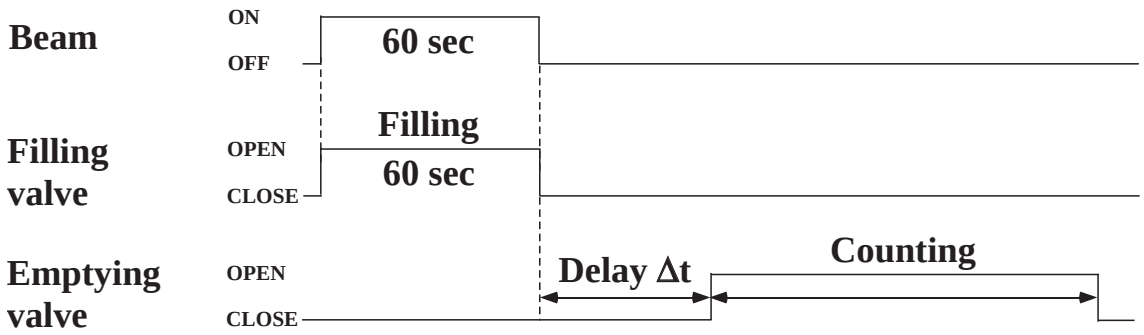

Figure 6.8: Time diagram of the filling/emptying valve operation.

We changed the delay time Δt, and measured the UCN time spectra. Then, we plotted the total UCN counts in the UCN storage bottle as a function of the delay time. We obtained a curve represented by one or two exponential components. The UCN storage time was obtained by fitting the curve.

Then, we changed the height of the SUS disk and repeated the time spectra measurement. We obtained the UCN storage time at the disk heights of 91.7, 20, 10 and 5 cm.

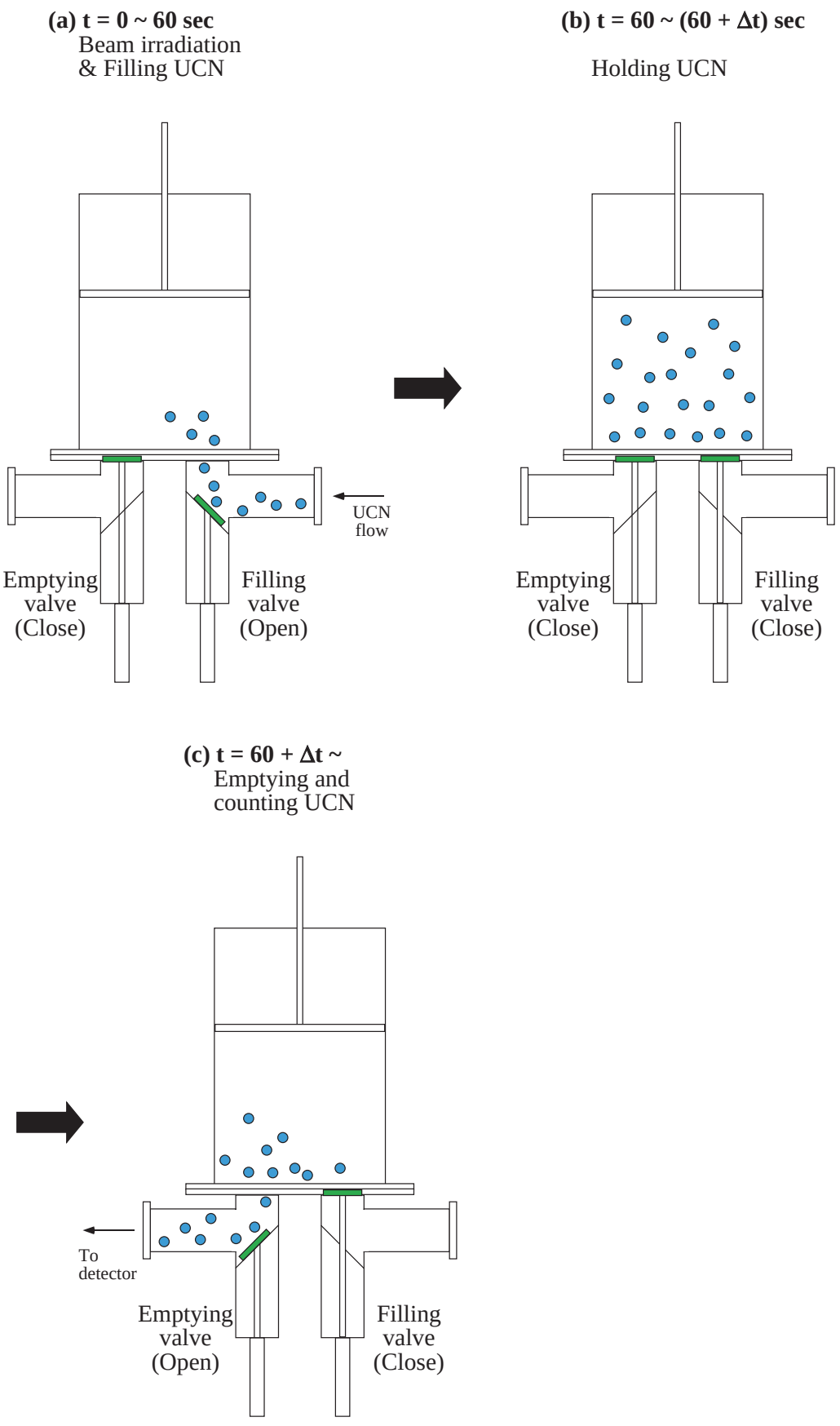

Figure 6.9: Schematic view of the UCN flow in the UCN storage experiment with SUS disk.

6.3.3 Time Spectra with SUS Disk

We set the height of the SUS disk at 91.7, 20, 10 and 5 cm, and measured the time spectra. The sets of UCN storage time were obtained at each height.

h = 91.7 cm

First, we set the height of the SUS disk h to be 91.7 cm. Fig. 6.10 shows the obtained time spectra.

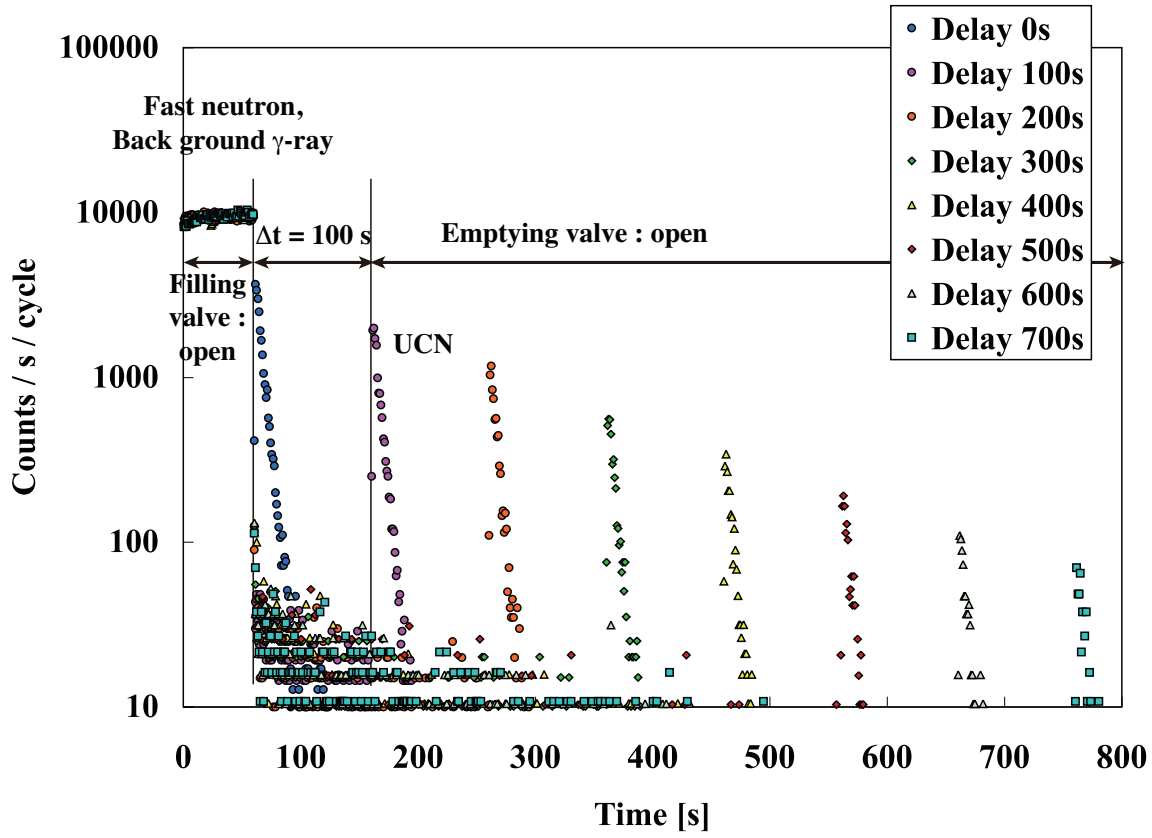

Figure 6.10: Time spectra of UCN storage experiment with the SUS disk. The height of the SUS disk h was 91.7 cm. The delay time Δt were 0, 100, 200, 300, 400, 500, 600 and 700 sec.

The delay time Δt were 0, 100, 200, 300, 400, 500, 600 and 700 sec. After the emptying valve was opened, the UCN counts rose and decayed very quickly. Since there was no annular disk in front of the UCN detector, UCN in the gravity accelerator tube were soon absorbed by the detector. In this case, the typical decay constant was $\sim$ 2 sec.

In Fig. 6.10, UCN less than 100 cps were observed after the beam was stopped before the emptying valve was opened. They were UCN leaking from the UCN storage bottle through the gap of the emptying valve.

Fig. 6.11 shows the total UCN counts as a function of the delay time Δt. The UCN storage

time in the UCN storage bottle was obtained by fitting. The UCN storage time τ was 170 ± 3 sec.

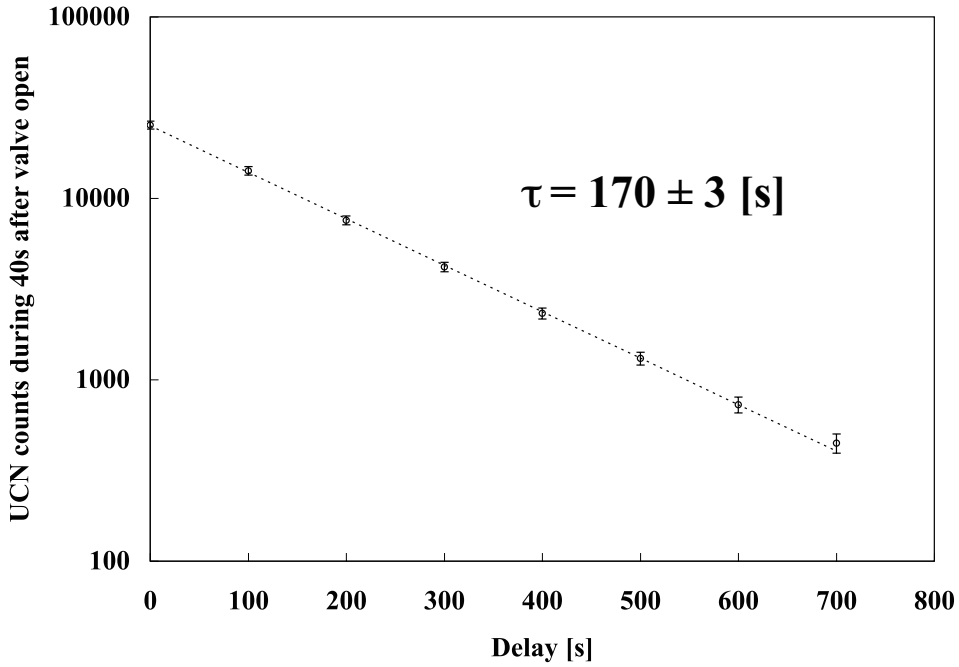

Figure 6.11: The total UCN counts as a function of the delay time Δt. The height of the SUS disk h was 91.7 cm.

h = 20 cm

We changed the height of the SUS disk from 91.7 cm to 20 cm and measured the time spectra. The obtained time spectra are shown in Fig. 6.12. And the total UCN counts as a function of the delay time are shown in Fig. 6.13.

Fig. 6.13 shows that the time dependence of the total UCN counts in the bottle can be represented by two exponential components. The short time constant, τ_1, was 59^{+11}_{-8} sec. The long time constant, τ_2, was 145^{+15}_{-12} sec.

The energy of UCN ranges 0 to $E_c = 75$ neV at the bottom of the UCN storage bottle. In this case, the height of the SUS disk was 20 cm. UCN with an energy larger than 20 neV can be reflected on the surface of the SUS disk. Since most of the reflections are specular reflections, UCN reflected on the surface of the SUS disk are expected to go back and forth between the bottom and the top of the bottle. On the other hand, UCN reflected on the side surface go back and forth in a horizontal direction. The mean free paths of these two cases are almost same. Those values are about 20 cm.

If we assume all surfaces have a same wall loss probability, the UCN storage time of the bottle has only one component because the mean free paths are almost same. However, the surface of the SUS disk is considered to have a larger wall loss probability than the side surface

because the baking temperature at the SUS disk was low. So, UCN reflected by the SUS disk are lost more quickly than UCN moving in a horizontal direction.

As a conclusion, it is suggested that the short component consists of the UCN reflected on the top surface, and the long component consists of the UCN reflected on the side surface or UCN with an energy lower than 20 neV.

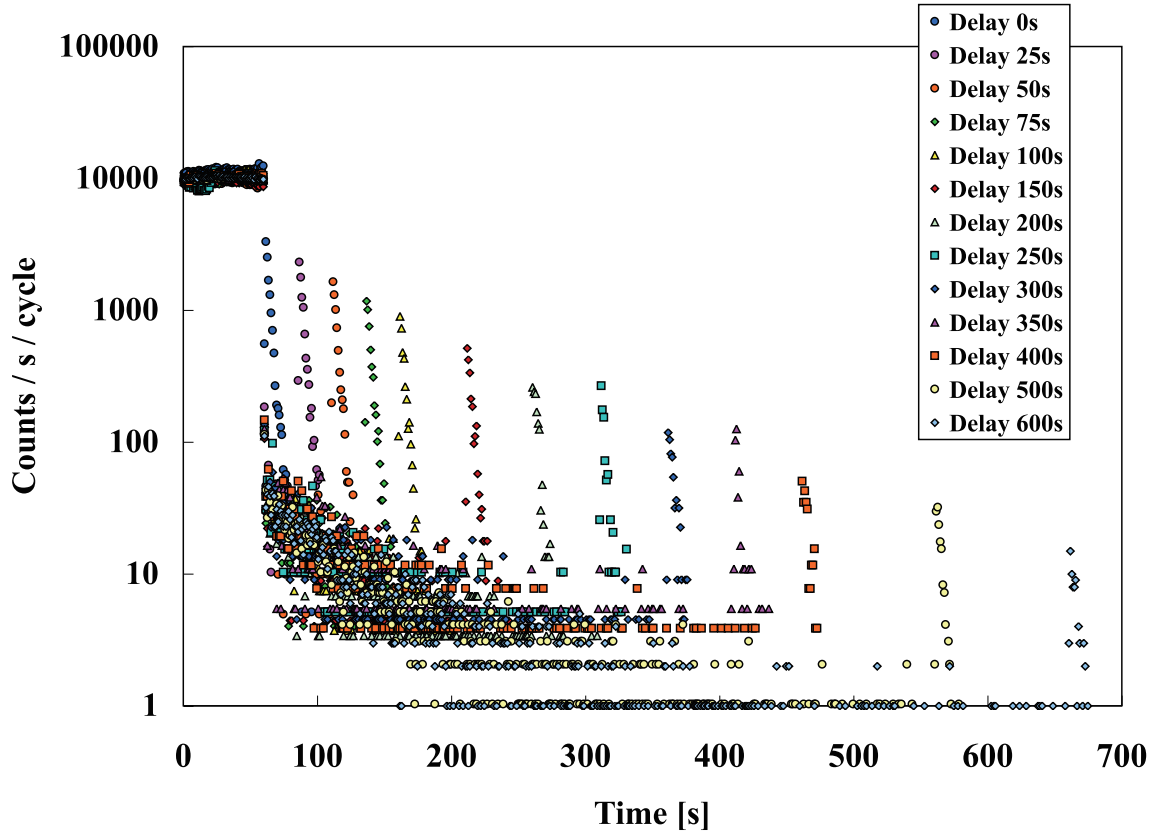

Figure 6.12: Time spectra of UCN storage experiment with the SUS disk. The height of the SUS disk h was 20 cm. The delay time Δt were 0, 25, 50, 75, 100, 150, 200, 250, 300, 350, 400, 500 and 600 sec.

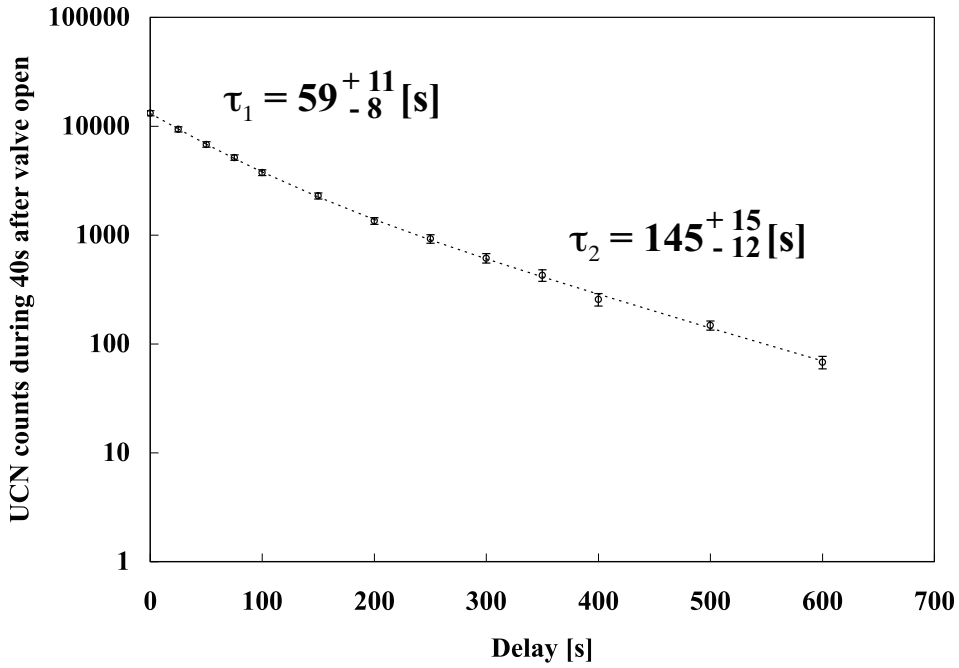

Figure 6.13: The total UCN counts as a function of the delay time Δt. The height of the SUS disk h was 20 cm.

h = 10 cm

Then, we changed the height from 20 cm to 10 cm. The obtained time spectra are shown in Fig. 6.14. The total UCN counts as a function of the delay time are shown in Fig. 6.15. The short time constant, τ_1, was $39.1^{+3.0}_{-2.6}$ sec. The long time constant, τ_2, was 150^{+21}_{-17} sec. τ_1 was smaller than that of 20 cm height. UCN reflected on the surface of the SUS disk mainly go back and forth between the surface of the bottom and the surface of the top disk because most of the UCN reflections are specular reflections. The mean free path of such UCN is almost same as the height h. Therefore, as the height h becomes smaller, the short component τ_1 becomes shorter.

On the other hand, the long component τ_2 is considered to be determined by UCN reflected on the side surface. UCN reflected on the side surface go back and forth in a horizontal direction. The mean free path of such UCN is determined by the diameter of the bottle, i.e. $D = 20.6$ cm. This value is not affected by the height change. Therefore, the long component τ_2 did not change so largely.

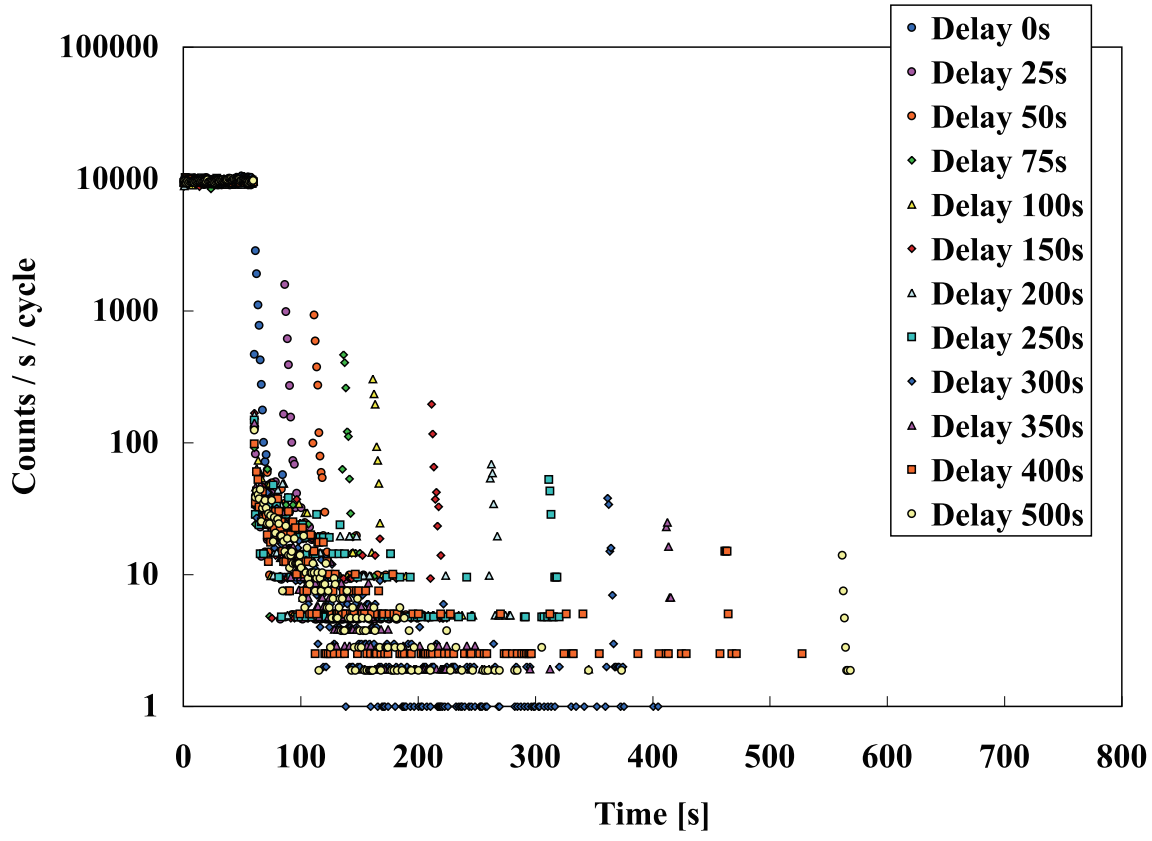

Figure 6.14: Time spectra of UCN storage experiment with the SUS disk. The height of the SUS disk h was 10 cm. The delay time Δt were 0, 25, 50, 75, 100, 150, 200, 250, 300, 350, 400 and 500 sec.

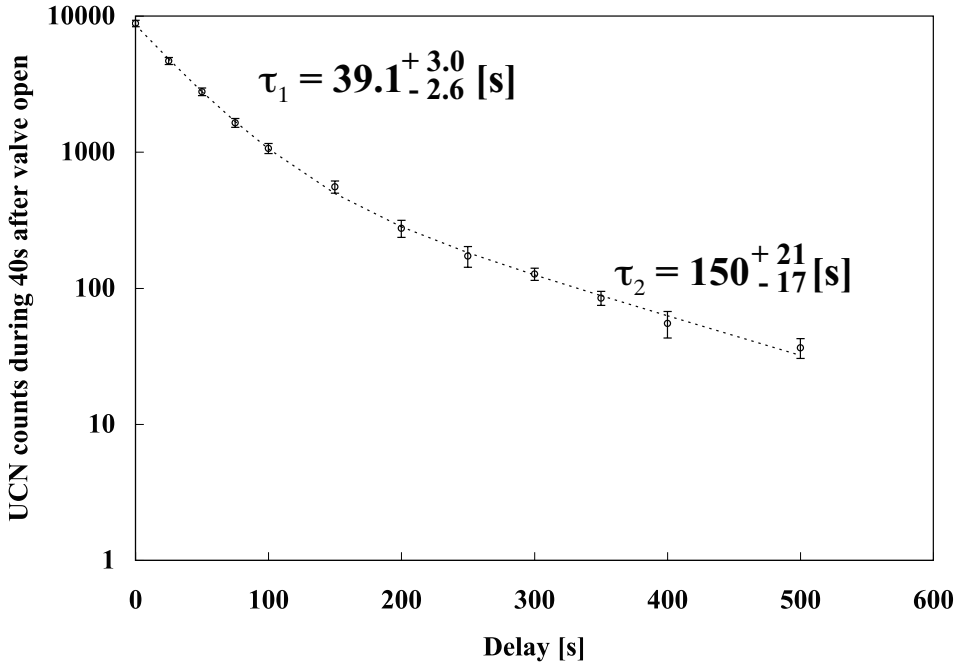

Figure 6.15: The total UCN counts as a function of the delay time Δt. The height of the SUS disk h was 10 cm.

h = 5 cm

Finally, we measured the UCN time spectra at a height of 5 cm. The obtained time spectra are shown in Fig. 6.16. The total UCN counts as a function of the delay time are shown in Fig. 6.17.

The short time constant, τ_1, was $21.2^{+1.8}_{-1.5}$ sec. τ_1 became shorter as the height h of the SUS disk became lower.

The long time constant, τ_2, was 106^{+18}_{-14} sec. τ_2 became shorter than the previous cases. Although τ_2 is mainly influenced by UCN reflected on the side surface, some of them are reflected diffusely with a diffuse reflection probability f. By Geant4-UCN Monte Carlo simulation, the value of f in the UCN source was determined to be (0.057 ± 0.021) (see Chapter 7). The ECB(Electro-Chemical Bufffing) was applied on the inner surface of the UCN storage bottle as well as the UCN source. It is expected that the surface of the UCN storage bottle has same or near diffuse reflection probability f. If the bottle surface has some diffuse reflection probability, some of UCN are reflected diffusely and then reflected on the surface of the SUS disk. Therefore, if the height h is enough low, the long component τ_2 becomes shorter.

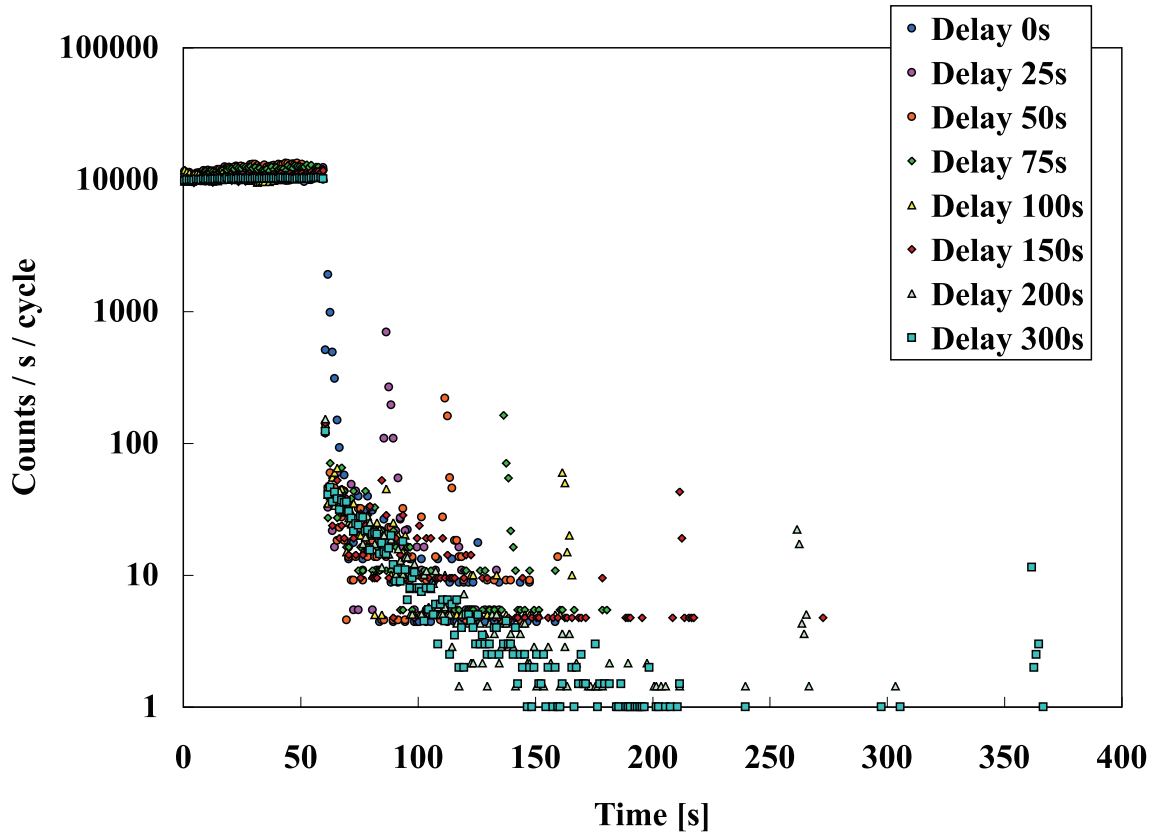

Figure 6.16: Time spectra of UCN storage experiment with the SUS disk. The height of the SUS disk h was 5 cm. The delay time Δt were 0, 25, 50, 75, 100, 150, 200 and 300 sec.

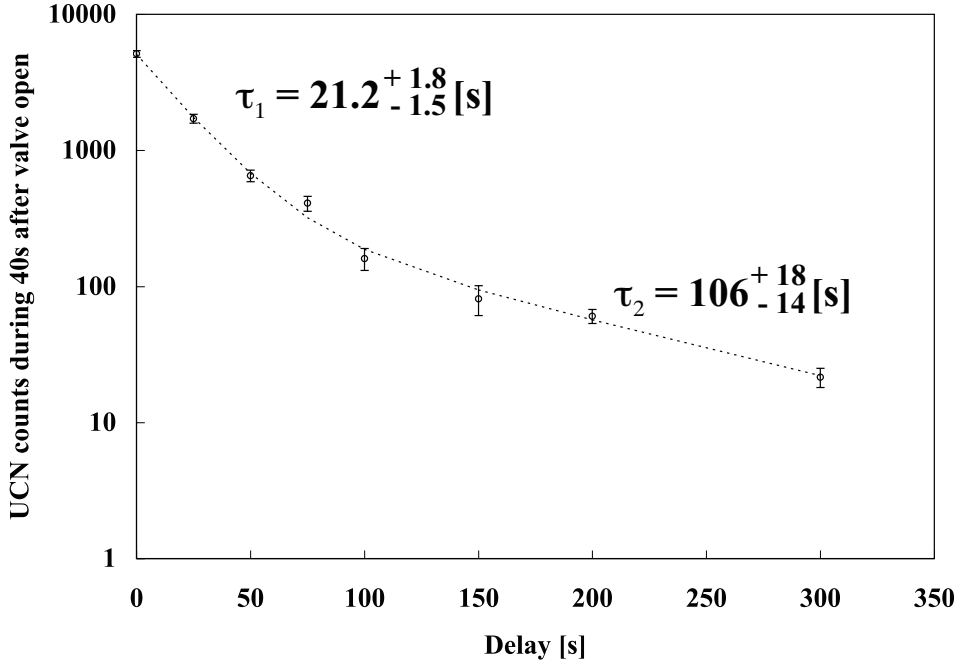

Figure 6.17: The total UCN counts as a function of the delay time Δt. The height of the SUS disk h was 5 cm.

6.3.4 Wall Loss Estimation

Table 6.1 shows the fitting results of the inverse of the decay constants, $1/\tau_1$ and $1/\tau_2$ at each height.

Height h [cm]	$1/h$ [cm^{-1}]	$1/\tau_1$ [s^{-1}]	$1/\tau_2$ [s^{-1}]
91.7	0.011	—	$(5.90 \pm 0.12) \times 10^{-3}$
20	0.05	$(1.69 \pm 0.26) \times 10^{-2}$	$(6.88 \pm 0.64) \times 10^{-3}$
10	0.10	$(2.56 \pm 0.19) \times 10^{-2}$	$(6.68 \pm 0.84) \times 10^{-3}$
5	0.20	$(4.71 \pm 0.36) \times 10^{-2}$	$(9.40 \pm 1.39) \times 10^{-3}$

Table 6.1: Fitting results of the inverse of the decay constants, $1/\tau_1$ and $1/\tau_2$ at each height.

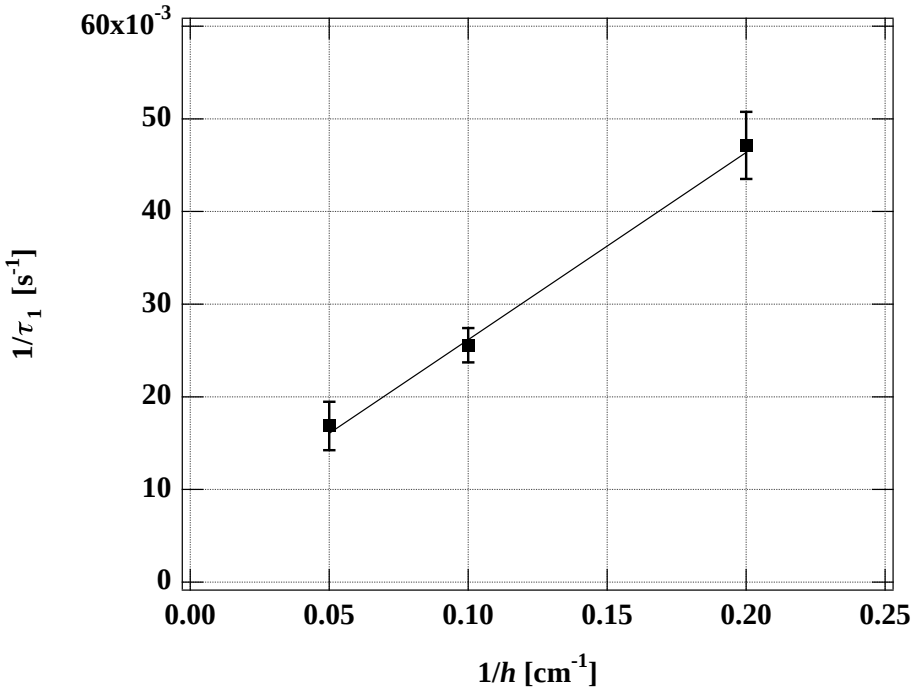

Figure 6.18: Plot of $1/\tau_1$ as a function of $1/h$. The fitting curve is $1/\tau_1 = a(1/h) + b$. The obtained value of a was 0.202 ± 0.030, and b was 0.0060 ± 0.0033.

We used (6.9) $\sim$ (6.11) to estimate the wall loss probability per bounce $\overline{\mu}$ in the UCN storage bottle. First, we did fitting of $1/\tau_1$ by a function (6.9) and determined the parameter a and b. Fig. 6.18 is a plot of the fitting results of $1/\tau_1$. $1/\tau_1$ is shown as a function of the inverse of the height h. The fitting curve by (6.9) is also shown in Fig. 6.18. The obtained value of a and b were as follows.

$$a = 0.202 \pm 0.030 \quad (6.12)$$

$$b = 0.0060 \pm 0.0033 \quad (6.13)$$

Here, a and b are given by

$$a = \frac{\overline{\mu}_1\overline{v}}{4} + \frac{\overline{\mu}_2\overline{v}}{4} + \frac{2\overline{v}\Delta S}{\pi D^2} \tag{6.14}$$

$$b = \frac{\overline{\mu}_2\overline{v}}{D} + \frac{1}{\tau_{He}} + \frac{1}{\tau_\beta} \tag{6.15}$$

where $D = 20.6$ cm, $\Delta S = 0.118$ cm^2, $\tau_{He} = 1246$ sec and $\tau_\beta = 885.7 \pm 0.8$ sec. If we assume the UCN energy spectrum is proportional to $\sqrt{E}$ and $E_c = 75$ neV at the bottom, the averaged velocity is $\overline{v} = 2.8$ m/s. Then, we obtained

$$\frac{\overline{\mu}_1 + \overline{\mu}_2}{2} = (1.07 \pm 0.21) \times 10^{-3} \tag{6.16}$$

$$\overline{\mu}_2 = (3.0 \pm 2.4) \times 10^{-4} \tag{6.17}$$

$$\overline{\mu}_1 = (1.84 \pm 0.48) \times 10^{-3} \tag{6.18}$$

where $\overline{\mu}_1$ is the effective wall loss probability per bounce on the top surface. $\overline{\mu}_2$ is that of the side and the bottom surfaces. These results show the wall loss on the top surface is much larger than the wall loss on the side and the bottom surfaces. The ratio of them was $\overline{\mu}_1/\overline{\mu}_2 = 6.1$. It is suggested that the UCN decay of the short component is occupied mainly by the wall loss on the top surface.

We first assumed that the bottom surface and the side surface had a same wall loss probability $\overline{\mu}_2$, and only the top surface had a different wall loss probability $\overline{\mu}_1$. Was this assumption correct ? The value of b obtained above is same as $1/\tau_2$ at $h = 91.7$ cm. $1/\tau_2$ at $h = 91.7$ cm was $(5.90 \pm 0.12) \times 10^{-3}$ s^{-1} (see Table 6.1). At $h = 91.7$ cm, the wall loss on the top surface does not contributed to the total loss rate $1/\tau_2$ because the UCN critical energy E_c is 75 neV. $1/\tau_2$ at $h = 91.7$ cm includes only the wall loss on the side and bottom surfaces. If the wall loss on the bottom surface is much larger than that of the side surface, b is not same as the value of $1/\tau_2$ at $h = 91.7$ cm. Therefore, the first assumption is considered to be correct.

As a conclusion of the UCN storage experiment with SUS disk, the following things are suggested.

1. The wall loss on the top surface was estimated to be 6.1 times larger than that of the side and bottom surfaces.

2. The short components are mainly occupied by the UCN reflecting on the top surface.

3. The long components are mainly occupied by the UCN reflecting on the side and bottom surfaces.

6.4 UCN Storage Experiment with Polyethylene Disk

After the UCN storage experiment with the SUS disk, we removed the SUS disk and attached the Polyethylene disk to the piston. Then, we measured the energy spectrum of UCN extracted from the He-II superthermal UCN source.

Polyethylene is known as a good UCN absorber because it has a negative Fermi potential (-8.54 neV). If the Polyethylene disk is at a height of h, UCN with an energy above $m_n gh$ are absorbed by the Polyethylene disk. On the other hand, UCN with an energy below $m_n gh$ survives. Therefore, we can extract UCN with an energy below $m_n gh$. If we change the height h between 0 to 90 cm and measure the UCN counts at each height, we obtain a curve of UCN with an energy between 0 to $m_n gh$ as a function of h. Then, we can obtain the UCN energy spectrum by differentiating the obtained curve with respect to h.

In this section, we omit the word "Polyethylene" to "P.E.".

6.4.1 Sequence of Measurement with P.E. Disk

Fig. 6.19 shows the time diagram for the UCN storage experiment with the P.E. disk. We irradiate a proton beam for 60 sec. During the beam irradiation, the filling valve is closing. The filling valve is opened right after the beam is stopped. Then, the bottle is filled with UCN from the UCN source. The Filling valve is kept opening for 20 sec. In other words, the filling time of UCN is 20 sec. After the filling time of 20 sec, the filling valve is closed. UCN are confined in the UCN storage bottle for a delay time Δt. After the delay time Δt, the emptying valve is opened. UCN are extracted from the bottle, and they go into the UCN detector through the gravity accelerator tube and are observed. The UCN valve at the experimental port is opening in this measurement. Fig. 6.20 shows the schematic view of the UCN flow in this measurement.

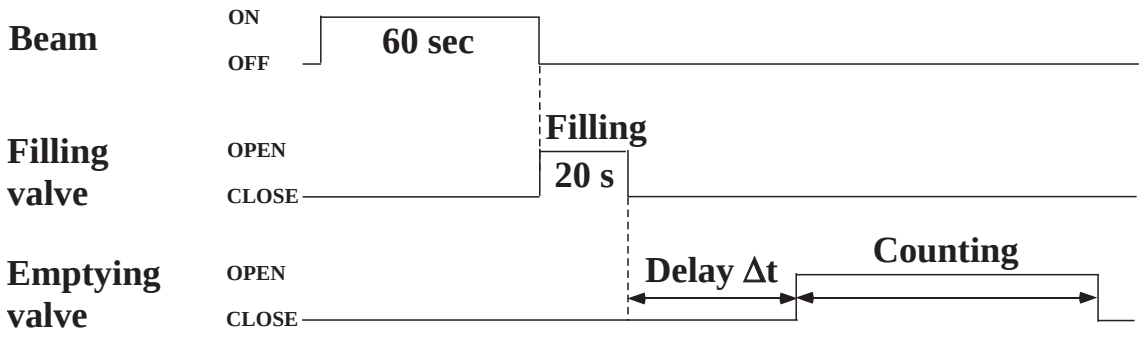

Figure 6.19: Time diagram of the measurement with the P.E. disk.

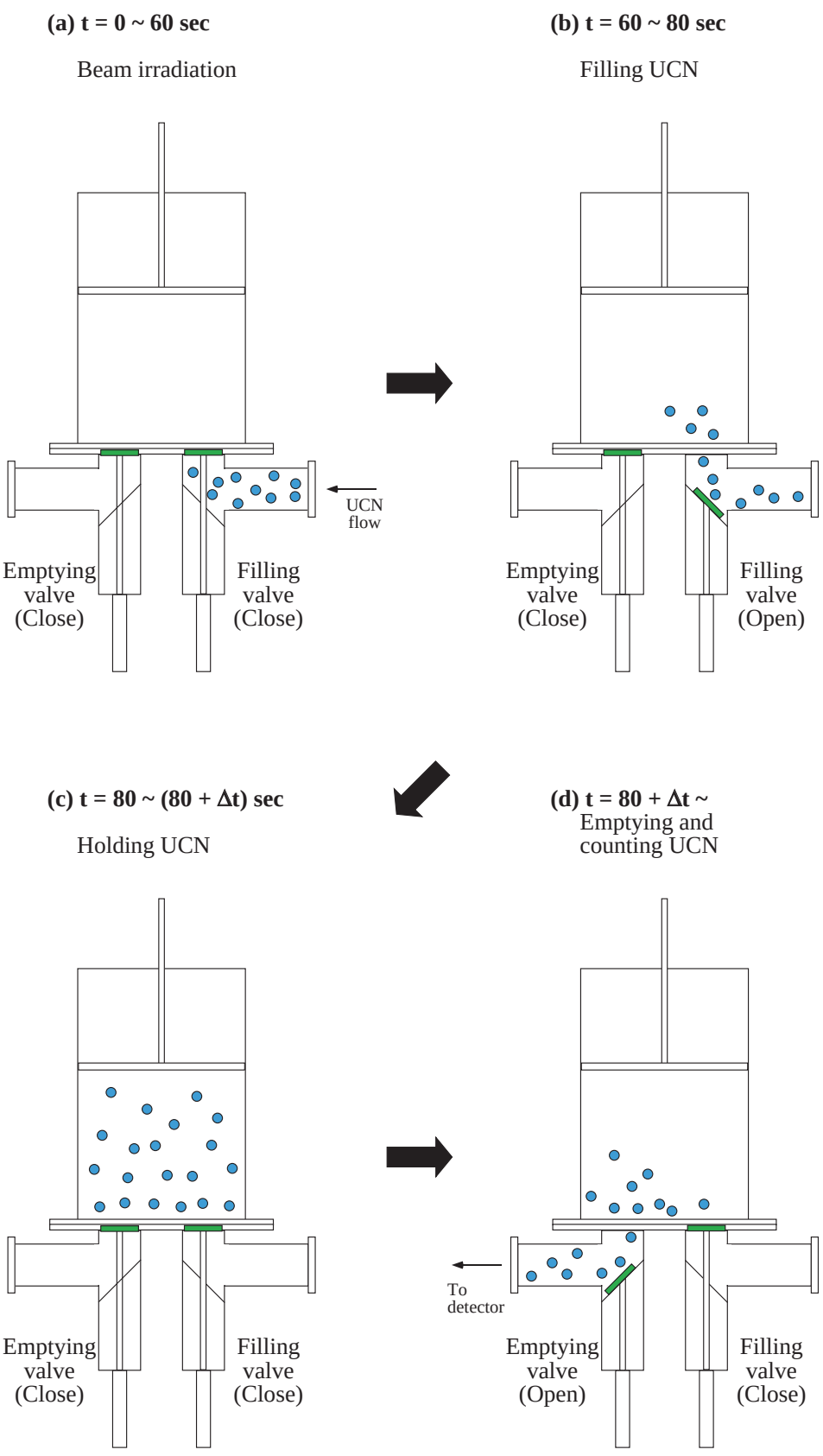

Figure 6.20: Scheme of the UCN flow in the UCN storage experiment with the P.E. disk.

6.4.2 Typical Time Spectra with P.E. Disk

We measured the time spectra of UCN in the UCN storage bottle with the P.E. disk at a height of 84.5 cm, 80 cm, 75 cm, ..., 10 cm and 5 cm. Here, the time spectra obtained at a height of 84.5 cm and 5 cm are shown as the typical samples. The rest of the time spectra are shown in the Appendix.

h = 84.5 cm

First, we set the height of the P.E. disk h to be 84.5 cm. A proton beam with a power of 400 W (392MeV $\times$ 1 μA) was irradiated for 60 sec. The filling / emptying valves were controlled as shown in Fig. 6.19 and Fig. 6.20. Then, we obtained the time spectra at this height.

The obtained time spectra are shown in Fig. 6.21. The time dependence of the total UCN counts after the emptying valve was opened is shown in Fig. 6.22. Fitting this curve, the UCN storage time in the UCN storage bottle was obtained to be 165^{+5}_{-4} sec. The total UCN counts at each delay time are shown in Table 6.2.

Delay Δt [s]	total UCN counts
0	11457 $\pm$ 570
100	5672 $\pm$ 323
200	3262 $\pm$ 198
300	1763 $\pm$ 117
400	977 $\pm$ 76
500	564 $\pm$ 53

Table 6.2: The total UCN counts obtained at each delay time. The height of the P.E. disk was 84.5 cm.

When the P.E. disk was installed at the higher position, the time dependence of the total UCN counts was represented by one exponential component. On the other hand, the time dependence of the total UCN counts at the lower position is represented by two exponential components as shown later. Similarly to the case with the SUS disk, the short component is supposed to be composed of the UCN with an energy larger than $m_n gh$ and the long component is composed of the UCN with an energy smaller than $m_n gh$. If the position of the P.E. disk is higher, the number of UCN that collide against the P.E. disk is less. Therefore, the decay curve obtained at a height of 84.5 cm can be represented by only one component.

h = 5 cm

We changed the height of the P.E. disk from 84.5 cm to 80, 75, 70, ... 10 cm and 5 cm, by 5 cm skip. The height of 5 cm was the lowest height among we measured. The time spectra

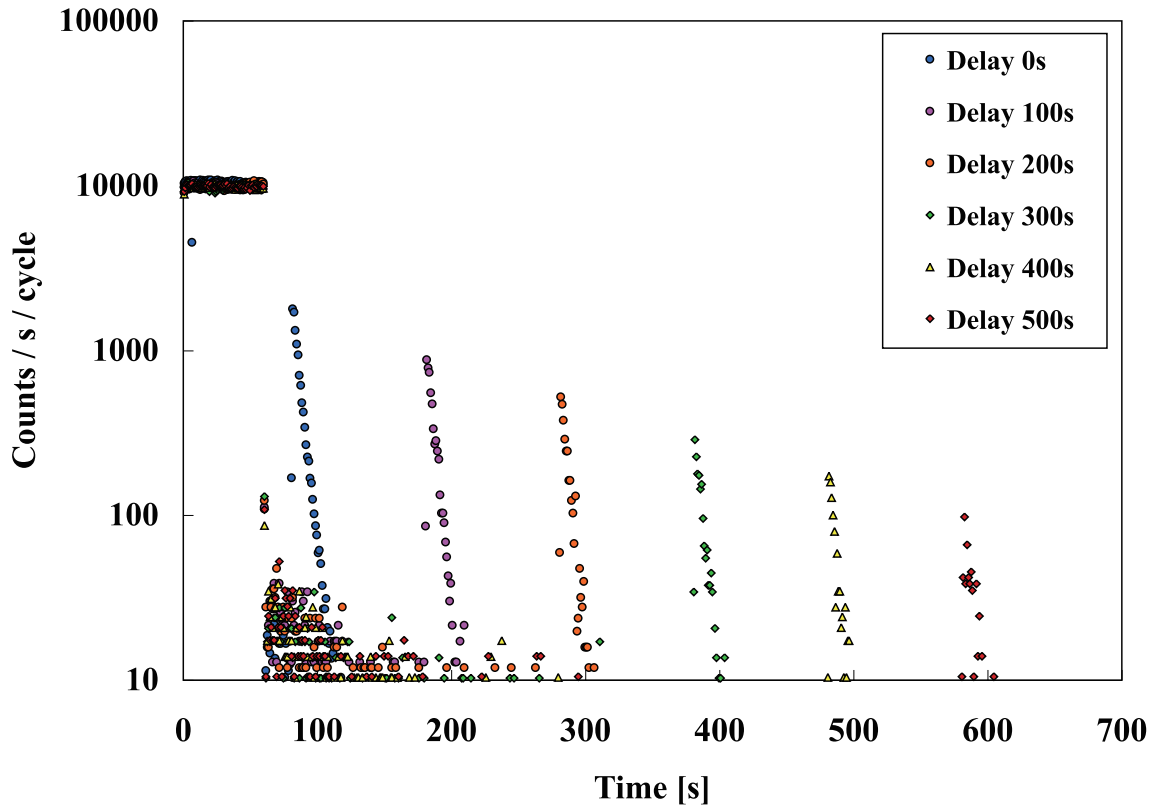

Figure 6.21: Time spectra of the UCN storage experiment with the P.E. disk. A proton beam with a power of 400 W was irradiated for 60 sec. The height of the P.E. disk was 84.5 cm. The delay time Δt were 0, 100, 200, 300, 400 and 500 sec.

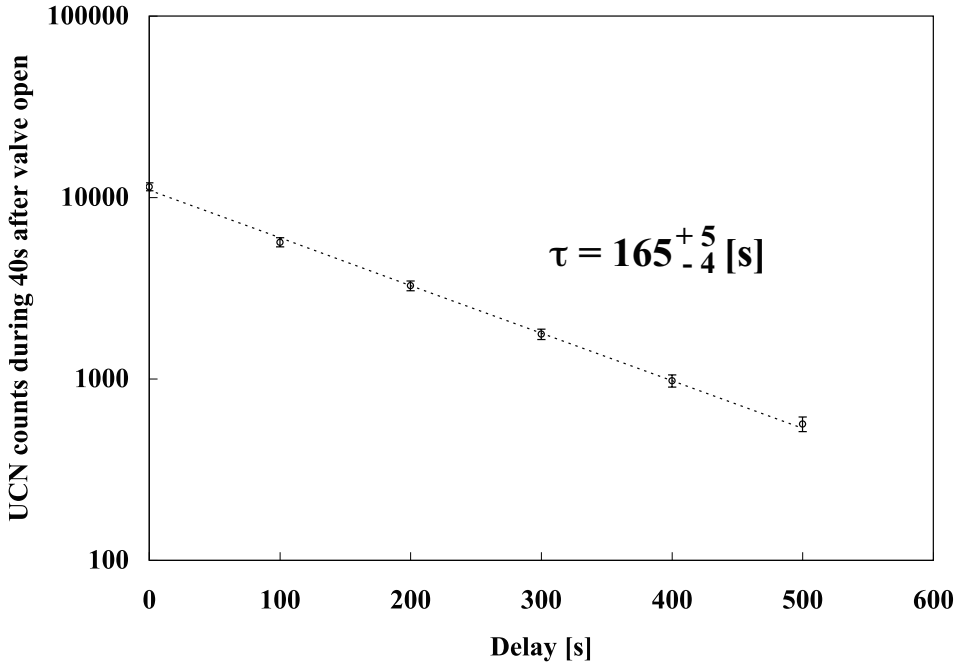

Figure 6.22: The total UCN counts as a function of the delay time. The height of the disk h was 84.5 cm. The UCN storage time was 165^{+5}_{-4} sec.

obtained at a height of 5 cm are shown in Fig. 6.23. The time dependence of the total UCN counts is shown in Fig. 6.24. The total UCN counts at each delay time are shown in Table 6.3.

At this height, the time dependence of the total UCN counts has two exponential components. It is suggested that the short component consists of UCN with an energy above $m_n gh$. Such UCN collide against the P.E. disk and they are soon lost by absorption. Therefore, its UCN storage time is short. The UCN storage time of the short component τ_1 was 18^{+6}_{-3} sec in this case. On the other hand, the long component consists of UCN with an energy below $m_n gh$. Those UCN can not collide against the P.E. disk because of their low energy. They are lost by the wall loss on the side surface and the bottom surface. At this height, the UCN storage time of the long component τ_2 was 117^{+28}_{-19} sec.

We have also measured the time spectra at the other heights. Those time spectra and the time dependence of the total UCN counts in the bottle are shown in the Appendix.

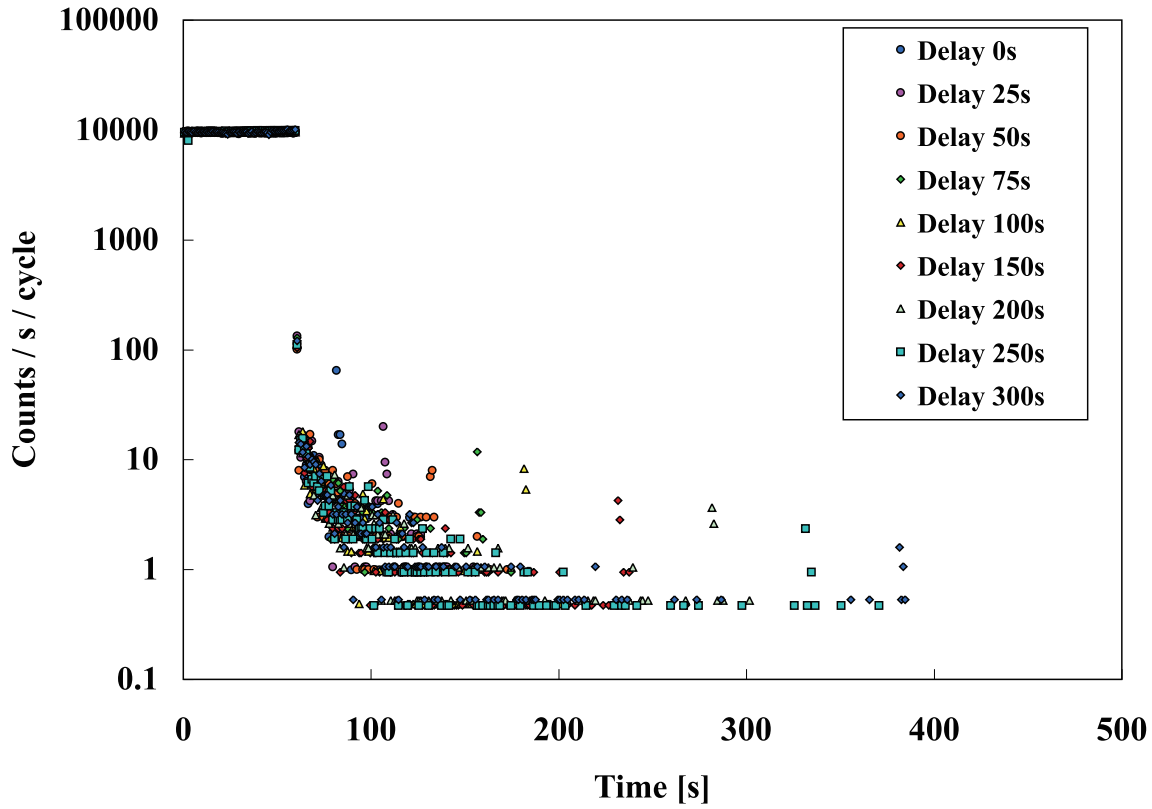

Figure 6.23: Time spectra of the UCN storage experiment with the P.E. disk. The height of the P.E. disk was 5 cm. The delay time Δt were 0, 25, 50, 75, 100, 150, 200, 250 and 300 sec.

Delay Δt [s]	total UCN counts
0	183 ± 16
25	70 ± 9
50	31 ± 6
75	27 ± 4
100	18 ± 3
150	10.0 ± 2.2
200	7.9 ± 2.1
250	4.7 ± 1.5
300	3.7 ± 1.4

Table 6.3: The total UCN counts obtained at each delay time. The height of the P.E. disk was 5 cm.

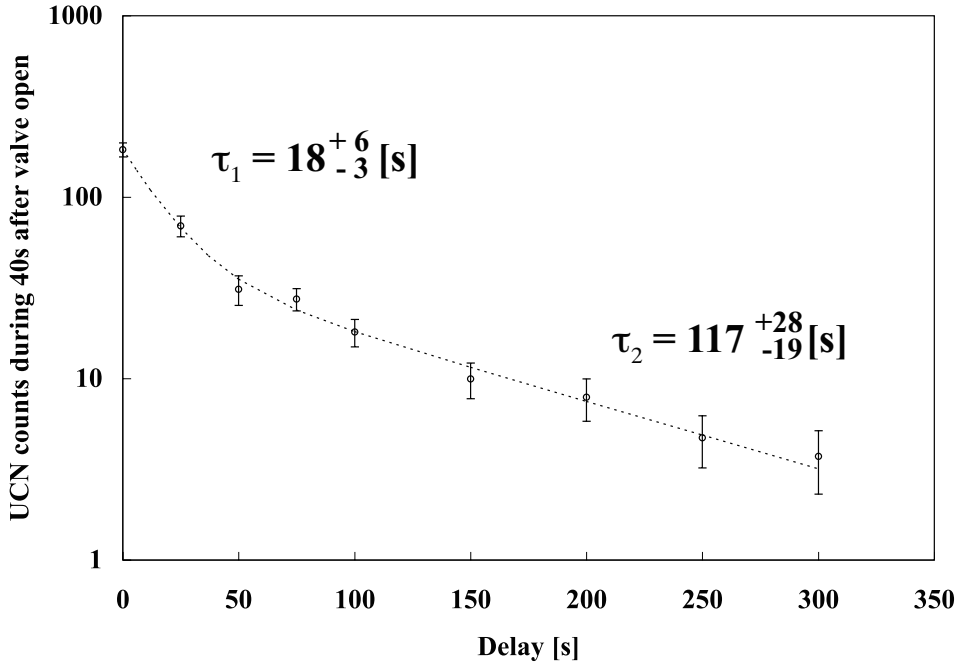

Figure 6.24: The total UCN counts as a function of the delay time. The height of the disk h was 5 cm. The UCN storage time of the short component was 18^{+6}_{-3} sec. The UCN storage time of the long component was 117^{+28}_{-19} sec.

6.5 UCN Energy Spectrum

6.5.1 Energy Spectrum right after Filling of UCN

Fig. 6.25 shows the time dependences of the total UCN counts at each height obtained by the UCN storage experiment. The fitting results of the obtained curves are shown in Table 6.4. We used the following function as a fitting function.

$$f(t) = A_1 \exp(-t/\tau_1) + A_2 \exp(-t/\tau_2) \tag{6.19}$$

A_1 and τ_1 are the amplitude and the UCN storage time of the short component. A_2 and τ_2 are the amplitude and the UCN storage time of the long component. Since the decay curves above 70 cm have only one exponential component, they were fitted by one exponential function. The decay curves at a height of 65, 55, 45, 35 and 25 cm have two exponential components. However, these curves do not have enough data points for the fitting. In these case, we used an arithmetic average of the UCN storage time obtained at the previous and the next height for τ_1 and τ_2.

Height h [cm]	A_1	$1/\tau_1$ [s^{-1}]	A_2	$1/\tau_2$ [s^{-1}]
84.5	—	—	10967 ± 442	$(6.05 \pm 0.17) \times 10^{-3}$
80	—	—	10288 ± 269	$(6.12 \pm 0.14) \times 10^{-3}$
75	—	—	9409 ± 433	$(6.14 \pm 0.42) \times 10^{-3}$
70	—	—	8726 ± 366	$(6.14 \pm 0.19) \times 10^{-3}$
65	1255 ± 604	0.0488 (fixed)	7590 ± 295	6.01×10^{-3} (fixed)
60	1631 ± 532	0.0488 ± 0.0296	6349 ± 399	$(5.87 \pm 0.33) \times 10^{-3}$
55	1332 ± 458	0.0594 (fixed)	5488 ± 218	5.90×10^{-3} (fixed)
50	1462 ± 423	0.0700 ± 0.0497	4539 ± 260	$(5.92 \pm 0.24) \times 10^{-3}$
45	1240 ± 367	0.0586 (fixed)	3853 ± 172	5.81×10^{-3} (fixed)
40	1469 ± 324	0.0473 ± 0.0203	3055 ± 243	$(5.69 \pm 0.35) \times 10^{-3}$
35	1446 ± 275	0.0477 (fixed)	2185 ± 125	5.91×10^{-3} (fixed)
30	849 ± 181	0.0482 ± 0.0200	1706 ± 108	$(6.13 \pm 0.26) \times 10^{-3}$
25	690 ± 169	0.0727 (fixed)	1213 ± 72	6.31×10^{-3} (fixed)
20	820 ± 124	0.0973 ± 0.0274	770 ± 63	$(6.49 \pm 0.50) \times 10^{-3}$
15	334 ± 83	0.0783 ± 0.0368	449 ± 38	$(6.85 \pm 0.37) \times 10^{-3}$
10	314 ± 63	0.1728 ± 0.0631	194 ± 22	$(6.84 \pm 0.65) \times 10^{-3}$
5	142 ± 19	0.0568 ± 0.0138	42 ± 12	$(8.57 \pm 1.66) \times 10^{-3}$

Table 6.4: Fitting results of the time dependences of the total UCN counts at each height. At a height of 65, 55, 45, 35 and 25 cm, $1/\tau_1$ and $1/\tau_2$ are fixed value. They are the arithmetic averages of the UCN storage time obtained at the previous and the next height.

It is expected that each long component consists of the UCN with an energy below $m_n gh$. Therefore, the amplitude of the long component A_2 represents the total UCN counts with an

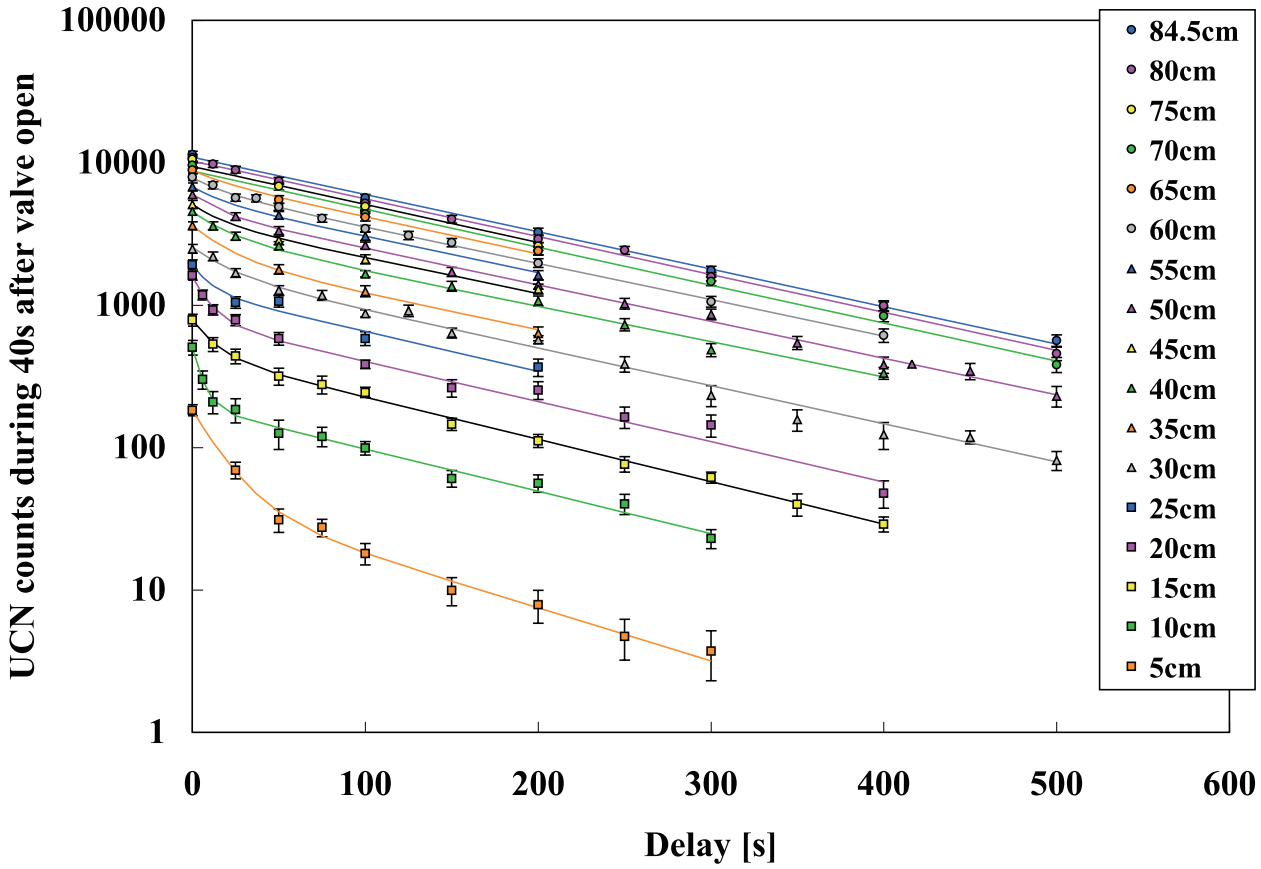

Figure 6.25: Time dependence of the total UCN counts at each heights. The height of the P.E. disk are 84.5, 80, 75, 70, ..., 15, 10 and 5 cm, respectively. The solid curves are the fitting curves. The fitting results is shown in Table 6.4.

energy between 0 to $m_n gh$. Using the UCN energy spectrum $\rho(E)$, A_2 is given by

$$A_2 = \int_0^{m_n gh} \rho(E) dE \ . \tag{6.20}$$

Here, $\rho(E)$ is the UCN energy spectrum right after the filling valve was closed.

The height dependence of the amplitude of the long component A_2 is shown in Fig. 6.26. Each point at a height of h represents the total UCN counts integrated between 0 to $m_n gh$.

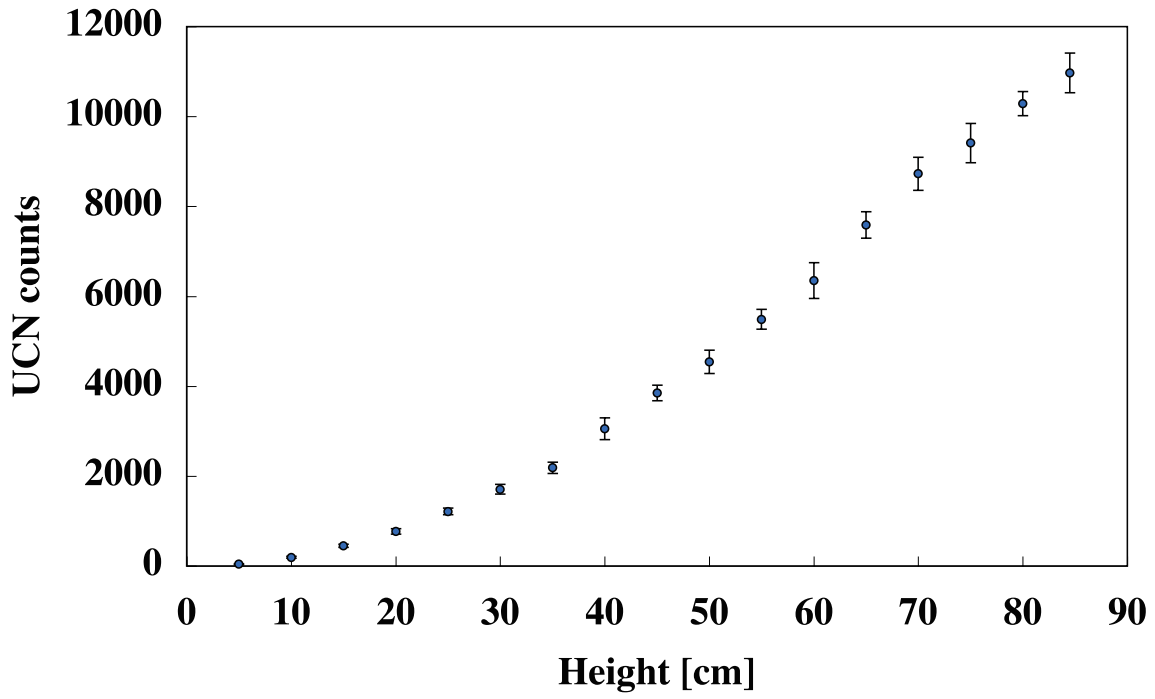

Figure 6.26: Height dependence of the amplitude of the long components A_2.

By differentiating this curve with respect to the height h, we obtained the UCN energy spectrum in the UCN storage bottle right after the filling of UCN. To obtain a smooth curve, we used three types of differentiation as following.

(1) Differentiation of 2 adjacent points.

$$\frac{dN}{dE} = \frac{N_{i+1} - N_i}{m_n g(h_{i+1} - h_i)}$$

(2) Differentiation of 2 adjacent points with skipping 1 point between them.

$$\frac{dN}{dE} = \frac{N_{i+2} - N_i}{m_n g(h_{i+2} - h_i)}$$

(3) Differentiation of 2 adjacent points with skipping 2 point between them.

$$\frac{dN}{dE} = \frac{N_{i+3} - N_i}{m_n g(h_{i+3} - h_i)}$$

where h_i is the ith height and N_i is the total UCN counts obtained at a height of h_i.

The obtained three types of the UCN spectra are shown in Fig. 6.27. The differentiated curve by the third method is also shown in Fig. 6.28.

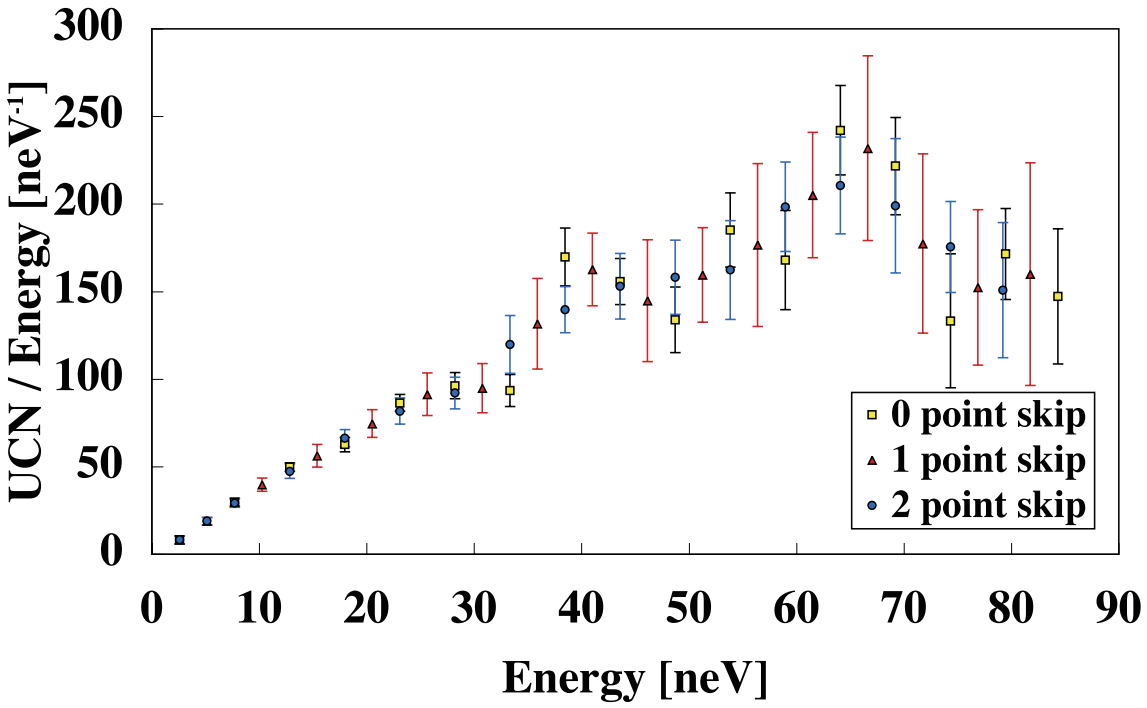

Figure 6.27: UCN energy spectra obtained by differentiating the curve shown in Fig. 6.26.

When UCN are produced in superfluid helium, the UCN phase space distribution is considered to be uniform theoretically. In such case, the UCN energy spectrum is proportional to $\sqrt{E}$.

$$\rho_{He-II}(E)dE \propto \sqrt{E}dE \tag{6.21}$$

where $\rho_{He-II}(E)$ is the UCN energy spectrum in the He-II bottle.

In our UCN source, the UCN critical energy E_c is 214 neV, which is same as the Fermi potential of the Ni-P coating covering the He-II bottle. UCN are extracted from the He-II bottle to the UCN storage bottle through the UCN vertical guide and the UCN horizontal guide. The height of the center of the UCN horizontal guide is 127.0 cm from the bottom of the He-II bottle. This height is corresponding to the gravity potential of 130.2 neV. UCN are trapped by the gravity interaction, so the UCN critical energy reduces to 84 neV in the UCN horizontal guide.

The bottom of the UCN storage bottle is 84.8 mm higher from the center of the UCN horizontal guide. This height is corresponding to 8.7 neV. Therefore, the UCN critical energy in the bottle reduces to 75 neV. If there is no UCN loss in the UCN source, the shape of the UCN energy spectrum does not change and is proportional to $\sqrt{E}$ with the critical energy

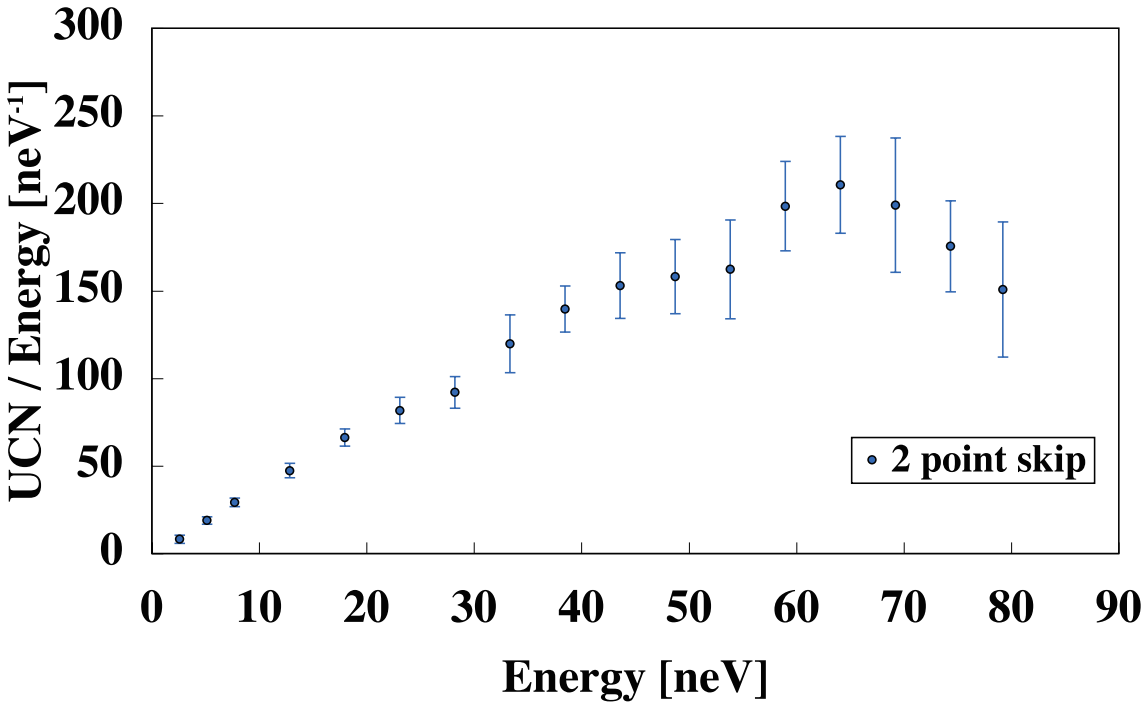

Figure 6.28: One of the UCN energy spectra obtained by differentiating the curve shown in Fig. 6.26. This result was obtained by differentiating with 2 points skip.

of 75 neV. However, the UCN energy spectrum deviates from the original shape $\sqrt{E}$ because the wall loss process is energy dependent. The UCN energy spectra shown in Fig. 6.27 and Fig. 6.28 appear to deviate from $\sqrt{E}$ in the region between 0 to about 70 neV because of such reason.

Fig. 6.27 and Fig. 6.28 appear to show that the peak of the UCN energy spectrum is between 70 to 80 neV. It is consistent with the UCN critical energy of 75 neV. In the region above the UCN critical energy E_c, the UCN energy spectrum drops to 0. This drop is not like a step function, and the intersection of the UCN energy spectrum and the horizontal axis is larger than 80 neV. This is due to the following reasons.

1. Even if a UCN has an energy larger than the Fermi potential V_F of a reflecting surface, it can be reflected on the surface when the incident angle of the UCN is shallow. In such case, the following condition is satisfied.

$$E_{ucn} \sin^2 \theta \leq V_F \tag{6.22}$$

   where E_{ucn} is the kinetic energy of the incident UCN and θ is the incident angle.

2. The UCN critical energy E_{ucn} is calculated with reference to the bottom of the He-II bottle. UCN are also produced in the upper region of the He-II bottle and the height of the He-II bottle is 408 mm. Those UCN could have a kinetic energy larger than the UCN critical energy E_{ucn}.

3. The Fermi potential of He-II is 18.6 neV. UCN is accelerated by the Fermi potential of He-II when it goes out from the He-II bottle.

For these reasons, UCN with an energy larger than the critical energy E_c can be confined in the UCN storage bottle.

6.5.2 Time dependence of UCN Energy Spectrum

Fig. 6.25 shows that the short components decay and vanish by the delay 100 sec. We can calculate the UCN energy spectra after 100 and 200 sec passed, using the UCN counts at each delay time.

Fig. 6.29 shows the height dependence of the total UCN counts at a delay of 0, 100 and 200 sec. By differentiating these curves, the UCN energy spectra after 100 and 200 sec passed were obtained. The obtained UCN energy spectra are shown in Fig. 6.30. The energy spectra shown in Fig. 6.30 were normalized.

The UCN energy spectra after 100 and 200 sec passed did not change from the energy spectrum of the delay 0 sec. It is suggested that the UCN motions of the long components were entirely randomized due to a repeat of the diffuse reflection. And also, the energy dependence of the UCN loss and the position dependence of the wall loss were averaged by the randomized UCN motion.

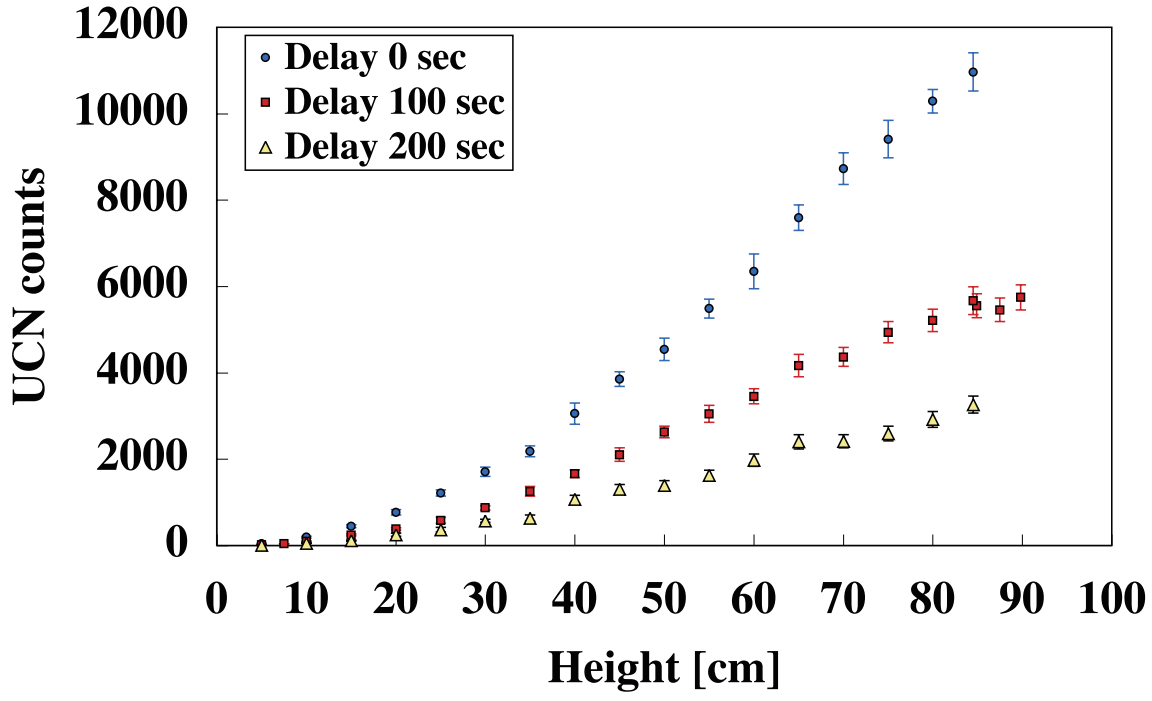

Figure 6.29: Height dependence of the total UCN counts at each delay time. Blue circles are at a delay of 0 sec, same as Fig. 6.26. Red squares are at a delay of 100 sec. Yellow triangles are at a delay of 200 sec.

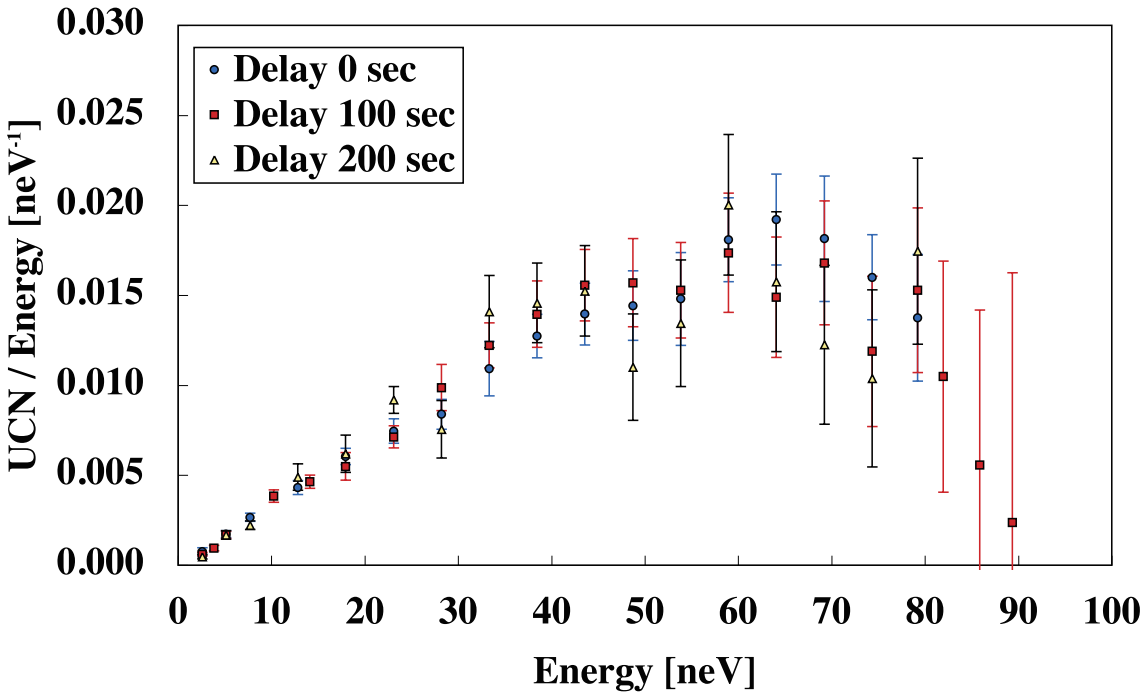

Figure 6.30: UCN energy spectra obtained by differentiating the curves shown in Fig. 6.29. Each spectrum was normalized. The differentiations were done with 2 points skip.

Chapter 7

Geant4 Simulation

7.1 Geometry and Material Settings

In Geant4-UCN code, a geometry of experimental apparatuses is constructed by "UCNDetectorConstruction" class (class is a small package of programing tools in C++) . The information about the experimental apparatuses is written in a source file of this class. The source file name is "UCNDetectorConstruction.cc."

The structures of the He-II bottle, UCN vertical and horizontal guide, UCN valve, Gravity accelerator tube, and UCN detector were written in the source file. Then, the geometry of the UCN source was recostructed in the computer. Fig. 7.1 shows the geometry of the UCN source reconstructed in the computer.

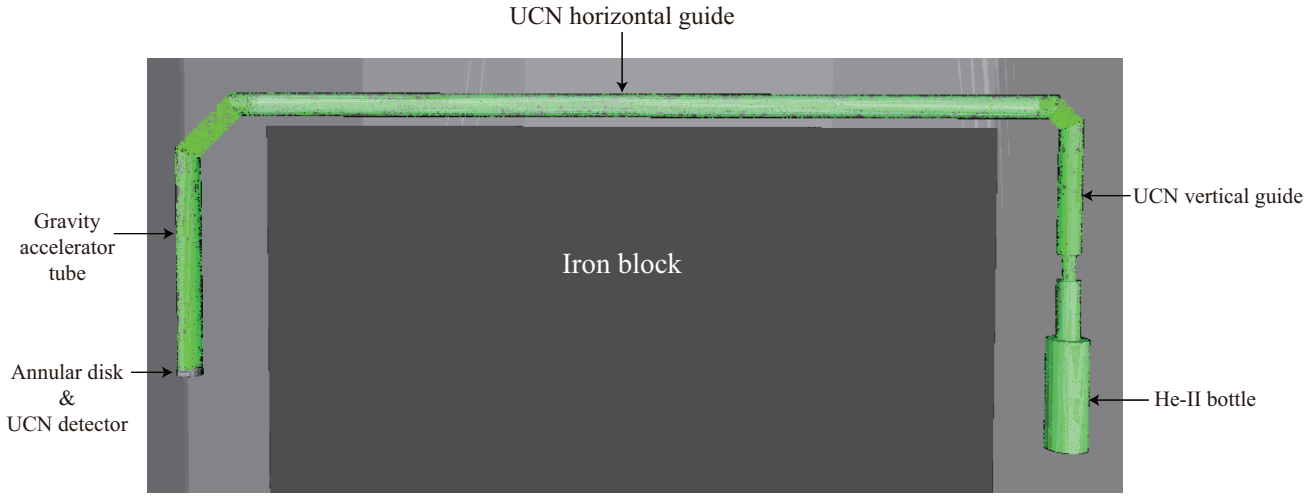

Figure 7.1: Geometry of the UCN source by Geant4-UCN. The green lines in the UCN source are trajectories of some UCN.

The He-II bottle is filled with superfluid helium (He-II). The UCN vertical and horizontal guide are filled with vapor of helium at the saturated vapor pressure. The UCN horizontal guide is coated with Fomblin grease.

The material features like a Fermi potential, a wall loss rate, and a diffuse reflection probability are also reconstructed by UCNDetectorConstrucion class. We have to input the following informations to a material.

1. Fermi potential : V_F
2. Wall loss parameter : η
3. Diffuse reflection probability : f
4. Scattering cross section : σ_s
5. Absorption cross section : σ_a

For example, the He-II bottle is made of aluminum with electroless nickel plating (Ni-P coating). In Geant4-UCN, the Ni-P coating on the He-II bottle was named "NickelMaterial". The parameters of the "NickelMaterial" are as follows.

$$V_F = 214 \text{ [neV]}, \tag{7.1}$$
$$\eta = 4.3 \times 10^{-4}, \tag{7.2}$$
$$f = 0.057, \tag{7.3}$$
$$\sigma_s = 15.8 \text{ [barn]}, \tag{7.4}$$
$$\sigma_a = 3.8 \text{ [barn]}, \tag{7.5}$$

The thickness of the Ni-P coating is $10 \sim 15$ μm. Since this value is much longer than a wavelength of UCN (typically 500 Å or 50 nm), aluminum under the Ni-P coating can be neglected.

The UCN vertical and horizontal guide, UCN valve, and the annular disk are made of stainless steel (SUS316L). SUS316L was named "SUS316Material".

The vapor of helium at the saturated vapor pressure filling the UCN guide was named "HeliumMaterial".

The He-II in the He-II bottle was named "He2Material".

The Fomblin coating on the UCN horizontal guide was named "FomblinMaterial".

The entrance window of the UCN detector is made of aluminum. Aluminum was named "AluMaterial". The counting volume of the UCN detector is filled with Helium-3, Argon, and CO_2. However, we treated this volume as a black body because the attenuation length of UCN in this volume was enough short.

All material settings used for Geant4-UCN simulation are shown in Table 7.1. η and f were the best fitting parameters for the experimental results in April 2008.

A Fermi potential V_F, an absorption cross section σ_a and a scattering cross section σ_s are determined by data tables.

A wall loss parameter η and a diffuse reflection probability f are to be determined to reproduce the experimental results. The values of η and f are material-dependent. Nevertheless,

	V_F [neV]	η [$\times 10^{-4}$]	f	σ_s [b]	σ_a [b]
Ni-P coating	214	4.3	0.057	15.75	3.84
SUS316L	188	4.3	0.057	10.86	2.88
Helium	0	0	0	0	0.0274
Helium-II	18.6	0	0	0	3.399×10^{-7}
Fomblin	106.5	4.3	0.057	4.50	0.00683
Aluminum	54	4.3	0.057	1.503	0.231

Table 7.1: Material settings for Geant4-UCN. η and f was determined by fitting for April 2008.

in Table 7.1, η and f are all same, respectively, except for Helium and He-II that are without wall loss effects.

A wall loss probability of UCN is influenced by contaminations on material's surfaces. Especially, hydrogen atoms trapped on surfaces cause a large UCN wall loss because hydrogen has a large scattering cross section, $\sigma_s = 82.02(6)$ b. This effect is called "UCN anomaly" and masks a native surface feature of the hydrogen-trapped material.

And also, η is temperature-dependent. However, we don't know the detail of the temperature distribution in the UCN source. Therefore, it is very difficult to calculate η of each material accurately.

Fortunately, UCN in the source go forth and back again and again through the He-II bottle and the UCN guide. Such UCN are reflected by all materials, so their wall loss probabilities can be averaged. So we assumed that all materials have a same value of η.

On the other hand, a diffuse reflection probability f depends on a shape of a surface. We have no reliable information about surfaces of the materials. As a case of the wall loss parameter, we assumed that f can be averaged and is to be replaced by one effective value.

7.2 Initial Condition of UCN

A UCN production process is recostructed by "UCNPrimaryGeneratorAction" class. Its source file name is "UCNPrimaryGeneratorAction.cc". The UCNPrimaryGeneratorAction class makes a space and an energy distribution of UCN at the initial time.

The cold neutron flux in the He-II bottle depends on the height from the bottom. Therefore, the UCN production rate in the He-II bottle is also height-dependent. We calculated the cold neutron fluxes at 8-divided volumes in the He-II bottle and 3-divided volumes in the UCN vertical guide under the orifice of the UCN guide by PHITS2 (Fig. 7.2).

Fig. 7.3 shows the height dependence of the UCN production rates in each volume. The UCN production rates is distributed like a gaussian along the axis of the He-II bottle.

We simulated the UCN production by Geant4-UCN to reconstruct the UCN height distribution obtained by PHITS2, as shown in Fig. 7.3. In Fig. 7.4, the value of the vertical axis was normalized by the total number of the produced UCN and the cross sectional areas of the

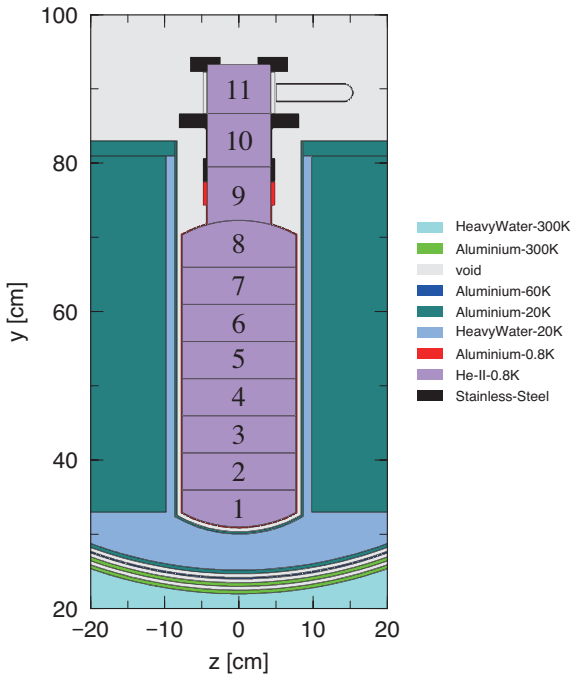

Figure 7.2: The divided volumes of the He-II bottle and UCN vertical guide. The purple colored area is filled with He-II. The divided volumes are labeled 1 to 11.

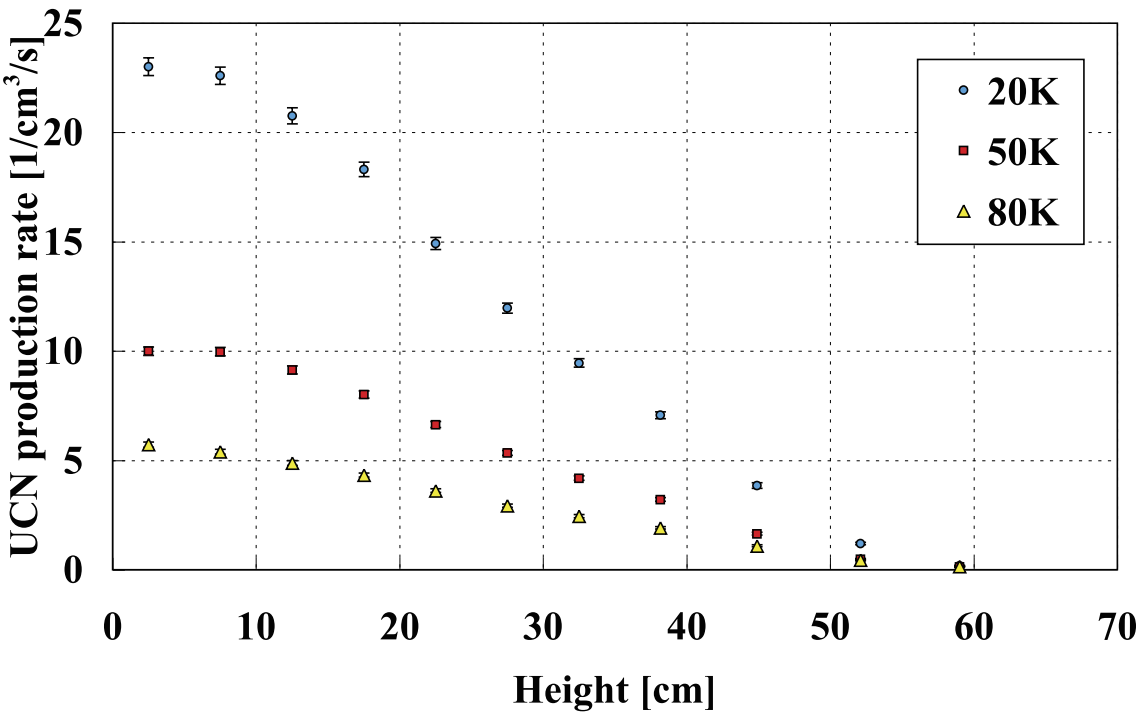

Figure 7.3: Height dependence of UCN production rate in the He-II bottle. The three results in the case of a D_2O temperature of 20K, 50K, and 80K are shown, respectively.

He-II bottle or the UCN vertical guide. The cross sectional area of the He-II bottle A_{He-II} is 183.9 cm^2 and that of the UCN vertical guide A is 56.6 cm^2. Therefore, a UCN production rate per unit length in the UCN vertical guide is $A/A_{He-II} = 0.308$ times as large as that of the He-II bottle. As a results, the number of UCN produced in the UCN vertical guide is very small and we ignored the UCN production in the UCN vertical guide, namely, Height $>$ 408 mm.

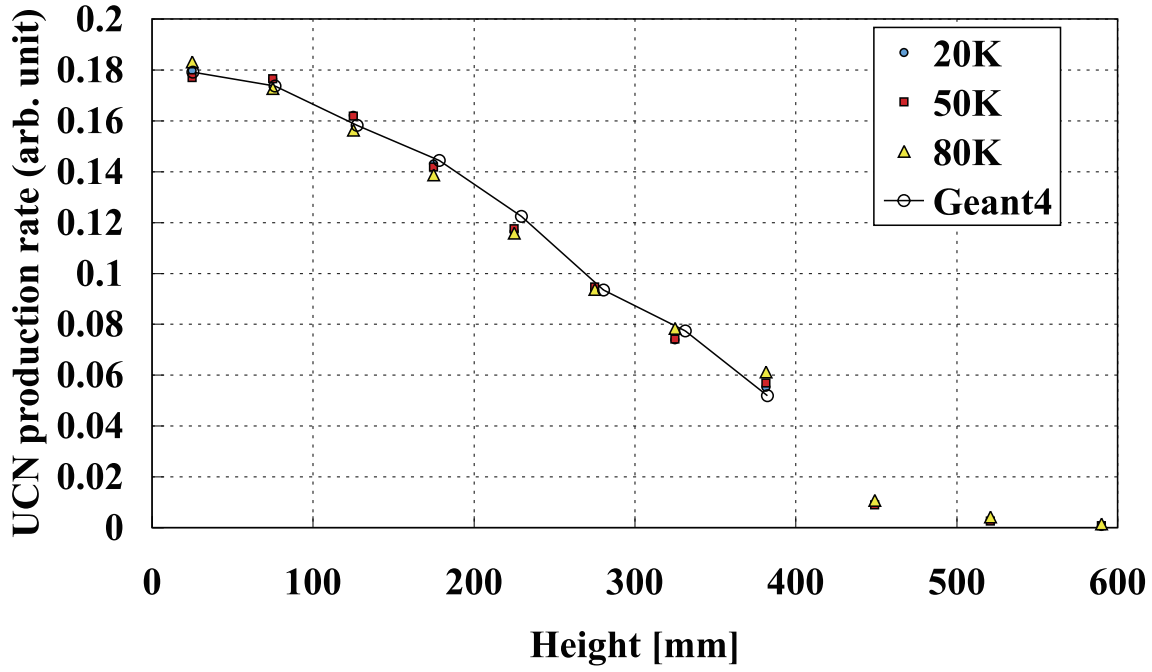

Figure 7.4: Height dependence of UCN production rate in the He-II bottle by Geant4-UCN, compared to that of PHITS2. The vertical axis was normalized by the cross sectional areas and total UCN numbers. We ignored the UCN production in the UCN vertical guide (Height $>$ 408 mm).

The energy spectrum of UCN produced in the He-II bottle is proportional to a square root of the energy, $\rho(E) \propto \sqrt{E}$. Fig. 7.5 is a UCN energy spectrum reconstructed by Geant4-UCN. The cut off velocity was 0.1 m/s, corresponding to 0.05 neV. A UCN below this energy was not produced in this simulation to save the processing time. The critical velocity was 7.0 m/s, corresponding to 256 neV. Although the Fermi potential of Ni-P coating is 214 neV, some of UCN with an energy higher than 214 neV are reflected by the surfaces because of their shallow incident angle and go into the UCN detector through the UCN guide.

Fig. 7.6 shows a UCN transmission rate in our UCN source as a function of velocity. The velocity of a UCN with an energy of 214 neV is 6.4 m/s. However, UCN with a velocity of 7.0 m/s, corresponding to 256 neV, were observed at the UCN detector. On the other hand, the lowest velocity of the observed UCN was 3.6 m/s that corresponded to 68 neV. The distance between the top of the He-II bottle and the UCN horizontal guide is 820 mm. This height corresponds to 84 neV, or 4.0 m/s. However, when UCN go out from the He-II surface, they

are accelerated by the He-II Fermi potential with an energy of 18.6 neV. This is why the slower UCN were observed. We set the initial UCN energy to be between 68 neV and 256 neV to save the processing time.

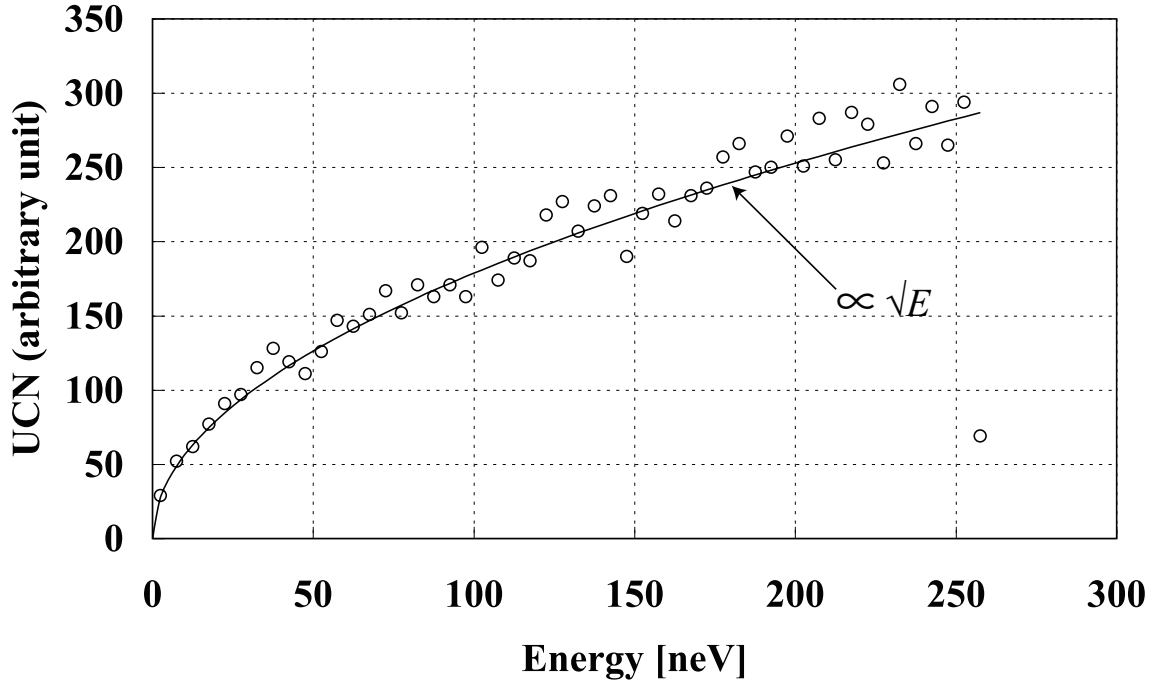

Figure 7.5: The energy spectrum of UCN produced in the He-II bottle reconstructed by Geant4-UCN. The cut off velocity is 0.1 m/s, corresponding to 0.05 neV. The critical velocity is 7.0 m/s, corresponding to 256 neV.

7.3 Wall Loss Parameter

A wall loss probability per bounce is given by

$$\mu(E,\theta) = 2\eta \left(\frac{E\cos^2\theta}{V - E\cos^2\theta} \right)^{1/2} \tag{7.6}$$

as shown in (2.47). E is the total energy of reflecting UCN and θ is the angle of incidence with respect to the surface normal. η is a constant parameter of wall loss which is given by (2.48). However, η is much larger than the theoretically predicted value by $10 \sim 10^2$ times due to surface contaminations like hydrogen atoms or other unknown sources.

So we determined the value of η by fitting to reproduce the UCN storage time τ_s obtained in the delay mode. The obtained η is an averaged value of all surface states of materials used for the UCN source.

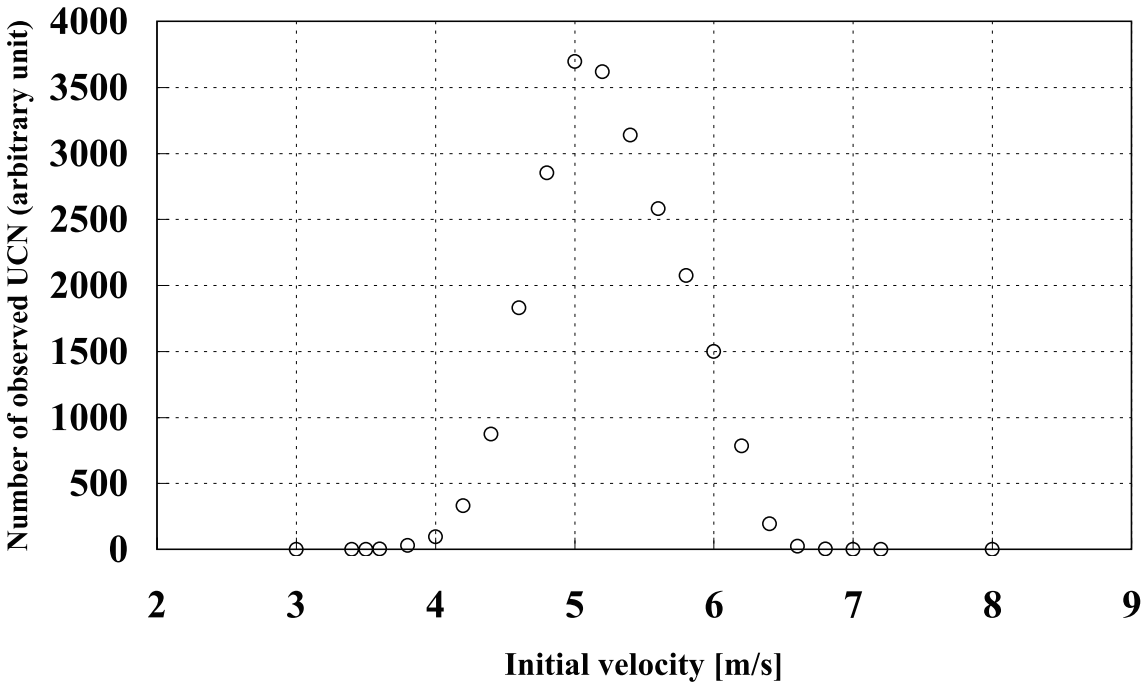

Figure 7.6: UCN transmission rate as a function of velocity. Solid circles show the number of UCN observed by the UCN detector through the UCN guide. The number of UCN produced in the He-II bottle was $N_0 = 10^5$.

7.4 Diffuse Reflection Probability

In the simplest model, a reflection of UCN on surfaces is represented by a diffuse reflection probability f and a specular reflection probability $(1 - f)$. A typical electropolished stainless steel has f of about $5 \sim 20$ %. In our case, the ECB method was used for the inner surfaces of UCN guide to make more flat and purer surfaces than electropolishing. Therefore, the value of f in our case is expected to be smaller than 5%.

We determined the value of f by fitting to reproduce a time spectrum obtained with a short pulse (1 sec) proton beam. When the proton beam of 1 sec was irradiated, the rise of UCN counts was observed right after the beam was stopped. This was a diffusion process of UCN and expected that the speed was expected to be dependent on the diffuse reflection probability f. The determined value of f is the averaged value as well as the wall loss parameter η.

7.5 Reproduction of Experiment in April 2008

We simulated UCN time spectra shown in Fig. 5.18, which was obtained by the delay mode in April 2008. Fig. 7.7 shows time spectra reproduced by Geant4-UCN. In these spectra, $\eta = 4.3 \times 10^{-4}$, and $f = 0.057$ were used. The total number of produced UCN in the He-II bottle was $N_0 = 10^5$.

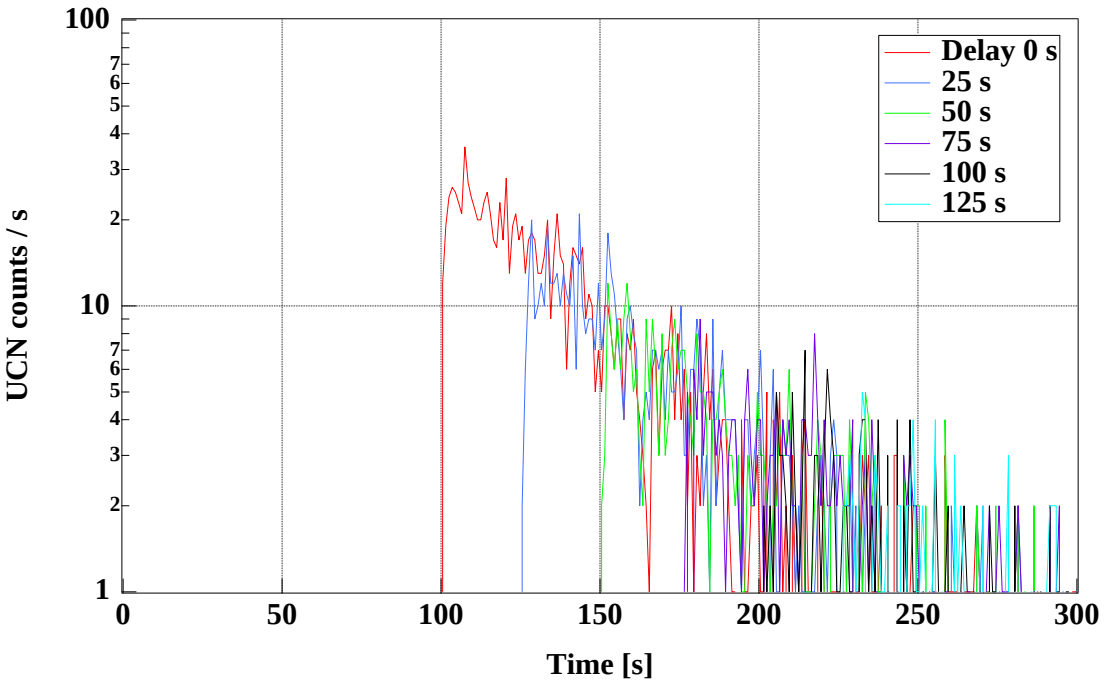

Figure 7.7: Time spectra of delay mode in April 2008, reproduced by Geant4-UCN. $\eta = 4.3 \times 10^{-4}$ and $f = 0.057$ were used. The total number of produced UCN in the He-II bottle was $N_0 = 10^5$.

Fig. 7.8 shows the total numbers of the observed UCN as a function of the delay time. The UCN storage time was $47.3^{+1.3}_{-1.2}$ s. This was consistent with the experimental result, $\tau_s = 47.8 \pm 1.4$ s.

To obtain these results, we determined the value of wall loss parameter η by χ^2 fitting method at first. We simulated time spectra by the delay mode, changing the value of η. Then, we calculated the values of χ^2 of each η. Here, $\chi^2(\eta)$ was defined as follows.

$$\chi^2(\eta) = \sum_i \frac{(N_{cal}^{(i)} - N_{exp}^{(i)})^2}{\sigma_{exp}^{(i)2}} \tag{7.7}$$

$N_{cal}^{(i)}$ is a total number of UCN with an i th delay time of Δt_i obtained by Geant4-UCN and $N_{exp}^{(i)}$ is that of the experimental results. $\sigma_{exp}^{(i)}$ is the statistical error of $N_{exp}^{(i)}$. Each $N^{(i)}$ was

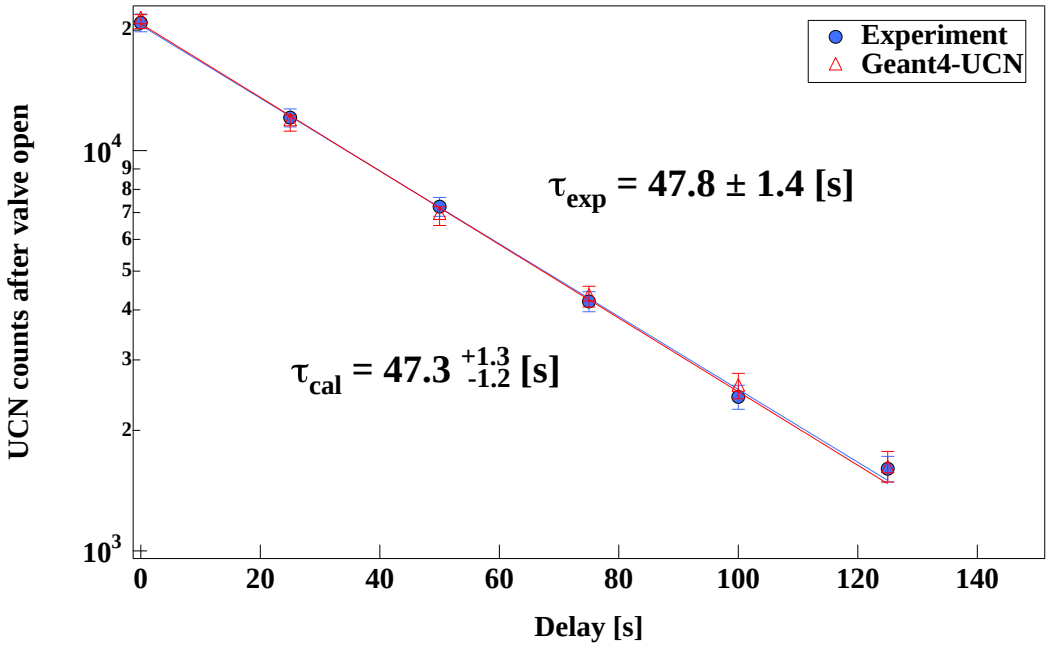

Figure 7.8: The total number of UCN counts as a function of delay time Δt and a fitting curve by an exponential function $y = \exp(-x/\tau)$. A UCN storage time of $47.3^{+1.3}_{-1.2}$ sec was obtained.

normalized by sum of them, $\sum_i N^{(i)}$. $N^{(i)}_{cal}$ has a statistical error, $\sigma^{(i)}_{cal}$, respectively. So, χ^2 has an error by error propagation. The error of χ^2 was calculated by the error propagation law.

$\chi^2(\eta)$ is shown in Fig. 7.9 as a function of η. In Fig. 7.9, f was 0.05. The minimum point of χ^2 was determined by a parabola fitting function, $\chi^2 = a(\eta - b)^2 + \chi^2_{min}$ where a, b, and χ^2_{min} are the fitting parameters. $b = 4.3 \times 10^{-4}$ was obtained at χ^2_{min}. σ is the standard deviation of η and obtained at a point where $\chi^2 = \chi^2_{min} + 1$. η was determined to be $\eta = (4.3 \pm 0.4) \times 10^{-4}$.

Then, the diffuse reflection probability f was determined. Fig. 7.10 shows a time spectrum in which a proton beam was irradiated for 1 sec and the UCN valve remained open (Open mode). The rise of UCN count rate just after the beam was stopped was a diffusion of UCN in the UCN guide. The velocity of the diffusion is expected to be dependent on a diffuse reflection probability f of the UCN guide.

We simulated the time spectrum of this mode, changing the value of f, and calculated the values of χ^2 of each f. Fig. 7.11 shows time spectra obtained by Geant4-UCN with a diffuse reflection probability of 0, 0.05, 0.06 and 0.15, respectively. It was confirmed that the rise of the UCN count rate was dependent on f. $\chi^2(f)$ was calculated between $t = 1.5$ s and 8.5 s.

$\chi^2(f)$ was shown in Fig. 7.12 as a function of f. In this Figure, η was 4.3×10^{-4}. f was determined to be $f = 0.057 \pm 0.021$.

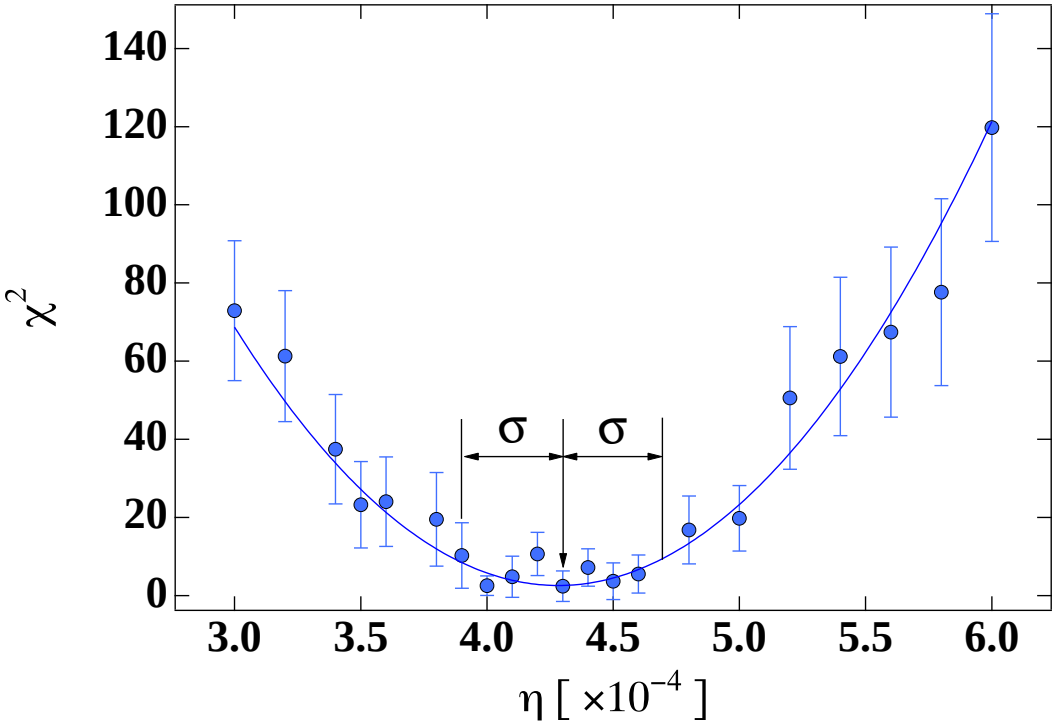

Figure 7.9: χ^2 as a fuction of η in the experiment of April 2008. f was 0.05. σ is the standard deviation of η. η was determined to be $\eta = (4.3 \pm 0.4) \times 10^{-4}$. ndf (number of degree of freedom) is 4.

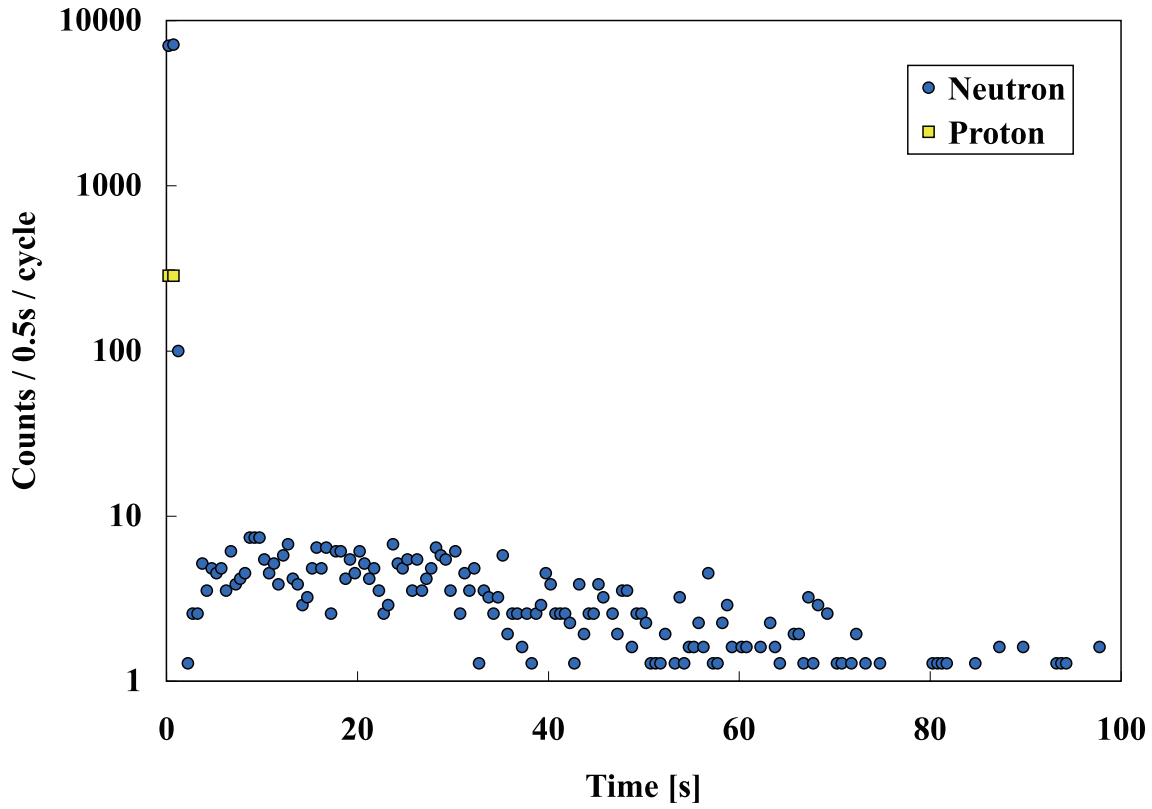

Figure 7.10: A time spectrum with a beam duration of 1 sec. UCN valve was opened during the measurement. The rise of UCN count rate just after the beam was stopped was a diffusion of UCN.

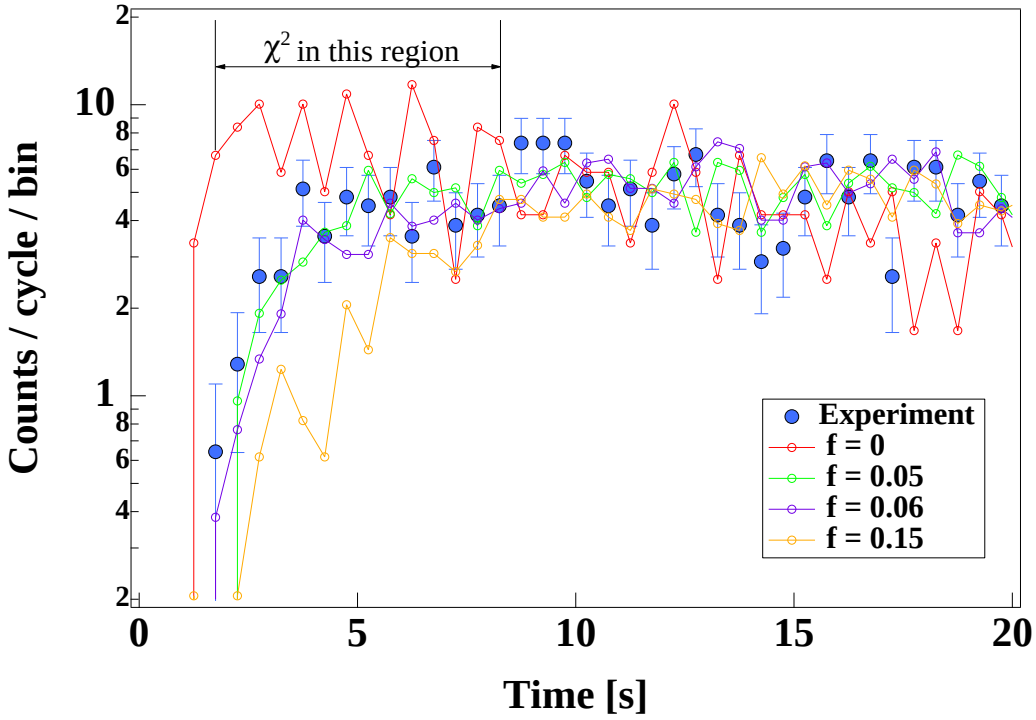

Figure 7.11: Time spectra obtained by Geant4-UCN with a diffuse reflection probability of 0, 0.05, 0.06 and 0.15, respectively. Full dots are the experimental results. χ^2 was caiculated between $t = 1.5$ s and 8.5 s.

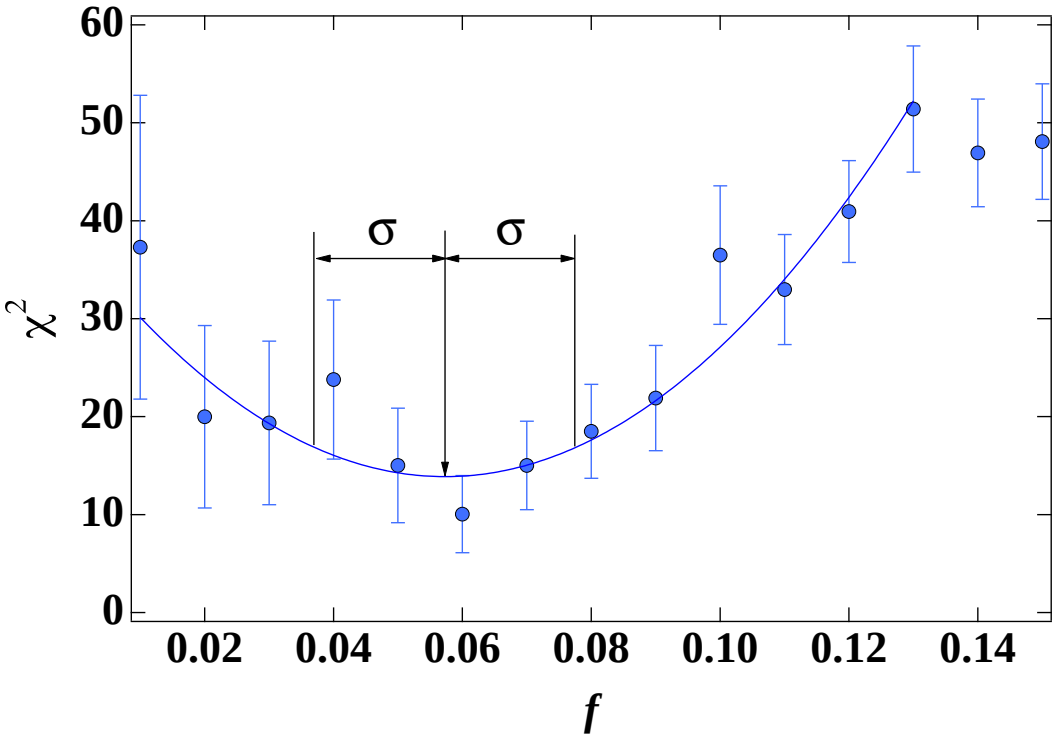

Figure 7.12: χ^2 as a fuction of f in the experiment of April 2008. $\eta = 4.3 \times 10^{-4}$ in this figure. f was determined to be $f = 0.057 \pm 0.021$. ndf is 12.

7.6 UCN Storage Experiment with SUS Disk

We simulated the UCN storage bottle experiment with the SUS disk by Geant4-UCN Monte Carlo simulation. The goal of this simulation was to determine the wall loss parameter η on the surfaces in the UCN storage bottle. As discussed in Chapter 5, the wall loss probability is position dependent. In our UCN storage bottle, the top surface has larger wall loss probability than the side and bottom surfaces. The ratio was determined to be $\overline{\mu_1}/\overline{\mu_2} = 6.1$ in Chapter 5. This value was used in the following simulation.

Geometry and Material Settings

Fig. 7.13 shows the geometry of the He-II superthermal UCN source and the UCN storage bottle with the SUS disk.

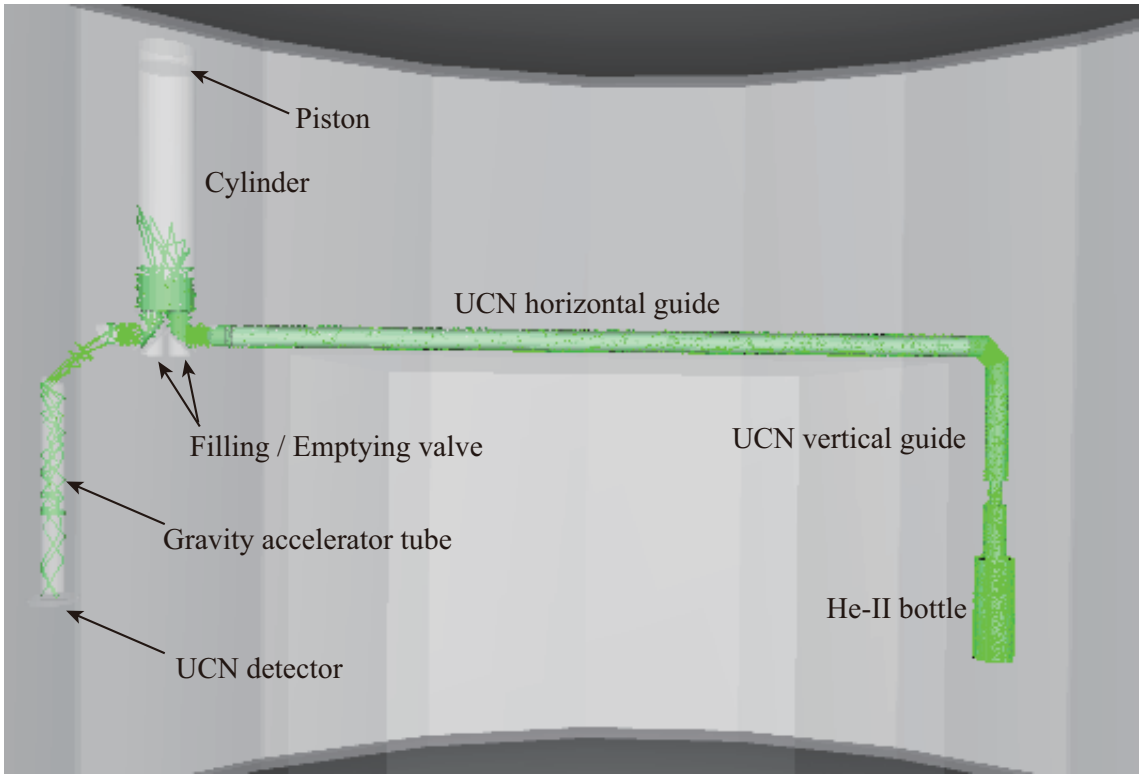

Figure 7.13: Geometry of the He-II superthermal UCN source and the UCN storage bottle with the SUS disk. The green lines in the volume are the trajectories of UCN.

The geometry and the material settings of the UCN source are entirely same as the condition of April 2008 which was discussed above. The initial condition when UCN are produced in the He-II bottle is also same. The UCN valve is always opening.

The UCN storage bottle with the SUS disk is connected to the experimental port. Each part of the UCN storage bottle, i.e. the cylinder, the filling/emptying valve, and the piston

are made of SUS316L.

The gravity accelerator tube and the ^{3}He UCN detector are attached to the emptying valve. The material settings of them are same as that of the previous simulation. There is no annular disk in front of the UCN detector.

The material settings of the UCN source are shown in Table 7.1. The material settings of the UCN storage bottle are shown in Table 7.2. The diffuse reflection probability f of the inner surface is set to be 0.04. This value is same as that of the UCN source. The UCN storage bottle is filled with the vapor of helium at a temperature of 0.8 K. The settings of this helium gas is same as the previous settings.

	V_F [neV]	η [$\times 10^{-4}$]	f	σ_s [b]	σ_a [b]
SUS316L	188	(To be determined)	0.04	10.86	2.88
Helium	0	0	0	0	0.0274

Table 7.2: Material settings of the UCN storage bottle with the SUS disk.

Our purpose is to determine the wall loss parameter η of SUS316L in the UCN storage bottle. We used two wall loss parameters. One is η_1 used for the top surface. The another is η_2 used for the side and bottom surfaces. The simulation results are shown in the following.

Wall Loss of UCN Storage Bottle

We simulated the time spectra with two wall loss parameters, η_1 and η_2. Here, η_1 is a wall loss parameter of the top surface. η_2 is a wall loss parameter of the side and bottom surfaces. In Chapter 5, we roughly estimated the effective wall loss probability per bounce $\overline{\mu}_1$ and $\overline{\mu}_2$. The obtained values were

$$\overline{\mu}_1 = (1.84 \pm 0.48) \times 10^{-3} \tag{7.8}$$

$$\overline{\mu}_2 = (3.0 \pm 2.4) \times 10^{-4} \ . \tag{7.9}$$

$\overline{\mu}$ is proportional to η. So, we assumed the ratio between η_1 and η_2 to be equal to the ratio between $\overline{\mu}_1$ and $\overline{\mu}_2$, i.e.,

$$\frac{\eta_1}{\eta_2} = \frac{\overline{\mu}_1}{\overline{\mu}_2} = 6.1 \ . \tag{7.10}$$

We changed the values of η_1 and η_2 to reproduce the time spectra and the UCN storage time in the case with the SUS disk at a position of $h = 91.7$ cm, keeping this ratio.

We simulated the time spectra in the case with the SUS disk at a height of 91.7 cm. Fig. 7.14 shows the simulated time spectra with $\eta_1 = 1.8 \times 10^{-3}$ and $\eta_2 = 2.9 \times 10^{-4}$. This value was the best fitting result.

We obtained the UCN storage time in the bottle by using the simulated UCN counts. The total UCN counts as a function of the delay time is shown in Fig. 7.15. The UCN storage time τ of the best fitting result was $168.5^{+2.5}_{-2.4}$ sec. It was consistent with the experimental result.

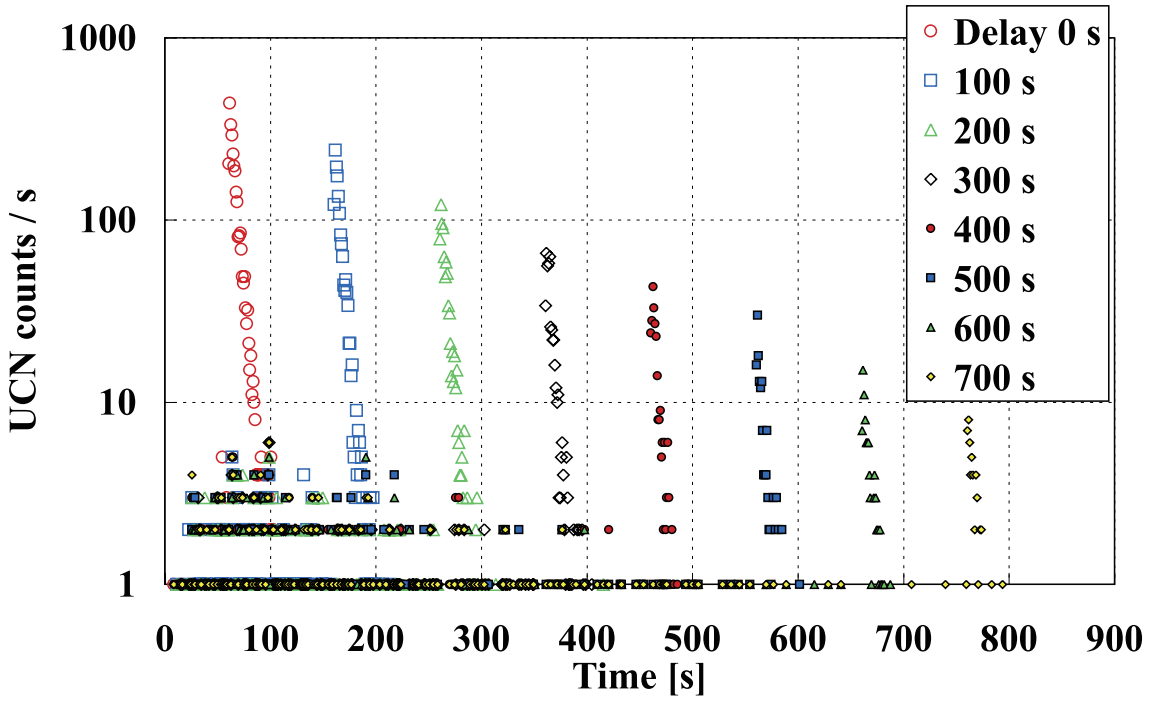

Figure 7.14: Time spectra simulated with $\eta_1 = 1.8 \times 10^{-3}$ and $\eta_2 = 2.9 \times 10^{-4}$. The SUS disk was at a height of 91.7 cm.

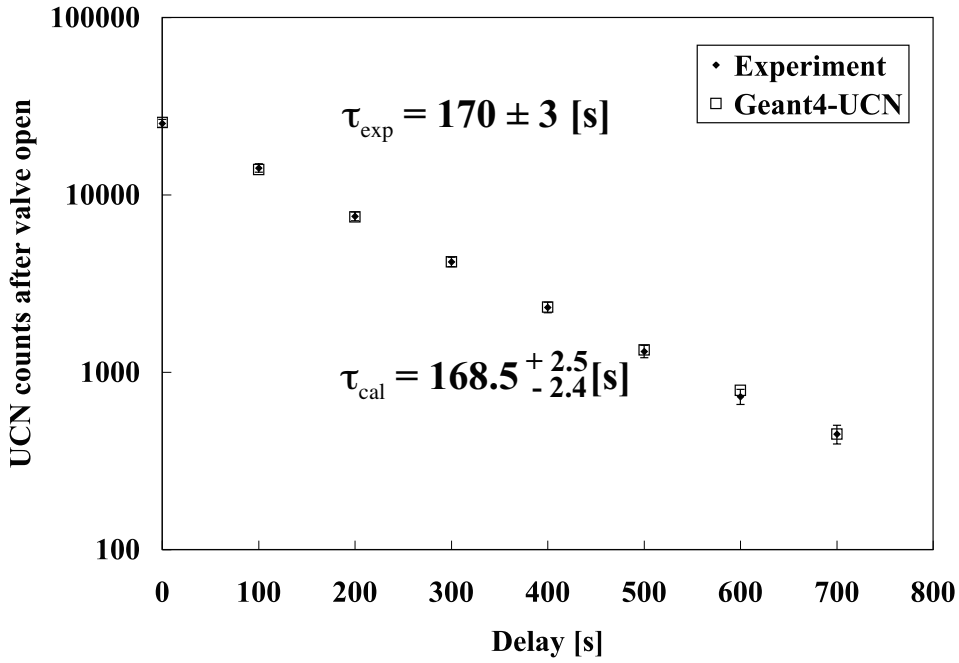

Figure 7.15: Total UCN counts as a function of the delay time. $\eta_1 = 1.8 \times 10^{-3}$ and $\eta_2 = 2.9 \times 10^{-4}$. The SUS disk was at a height of 91.7 cm. The simulated UCN storage time was $168.5^{+2.5}_{-2.4}$ sec.

To determine the values of η_1 and η_2, we calculated the value of χ^2 as a function of η_1 and η_2. We used the following formula as χ^2.

$$\chi^2(\eta) = \sum_i \frac{(N_{cal}^{(i)} - N_{exp}^{(i)})^2}{\sigma_{cal}^{(i)2} + \sigma_{exp}^{(i)2}}. \tag{7.11}$$

$N_{cal}^{(i)}$ is a total UCN count with an i th delay time Δt_i simulated by Geant4-UCN and $N_{exp}^{(i)}$ is that of the experimental result. $\sigma_{cal}^{(i)}$ is the statistical error of $N_{cal}^{(i)}$, and $\sigma_{exp}^{(i)}$ is that of $N_{exp}^{(i)}$. In our simulation, $N_{cal}^{(i)}$ were much less than $N_{exp}^{(i)}$ because the number of UCN produced in the He-II bottle was much less than the experimental value. So, we normalized each $N^{(i)}$ by sum of them, $\sum_i N^{(i)}$.

$\chi^2(\eta)$/ndf is shown in Fig. 7.16. Since we assumed $\eta_1 = 6.1 \times \eta_2$, χ^2 is actually a function of η_2. The minimum value of χ^2/ndf was obtained in the case with a parameter of $\eta_2 = 2.9 \times 10^{-4}$. We determined the error of η_2 at the same time. The determined values of η_1 and η_2 are given as follows.

$$\eta_2 = (2.9^{+0.6}_{-0.3}) \times 10^{-4} \tag{7.12}$$

$$\eta_1 = 6.1 \times \eta_2 = 1.8 \times 10^{-3} \tag{7.13}$$

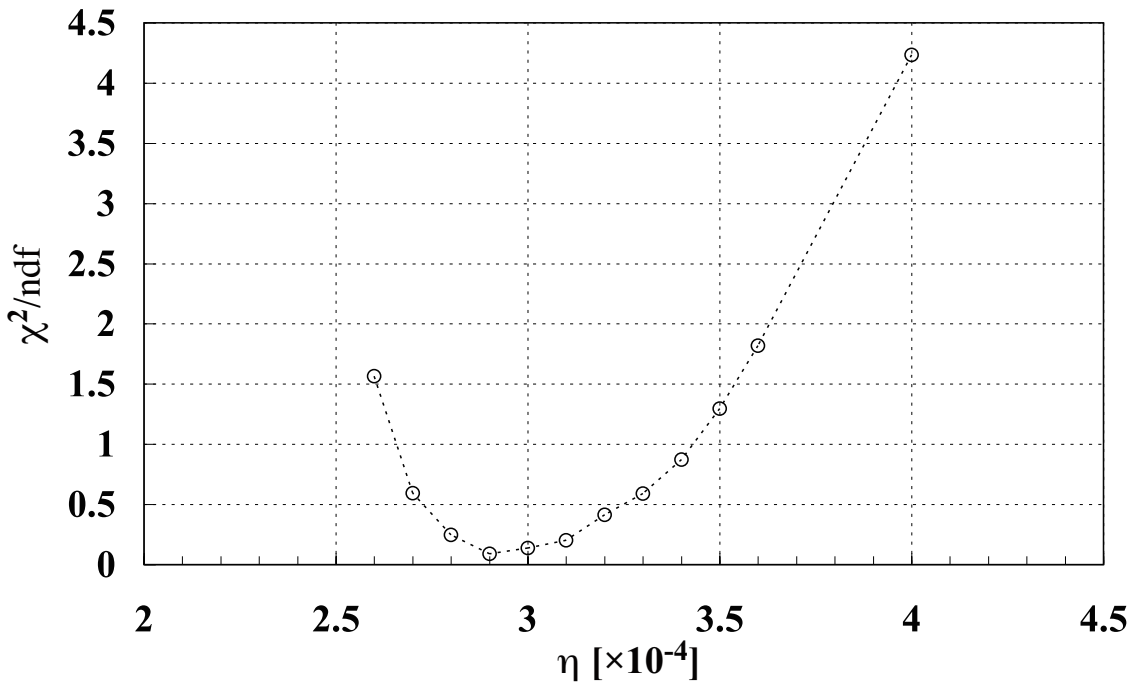

Figure 7.16: χ^2/ndf as a function of η_2 in the case with the SUS disk at a height of 91.7 cm. η_1 was fixed to be $6.1 \times \eta_2$.

We succeeded to obtain the wall loss parameters of the UCN storage bottle. Then, we calculated the time dependence of the total UCN counts at a height of 20, 10 and 5 cm, using

the obtained η_1 and η_2. Fig. 7.17 shows the obtained time dependence of the UCN counts at each height. The time dependence of the UCN counts in the UCN storage bottle were well reproduced at each height. It was confirmed that the values of the wall loss parameters η_1 and η_2 obtained here were correct. And also, it was confirmed to be correct that the assumption that the top disk was dirtier than the side and bottom surfaces.

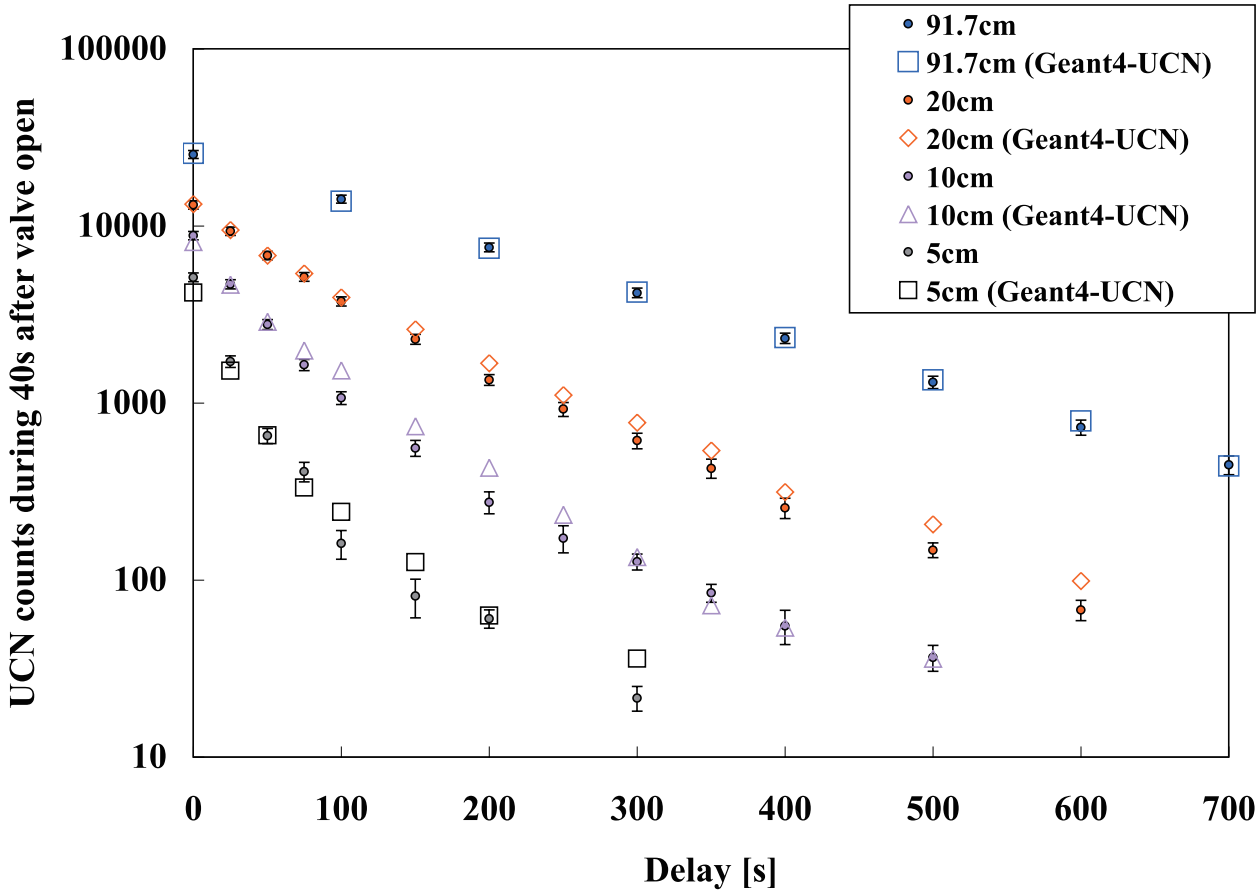

Figure 7.17: Time dependence of the total UCN counts at each height. The height of the SUS disk are 91.7, 20, 10 and 5 cm, respectively. In this Figure, $\eta_2 = 2.9 \times 10^{-4}$ and $\eta_1 = 6.1 \times \eta_2 = 1.8 \times 10^{-3}$ were used.

7.7 UCN Energy Spectrum

We simulated the UCN storage experiment with the P.E. disk by Geant4-UCN Monte Carlo simulation. The UCN energy spectrum was reproduced by this simulation.

Material Settings of Polyethylene

The geometry of the UCN source and the UCN storage bottle is almost same as the case with the SUS disk. Only one difference is the P.E. disk with a thickness of 10 mm was attached to the bottom of the SUS disk. The material settings of polyethylene are shown in Table 7.3.

	V_F [neV]	η [$\times 10^{-4}$]	f	σ_s [b]	σ_a [b]
Polyethylene	- 8.54	—	0.057	56.5	0.223

Table 7.3: Material settings for the Polyethylene disk.

The wall loss parameter of the UCN storage bottle was once determined in the simulation with the SUS disk. $\eta_2 = 2.9 \times 10^{-4}$ and $\eta_1 = 6.1 \times \eta_2 = 1.8 \times 10^{-3}$ were obtained. In this simulation, we determined the wall loss parameter of the UCN storage bottle again. The wall loss probability of SUS316L might have changed from the experiment with the SUS disk because we opened the bottle and exposed it to the atmosphere to attach the P.E. disk. We simulated the time spectra with the P.E. disk at a height of 84.5 cm using the wall loss parameter η_2 for the side and bottom surfaces. η_1 was used for the polyethylene disk, but this was actually meaningless because polyethylene had the negative potential and absorbed all UCN.

The diffuse reflection probability f was fixed to be 0.057, similarly to the case with the SUS disk.

Wall Loss of UCN Storage Bottle

We simulated the time spectra in the case with the P.E. disk at a height of 84.5 cm. Fig. 7.18 shows the simulated time spectra with a parameter η_2 of 3.9×10^{-4}. This value was the best fitting result.

The UCN storage time in the UCN storage bottle with the P.E. disk was obtained by using the simulated UCN counts. The total UCN counts as a function of the delay time is shown in Fig. 7.19. The UCN storage time τ was 160 ± 5 sec. It was consistent with the experimental results.

The wall loss parameter η was determined by χ^2. χ^2 in this analysis was defined to be

$$\chi^2(\eta_2) = \sum_i \frac{(N_{cal}^{(i)} - N_{exp}^{(i)})^2}{\sigma_{exp}^{(i)2}}. \tag{7.14}$$

$N_{cal}^{(i)}$ is a total UCN count with an i th delay time Δt_i calculated by Geant4-UCN, and $N_{exp}^{(i)}$ is that of the experimental result. $\sigma_{exp}^{(i)}$ is the statistical error of $N_{exp}^{(i)}$. $N_{cal}^{(i)}$ has a statistical error

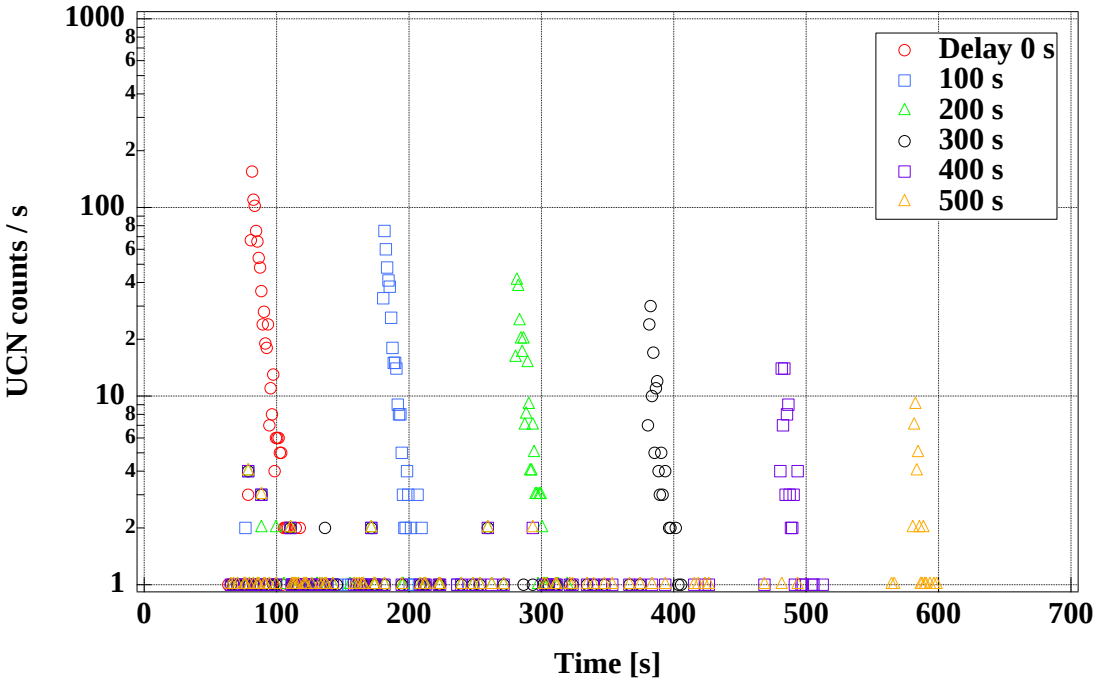

Figure 7.18: Time spectra calculated with a parameter η_2 of 3.9×10^{-4}. $f = 0.057$ was used. The P.E. disk was at a height of 84.5 cm.

$\sigma_{cal}^{(i)}$. The error of χ^2 was calculated by the error propagation law. In this simulation, each $N^{(i)}$ was normalized by sum of them, $\sum_i N^{(i)}$.

The χ^2 as a function of η_2 is shown in Fig. 7.20. The determined value of η_2 was given by

$$\eta_2 = (3.9 \pm 0.3) \times 10^{-4}. \tag{7.15}$$

The error of η_2 was given at a point of minimum $\chi^2 + 1$.

This value is larger than the case with the SUS disk. In the case with the SUS disk, η_2 was $(2.9^{+0.6}_{-0.3}) \times 10^{-4}$. When the P.E. disk was attached, the UCN storage bottle was exposed to the atmosphere for a few hours. It was possible that the surfaces inside the bottle were covered by some contaminations from the atmosphere.

UCN Energy Spectrum

We simulated the time spectra in the case with the P.E. disk at each height. Fig. 7.21 shows the time dependence of the total UCN counts at each height using η_2. The experimental results were reproduced well by Geant4-UCN.

We simulated the UCN energy spectrum at a delay of 100 sec. Fig. 7.22 shows the height dependence of the total UCN counts at a delay of 100 sec. By differentiating these curves, the UCN energy spectra after 100 sec delay by Geant4-UCN were obtained. The obtained UCN

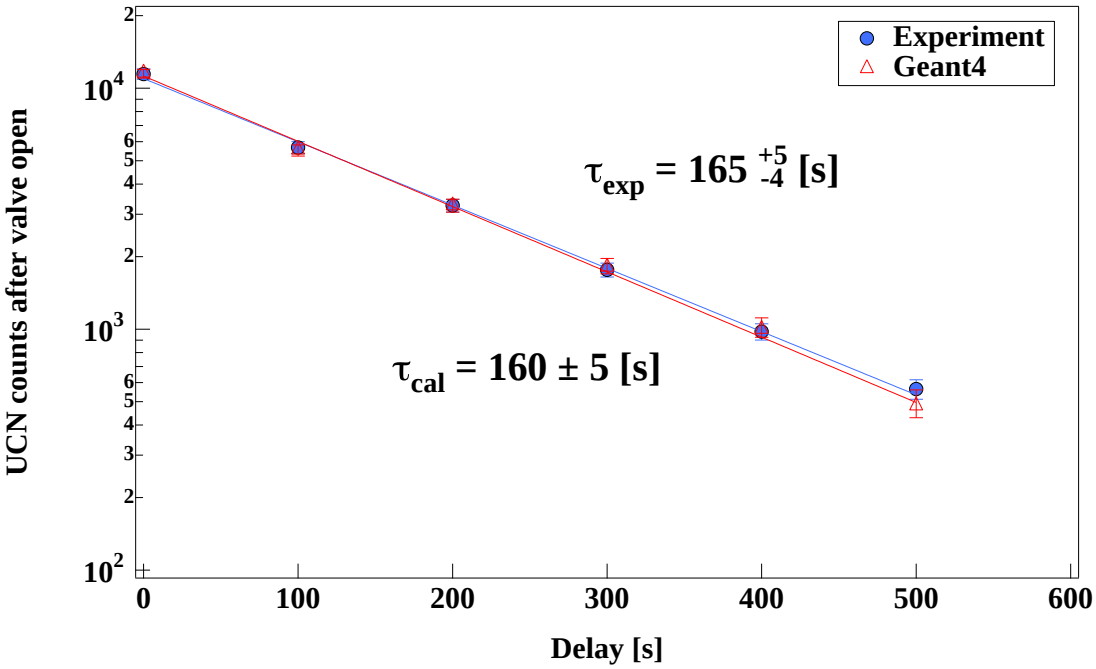

Figure 7.19: The total UCN counts as a function of the delay time. The parameter η_2 was 3.9×10^{-4}. $f = 0.057$ was used. The height of the P.E. disk was 84.5 cm. The UCN storage time simulated by Geant4-UCN was 160 ± 5 sec.

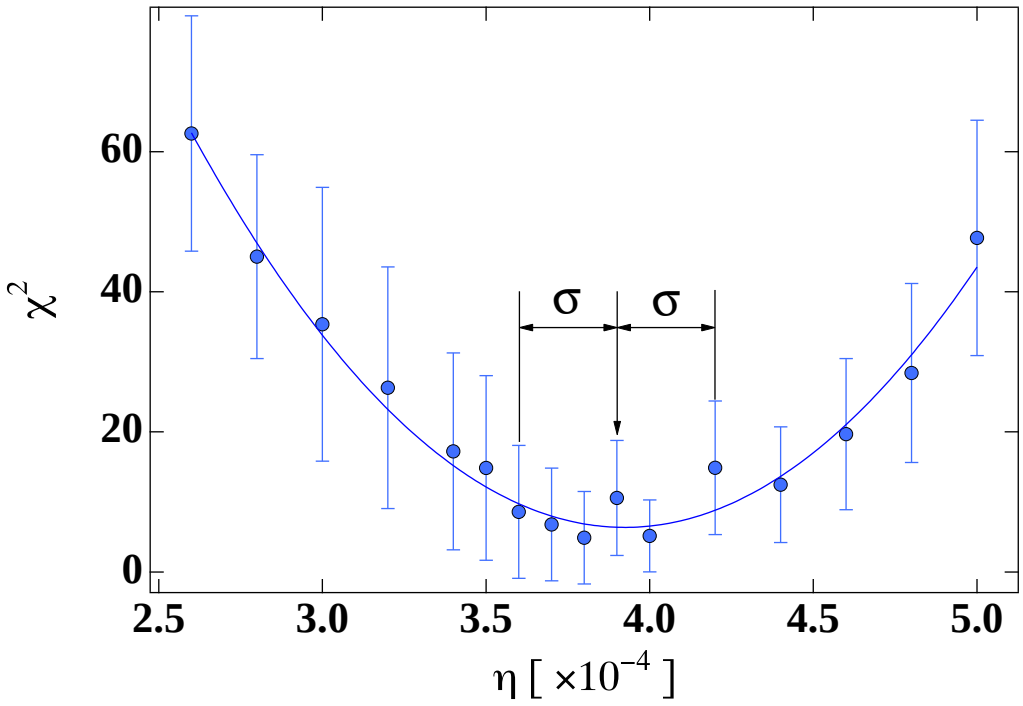

Figure 7.20: χ^2 as a function of η_2 in the case with the PE disk at a height of 84.5 cm. The ndf (number of degree of freedom) is 4. The solid line is a parabola fitting curve. σ is the standard deviation of η_2. η_2 was determined to be $(3.9 \pm 0.3) \times 10^{-4}$.

energy spectra are shown in Fig. 7.23. Fig. 7.23 shows that the UCN energy spectrum was well reproduced by Geant4-UCN.

We could reproduced the UCN energy spectrum by assuming the initial UCN energy spectrum was proportional to $\sqrt{E}$. The theoretical expectation said that UCN produced in He-II are distributed uniformly in the phase space. It was confirmed to be correct by this analysis.

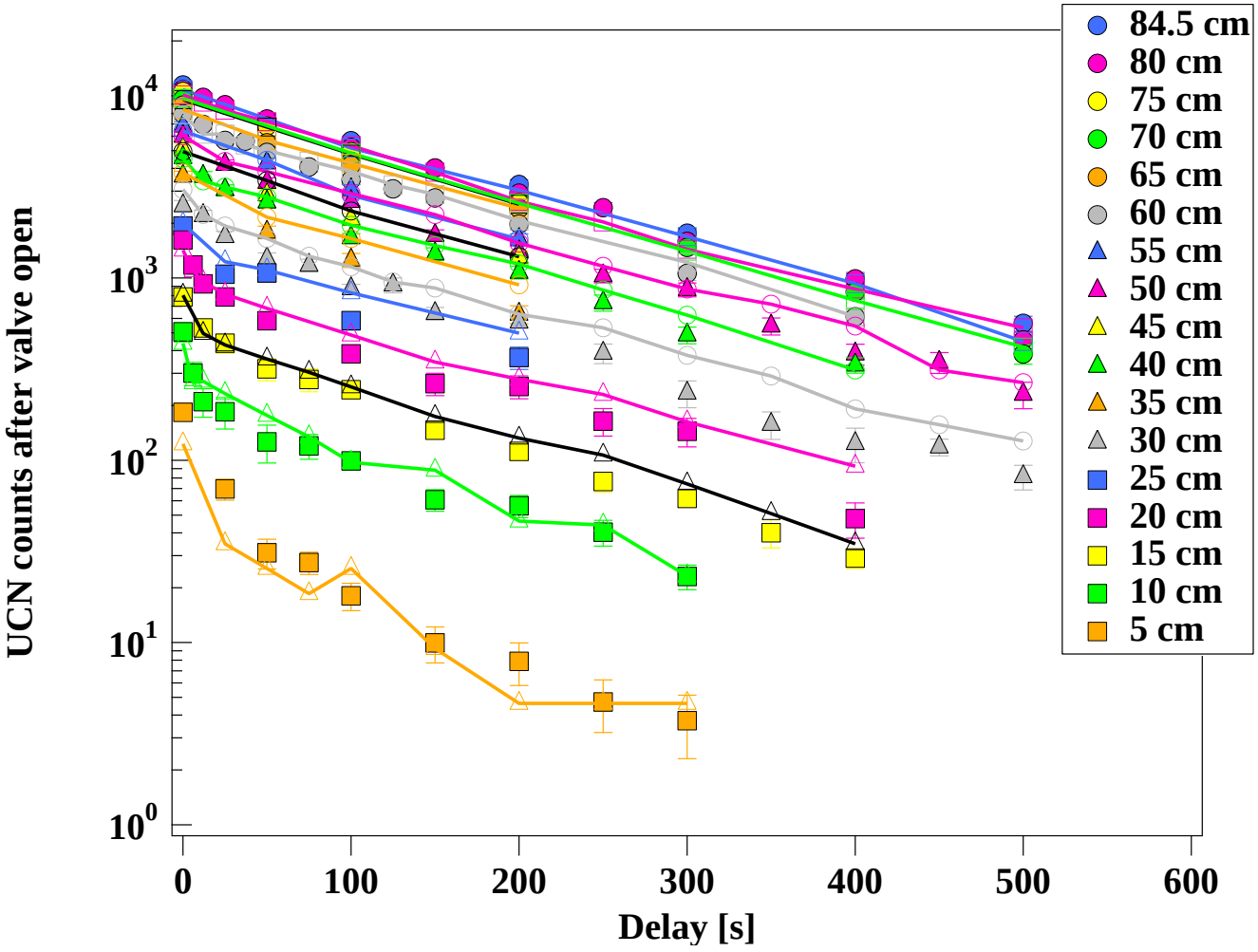

Figure 7.21: Time dependence of the total UCN counts at each height by Geant4-UCN, compared with the experimental data. The simulation results are connected by the solid lines. The height of the P.E. disk are 84.5, 80, 75, 70, ..., 15, 10 and 5 cm, respectively. In this Figure, $\eta_2 = 3.9 \times 10^{-4}$ and $f = 0.057$ were used.

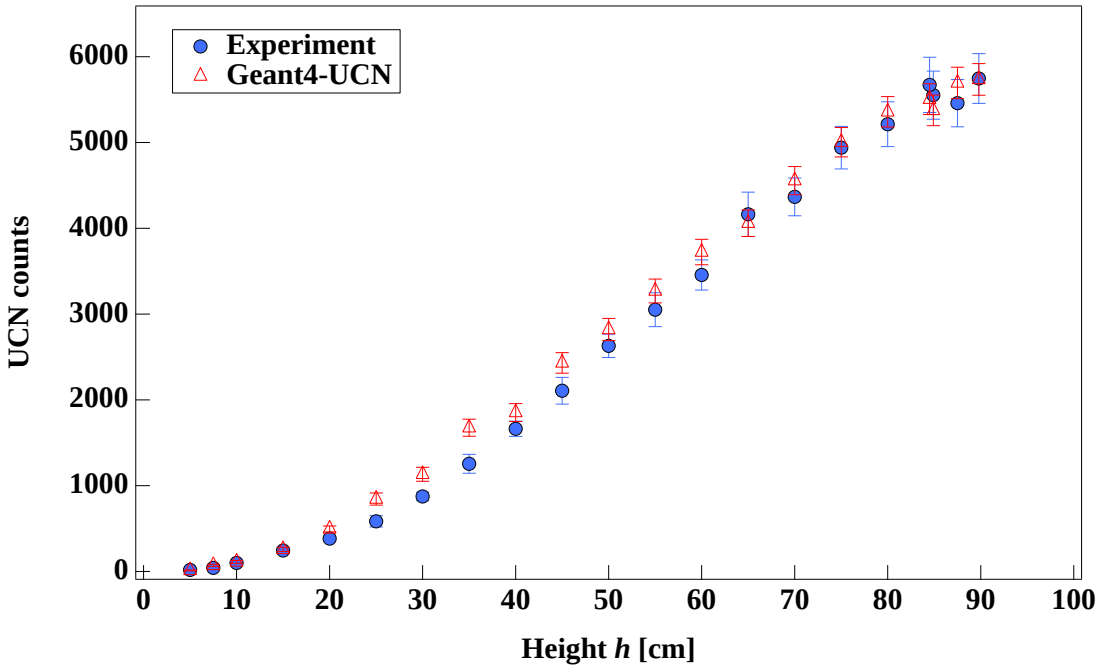

Figure 7.22: Height dependence of the total UCN counts at 100 sec delay. Blue circles are the experimental results that are same as Fig. 6.29. Red triangles are the values calculated by Geant4-UCN with $\eta_2 = 3.9 \times 10^{-4}$ and $f = 0.057$.

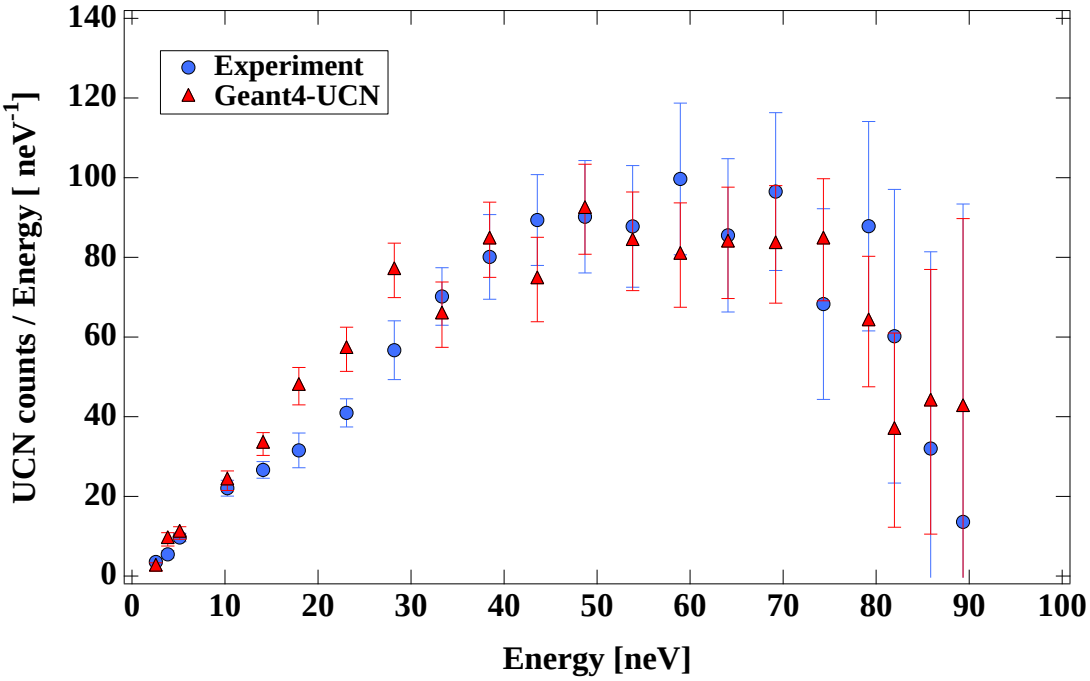

Figure 7.23: UCN energy spectra obtained by differentiating the curves shown in Fig. 7.22. The differentiations were done with 2 points skip.

Chapter 8

Summary

8.1 UCN Source Development

We have developed the new generation UCN source using the superthermal method with He-II coupled to a lead spallation target installed at the proton beam line of the ring cyclotron facility in RCNP. The UCN density at the conventional UCN facility is limited due to the Liouville's theorem and is saturated since the 1980's. To overcome this problem, we focused attention on the superthermal method which utilize the phonon scattering of a neutron in superfluid helium (He-II). In the superthermal UCN production in He-II, extra phase space of phonon is used to be free from Liouville's theorem. The dispersion curve of a neutron and that of phonons in He-II intersect at a certain momentum, where all the momentum and the energy of the scattered neutron can be transferred to the phonon in He-II and the scattered neutron becomes an UCN because the conservation law of energy and momentum are met at the intersection. This down-scattering process occurs at $k_i = 0.706$ Å^{-1} where k_i is the incident neutron momentum, or the neutron kinetic energy of 1 meV or the neutron temperature of 11.8 K. The produced UCN is possible to be scattered by phonons again and gains energy. The probability of this up-scattering process, however, becomes low enough if the He-II temperature is below 1 K.

Table 8.1 shows the evolution of the UCN density and the UCN storage life time of our He-II superthermal UCN source at RCNP.

The first UCN production experiment in our UCN source was carried out in 2002, and the obtained UCN density at the experimental port was 0.7 UCN cm^{-3} at $E_c = 90$ neV and the UCN storage lifetime was 14 sec. The He-II temperature at that time was 1.2 K. Then, the He-II cooling system was improved, and the He-II temperature became as low as 0.8 K by November 2006. Then, the UCN density was improved to 10.6 ± 1.1 UCN cm^{-3}. As well as the improved UCN storage life time in the UCN source, as 33.8 ± 0.6 sec.

Then, the isopure ^{4}He gas was introduced to condense the He-II with less abundance of ^{3}He impurities. ^{3}He has the very large neutron absorption cross section ($\sigma_a = 5333(7)$ b), so that ^{3}He impurities absorb UCN in the He-II UCN source. By use of the isopure ^{4}He, the UCN storage life time in the source was improved to 39.5 ± 0.5 sec. The UCN density was 12.3 ± 0.9

UCN cm^{-3}.

For the improvement of the storage life time, we coated the inner surface of the UCN horizontal guide with a hydrogen-free fomblin oil for the first trial to have a very small wall loss probability. The UCN storage life time in the source was improved to 47.8 ± 1.4 sec, which corresponds to the UCN density of 15.3 ± 1.1 UCN cm^{-3}. The UCN production rate per volume in He-II was estimated to be 3.84 ± 0.21 UCN cm^{-3} s^{-1} in this experiment.

The alkali degreasing applied on the surface of the UCN guide and the He-II bottle improved the UCN storage time to 61.4 ± 0.8 sec.

The baking before experiment done at 140 K improved the UCN storage life time to 81.5 ± 0.6 sec, which was the best record of the UCN storage life time obtained so far. The UCN density at the experimental port reached 26.0 ± 2.0 UCN cm^{-3}, which is world competitive value.

Year	T_{He-II} [K]	τ_s [s]	ρ_{ucn} [UCN/cm^3]	Comment
2002	1.2	14	0.7	-
2006 June	0.9	33.7 ± 0.6	7.6 ± 0.5	Cooling by ^{3}He
2006 Nov.	0.8	33.8 ± 0.6	10.6 ± 1.1	Cut Film flow
2007	0.8	39.5 ± 0.5	12.3 ± 0.9	Isopure ^{4}He
2008 April	0.8	47.8 ± 1.4	15.3 ± 1.1	Fomblin coating
2010 April	0.8	61.4 ± 0.8	19.5 ± 1.4	Alkali degreasing
2011 Feb.	0.8	81.5 ± 0.6	26.0 ± 2.0	Baking at 140 K

Table 8.1: The evolution of the He-II superthermal UCN source at RCNP. T_{He-II} is the He-II temperature, τ_s is the UCN storage life time of the UCN source and ρ_{ucn} is the UCN density at the experimental port at $E_c = 90$ neV.

8.2 Measurement of UCN Energy Spectrum

We have developed the UCN storage bottle and confined UCN extracted from the UCN source into the bottle. The UCN storage bottle was made of stainless steel (SUS316L), and the inner surface was polished by the Electrically-Chemical Buffing (ECB) method. And also, the alkali degreasing was applied on its inner surface.

We confined UCN in the bottle and measured the UCN storage life time. The longest UCN storage life time in the bottle was 170 sec. By this measurement, it was confirmed that the ECB method on stainless steel (SUS316L) and the alkali degreasing were very useful to confine UCN in a vessel for a long time. Then, we measured the UCN storage life time in the bottle, changing the height of the top plate. We obtained the height dependence of the UCN storage life time. And the wall loss parameters of the inner surface were estimated from the obtained data.

Then, we replaced the top plate of the UCN storage bottle by the polyethylene (P.E.) disk. We confined UCN in the UCN storage bottle again, and changed the height of the P.E. disk. The P.E. disk at a height of h absorbs UCN with an energy above $m_n gh$, so that only the UCN with energies below $m_n gh$ can be stored. Changing the height h, we obtained the height dependence of the UCN counts confined in the bottle. By differentiating the obtained height dependence of the UCN counts, we obtained the UCN energy spectrum.

We compared the UCN energy spectrum with the Monte Carlo simulation using Geant4-UCN code. In this simulation, we assumed a uniform phase space density when UCN are produced in He-II so that the initial energy spectrum of UCN is proportional to $\sqrt{E_{ucn}}$, where E_{ucn} is the UCN kinetic energy. As a result, this simulation well reproduced the UCN energy spectrum obtained in the experiment.

8.3 Future Outlook

Our He-II superthermal UCN source has more capability, after improvement to obtain much more UCN density. In the present UCN source, UCN are produced in the He-II bottle, then they are extracted through the vertical UCN guide. When they go up through the vertical guide, some of them are trapped by the gravity. So the vertical UCN extraction reduces the UCN density. The UCN space density is proportional to $(E_c)^{3/2}$. Based on the present knowledge, we are constructing a new source where the UCN is extracted horizontally so that the UCN density reduction by the gravity is removed and full energy can be used.

The proton beam power from the ring cyclotron at the RCNP is now at 400 W (1 μA $\times$ 392 MeV), which will be increased by a factor of 10, in the near future. The heat deposit on the He-II cryostat by the beam is about 150 mW at 400 W. The cooling power of the ^{3}He cryostat can cover the ten times larger heat deposit at 4 kW beam irradiation without causing temperature rise by use of a more powerful pump. So, ten times larger UCN density can be expected.

The UCN storage time in the UCN source was 81.5 ± 0.6 sec at present. The life time of the wall loss was about 100 sec and suppressed the UCN storage time. According to Ref. [57], the Beryllium coated electropolished stainless steel tube with a 300cm long and 6.7cm inner diameter achieved the UCN storage time of 246 sec at 6.7 K. This result leads to much longer UCN storage time than the present value in our UCN source. About 150 sec UCN storage time can be obtained with the Beryllium coating at low temperature.

Present success of the UCN production leads to the physics experiment such as EDM measurement. Regarding the future EDM experiment, our best estimation of UCN density with the improved horizontal UCN source is 260 UCN cm^{-3} with the critical energy of 90 neV at the EDM cell, with 95 % polarization. With the best condition of the spin relaxation time, the sensitivity of EDM can be as good as the statistical error of 3.6×10^{-26} e cm with the one day running time.

Appendix A

Fermi Potential

For the dataset of scattering lengths and cross sections, see Neutron Data Booklet [58].

A.1 Fermi Pseudo Potential

The Fermi pseudo potential is a potential that an UCN feels on a material surface and it is represented by an abrupt step function. In many cases, the Fermi potential V_F is a positive energy for UCN because most of materials have positive coherent scattering lengths. The order of V_F is about $10^1 \sim 10^2$ neV. The material that has the highest Fermi potential is ^{58}Ni. The Fermi potential of ^{58}Ni is 335 neV.

A surface of a material that has the Fermi potential V_F can reflect UCN with an energy below V_F. A UCN with an energy above V_F penetrates the material surface.

Some of materials have negative scattering lengths. The typical example is hydrogen (H). The scattering length of hydrogen is - 3.7409(11) fm. A material including hydrogen has low or negative Fermi potential because hydrogen's negative scattering length lowers the potential wall. Polyethylene $(CH_2)_n$ is well known as a good neutron absorber, because it has negative Fermi potential. The Fermi potential of polyethylene is - 8.54 neV.

The formula of the Fermi potential for one component material is given by

$$V_F = \frac{2\pi\hbar^2}{m_n} N b_c \tag{A.1}$$

where N is the number density of the material and b_c is the bound coherent scattering length of the material. N is given by $N = \rho N_a/A$ where ρ is the density of the material, N_a is Avogadro's number and A is the mass number.

If a material has many components, the mass number A and the bound coherent scattering length b_c are replaced by as follows.

$$A \to \overline{A} = \sum_i p_i A_i \tag{A.2}$$

$$b_c \to \overline{b_c} = \sum_i p_i b_c^{(i)} \tag{A.3}$$

where p_i is the occupation probability of each component, A_i is the mass number of the ith component and $b_c^{(i)}$ is the bound coherent scattering length of the ith component.

For example, calculate the Fermi potential of stainless steel (SUS316L). The chemical components of SUS316L are 68 % of iron (Fe), 18 % of chromium (Cr), 12 % of nichkel (Ni), and 2 % of molybdenim (Mo). The mass number $\overline{A}$ is given by

$$\begin{aligned} \overline{A} &= \sum_i p_i A_i & \text{(A.4)} \\ &= 0.68 \times A(\mathrm{Fe}) + 0.18 \times A(\mathrm{Cr}) + 0.12 \times A(\mathrm{Ni}) + 0.02 \times A(\mathrm{Mo}) & \text{(A.5)} \\ &= 56.3 & \text{(A.6)} \end{aligned}$$

and the bound coherent scattering length $\overline{b_c}$ is given by

$$\overline{b_c} = \sum_i p_i b_c^{(i)} = 8.45 \text{ [fm]} \ . \tag{A.7}$$

Therefore, the Fermi potential of SUS316L is given as follows.

$$V_F = \frac{2\pi\hbar^2}{m_n} \cdot \frac{\rho N_A}{\overline{A}} \cdot \overline{b_c} = 188 \text{ [neV]} \tag{A.8}$$

Here, the density of SUS316L is $\rho = 7.98$ g/cm^3.

A.2 Material List

Table A.1 shows the Fermi potential of the typical materials.

Material	ρ [g/cm^3]	A	b_c [fm]	V_F [neV]	Comment
Fe	7.874	55.8	9.45	209	-
Al	2.70	27.0	3.449	54	-
Ni	8.908	58.7	10.3	245	-
^{58}Ni	8.908	57.9	14.4	347	-
Cu	8.94	63.5	7.718	170	-
Be	1.85	9.01	7.79	251	-
BeCu(25)	8.36	62.5	7.72	162	Cu(98%), Be(2%)
BeCu(50)	8.83	62.5	7.72	171	Cu(98%), Be(2%)
BeO	3.02	12.5	6.80	257	-
SUS316L	7.98	56.3	8.45	188	Fe(68%), Cr(18%), Ni(12%), Mo (2%)
Ni-P coating	7.8	54.5	9.52	214	Ni(85%), P(15%)
C	2.26	12.0	6.65	196	graphite
SiO_2	2.2	20.0	5.25	90	silica glass
PTFE	2.2	16.7	5.99	124	Teflon, $(C_2F_4)_n$
Polyethylene	0.92	4.68	-0.278	-8.57	$(C_2H_4)_n$
Fomblin	1.89	16.6	5.97	106.5	$(C_3F_6O)_n$
Ti	4.506	47.9	-3.370	-49.7	-
Zn	7.14	65.4	5.680	97	-
He-II	0.145	4.00	3.26	18.6	-

Table A.1: Fermi potential of the typical materials. A and b_c are replaced by $\overline{A}$ and $\overline{b_c}$ about a compound or a composition metal. The chemical formula of fomblin can be approximated to be $(C_3F_6O)_n$ as shown above.

Appendix B

Detector and Circuit

B.1 ^{3}He UCN Detector

We used a ^{3}He gas proportional counter to detect UCN. The counter utilizes the following reaction:

$$n + {}^3\mathrm{He} \rightarrow p + t + 764 \text{ keV} \tag{B.1}$$

The maximum energy of the daughter proton is 191 keV, and that of the triton is 573 keV.

Our UCN detector, type Dunia-10 ([45], [46]), is attached to the end of the gravity accelerator tube. Fig. B.1 shows the views of the Dunia-10 UCN detector.

Figure B.1: (a) The side view of the UCN detector. (b) The top flange of the UCN detector. The inner diameter of the top flange is ϕ 84.9, same as the UCN guides. The aluminum foil with a thickness of 100 μm is used for the entrance window of the detector. Some aluminum grids are installed to support and protect the aluminum window.

The scheme of the UCN detector is shown in Fig. B.2. The gas composed of 10 ± 0.5 Torr ^{3}He, 10 ± 0.5 Torr CO_2 and about 1.1 bar Ar is confined in the gas chamber. The gas chamber

is a cylinder with a diameter of about 120 mm and a height of about 50 mm. The high voltage of +1,100 V is applied on the tungsten gilt thread with a diameter of 50 μm in the gas chamber.

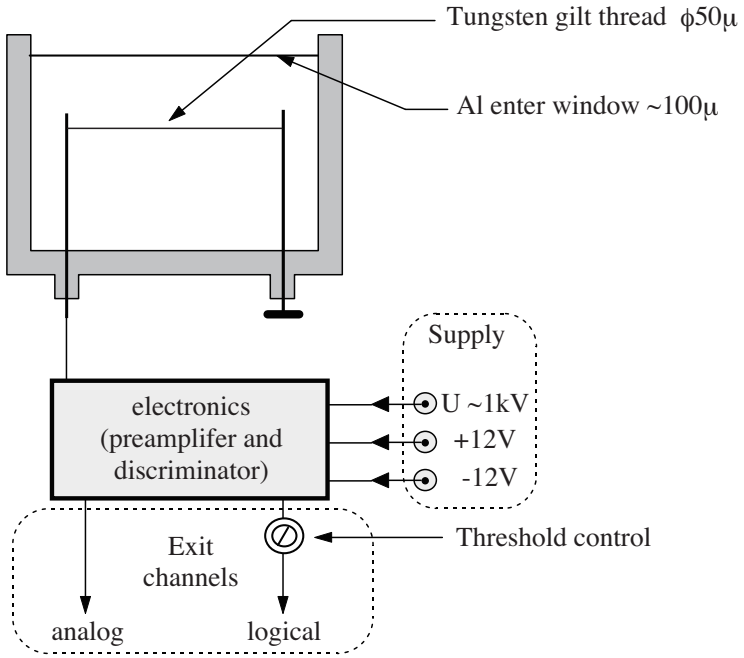

Figure B.2: The scheme of the Dunia-10 UCN detector (from the data sheet of Dunia-10).

The analog signal output from the UCN detector was obtained using a ^{252}Cf neutron source. ^{252}Cf decays by spontaneous fission and emits 3.8 neutrons on average. We surrounded the UCN detector with paraffin blocks and put the ^{252}Cf neutron source inside the paraffin blocks to moderate the emitted neutrons. The observed signal is shown in Fig. B.3.

Then, we measured the pulse height spectrum of the UCN detector. The obtained pulse height spectrum is shown in Fig. B.4. It exhibits a single narrow peak corresponding to the total ionization of the proton and the triton. We adjusted the threshold level of the scaler which is used for the measurement of time spectra of UCN counts. The threshold was adjusted to be 43 ch.

B.2 Detection Efficiency of UCN Detector

The mean free path of UCN in ^{3}He is $l = (n\sigma_a)^{-1}$, where n is the number density of ^{3}He and σ_a is the neutron absorption cross section of ^{3}He. Here, $n = 2.8 \times 10^{17}$ cm^{-3} for 8.6 Torr ^{3}He at a room temperature, and $\sigma_a = 5333(7)$ b for a thermal neutron ($v = 2200$ m/s). It is known that the neutron absorption cross section is proportional to the inverse of the neutron velocity in low energy region, i.e. $\sigma_a \propto 1/v$. For the UCN with the averaged velocity 5.4 m/s in front of the UCN detector, $\sigma_a = 2.2 \times 10^6$ b. Then, $l = 1.5$ cm was obtained. This value is enough long, compared to the size of the gas chamber filled with ^{3}He. Therefore, the detection

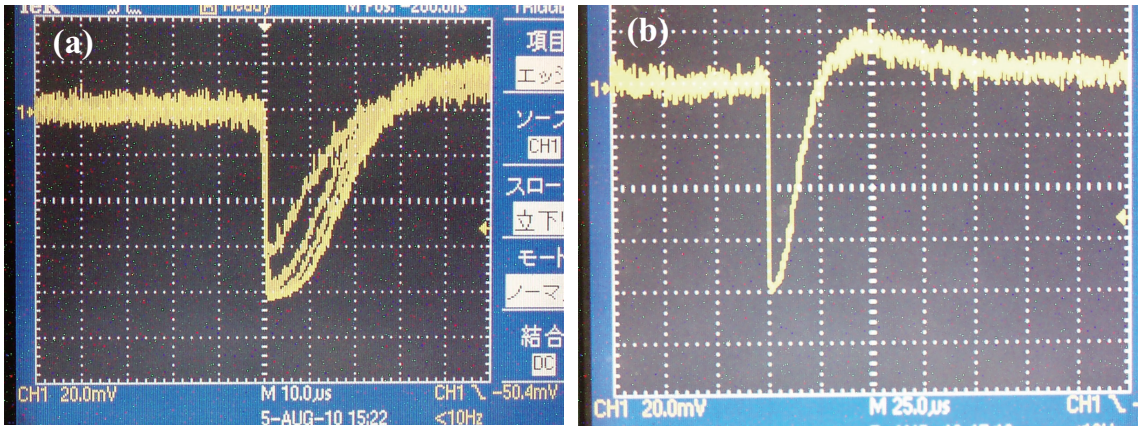

Figure B.3: The analog signal output from the UCN detector. One bin is 20.0 mV × 10.0 μs. ^{252}Cf was used as a neutron source. The paraffin blocks were used to moderate the neutrons emitted from ^{252}Cf. From (b), the length of the overshoot is about 100 μs. Therefore, a count rate of about 10 kHz is the limit of this detector. The colorful dots on the picture are due to radiation damages to CCD.

efficiency of the counting volume itself is almost 100 %.

However, UCN are also absorbed when they go through the aluminum window. In addition to the aluminum foil with a thickness of 100 μm, the aluminum grids installed at the entrance window also absorbs incoming UCN. If we were to assume that UCN are mechanical equilibrium, in other words, UCN motion are perfectly randomized, the aluminum grids and foil can be replaced by an uniform aluminum foil with a certain effective thickness. Considering the mass of the grids, the effective thickness d_{eff} becomes 0.456 mm. The number of the UCN passing through this effective aluminum foil is proportional to $e^{-n\sigma_a d_{eff}}$. Here, n is the number density of aluminum, $n = 1.25 \times 10^{23}$ cm^{-3}. σ_a is the neutron absorption cross section of aluminum. For a thermal neutron, $\sigma_a = 0.231(3)$ b, and for UCN with the averaged velocity 5.4 m/s, $\sigma_a = 93$ b. Then, $e^{-n\sigma_a d_{eff}} = 0.587$ was obtained. The detection efficiency was roughly estimated to be $\varepsilon = 59$ %.

We calculated the detection efficiency ε by the Monte Carlo simulation code (Geant4-UCN). The simulation using this code is well discussed in Chapter 7. We reconstructed the gemoetry of the He-II superthermal UCN source including the gravity accelerator tube and the UCN detector. Then, we produced a number of UCN in the He-II bottle and counted the number of UCN incoming to the UCN detector in the simulation. Then, we removed the aluminum foil and the grids of the UCN detector to confirm the effect of the absorption in the entrance window. We compared the number of incoming UCN with/without the foil and grids. We also simulated the case where an annular disk with a ϕ10 hole was installed in front of the UCN detector. The results are shown in Table. B.1.

We concluded that the detector efficiency without the annular disk is $\varepsilon = 81 \pm 1$ % and the efficiency with the annular disk is $\varepsilon = 70 \pm 2$ %. The detection efficiency differs between two

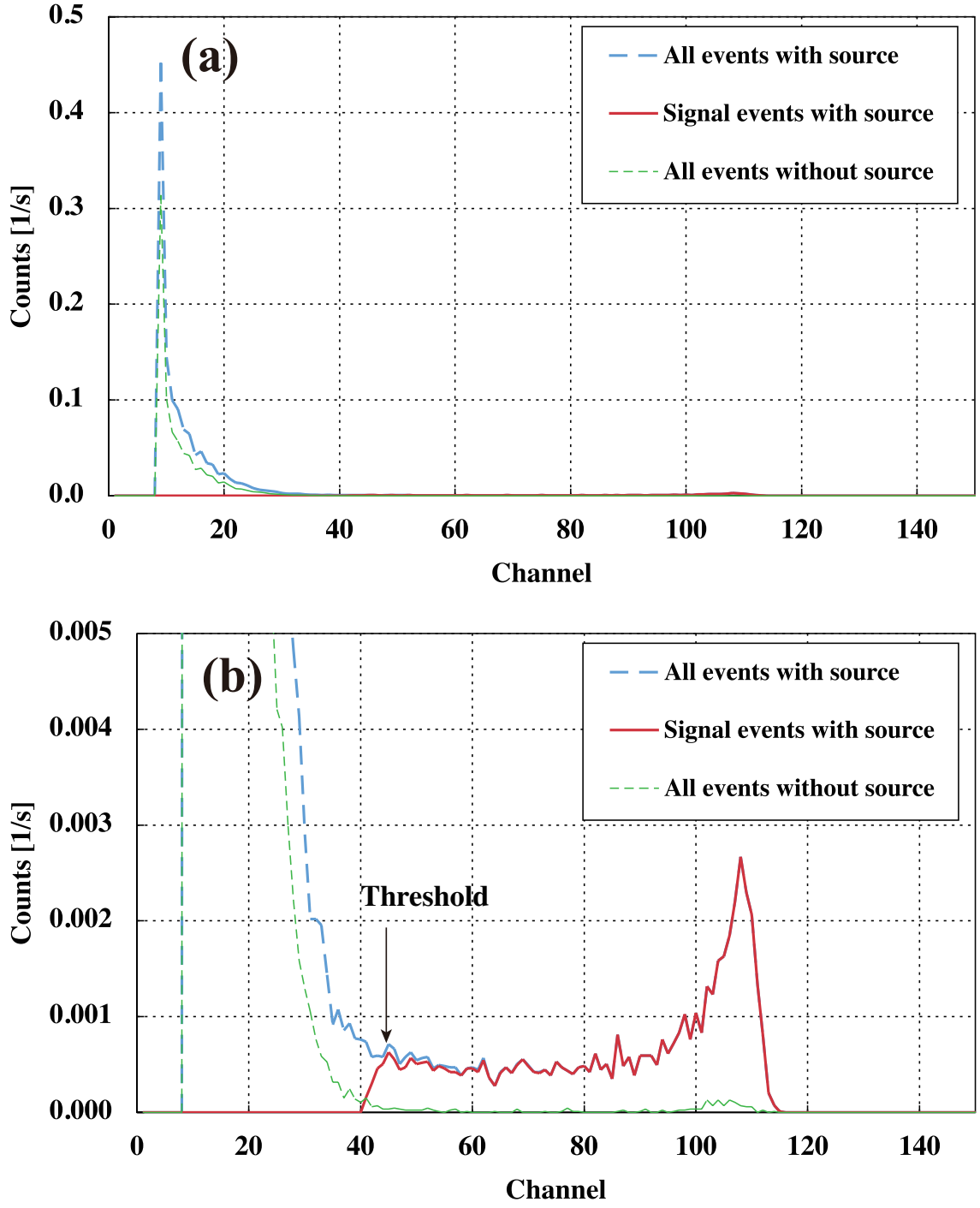

Figure B.4: The pulse height spectrum of the Dunia-10 UCN detector. The blue line shows all events with source, the red lines shows the events discriminated at a certain threshold and the green line shows all events without source, i.e. the back ground. The threshold was adjusted to be 43 ch. The signals above the threshold level are counted by our scaler when we measure the time spectrum of UCN counts.

	with Al foil and grids	without Al foil and grids	ε
without annular disk	9737 ± 99	12025 ± 110	0.810 ± 0.011
with annular disk	1557 ± 39	2233 ± 47	0.697 ± 0.023

Table B.1: The number of the UCN incoming to the UCN detector are shown. Calculation by Geant4-UCN. The number of the produced UCN in the He-II bottle was 10^5. The UCN valve was operated by Delay mode with a delay time of 0 sec. About the UCN valve operation, see Chapter 5.

cases. As a reason, it is deduced that the UCN motion was not perfectly randomized in the case without the annular disk. In such cases, some of UCN go through only the thin aluminum foil and the loss of them is relatively small.

B.3 Electric Circuits

The scheme of the electric circuit for measurement are shown in Fig. B.5. The signal from the analog output of the Dunia-10 UCN detector is sent to the spectroscopy amplifier (S. Amp, ORTEC model 472A). The waveform of the signal is shaped to be a gaussian pulse by the S. Amp. The typical pulse height of the shaped pulse is ~ 2 V and the pulse width is ~ 2.5 μs. The shaped pulse is sent to the scaler installed in a VME crate. The pulse height analyzer is also installed in the VME crate. The pulse height spectrum of Dunia-10 shown in Fig B.4 was taken by this module. The VME crate and the data acquisition computer is connected via the interface module with USB. The view of the VME crate and the modules is shown in Fig. B.6. The module which is labeled "TA17-100" is the scaler and the "KP GATE & PHA" is the pulse height analyzer. The leftmost module is the interface module.

In addition to the signals from the UCN detector, signals from the secondary electron counter (SEC) is counted by the scaler. The SEC is composed of a thin aluminum foil with deposited gold and electrodes. The thin foil is installed on the proton beam line. When the proton beam is irradiated, secondary electrons are emitted from the foil by colliding protons. The secondary electrons are collected by the electric field generated by the electrodes with an applied voltage of 100 V. The current of the secondary electrons is about 5 % of the proton beam. For example, if the proton beam current is 1 μA, the secondary current is about 50 nA. The current from the SEC is digitized by the digital current integrator (ORTEC, model 439) and sent to the scaler. The typical count rate of the SEC is about 500 cps for 1μA proton beam. This count rate is used to normalize the beam intensity.

During the experiments, we have to control the timing of the beam irradiation and the UCN valve operation. The master signal is output by the function generator, Agilent model 33220A. The proton beam gate is made by shaping the master signal by the NIM modules. The trigger signal to start counting is made and sent to the VME crate at the same time. This signal used to start counting is called "kicker" pulse.

The signal to open or close the UCN valve is made by the another function generator, NF model WF-1946A. The master signal is sent to the NF function generator after the pulse shaping by the NIM modules. The NF function generator makes the UCN valve open/close signal after the trigger signal is input. The signals for the UCN valve operation is sent to the control box of the UCN valve.

For the UCN storage experiment using the UCN storage bottle (Section 6), the UCN valve open signal is used to control the filling valve of the UCN storage bottle, and the UCN valve close signal is used to control the emptying valve of the UCN storage bottle.

Since the experiment in November 2008, the electric circuit was partly replaced to the new system using CAMAC (Fig. B.7). The signals to control the proton beam, UCN valve, the filling/emptying valve and the trigger to the scaler are output from the 8-bit output register (OULNS, model 8413) in the CAMAC crate. The timing of each signal is controlled by the sequencer software on the control computer connected to the CAMAC crate controller (model CC-7000).

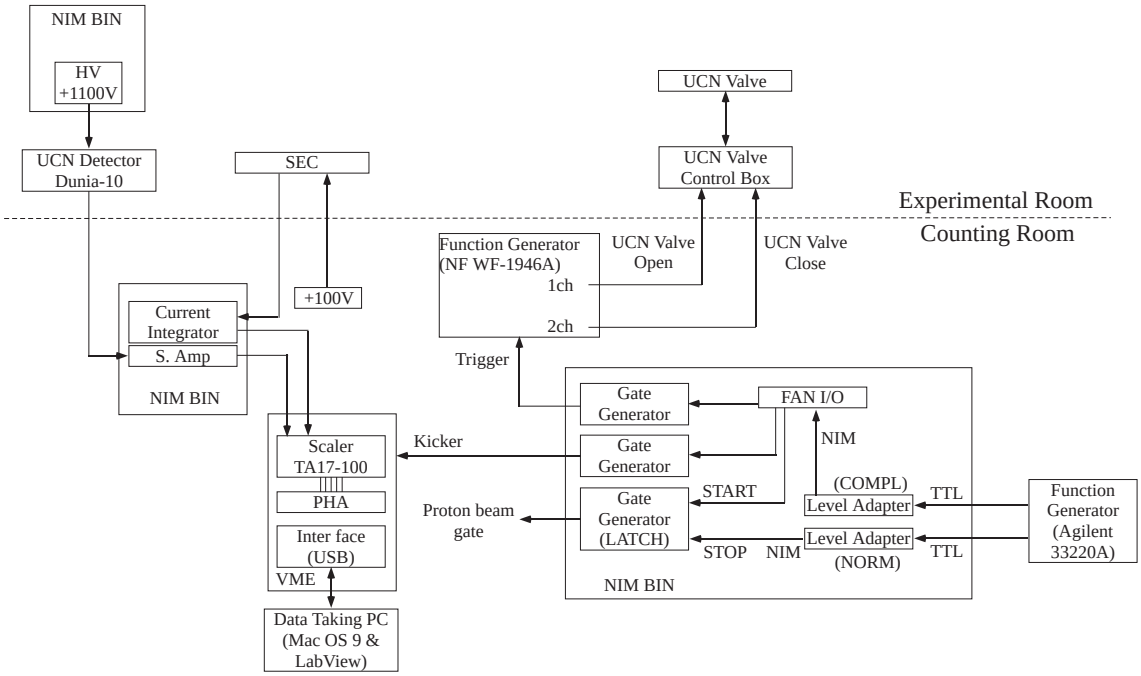

Figure B.5: The diagram of the electric circuit for measurement.

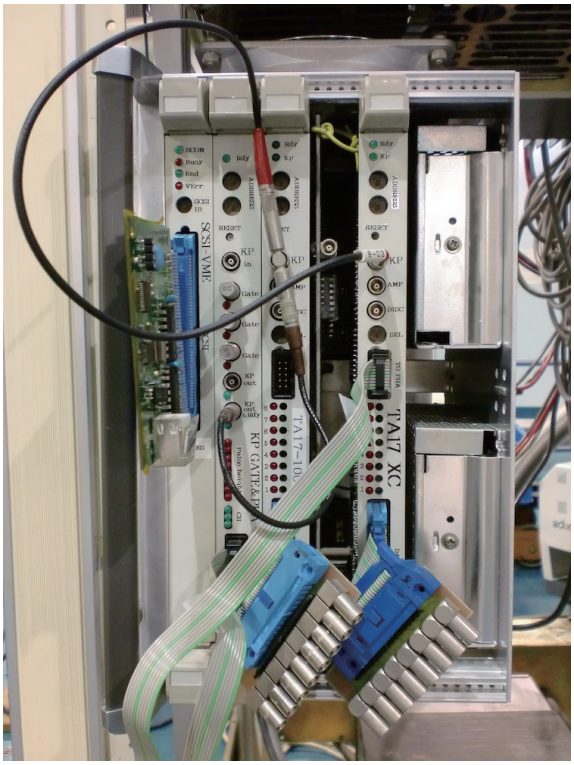

Figure B.6: The view of the VME modules. The leftmost module is the interface to connect between the VME and the data taking PC. The module labeled "KP GATE & PHA" is the pulse height analyzer. The module labeled "TA17-100" is the scaler. The rightmost module labeled "TA17 XC" is the fast scaler and not used for our experiment with UCN.

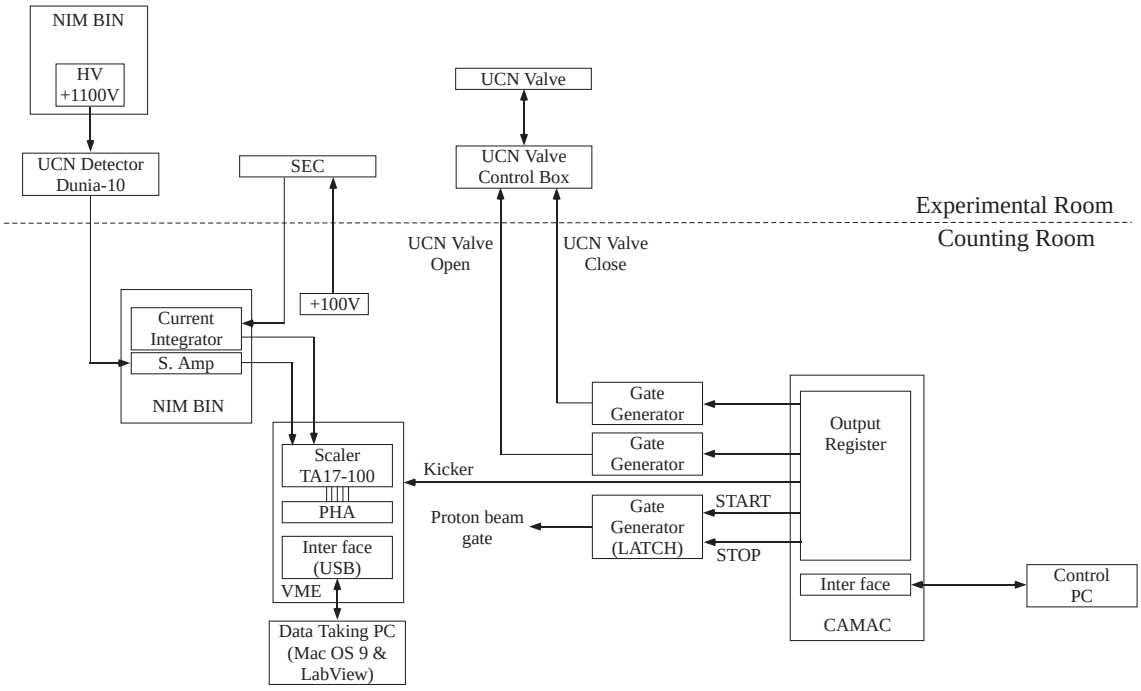

Figure B.7: The diagram of the electric circuit for measurement since November 2008. The function generators and the NIM modules to control the beam irradiation and the valves were replaced by the CAMAC and its control PC. The sequence of the signals is controlled by the software installed on the control PC.

Appendix C

Heat Deposit in UCN Cryostat

Our UCN source is installed just above the lead spallation target. This makes it possible for us to obtain high intensity neutron flux, compared to the neutron extraction through neutron guides. On the other hand, heat deposit by spallation reaction is possible to be heavy heat load on the He-II cooling system, especially when a high power proton beam is used for the spallation reaction. In this chapter, we measured the heat load on our UCN cryostat when the proton beam with a power of 400 W (392 MeV $\times$ 1 μA) was irradiated. And also, we estimated the heat deposit of γ-ray by the Monte Carlo simulation code, PHITS2.

C.1 Heat Deposit by Beam Irradiation

The lead spallation target, D_2O moderators, the apparatuses in the UCN cryostat are activated by the proton beam irradiation, the neutron collisions and the emitted γ-ray from the activated materials. The γ-rays emitted from those activated materials deposit their energies in the He-II. So, the heat deposit becomes heat load on the ^{3}He cryostat. The ideal cooling power of the ^{3}He cryostat was estimated to be 1.7 W in our UCN cryostat. The heat deposit must be covered by this cooling power. Otherwise the temperature of the He-II rises and the UCN loss rate in the He-II increases. In the worst case, the He-II temperature exceeds the lambda point at 2.18 K and changes to be normal fluid helium.

We measured the changes of the ^{3}He flow rate and the temperatures of the He-II cooling system when the 400 W proton beam was irradiated for a long time. The result is shown in Fig. C.1.

In Fig. C.1, the 400 W proton beam was irradiate between 0 sec and 1200 sec. The total beam irradiation time was 20 minutes. The heat deposit in this system during the beam irradiation can be calculated by the change of the ^{3}He flow rate. Just before the beam irradiation, the ^{3}He flow rate was 7.0 SLM. During the beam irradiation, the ^{3}He flow rate increased and was saturated to be 13.2 SLM. The increase of the ^{3}He flow rate was 6.2 SLM. 6.2 SLM corresponds to 0.28 mol/min. The ^{3}He temperature was saturated to be 0.72 K. The latent heat of ^{3}He at 0.72 K is 32 J/mol. Therefore, the heat load on the ^{3}He cryostat is given by 32 J/mol $\times$ 0.28 mol/min = 8.9 J/min = 0.15 W.

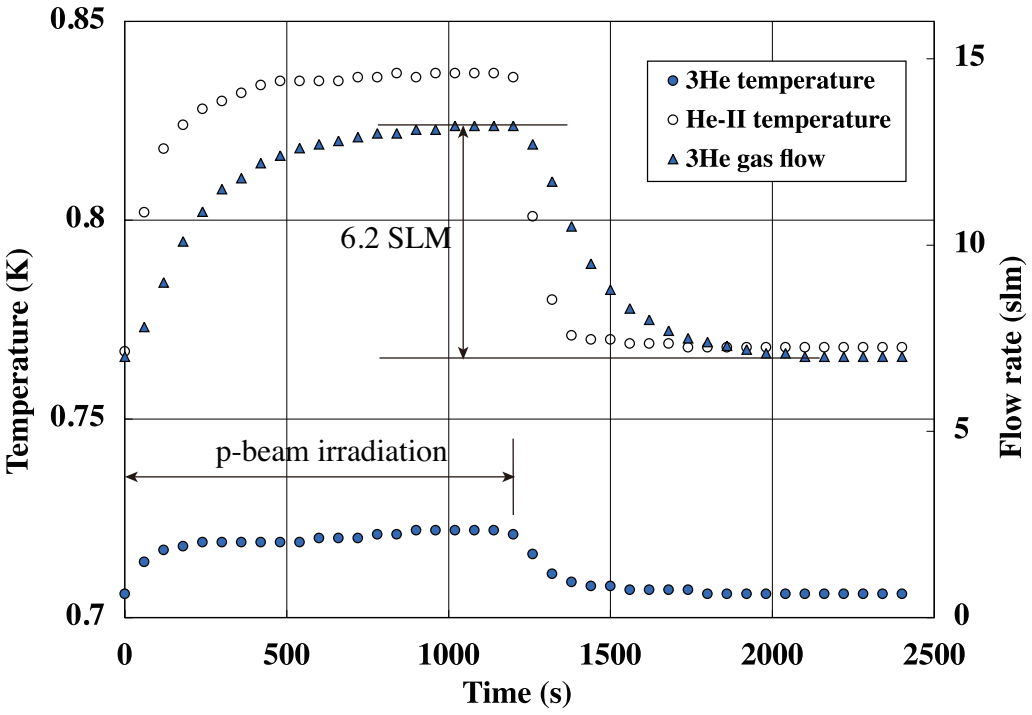

Figure C.1: The changes of the ^{3}He flow rate, the He-II temperature and the ^{3}He cryostat temperature when the 400 W proton was irradiated for 20 minutes. The proton beam irradiation began at 0 sec and ended at 1200 sec.

We also estimated the heat load on the ^{3}He cryostat by using the nichrome wire heaters surrounding the He-II bottle. Fig. C.2 shows the changes of the ^{3}He flow rate and the temperatures of the ^{3}He and the He-II when the heaters was turned on for 20 minutes with a power of 174 mW.

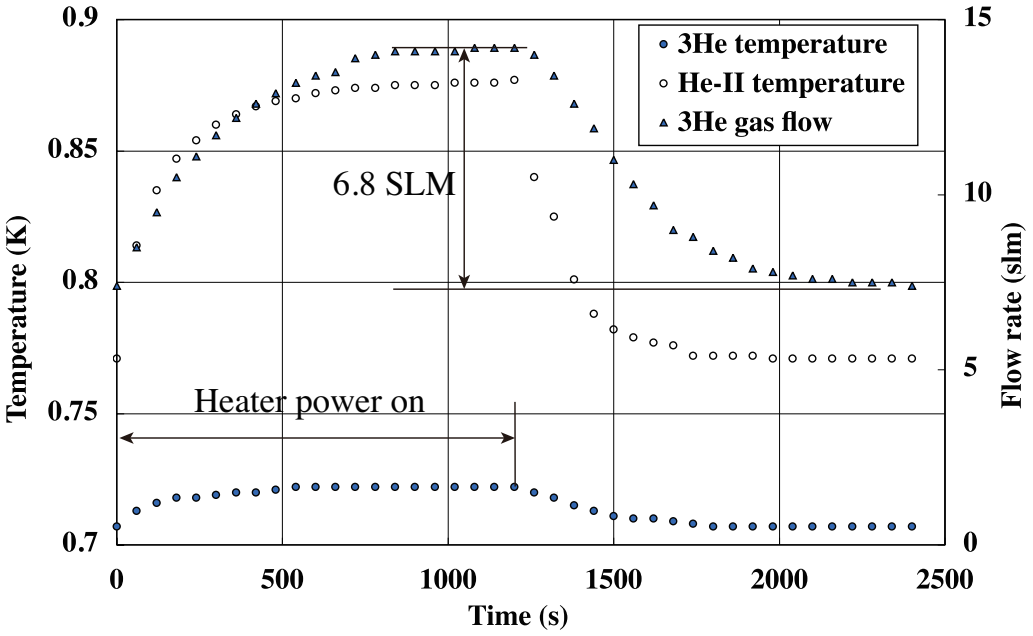

Figure C.2: The changes of the ^{3}He flow rate, the He-II temperature and the ^{3}He cryostat temperature when the heater arround the He-II bottle was turned on with a power of 174 mW. The heater was turned on at 0 sec and turned off at 1200 sec.

Just before the heaters was turned on, the ^{3}He flow rate was 7.4 SLM. The ^{3}He flow rate increased and was saturated to be 14.2 SLM. The increase of the ^{3}He flow rate was 6.8 SLM. Therefore, the 174 mW heat load on the ^{3}He cryostat corresponds to the ^{3}He flow rate increase of 6.8 SLM. The flow rate increase of 6.2 SLM by the beam irradiation corresponds to 174 mW $\times$ 6.2/6.8 = 159 mW. This value is consistent with the estimation using the ^{3}He latent heat.

The heat load induced by the 400 W proton beam irradiation was 0.15 W. Since the ideal cooling power of the ^{3}He cryostat is 1.7 W, our UCN cryostat will work if the proton beam with 10 times larger power (4 kW) is used. If the roots pump (RSV2000) is replaced by the much more powerful pump, the higher cooling power and the lower He-II temperature can be obtained.

C.2 γ-heating Estimation by PHITS2

The heat deposit by γ-ray and charged particles can be calculated by the Monte Carlo simulation code, PHITS2. The geometry of the He-II superthermal UCN source was reconstructed as shown in Fig. C.3. The He-II, He-II bottle, SUS guide and flange, UCN double tube, Heat exchange pot and Cu heat exchanger were also reconstructed in this geometry. These volumes are connected to the ^{3}He cryostat.

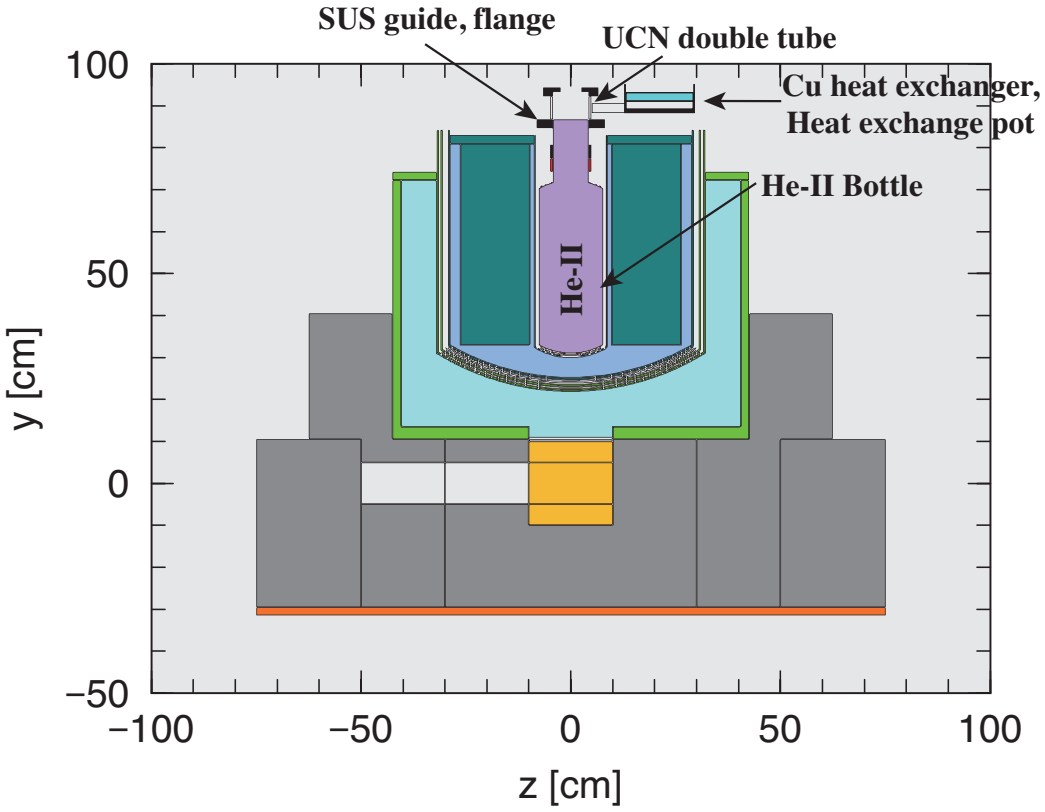

Figure C.3: The geometry of the He-II superthermal UCN source at RCNP reconstructed by PHITS2. The temperature of the solid D_2O moderator is 20 K in this output. The He-II, He-II bottle, SUS guide and flange, UCN double tube, Heat exchange pot and Cu heat exchanger were also reconstructed in this figure.

We calculated the heat deposit by γ-ray (photon) and charged particles in these volumes. The results are shown in Table C.1. Table C.1 shows the heat deposits by photon, neutron, proton and other particles. The other particles include electron, muon, pion, deuteron, triton, ^{3}He and α particle.

According to the calculation of PHITS2, the heat deposit of photons was the largest and the value was 78.2 mW. The heat deposit of neutron was 7.6 mW, that of proton was 3.0 mW, and that of the others was 1.9 mW. The total heat deposit was 90.7 mW.

The heat deposit by location was the largest in the SUS guide and flange because the atomic

	photon [mW]	neutron [mW]	proton [mW]	others [mW]	sum [mW]
He-II	12.88	6.54	1.87	1.50	22.78
He-II bottle	20.57	0.39	1.00	0.16	22.12
SUS guide, flange	33.53	0.07	0.58	0.03	34.21
UCN double tube	7.33	0.05	0.51	0.06	7.95
Heat exchange pot	2.78	0.003	0	0	2.79
Cu heat exchanger	2.90	0.005	0.22	0.0007	3.13
sum	80.0	7.1	4.2	1.7	93.0

Table C.1: Heat deposit by photon and each particle. Others include electron, muon, pion, deuteron, triton, ^{3}He and α particle.

number and the mass ware the largest. It was 32.93 mW. The heat deposit in the volume far from the solid D_2O moderator were small because the intensity of the photon and the particles were small.

The total heat deposit of 90.7 mW is smaller than the experimental value, 0.15 W. The cause of this discrepancy is unknown, but ^{28}Al can be considered to be the heat source. The He-II bottle is made of aluminum, ^{27}Al. ^{28}Al is produced via the radiative neutron caption reaction, i.e. ^{27}Al(n, γ)^{28}Al. ^{28}Al decays to ^{28}Si by β-decay with a life of 2.24 min. This emitted β-rays may deposit their energies in the He-II and the He-II bottle. This β-heating process is considered to be the unknown heat deposit.

Appendix D

Chemical Check of Nickel Coating

Before the experiment in July 2009, we checked the inner surface of the He-II bottle and found a stripped area on its Ni-P coating. The view of the stripped area is shown in Fig. D.1.

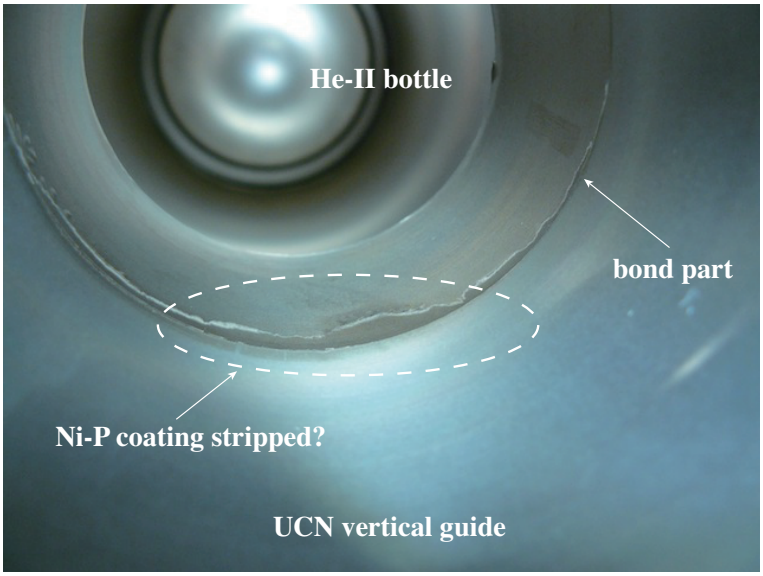

Figure D.1: View of the bond part between the He-II bottle and the UCN vertical guide. The Ni-P coating around the bond part was stripped.

The He-II bottle is made of aluminum. The inner surface of the He-II bottle was galvanized first to form a zinc coating layer on its surface. Then, the electroless nickel plating was done on the zinc coating. The electroless nickel plating was repeated for 3 times, and a Ni-P coating was formed. The thickness of the Ni-P coating is between $10 \sim 15$ μm.

If the Ni-P coating was entirely stripped and the zinc coating was exposed, this stripped area lead to UCN loss because the Fermi potential of zinc is low (97 neV). So, we checked whether this stripped area is nickel or zinc by chemical methods.

D.1 Check of Zinc

First, we checked whether the stripped area was zinc or not. We used aqueous sodium hydroxide (NaOH) and zincon ($C_{20}N_{16}N_4O_6S$). This check was done as follows.

1. Put a drop of NaOH of 10% on the stripped area.
2. Wait for 15 minutes. If the surface is zinc, zinc dissolves to the drop of NaOH.
3. Transfuse the drop of NaOH to a slip of paper.
4. Put a drop of zincon on the slip of a paper. If zinc dissolved to the drop of NaOH, the drop of zincon change the color to blue.

As a result of the check, the stripped area was not zinc. The color of zincon did not changed. And also, although aluminum dissolves to NaOH, there was no bubbling in the drops of NaOH. Therefore, it was concluded that the stripped area was not aluminum, either.

D.2 Check of Nickel

Then, we checked whether the stripped area was nickel or not. We used dilute nitric acid (HNO_3) and dimethylglyoxime ($CH_3C(N{=}OH)C(N{=}OH)CH_3$). This check was done as follows.

1. Put a drop of HNO_3 of 2.5% on the stripped area.
2. Wait for 2 minutes. If the surface is nickel, nickel dissolves to the drop of HNO_3.
3. Transfuse the drop of HNO_3 to a slip of paper.
4. Put a drop of dimethylglyoxime on the slip of a paper.
5. Put a drop of NaOH of 10% on the slip of a paper to alkalinize the mixed drop of HNO_3 and dimethylglyoxime. If nickel dissolved to the mixed drop, the mixed drop change the color to pink.

As a result of the check, the color of the mixed drop changed to pink. It was confirmed that the stripped area was nickel.

The Ni-P coating of the He-II bottle consists of 3 thin layers of nickel. In this time, it is suggested that only the top layer was stripped and the sub-layers were not dameged.

Appendix E

Geant4 Simulation for UCN

In Chapter 7, we used a Monte Carlo simulation code (Geant4-UCN) developed by F. Atchison et al.([59], [60]) to analyze the experimental results. Before the main analysis, we tested the validity of the code by some simple geometries. In the process of the simulation, some bugs were found. In this appendix, we report the validity check of Geant4-UCN code by simple geometries and the fix of the bugs.

E.1 Process

In Geant4-UCN code, UCN is introduced as a new type of particle which is affected by gravity. For interactions between UCN and materials, material boundary process and bulk material process are implemented. Material boundary process treats reflection of UCN. Bulk material process treats scattering and absorption of UCN in a material.

We first discuss reflection of UCN. Whether a UCN is reflected on a material surface depends on the UCN energy E, its incident angle θ_i and the Fermi potential V. The Fermi potential V is implemented as a parameter input by an user. The critical velocity of the material v_c is calculated from the Fermi potential, i.e., $V = m_n v_c^2/2$. If the normal velocity component v_n is smaller than v_c, the UCN will be reflected and different reflection models can be applied.

Specular and diffuse reflection are implemented as the reflection models. The user can specify the probability for either process to happen. We specified the probability f for diffuse reflection and the probability $(1 - f)$ for specular reflection. For example, $f = 0.04$ was used for the simulation shown in Chapter 7. It should be noted that this is a simple approach. Other models describing the influence of surface roughness are discussed in Ref.[50].

For diffuse reflection, the usual cosine distribution is implemented for the reflected intensity (Lambert's cosine law). The reflected intensity $P(\theta_f, \phi_f)d\Omega$ is given by

$$P(\theta_f, \phi_f)d\Omega \propto \cos\theta_f d\Omega \tag{E.1}$$

where θ_f and ϕ_f are the reflected angle and the azimuthal angle, respectively. For specular reflection, $\theta_i = \theta_f$ and $\phi_f = 0$.

The wall loss process is implemented for UCN reflected on the surface. The loss probability per wall collision μ is a function of E, θ_i and V and is written as :

$$\mu(E, \theta_i) = 2\eta\sqrt{\frac{E\cos^2\theta_i}{V - E\cos^2\theta_i}} = 2\eta\left(\frac{v_n/v_c}{\sqrt{1-(v_n/v_c)^2}}\right) \tag{E.2}$$

where η is the material dependent loss factor.

If the normal velocity component v_n is larger than v_c, the UCN can be reflected or it enters the material and can be scattered or absorbed (bulk material process). The amplitude of the reflected wave is given by

$$R = \frac{\sqrt{E_\perp} - \sqrt{E_\perp - V}}{\sqrt{E_\perp} - \sqrt{E_\perp + V}} \tag{E.3}$$

where $E_\perp = m_n v_n^2/2$ and the probability for reflection is given by $|R|^2$.

The absorption for UCN entering the material is calculated via an exponential attenuation law with the absorption cross-sections proportional to $1/v'$, where v' is the velocity of UCN in the material and is given by $v' = \sqrt{2(E-V)/m_n}$.

The scattering process is divided into elastic scattering and up-scattering, i.e. inelastic scattering to energies above the UCN regime. Elastic scattering is treated by calculating a mean-free path for the particle using user-defined scattering cross-sections. This elastic scattering can change only the direction of UCN motion. Up-scattering is calculated in the same way as the elastic scattering, but the up-scattered UCN are lost in the simulation, i.e. the process of the up-scattered UCN is killed.

E.2 Test by Simple Geometries

Fermi Potential

We placed a plate with a Fermi potential of 188 neV at a center of the simulation space. There is a spherical detector (4π detector) around the plate at the center. Fig. E.1 shows the scheme of the geometry. We produced 1000 UCN near the plate and calculated the number of UCN reflected on the plate surface and the number of UCN transmitting the plate, changing the energy of the produced UCN. Fig. E.2 shows the results. The number of reflected UCN were proportional to R^2 and the number of transmitting UCN were proportional to $1 - R^2$. It was confirmed that the Fermi potential worked well.

Wall Loss

We tested the wall loss process with the same geometry as Fig. E.1. We configured the wall loss parameter $\eta = 1.0 \times 10^{-2}$, the UCN energy $E = 131$ neV and the incident angle $\theta_i = 0$

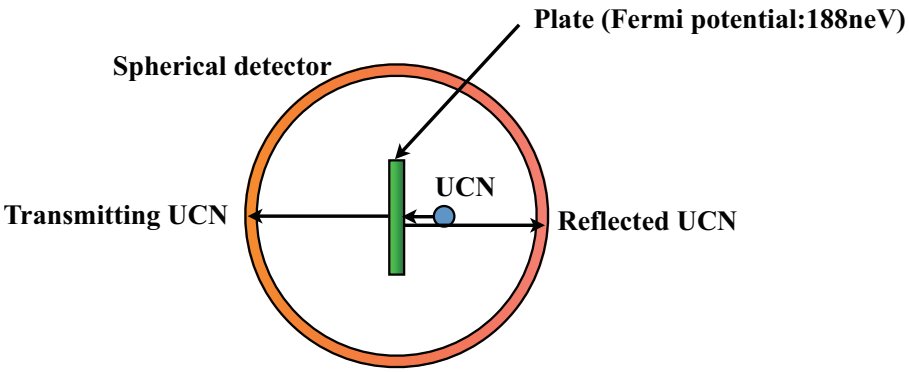

Figure E.1: Scheme of the geometry for the test of Fermi potential.

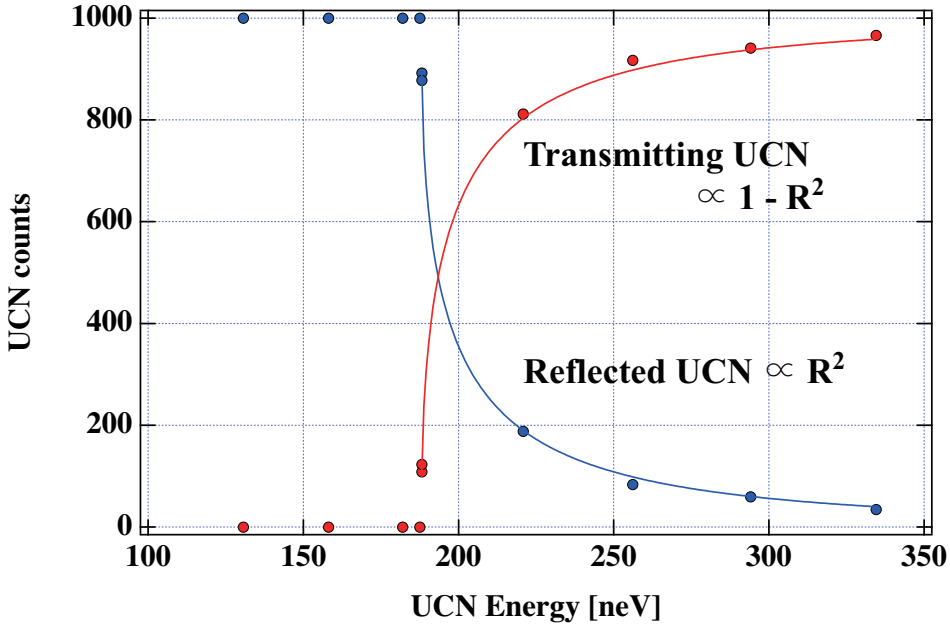

Figure E.2: Number of the reflected UCN and the transmitting UCN as a function of the energy.

degree. In this case, the wall loss probability per bounce on the plate $\mu(E, \theta_i)$ is 3.02^{-2}. We produced 10,000 UCN. Since the energy is smaller than the Fermi potential of the plate, all the UCN is expected to be reflected on the plate and the number of UCN lost on the plate will be $10,000 \times \mu = 300$ UCN.

As a result of the simulation, the number of the reflected UCN was 9,688. This was consistent with the theoretical expectation. It was confirmed that the wall loss process worked well.

Reflection Model

To test how the reflection model works, we placed a plate with a diffuse reflection f and a detector as shown in Fig. E.3. The detector covers the angle θ of 10 degree. We irradiated UCN with an incident angle θ_i of 45 degree. The UCN energy is smaller than the Fermi potential of the plate for the colliding UCN to be reflected.

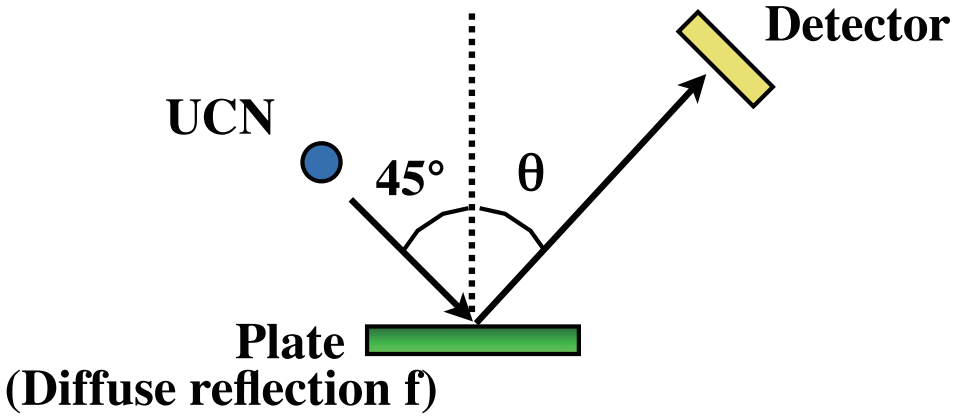

Figure E.3: Scheme of the geometry for the test of reflection model.

We first configured the diffuse reflection probability of the plate to be $f = 1.0$. In this case, all the UCN are reflected diffusely, and the reflected intensity $P(\theta_f, \phi_f)d\Omega$ should be proportional to $\cos\theta_f d\Omega$. Fig. E.4 shows the angular distribution of the reflected UCN. We confirmed that $P(\theta_f, \phi_f)d\Omega = \cos\theta_f d\Omega$.

Then, we configured the diffuse reflection probability to be $f = 0.5$. In this case, 50 % of the colliding UCN are reflected specularly, and observed at the detector when the detector is placed at $\theta = 45°$. Since the number of the produced UCN is 10,000, the number of UCN observed at $\theta = 45°$ should be 5,000. Fig. E.5 shows the angular distribution of the reflected UCN. Just as our expectation, the number of UCN observed at $\theta = 45°$ was about 5,000.

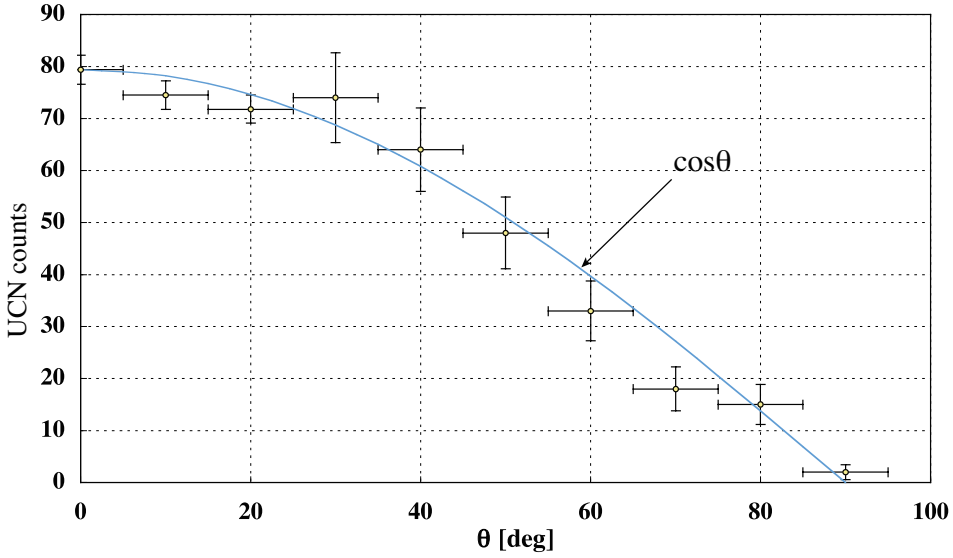

Figure E.4: The reflected intensity $P(\theta_f, \phi_f)$ in the case of $f = 1.0$.

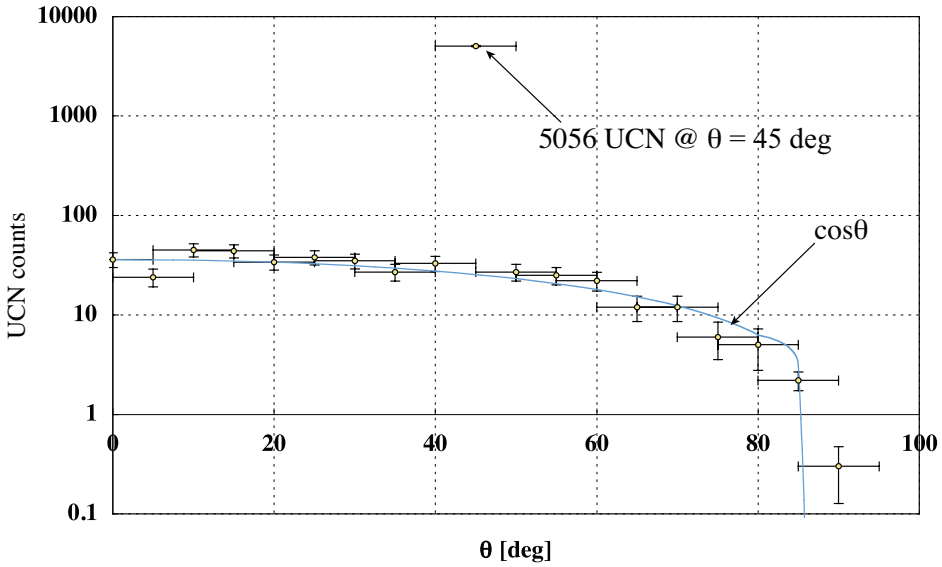

Figure E.5: The reflected intensity $P(\theta_f, \phi_f)$ in the case of $f = 0.5$. The number of the UCN reflected into $\theta_f = 45°$ was about 5,000.

E.3 Bug Fix

We found a bug in the code that controls time dependent volumes like the UCN valve. Fig. E.6 shows the one example of the time spectrum obtained by the simulation of the UCN storage bottle. In this example, the emptying valve was opened at 45 sec as shown in the figure. However, before the emptying valve was opened, UCN counts were observed between $t = 0$ s and $t = 45$ s. It looked like that the emptying valve became transparent.

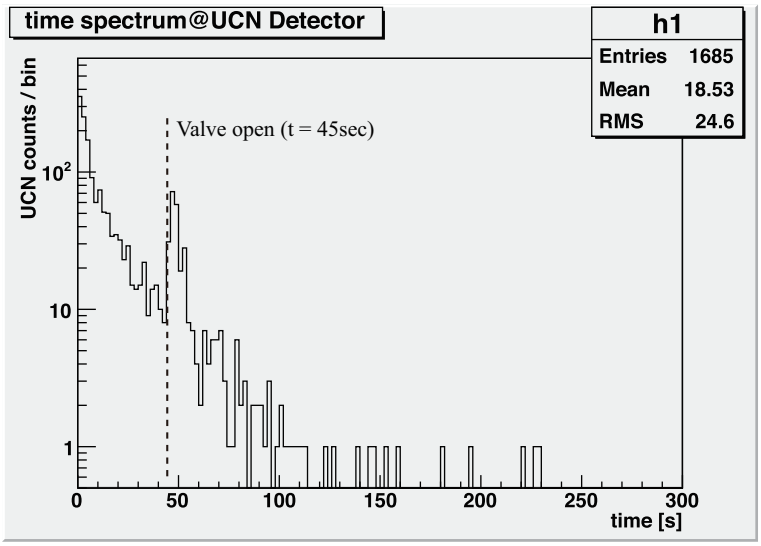

Figure E.6: One example of the time spectrum by the simulation of the UCN storage bottle. In this spectrum, the emptying valve was opened at 45 sec. However, before the emptying valve opening, UCN counts were observed between $t = 0$ s and $t = 45$ s.

Here, we explain the sequence of the time dependent volume in Geant4-UCN.

1. When UCN enters the time dependent volume, Geant4-UCN compares the particle time and the open time of the time dependent volume defined by the user.

2. If the particle time is between the open time of the time dependent volume, the parameters of the time dependent volume (Fermi potential and cross-sections) are overwritten to 0. The time dependent volume becomes transparent. UCN can pass through the time dependent volume. During this time, the initial settings of the parameters are saved in temporary parameters.

3. When this UCN goes out from the time dependent volume, the parameters of the time dependent volume are restored from the temporary parameters and configured to be the initial settings.

First, we thought that something like a memory leak caused this problem. We expected that the memory leak destroyed the information of the temporary parameters, and the system

could not restore the parameters of the time dependent volume. So, we deleted the dangerous functions that possibly cause the memory leak in the code and changed the memory allocation in the process of the valve operation. After the fix, we calculated this example again. The result is shown in Fig. E.7. It looked like that the problem was perfectly removed. However, the problem occurred again.

One more possibility of the cause is β-decay. If a UCN decays when it is inside the time dependent volume, the process of the UCN is shut down and the next process begins. In this case, the parameters of the time dependent volume is not restored because they are restored when the UCN goes out from the volume. So, the time dependent volume is remained to be transparent. To solve this problem, we inserted the new code to check the values of the parameters of the time dependent volume before the valve opening. If the parameters are 0, the new code kills all the processes and shuts down the program.

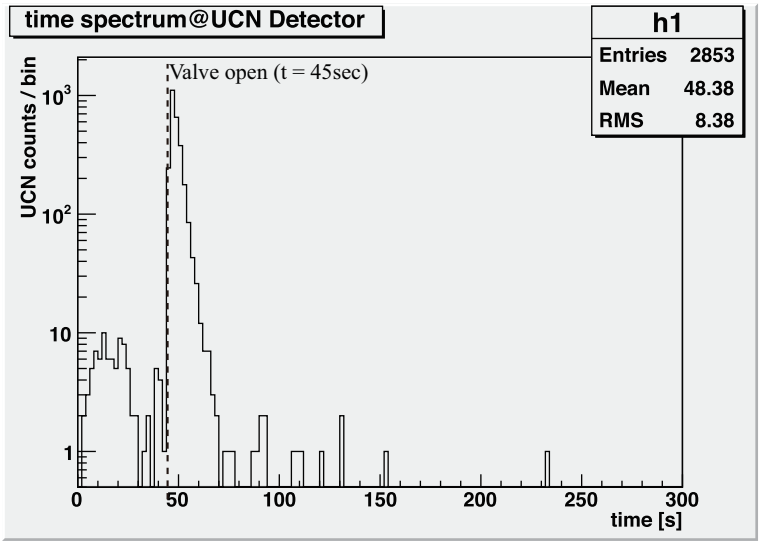

Figure E.7: Time spectrum by the simulation of the UCN storage bottle after the code fix. The emptying valve was opened at 45 sec. Anomaly of UCN counts before the emptying valve opening was removed. UCN counts observed between $t = 0$ s and $t = 45$ s are UCN leaking through the gap of the emptying valve.

E.4 Transmission in Elbow Guide

At the experimental port of the UCN source, the elbow guide and the gravity accelerator tube are attached. We have to know the transmission rate of UCN in this elbow guide to estimate the UCN density at the experimental port. We calculated it by Geant4-UCN. The simulation with a bending guide was also done. The results are shown here.

Fig. E.8 and Fig. E.9 shows the geometry for the simulation, respectively. We produced 1000 UCN at the end of the straight guide ($(x, y, z) = (0, 0, 0)$ in the figures) and observed the UCN counts by the UCN detector attached at the opposite end. The UCN critical energy is $E_c = 188$ neV and the UCN energy spectrum is proportional to $\sqrt{E}$. The gravity interaction was removed in this simulation.

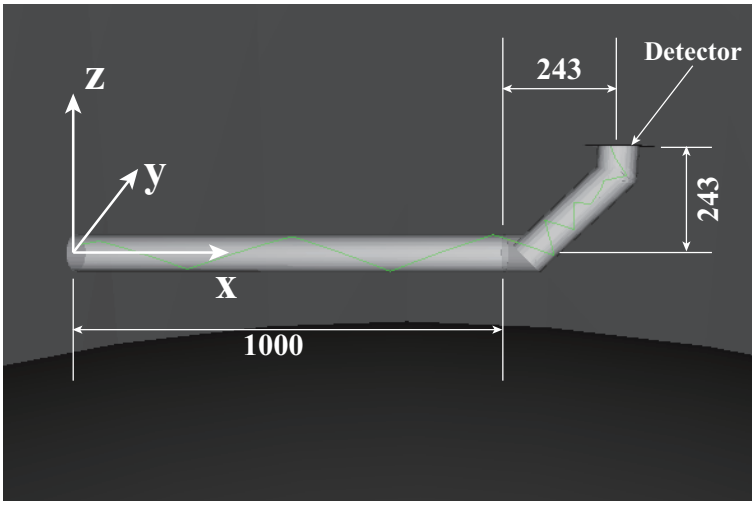

Figure E.8: Geometry of the elbow guide by Geant4-UCN. The green line is a trajectory of UCN. The UCN detector is attached at the end of the elbow guide. The diameter of the guide is 84.9 mm. The material of the guide is SUS316L with a Fermi potential of 188 neV. The diffuse reflection probability is $f = 0$ and the wall loss parameter is $\eta = 0$.

As a result of the simulation, the number of UCN observed at the UCN detector was obtained as shown in Table E.1. The transmission rate of the elbow guide was used to estimate the UCN density at the experimental port in Chapter 7.

	UCN counts at detector	Transmission rate
Elbow guide	480 ± 22	0.480 ± 0.022
Bending guide	433 ± 21	0.433 ± 0.021

Table E.1: UCN counts observed at the UCN detector attached at the end of the elbow or the bending guide. Each transmission rate is also shown.

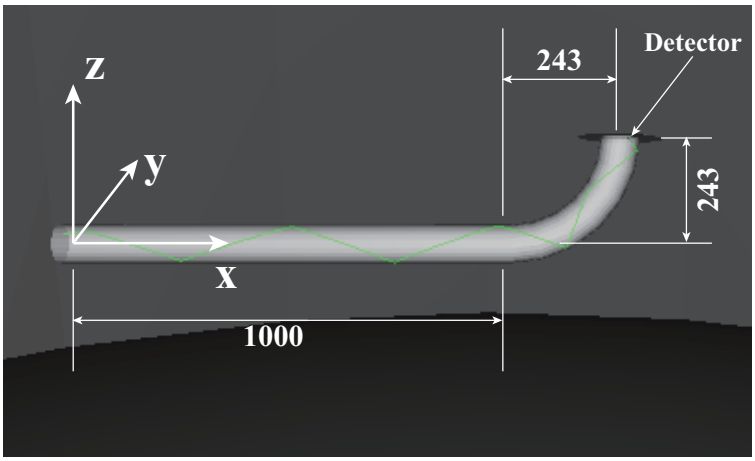

Figure E.9: Geometry of the bending guide by Geant4-UCN. The green line is a trajectory of UCN. The UCN detector is attached at the end of the bending guide. The settings of the geometry is same as Fig. E.8.

Appendix F

Error Propagation

Here, we note the error propagation. We consider n parameters a_1, a_2, a_3, ..., a_n. Here, each parameter has a symmetric standard deviation Δa_1, Δa_2, Δa_3, ..., Δa_n, respectively. In this case, we calculated the error propagation by use of the law of propagation of error. Namely, if a parameter b is given by a function $f(a_1, a_2, a_3, ..., a_n)$, the error of b is calculated as follows.

$$\Delta b = \sqrt{\left(\frac{\partial f}{\partial a_1}\right)^2 (\Delta a_1)^2 + \left(\frac{\partial f}{\partial a_2}\right)^2 (\Delta a_2)^2 + ... + \left(\frac{\partial f}{\partial a_n}\right)^2 (\Delta a_n)^2} \tag{F.1}$$

This is the well known law of propagation of error.

In our analysis, there are cases where parameters have asymmetric errors. For example, the UCN storage time is obtained by fitting with an exponential function, $f(x) = A\ \exp(-a \cdot x)$. The fitting result of the parameter a has a symmetric error Δa, i.e., $a \pm \Delta a$. The UCN storage time τ and its error are given as follows.

$$\tau = \frac{1}{a} \tag{F.2}$$

$$\Delta\tau_+ = \frac{1}{a - \Delta a} - \frac{1}{a} \tag{F.3}$$

$$\Delta\tau_- = \frac{1}{a} - \frac{1}{a + \Delta a}\ . \tag{F.4}$$

The UCN storage time including the errors is given by $\tau^{+\Delta\tau_+}_{-\Delta\tau_-}$.

If more than 2 parameters have asymmetric parameters, the above method cannot be used. In such case, we calculated the error propagation as follows.

We consider 2 parameters a and b. Each parameter has an asymmetric error, i.e., $a^{+\Delta a_+}_{-\Delta a_-}$ and $b^{+\Delta b_+}_{-\Delta b_-}$. When there is a parameter c which is given by a function $f(a, b)$, we calculate the

following 9 values.

$$f_1 = f(a + \Delta a_+, b + \Delta b_+) \quad \text{(F.5)}$$
$$f_2 = f(a + \Delta a_+, b) \quad \text{(F.6)}$$
$$f_3 = f(a + \Delta a_+, b - \Delta b_-) \quad \text{(F.7)}$$
$$f_4 = f(a, b + \Delta b_+) \quad \text{(F.8)}$$
$$f_5 = f(a, b) \quad \text{(F.9)}$$
$$f_6 = f(a, b - \Delta b_-) \quad \text{(F.10)}$$
$$f_7 = f(a - \Delta a_-, b + \Delta b_+) \quad \text{(F.11)}$$
$$f_8 = f(a - \Delta a_-, b) \quad \text{(F.12)}$$
$$f_9 = f(a - \Delta a_-, b - \Delta b_-) \quad \text{(F.13)}$$

c is given by $c = f_5 = f(a, b)$. Here, we write the parameter c as $c^{+\Delta c_+}_{-\Delta c_-}$. Δc_+ is given by subtracting f_5 from the maximum value of f, and Δc_- is given by subtracting the minimum value of f from f_5. If we assume that f_1 is the maximum value of f and f_9 is the minimum value of f, Δc_+ and Δc_- are given by

$$\Delta c_+ = f_1 - f_5 \quad \text{(F.14)}$$
$$\Delta c_- = f_5 - f_9 \ . \quad \text{(F.15)}$$

When considering more than 3 parameters, we calculated the function $f = f(a_1, a_2, ..., a_n)$ with respect to all combinations of the parameters and the errors. And we subtracted $f(a_1, a_2, ..., a_n)$ from the maximum vale of f, and subtracted the minimum value of f from $f(a_1, a_2, ..., a_n)$.

Note that this method replaces the probability distribution of each parameter by an uniform probability distribution which ranges $(a - \Delta a_-)$ to $(a + \Delta a_+)$.

Appendix G

Time Spectra with P.E. disk

In Chapter 6, we showed the time spectra obtained by the UCN storage experiment with P.E. disk at a height of 84.5 cm and 5 cm. In addition to $h = 84.5$ and 5 cm, we measured the time spectra between 10 and 80 cm. In this chapter, we show the obtained time spectra and the time dependence of the total UCN counts at each height. The tables of the measured UCN counts are also shown here.

h = 80 cm

The obtained time spectra is shown in Fig. G.1. The time dependence of the total UCN counts is shown in Fig. G.2. Fitting this curve, the UCN storage time was obtained to be 163 ± 4 sec. The total UCN counts at each delay time are shown in Table G.1.

Delay Δt [s]	total UCN counts
0	10844 ± 580
12	9799 ± 531
25	8931 ± 486
50	7462 ± 411
100	5212 ± 261
150	4020 ± 239
200	2923 ± 183
250	2434 ± 157
300	1590 ± 114
400	991 ± 82
500	457 ± 49

Table G.1: The total UCN counts obtained with the P.E. disk at a height of 80 cm.

h = 75 cm

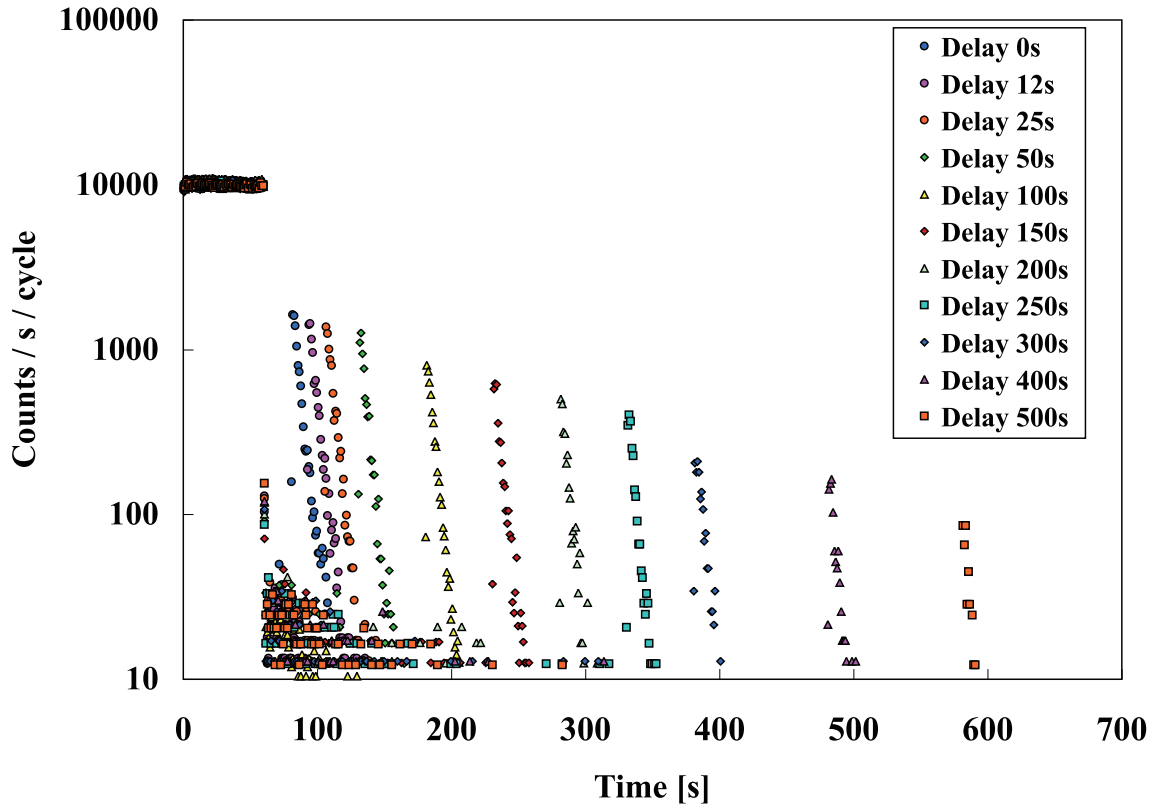

Figure G.1: Time spectra in the UCN storage experiment with the P.E. disk. The height of the P.E. disk was 80.0 cm. The delay time Δt were 0, 12, 25, 50, 100, 150, 200, 250, 300, 400 and 500 sec.

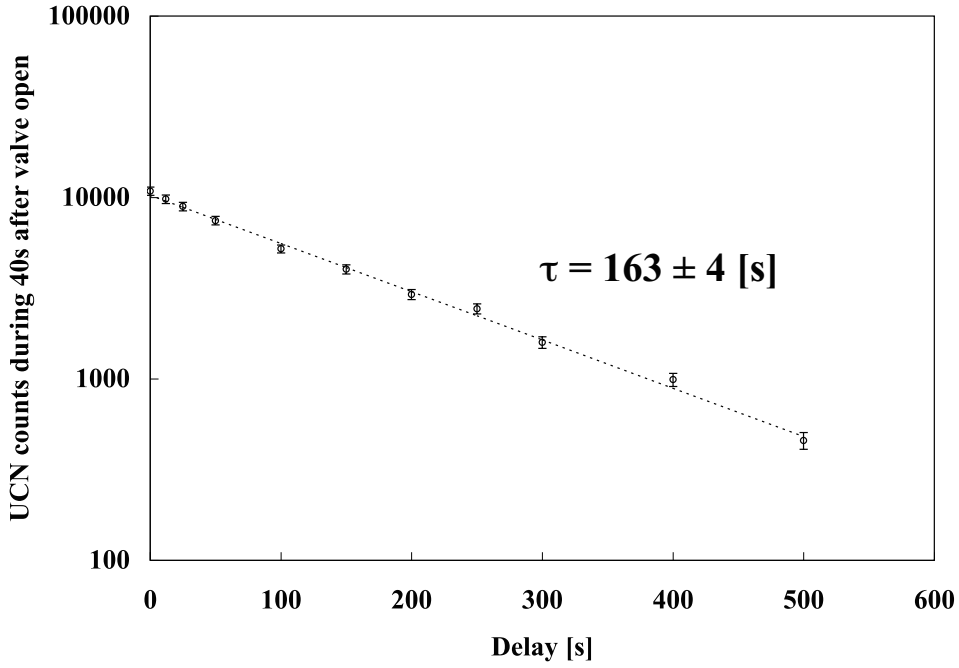

Figure G.2: The total UCN counts as a function of the delay time. The height of the disk h was 80.0 cm. The UCN storage time was 163 ± 4 sec.

The obtained time spectra is shown in Fig. G.3. The time dependence of the total UCN counts is shown in Fig. G.4. Fitting this curve, the UCN storage time was obtained to be 163^{+12}_{-10} sec. The total UCN counts at each delay time are shown in Table G.2.

Delay Δt [s]	total UCN counts
0	10561 ± 584
50	6830 ± 389
100	4940 ± 248
200	2593 ± 170

Table G.2: The total UCN counts obtained with the P.E. disk at a height of 75 cm.

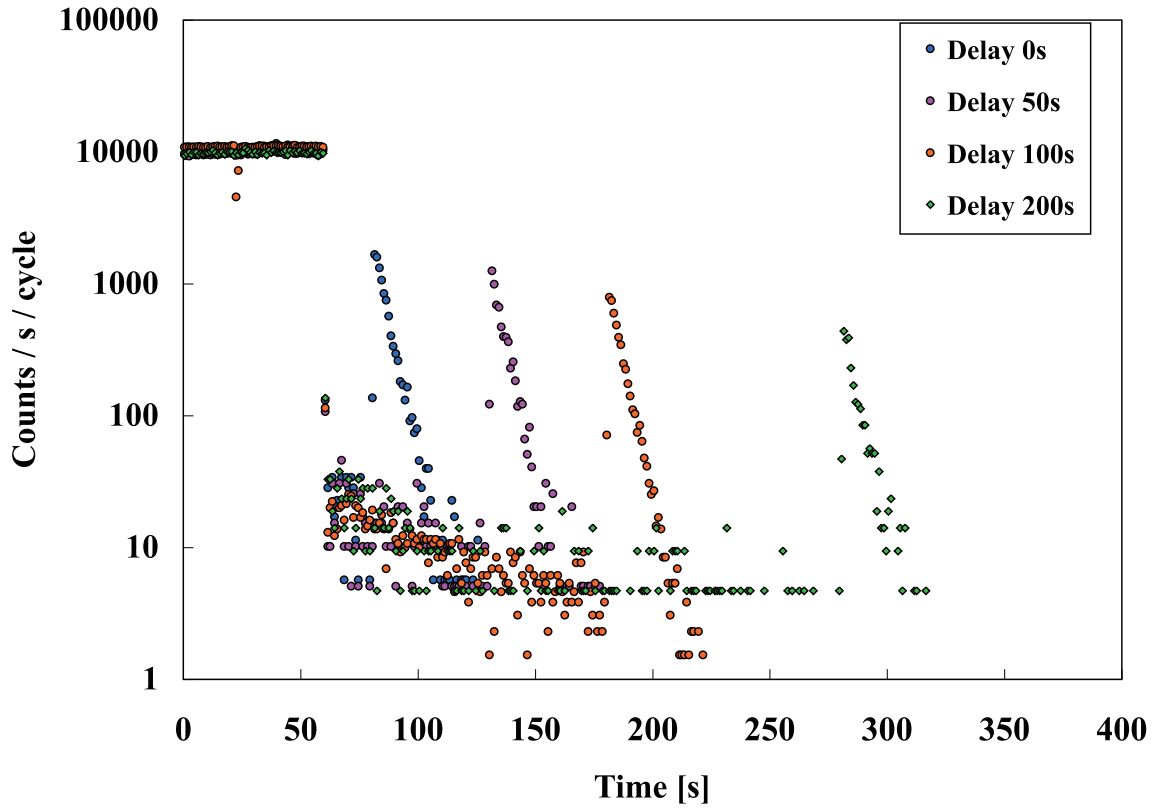

Figure G.3: Time spectra in the UCN storage experiment with the P.E. disk. The height of the P.E. disk was 75 cm. The delay time Δt were 0, 50, 100 and 200 sec.

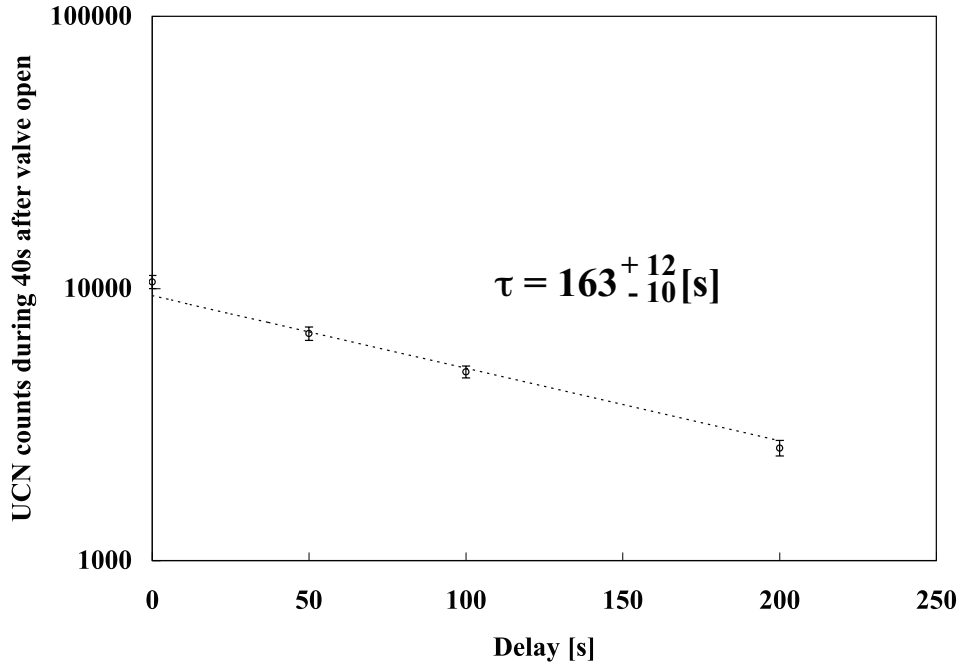

Figure G.4: The total UCN counts as a function of the delay time. The height of the disk h was 75 cm. The UCN storage time was 163^{+12}_{-10} sec.

h = 70 cm

The obtained time spectra is shown in Fig. G.5. The time dependence of the total UCN counts is shown in Fig. G.6. Fitting this curve, the UCN storage time was obtained to be 163 ± 5 sec. The total UCN counts at each delay time are shown in Table G.3.

Delay Δt [s]	total UCN counts
0	9616 ± 512
100	4366 ± 220
200	2416 ± 154
300	1473 ± 105
400	838 ± 73
500	383 ± 46

Table G.3: The total UCN counts obtained with the P.E. disk at a height of 70 cm.

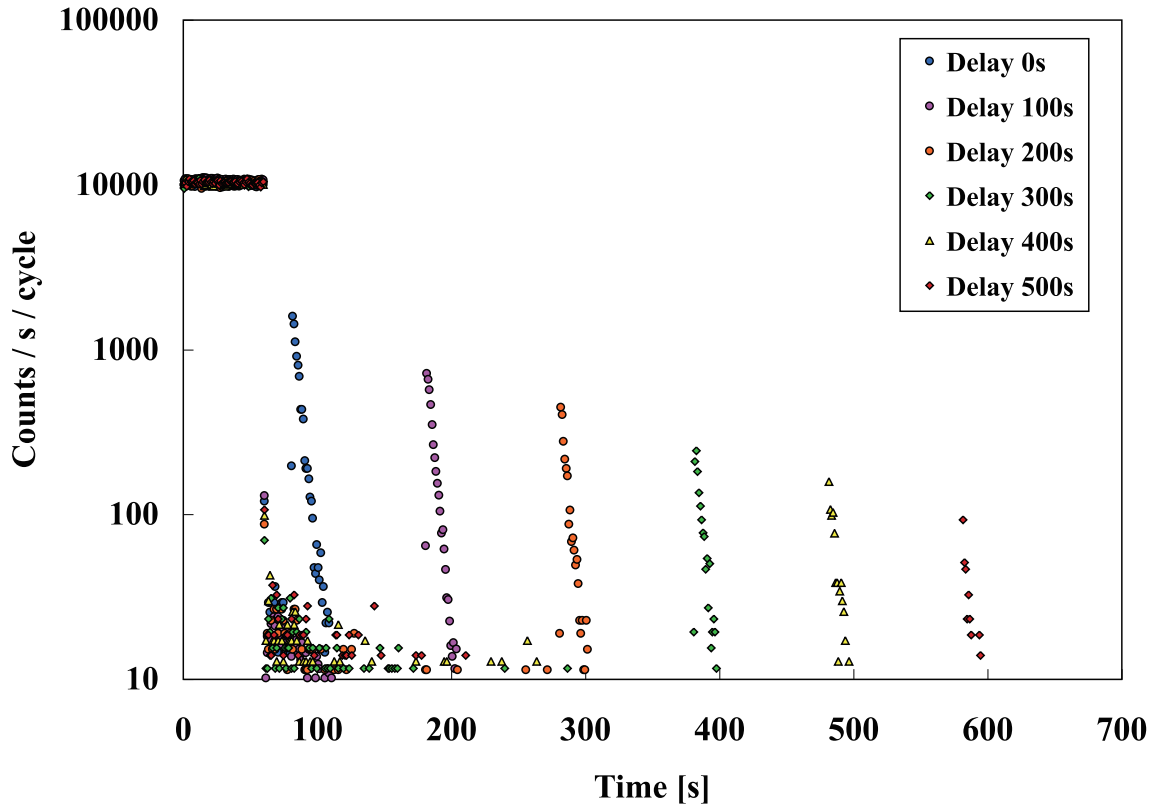

Figure G.5: Time spectra in the UCN storage experiment with the P.E. disk. The height of the P.E. disk was 70 cm. The delay time Δt were 0, 100, 200, 300, 400 and 500 sec.

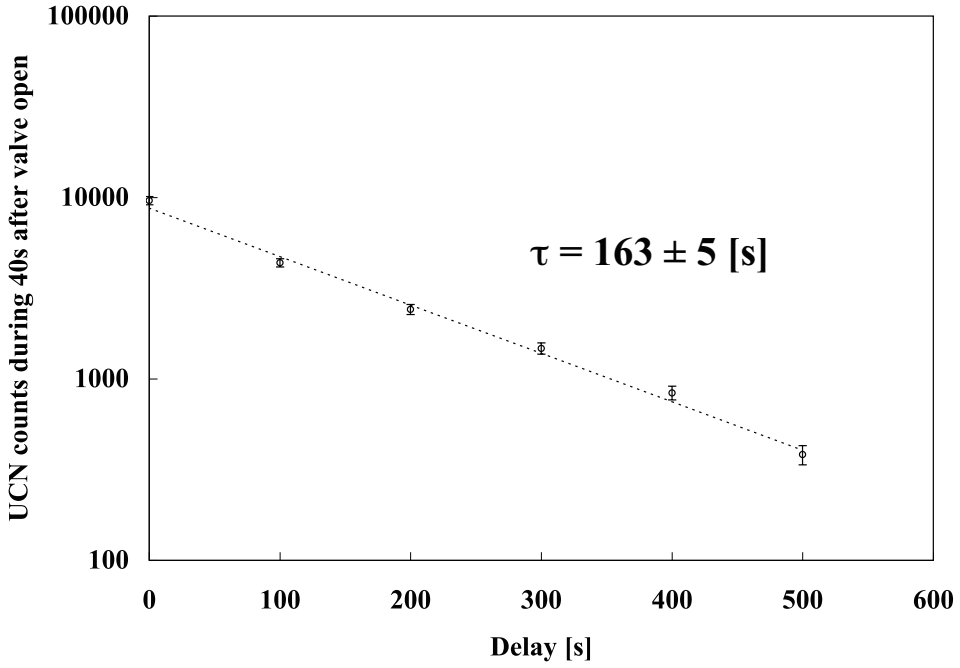

Figure G.6: The total UCN counts as a function of the delay time. The height of the disk h was 70 cm. The UCN storage time was 163 ± 5 sec.

h = 65 cm

The obtained time spectra is shown in Fig. G.7. The time dependence of the total UCN counts is shown in Fig. G.8. The total UCN counts at each delay time are shown in Table G.4.

At this height, the time dependence of the total UCN counts shown in Fig. G.8 appears to have two exponential components. We have less points for the fitting with a double exponential function. So, we used the arithmetic average of the UCN storage time at 70 and 60 cm for τ_1 and τ_2 at this height. The amplitudes of each exponential component were treated as free parameters.

Delay Δt [s]	total UCN counts
0	8886 ± 504
50	5525 ± 332
100	4163 ± 259
200	2402 ± 165

Table G.4: The total UCN counts obtained with the P.E. disk at a height of 65 cm.

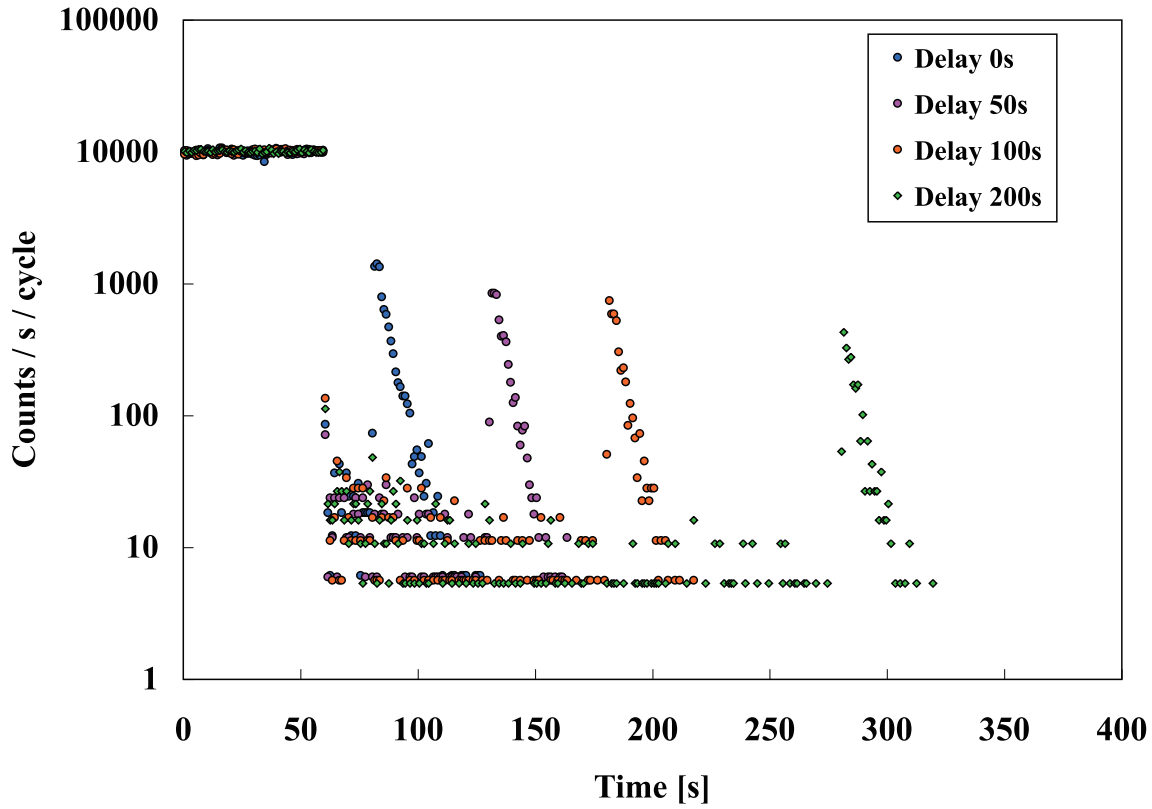

Figure G.7: Time spectra in the UCN storage experiment with the P.E. disk. The height of the P.E. disk was 65 cm. The delay time Δt were 0, 50, 100 and 200 sec.

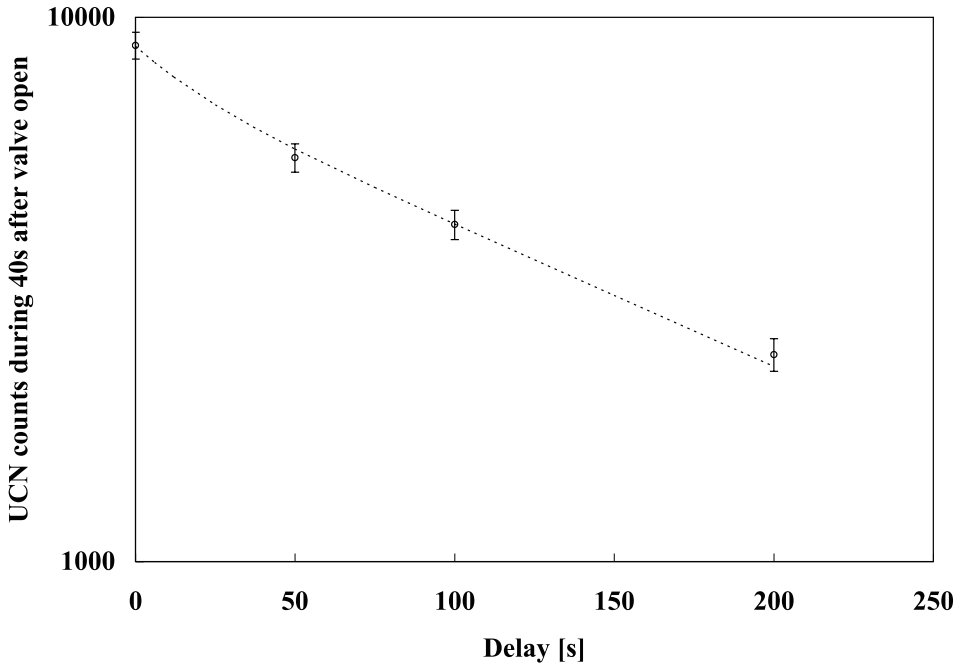

Figure G.8: The total UCN counts as a function of the delay time. The height of the disk h was 65 cm.

h = 60 cm

The obtained time spectra is shown in Fig. G.9. The time dependence of the total UCN counts is shown in Fig. G.10. The total UCN counts at each delay time are shown in Table G.5.

The time dependence of the total UCN counts shown in Fig. G.10 has two exponential components. A double exponential function was used for the fitting. All four parameters were treated as free parameters. The obtained UCN storage time of the short component was 21^{+32}_{-8} sec. And that of the long component was 170^{+10}_{-9} sec.

Delay Δt [s]	total UCN counts
0	7954 ± 444
12	6963 ± 400
25	5693 ± 334
37	5636 ± 323
50	4891 ± 267
75	4067 ± 254
100	3456 ± 176
125	3089 ± 201
150	2750 ± 185
200	1978 ± 142
300	1061 ± 93
400	613 ± 67

Table G.5: The total UCN counts obtained with the P.E. disk at a height of 60 cm.

h = 55 cm

The obtained time spectra is shown in Fig. G.11. The time dependence of the total UCN counts is shown in Fig. G.12. The total UCN counts at each delay time are shown in Table G.6.

The time dependence of the total UCN counts shown in Fig. G.12 appears to have two exponential components. Similarly to the case of 65 cm, we have less points for the fitting with a double exponential function. So, we used the arithmetic average of the UCN storage time at 60 and 50 cm for the fitting parameter τ_1 and τ_2. The amplitudes of each exponential component were treated as free parameters.

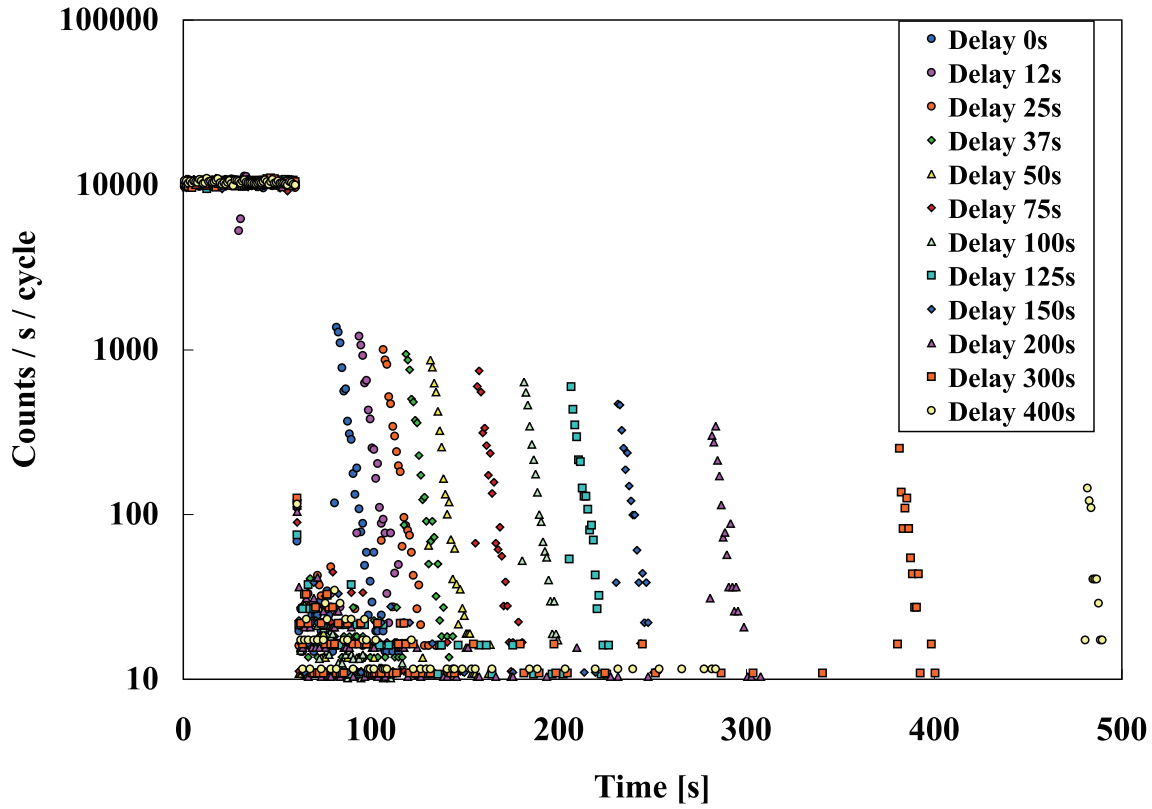

Figure G.9: Time spectra in the UCN storage experiment with the P.E. disk. The height of the P.E. disk was 60 cm. The delay time Δt were 0, 12, 25, 37, 50, 75, 100, 125, 150, 200, 300 and 400 sec.

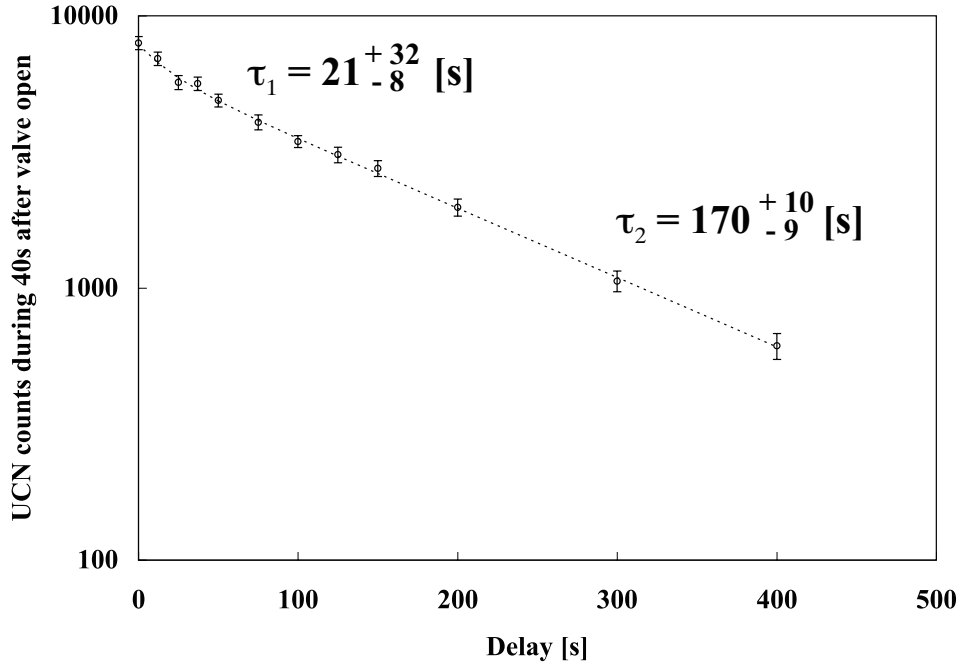

Figure G.10: The total UCN counts as a function of the delay time. The height of the disk h was 60 cm. The UCN storage time of the short component was 21^{+32}_{-8} sec. The UCN storage time of the long component was 170^{+10}_{-9} sec.

Delay Δt [s]	total UCN counts
0	6805 ± 393
50	4283 ± 265
100	3051 ± 198
200	1626 ± 120

Table G.6: The total UCN counts obtained with the P.E. disk at a height of 55 cm.

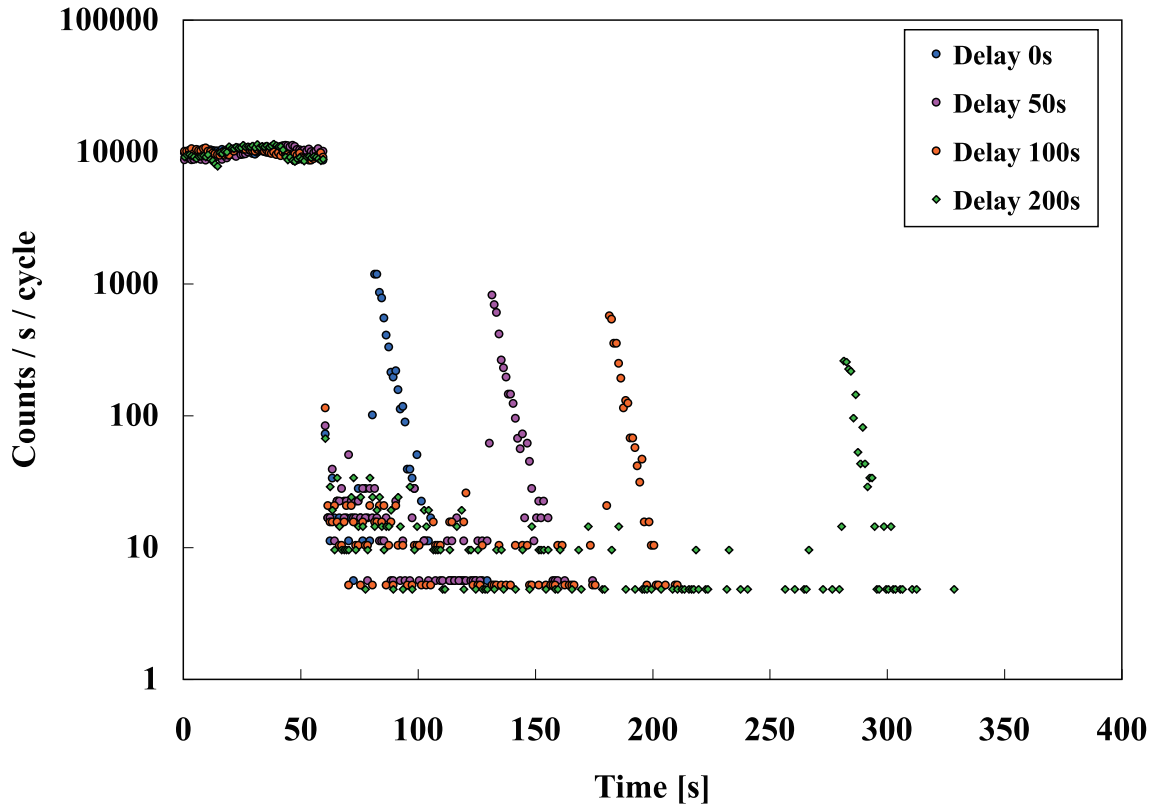

Figure G.11: Time spectra in the UCN storage experiment with the P.E. disk. The height of the P.E. disk was 55 cm. The delay time Δt were 0, 50, 100 and 200 sec.

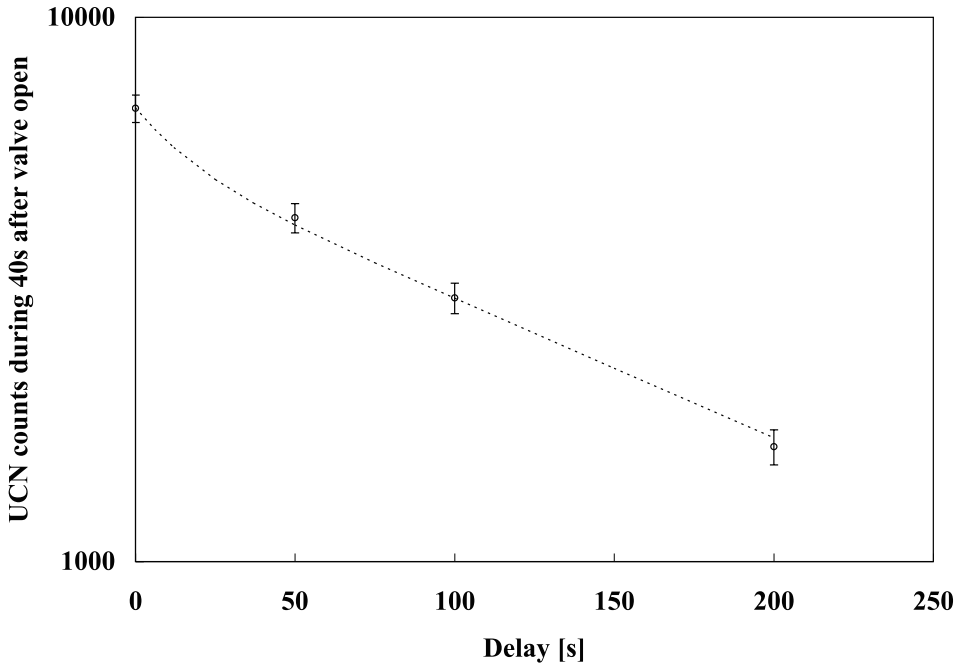

Figure G.12: The total UCN counts as a function of the delay time. The height of the disk h was 55 cm.

h = 50 cm

The obtained time spectra is shown in Fig. G.13. The time dependence of the total UCN counts is shown in Fig. G.14. The total UCN counts at each delay time are shown in Table G.7.

The time dependence of the total UCN counts shown in Fig. G.14 has two exponential components. A double exponential function was used for the fitting. All four parameters were treated as free parameters. The obtained UCN storage time of the short component was 14^{+35}_{-6} sec. And that of the long component was 169^{+7}_{-6} sec.

Delay Δt [s]	total UCN counts
0	5998 ± 341
25	4197 ± 251
50	3345 ± 207
100	2630 ± 136
150	1712 ± 127
200	1397 ± 104
250	1028 ± 88
300	864 ± 75
350	545 ± 58
400	383 ± 50
450	344 ± 45
500	230 ± 38

Table G.7: The total UCN counts obtained with the P.E. disk at a height of 50 cm.

h = 45 cm

The obtained time spectra is shown in Fig. G.15. The time dependence of the total UCN counts is shown in Fig. G.16. The total UCN counts at each delay time are shown in Table G.8.

The time dependence of the total UCN counts shown in Fig. G.16 appears to have two exponential components. Similarly to the case of 55 cm, we have less points for the fitting with a double exponential function. So, we used the arithmetic average of the UCN storage time at 50 and 40 cm for the fitting parameter, τ_1 and τ_2. The amplitudes of each exponential component were treated as free parameters.

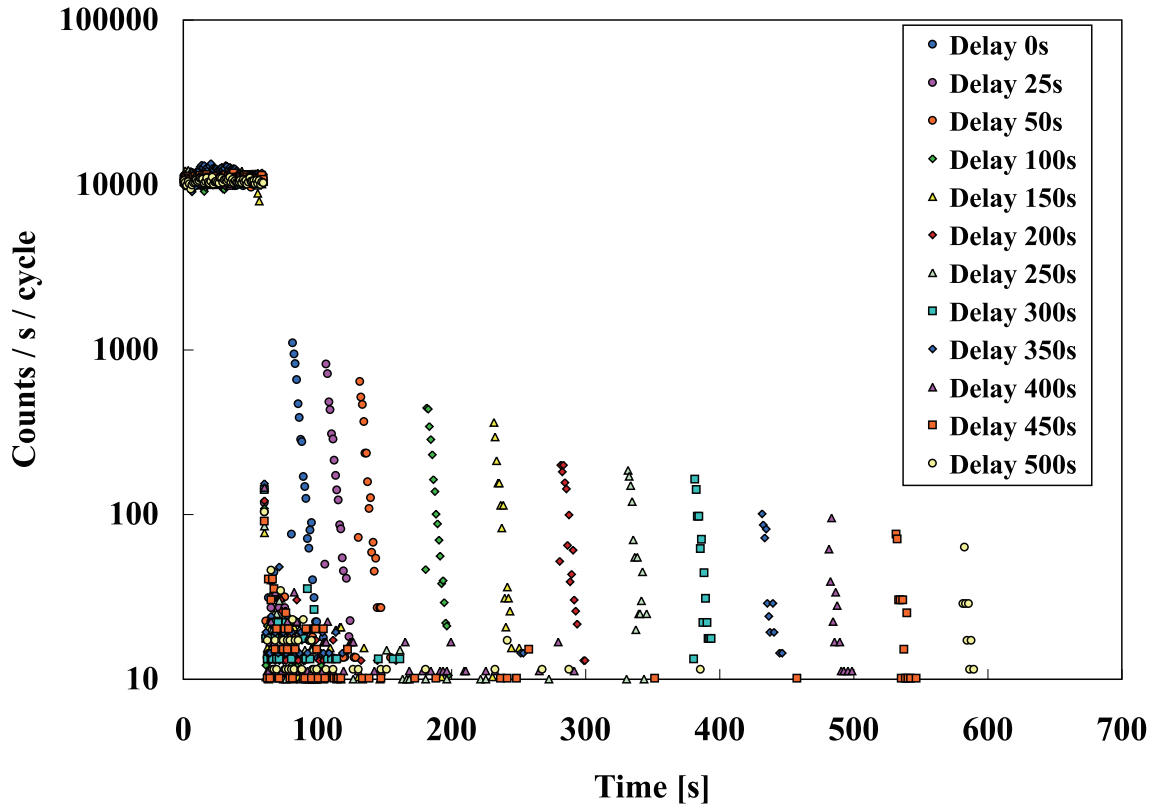

Figure G.13: Time spectra in the UCN storage experiment with the P.E. disk. The height of the P.E. disk was 50 cm. The delay time Δt were 0, 25, 50, 100, 150, 200, 250, 300, 350 400, 450 and 500 sec.

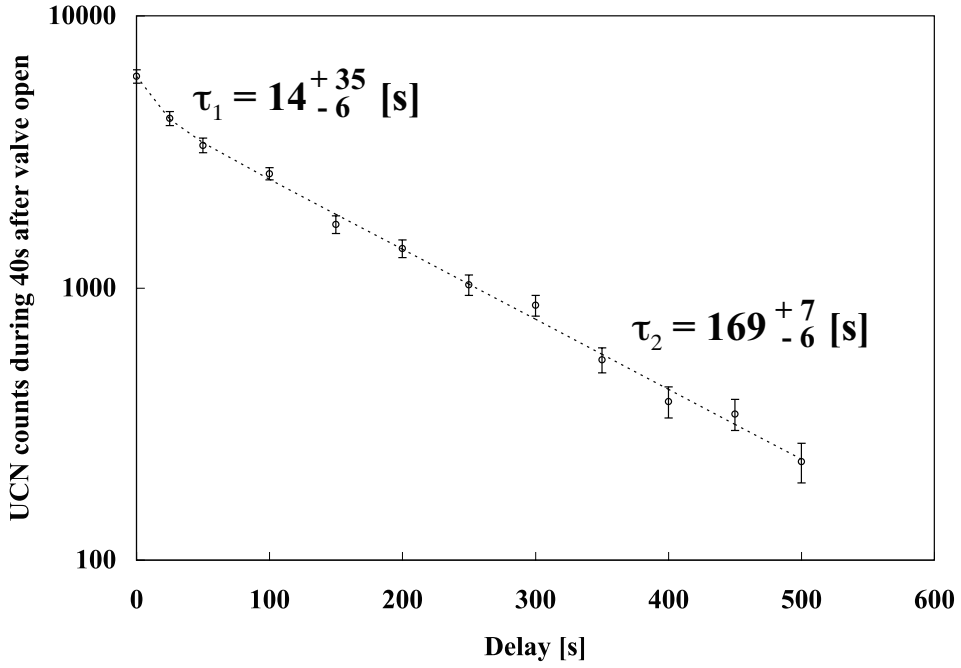

Figure G.14: The total UCN counts as a function of the delay time. The height of the disk h was 50 cm. The UCN storage time of the short component was 14^{+35}_{-6} sec. The UCN storage time of the long component was 169^{+7}_{-6} sec.

Delay Δt [s]	total UCN counts
0	5106 ± 316
50	2859 ± 201
100	2106 ± 155
200	1304 ± 105

Table G.8: The total UCN counts obtained with the P.E. disk at a height of 45 cm.

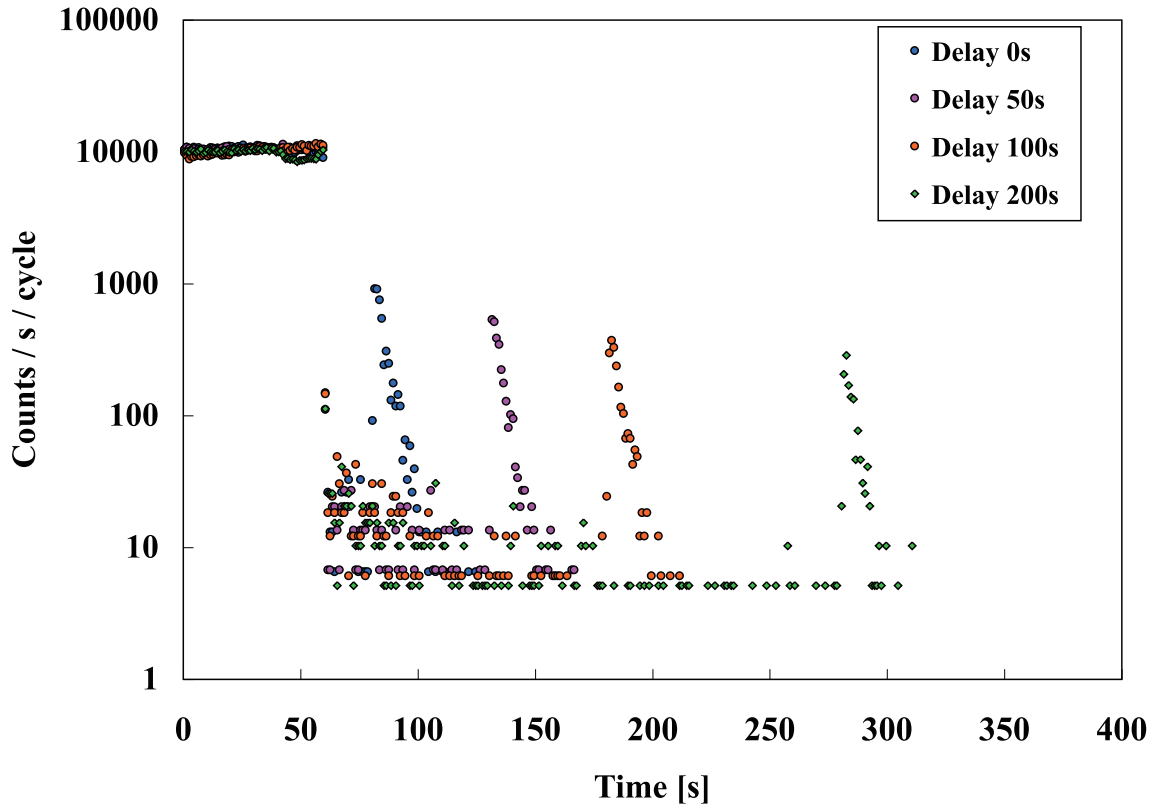

Figure G.15: Time spectra in the UCN storage experiment with the P.E. disk. The height of the P.E. disk was 45 cm. The delay time Δt were 0, 50, 100 and 200 sec.

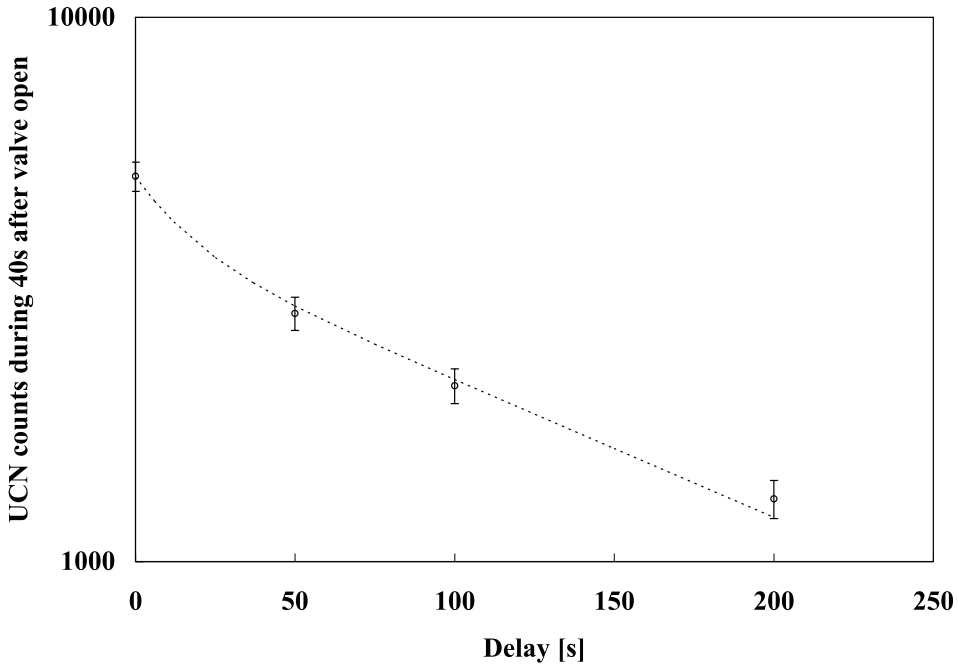

Figure G.16: The total UCN counts as a function of the delay time. The height of the disk h was 45 cm.

h = 40 cm

The obtained time spectra is shown in Fig. G.17. The time dependence of the total UCN counts is shown in Fig. G.18. The total UCN counts at each delay time are shown in Table G.9.

Fitting the time dependence curve, the UCN storage time of the short component τ_1 was obtained to be 21^{+16}_{-6} sec. And that of the long component τ_2 was obtained to be 176^{+12}_{-10} sec.

Delay Δt [s]	total UCN counts
0	4579 ± 270
12	3607 ± 230
25	3054 ± 196
50	2611 ± 172
100	1664 ± 89
150	1357 ± 108
200	1074 ± 87
250	732 ± 74
300	487 ± 51
400	333 ± 32

Table G.9: The total UCN counts obtained with the P.E. disk at a height of 40 cm.

h = 35 cm

The obtained time spectra is shown in Fig. G.19. The time dependence of the total UCN counts is shown in Fig. G.20. The total UCN counts at each delay time are shown in Table G.10.

The curve of the time dependence of the total UCN counts shown in Fig. G.20 was fitted by a double exponential function. As well as the previous cases, τ_1 and τ_2 of this curve were substituted by the arithmetic averages of the UCN storage time at h = 40 and 30 cm.

Delay Δt [s]	total UCN counts
0	3623 ± 234
50	1785 ± 140
100	1255 ± 110
200	633 ± 71

Table G.10: The total UCN counts obtained with the P.E. disk at a height of 35 cm.

h = 30 cm

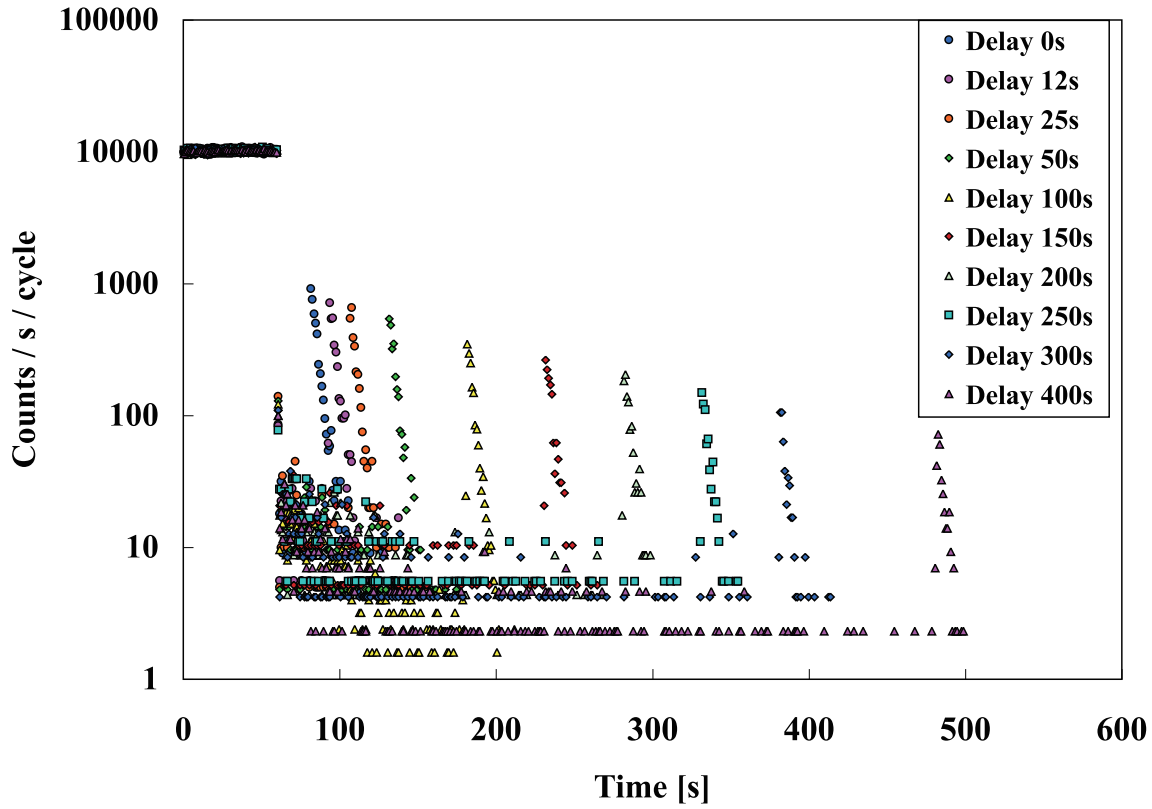

Figure G.17: Time spectra in the UCN storage experiment with the P.E. disk. The height of the P.E. disk was 40 cm. The delay time Δt were 0, 12, 25, 50, 100, 150, 200, 250, 300 and 400 sec.

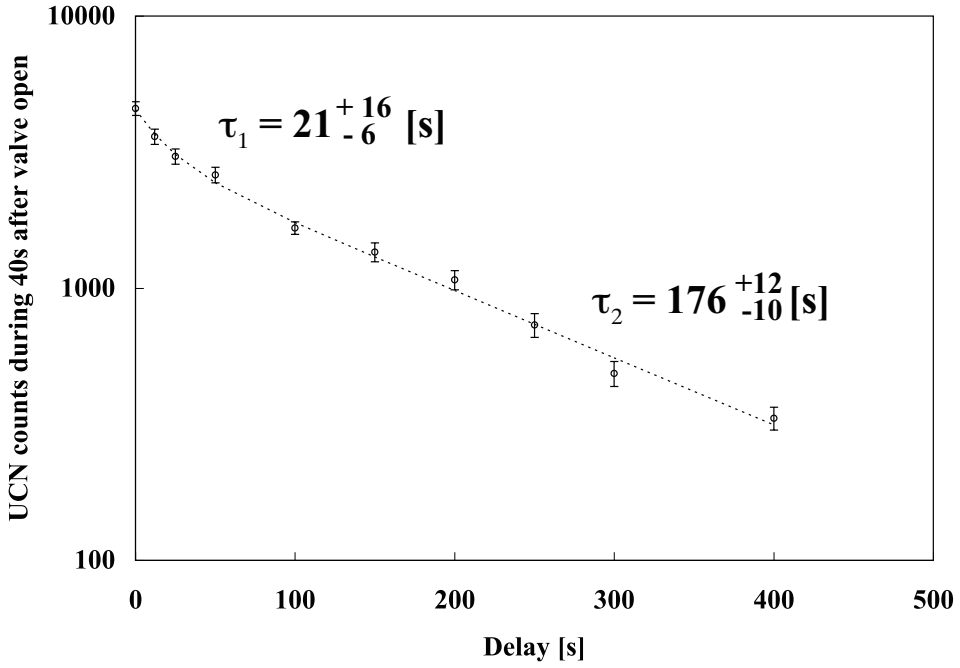

Figure G.18: The total UCN counts as a function of the delay time. The height of the disk h was 40 cm. The UCN storage time of the short component was 21^{+16}_{-6} sec. The UCN storage time of the long component was 176^{+12}_{-10} sec.

The obtained time spectra is shown in Fig. G.21. The total UCN counts as a function of the delay time is shown in Fig. G.22. The total UCN counts at each delay time are shown in Table G.11.

Fitting the curve shown in Fig. G.22, the UCN storage time of the short component τ_1 was obtained to be 21^{+15}_{-6} sec. And that of the long component τ_2 was obtained to be 163 ± 7 sec.

h = 25 cm

The obtained time spectra is shown in Fig. G.23. The time dependence of the total UCN counts is shown in Fig. G.24. The total UCN counts at each delay time are shown in Table G.12.

The curve shown in Fig. G.24 was fitted by a double exponential function. Although the number of the data points was enough for the fitting with four free parameters, the fitting curve could not be smooth due to the statistical dispersion. So, we substituted τ_1 and τ_2 by the arithmetic averages of the UCN storage time at h = 30 and 20 cm.

h = 20 cm

Fig. G.25 shows the time spectra obtained in the case with the P.E. disk at a height of 20 cm. The total UCN counts as a function of the delay time is shown in Fig. G.26. The UCN storage time of the short component was $\tau_1 = 10.3^{+4.0}_{-2.3}$ sec and that of the long component was

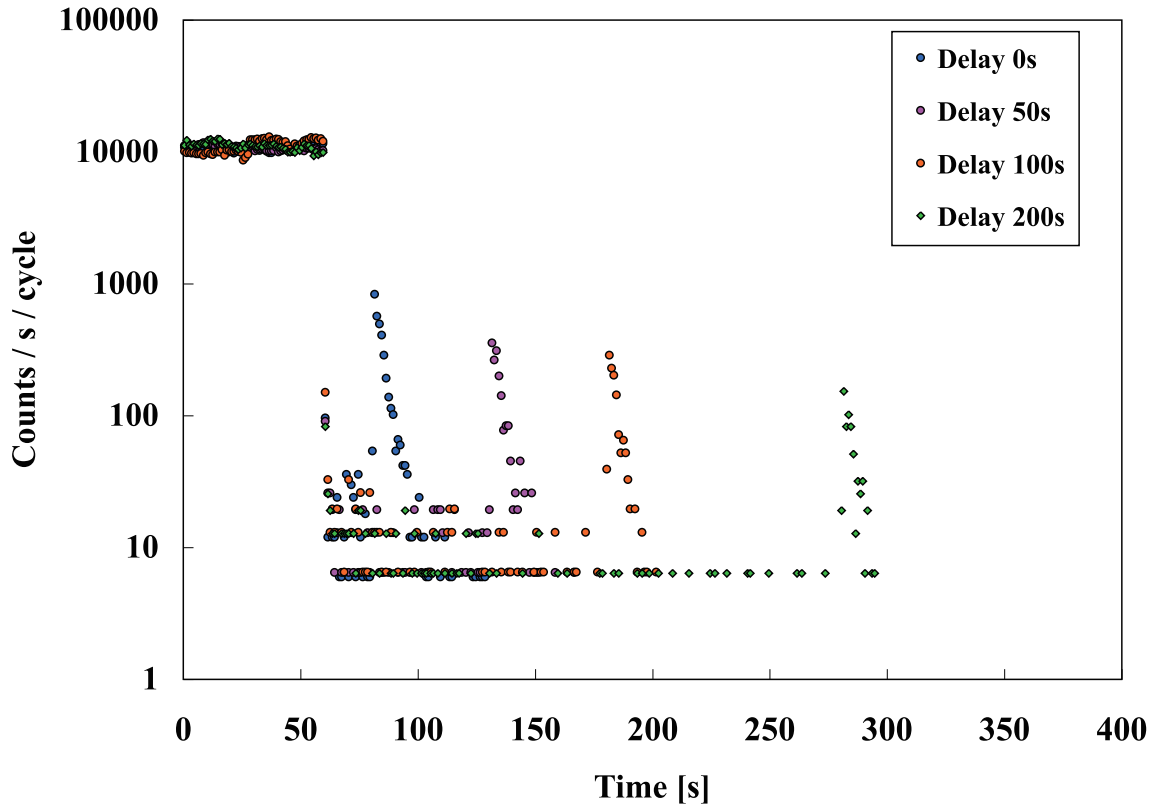

Figure G.19: Time spectra in the UCN storage experiment with the P.E. disk. The height of the P.E. disk was 35 cm. The delay time Δt were 0, 50, 100 and 200 sec.

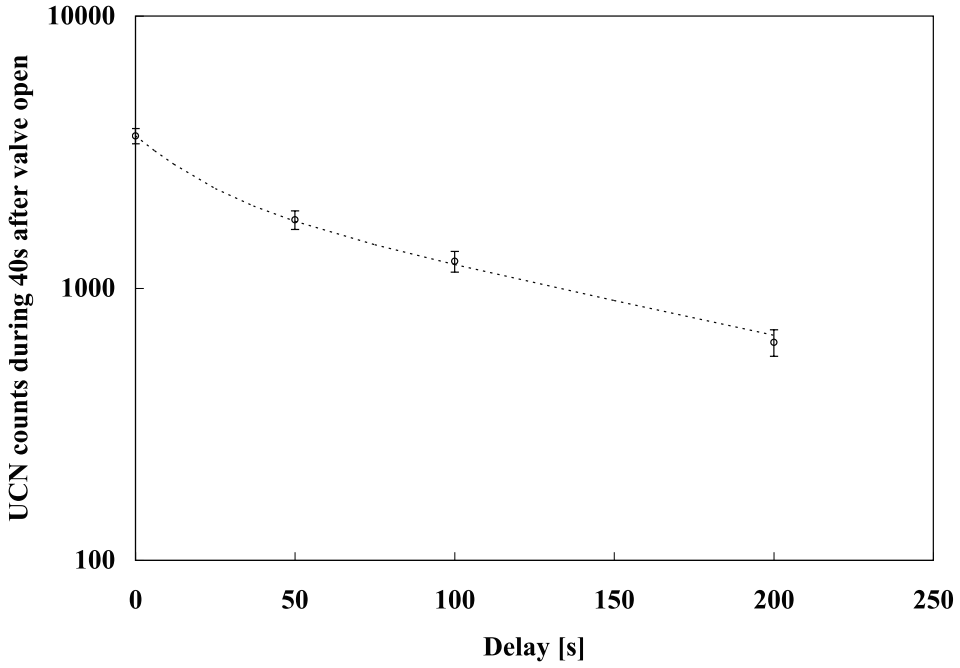

Figure G.20: The total UCN counts as a function of the delay time. The height of the disk h was 35 cm.

$\tau_2 = 154^{+13}_{-11}$ sec. The total UCN counts at each delay time are shown in Table G.13.

h = 15 cm

Fig. G.27 shows the time spectra obtained in the case with the P.E. disk at a height of 15 cm. The total UCN counts as a function of the delay time is shown in Fig. G.28. The UCN storage time of the short component was $\tau_1 = 13^{+11}_{-4}$ sec and that of the long component was $\tau_2 = 146^{+8}_{-7}$ sec. The total UCN counts at each delay time are shown in Table G.14.

h = 10 cm

Fig. G.29 shows the time spectra obtained in the case with the P.E. disk at a height of 10 cm. The total UCN counts as a function of the delay time is shown in Fig. G.30. The UCN storage time of the short component was $\tau_1 = 5.8^{+3.3}_{-1.5}$ sec and that of the long component was $\tau_2 = 146^{+15}_{-13}$ sec. The total UCN counts at each delay time are shown in Table G.15.

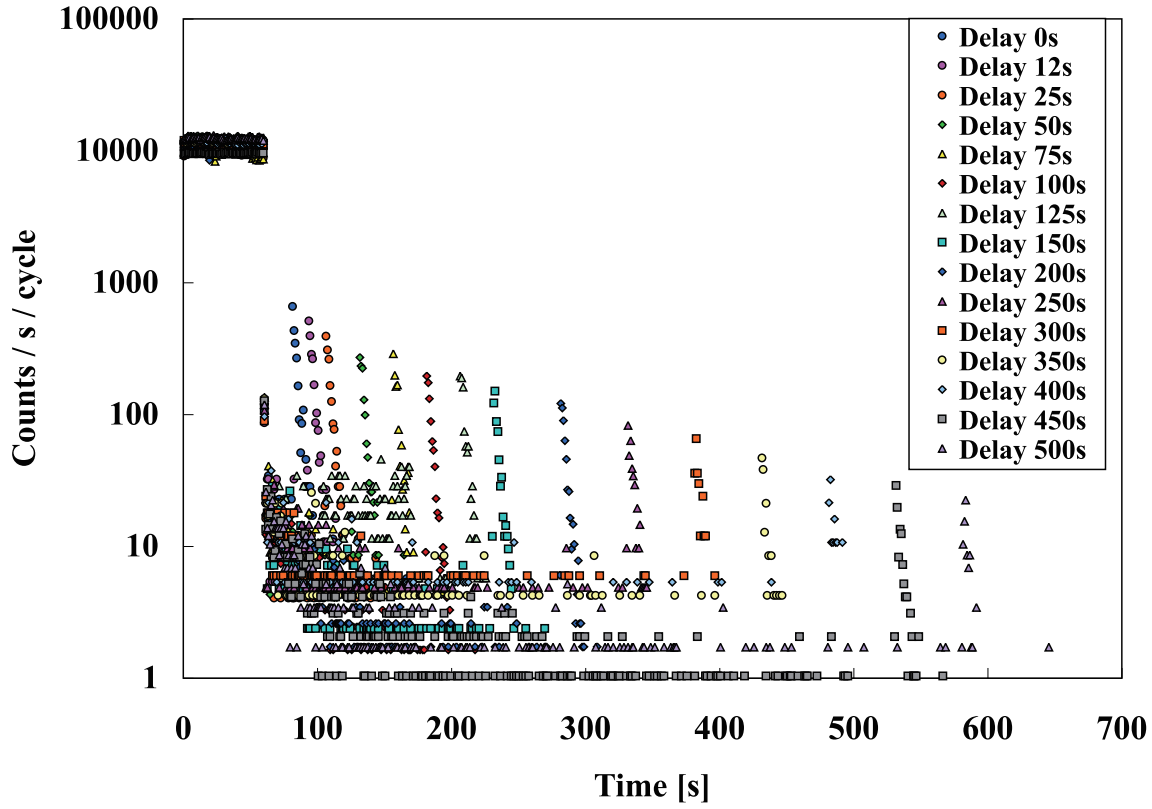

Figure G.21: Time spectra in the UCN storage experiment with the P.E. disk. The height of the P.E. disk was 30 cm. The delay time Δt were 0, 12, 25, 50, 75, 100, 125, 150, 200, 250, 300, 350, 400, 450 and 500 sec.

Delay Δt [s]	total UCN counts
0	2491 ± 173
12	2201 ± 155
25	1688 ± 118
50	1274 ± 98
75	1174 ± 94
100	874 ± 50
125	915 ± 86
150	638 ± 50
200	573 ± 36
250	386 ± 48
300	233 ± 39
350	157 ± 27
400	124 ± 27
450	118 ± 12
500	81 ± 12

Table G.11: The total UCN counts obtained with the P.E. disk at a height of 30 cm.

Delay Δt [s]	total UCN counts
0	1929 ± 146
25	1049 ± 98
50	1067 ± 98
100	584 ± 66
200	367 ± 51

Table G.12: The total UCN counts obtained with the P.E. disk at a height of 25 cm.

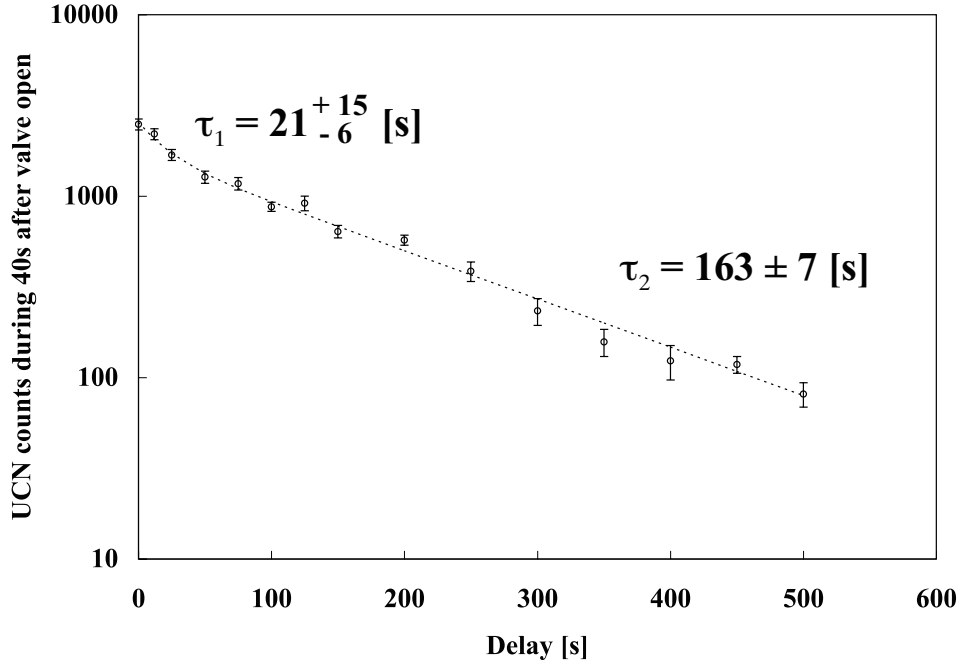

Figure G.22: The total UCN counts as a function of the delay time. The height of the disk h was 30 cm. The UCN storage time of the short component was 21^{+15}_{-6} sec. The UCN storage time of the long component was 163 ± 7 sec.

Delay Δt [s]	total UCN counts
0	1618 ± 122
6	1179 ± 94
12	928 ± 79
25	787 ± 69
50	583 ± 58
100	383 ± 26
150	263 ± 37
200	254 ± 36
250	164 ± 28
300	144 ± 26
400	48 ± 10

Table G.13: The total UCN counts obtained with the P.E. disk at a height of 20 cm.

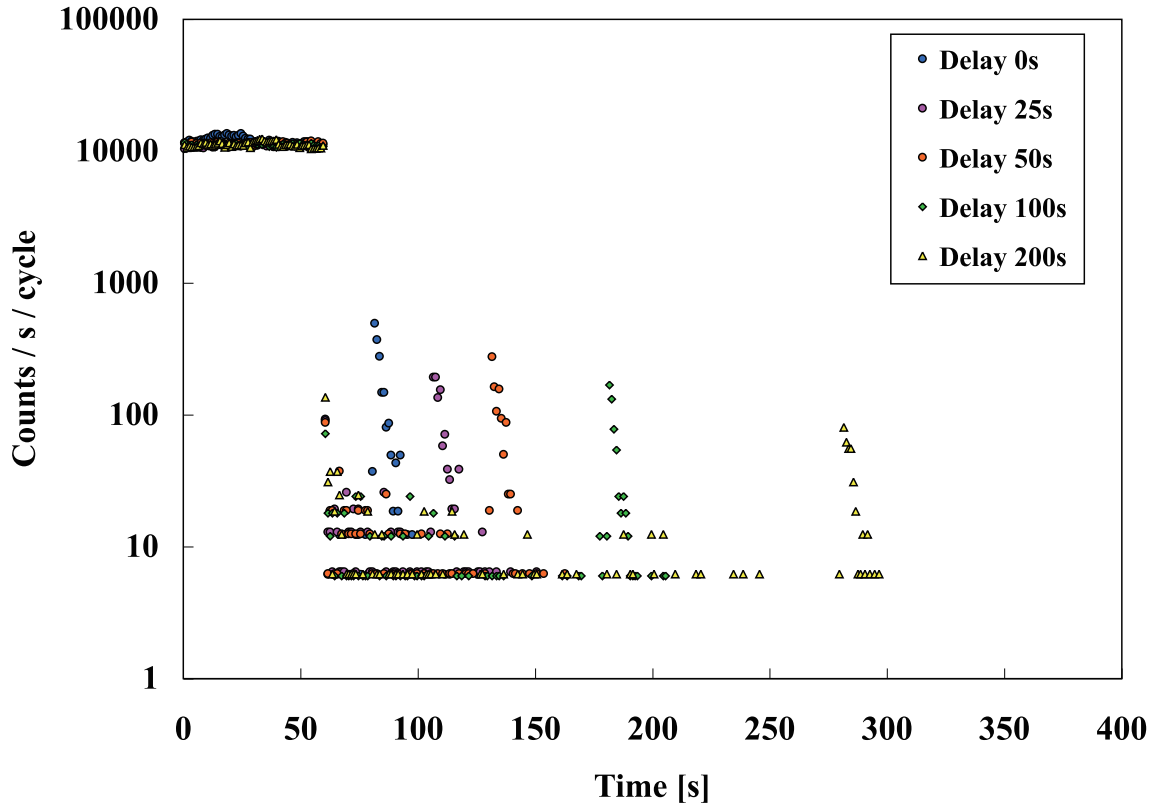

Figure G.23: Time spectra in the UCN storage experiment with the P.E. disk. The height of the P.E. disk was 25 cm. The delay time Δt were 0, 25, 50, 100 and 200 sec.

Delay Δt [s]	total UCN counts
0	787 ± 77
12	532 ± 59
25	439 ± 52
50	317 ± 44
75	277 ± 40
100	244 ± 20
150	146 ± 14
200	112 ± 12
250	77 ± 9
300	62 ± 6
350	40 ± 7
400	29 ± 4

Table G.14: The total UCN counts obtained with the P.E. disk at a height of 15 cm.

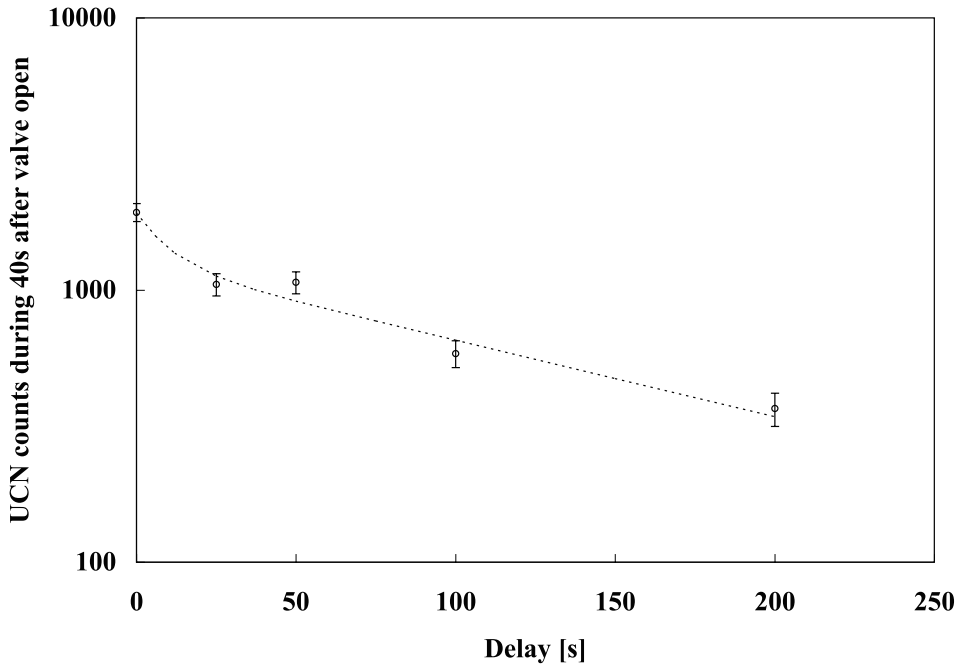

Figure G.24: The total UCN counts as a function of the delay time. The height of the disk h was 25 cm.

Delay Δt [s]	total UCN counts
0	521 ± 34
6	301 ± 44
12	279 ± 28
25	228 ± 28
50	157 ± 19
75	120 ± 19
100	99 ± 11
150	61 ± 8
200	56 ± 8
250	40 ± 7
300	23 ± 4

Table G.15: The total UCN counts obtained with the P.E. disk at a height of 10 cm.

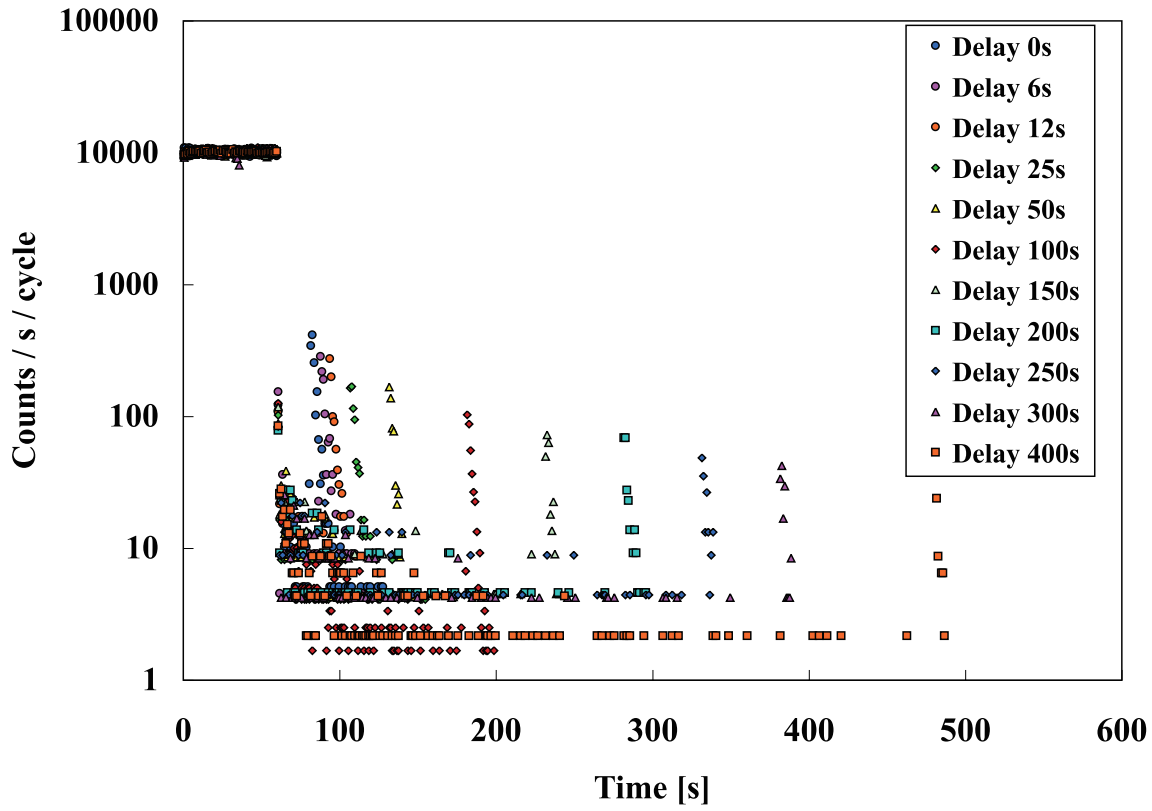

Figure G.25: Time spectra in the UCN storage experiment with the P.E. disk at a height of 20 cm. A proton beam with a power of 400 W was irradiated for 60 sec. The delay time Δt were 0, 6, 12, 25,50, 100, 150, 200, 250, 300 and 400 sec.

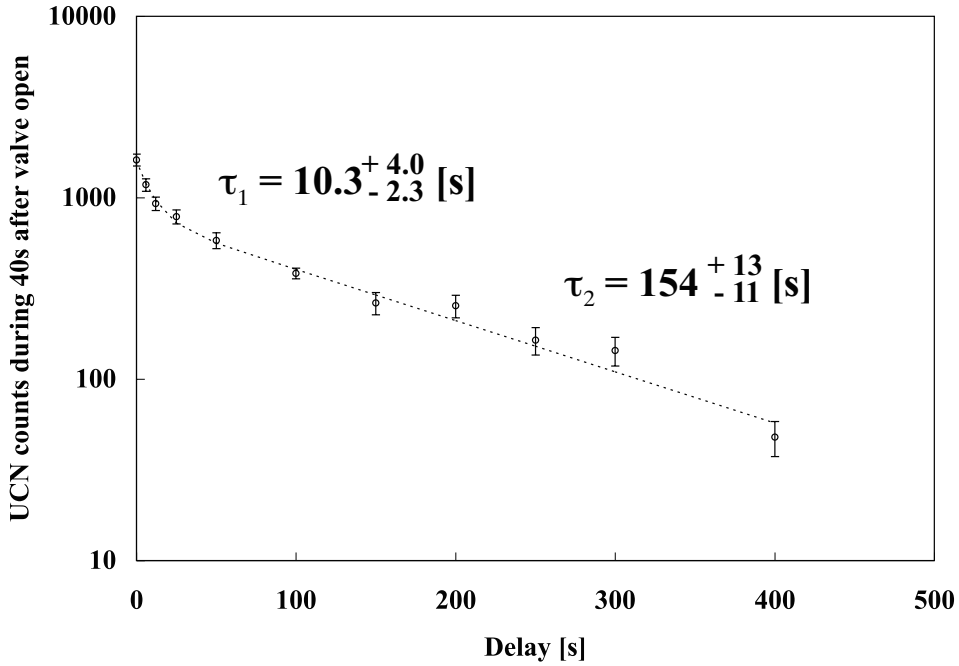

Figure G.26: The total UCN counts as a function of the delay time. The height of the disk h was 20 cm. The UCN storage time were $10.3^{+4.0}_{-2.3}$ sec and 154^{+13}_{-11} sec.

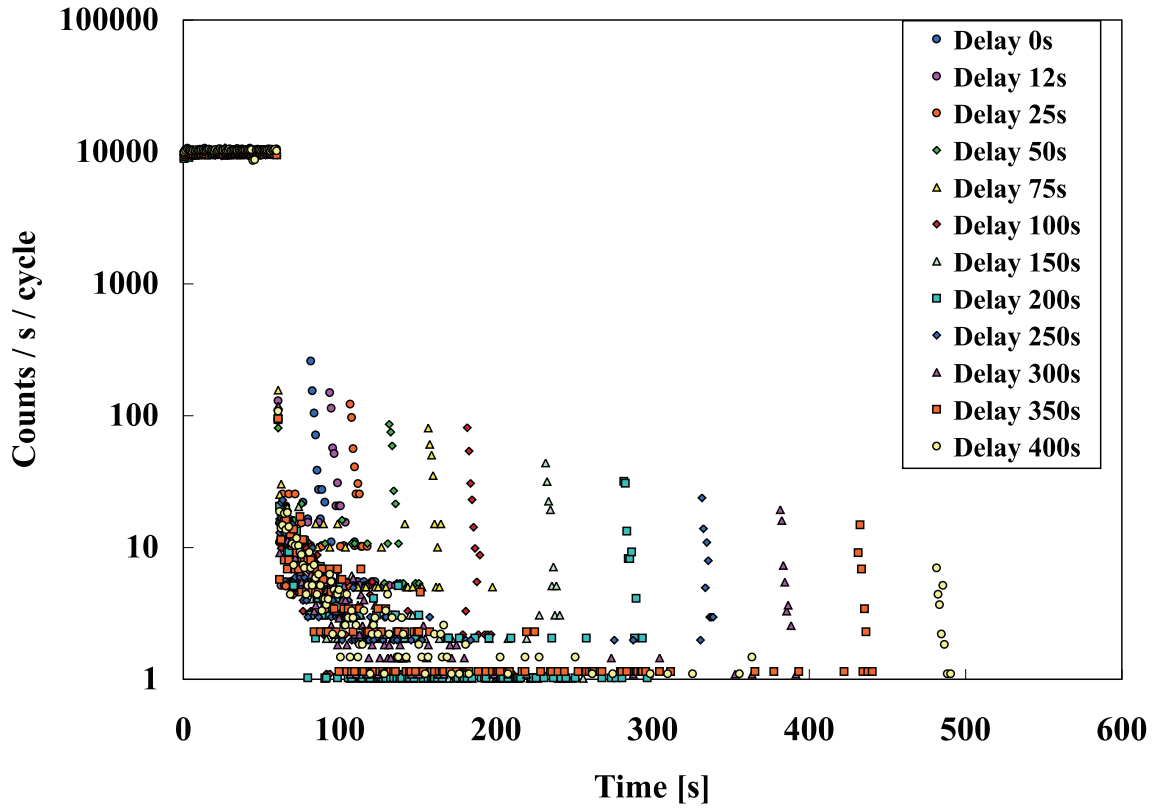

Figure G.27: Time spectra in the UCN storage experiment with the P.E. disk. The height of the P.E. disk was 15 cm. The delay time Δt were 0, 12, 25, 50, 75, 100, 150, 200, 250, 300, 350 and 400 sec.

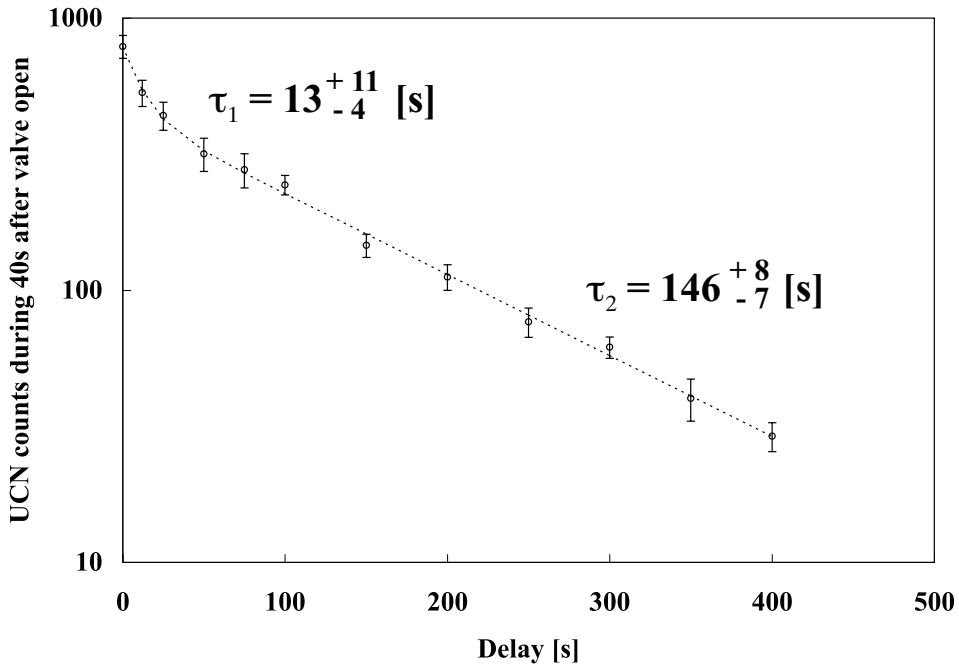

Figure G.28: The total UCN counts as a function of the delay time. The height of the disk h was 15 cm. The UCN storage time of the short component was 13^{+11}_{-4} sec. The UCN storage time of the long component was 146^{+8}_{-7} sec.

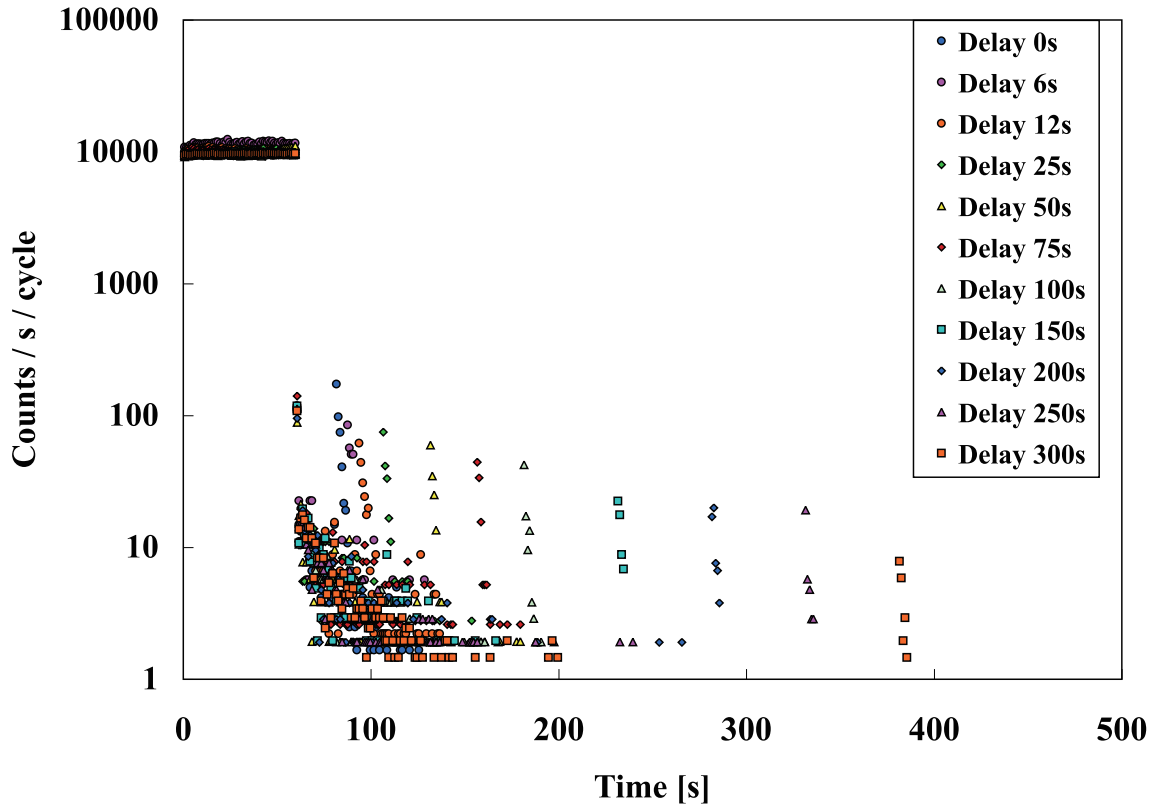

Figure G.29: Time spectra in the UCN storage experiment with the P.E. disk. The height of the P.E. disk was 10 cm. The delay time Δt were 0, 6, 12, 25, 50, 75, 100, 150, 200, 250 and 300 sec.

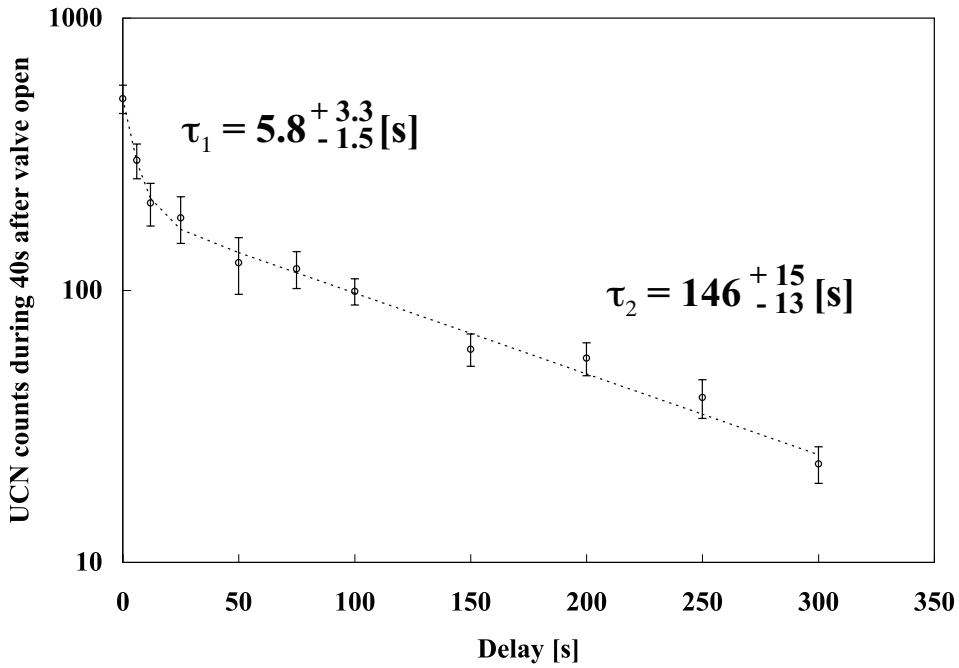

Figure G.30: The total UCN counts as a function of the delay time. The height of the disk h was 10 cm. The UCN storage time of the short component was $5.8^{+3.3}_{-1.5}$ sec. The UCN storage time of the long component was 146^{+15}_{-13} sec.

Bibliography

[1] E. Fermi and W. N. Zinn, Phys. Rev. **70** (1946) 103.

[2] E. Fermi and L. Marshall, Phys. Rev. **71** (1947) 666.

[3] Max Tegmark, et al., astro-ph/0310723.

[4] WMAP Collaboration, D.N.Spergel *et. al.*, Astrophys. J. Suppl. **148** (2003) 175.

[5] C. A. Baker, D. D. Doyle, P. Geltenbort, K. Green, M. G. D. van der Grinten, P. G. Harris, P. Iaydjiev, S. N. Ivanov, D. J. R. May, J. M. Pendlebury, J. D. Richardson, D. Shiers, and K. F. Smith, Phys. Rev. Lett. **97** (2006) 131801.

[6] Norman F. Ramsey, Phys. Rev. **78** (1950) 695.

[7] J. M. Pendlebury et al., Phys. Rev. A **70**, 032102 (2004)

[8] A. Styerl, Nucl. Inst. Meth. **125** (1975) 461.

[9] A. Steyerl et al., Phys. Lett. A **116** (1986) 347.

[10] V. I. Luschikov, Y. N. Pokotolovsky, A. V. Strelkov, F. L. Shapiro, Sov. Phys. JETP Lett. **9** (1969) 23.

[11] A. Steyerl, Phys. Lett. B **29** (1969) 33.

[12] R. Golub and J. M. Pendlebury, Phys. Lett. A **62** (1977) 337.

[13] A. D. B. Woods and R. A. Cowley, Rep. Prog. Phys. **36** (1973) 1135-1231.

[14] H. J. Maris, Rev. Mod. Phys. **49** (1977) 341.

[15] SNS Neutron EDM Experiment ; http://p25ext.lanl.gov/edm/edm.html

[16] R. Golub and K. Boning, Z. Phys. **B51** (1983) 95-98.

[17] Z-Ch. Yu, S. S. Malik, and R. Golub, Z. Phys. **B62** (1986) 137.

[18] C. A. Baker., et al., Phys. Lett. **A308** (2003) 67-74.

[19] O. Zimmer et al., Phys. Rev. Lett. **107**, 134801 (2011)

[20] C. L. Morris, et al., Phys. Rev. Lett. **89** (2002) 272501.

[21] Roger E. Hill, et al., Nucl. Inst. Meth. A **440** (2000) 674.

[22] A. Sauders, et al., Phys. Lett. B **593** (2004) 55.

[23] B. Lauss, arXiv:1202.6003v1 [nucl-ex] 27 Feb 2012

[24] G. Placzek and L. Van Hove, Phys. Rev. **93** (1954) 1207.

[25] M. Cohen and R. P. Feynman, Phys. Rev. **107** (1957) 13.

[26] E. Korobkina, et al., Phys. Lett. A **301** (2002) 462.

[27] Leon Van Hove, Phys. Rev, **95** (1954) 249.

[28] A. D. B. Woods and R. A. Cowley, Phys. Rev. Lett. **23** (1970) 646.

[29] A. D. B. Woods and R. A. Cowley, Rep. Prog. Phys. **36** (1973) 1135-1231.

[30] K. H. Anderson, et al., J. Phys.: Condens. Matter **6** (1994) 821-834.

[31] M. R. Gibbs, et al., J. Phys.: Condens. Matter **11** (1999) 603-628.

[32] M. R. Gibbs, et al., J. Low. Temp. Phys. 120 (2000) 55.

[33] P. Schmidt-Wellenburg, et al., Nucl. Inst. Meth. **A611** (2009) 259-262.

[34] K. Niita, N. Matsuda, Y. Iwamoto, H. Iwase, T. Sato, H. Nakashima, Y. Sakamoto and L. Sihver, PHITS: Particle and Heavy Ion Transport code System, Version 2.23, JAEA-Data/Code 2010-022 (2010)

[35] R. Golub, Phys. Lett. **72A** (1979) 387.

[36] R. Golub et al., Z. Phys. B **51** (1983) 187.

[37] E. Gutsmiedl et al., Physica B **169** (1991) 503.

[38] H. Yoshiki et al., Phys. Rev. Lett. **68** (1992) 1323.

[39] H. Yoshiki et al., Cryogenics **45** (2005) 399.

[40] W. A. Lanford and R. Golub, Phys. Rev. Lett. **39** (1977) 1509.

[41] Y. Kawabata et al., Nucl. Inst. Meth. **B30** (1988) 557.

[42] S. K. Lamoreaux and R. Golub, JETP Lett. **58** (1993) 792.

[43] A. V. Dementyev, N. M. Sobolevsky and Yu. Ya. Stavissky, Nucl. Inst. Meth. A **374** (1996) 70.

[44] A. Latourneau, J. Galin, F. Goldenbaum, B. Lott, A. Pegahaire, M. Enke, D. Hilscher, U. Jahnke, K. Nunighoff, D. Filges, R. D. Neef, N. Paul, H. Schaal, G. Sterzenbach and A. Tietze, Nucl. Inst. Meth. B **170** (2000) 299.

[45] L. V. Groshev, et al., Proc. All-Union COnference on Neutron Physics, Part 4, 1974, p. 264 (in Russian)

[46] V. K. Ignatovich, The Physics of Ultracold Neutrons, Clarendon, Oxford, 1990, p 62.

[47] K. Inoue, Journal of Nuclear Science and Technology, **7** [11] (1970) 580.

[48] E. Korobkina, R. Golub, J. Butterworth, P. Geltenbort and S. Arzumanov, Phys. Rev. B **70** (2004) 035409.

[49] S. Rezaie-Serej and R. A. Outlaw, J. Vac. Sci. Technol. A. **12(5)** (1994) 2814.

[50] R. Golub, D. Richardson, and S. Lamoreaux, *Ultra-Cold Neutrons* (Adam Hilger, 1991).

[51] V. K. Ignatovich, *The Physics of Ultracold Neutrons* (Oxford Science Publications 1986, 1990).

[52] A. Steyerl, Nucl. Inst. Meth. **101** (1972) 295.

[53] I. Altarev et al., Nucl. Inst. Meth **A570** (2007) 101.

[54] Y. Masuda et al., Phys. Rev. Lett. **89** (2002) 284801.

[55] F. Tervisidis and N. Tsagas, Nucl. Inst. Meth. **A305** (1991) 433.

[56] K. Inoue, Journal of Nuclear Science and Technology, **7** [11] (1970) 580.

[57] P. Ageron et al., Z. Phys. **B59** (1985) 261.

[58] Neutron Data Booklet, Albert-Jose Dianoux (ILL, Grenoble) and Gerry Lander (ITU, Karlsruhe) : OCP Science ; 2nd Edition (August 2003)

[59] F. Atchison et al., Nucl. Inst. Meth. **A552** (2005) 513.

[60] S. Agostinelli et al., Nucl. Inst. Meth. **A506** (2003) 250.